Symmetries and Boundary Conditions of Topological Materials
General Theory and Applications

Rosdahl, Tomas

DOI
10.4233/uuid:fc159c49-40c7-43e4-b0a5-3ebf0bbd8b53

Publication date
2019

Document Version
Final published version

Citation (APA)
Rosdahl, T. (2019). *Symmetries and Boundary Conditions of Topological Materials: General Theory and Applications*. [Dissertation (TU Delft), Delft University of Technology]. https://doi.org/10.4233/uuid:fc159c49-40c7-43e4-b0a5-3ebf0bbd8b53

Symmetries and Boundary Conditions of Topological Materials: General Theory and Applications

SYMMETRIES AND BOUNDARY CONDITIONS OF TOPOLOGICAL MATERIALS: GENERAL THEORY AND APPLICATIONS

Proefschrift

ter verkrijging van de graad van doctor
aan de Technische Universiteit Delft,
op gezag van de Rector Magnificus prof. dr. ir. T.H.J.J. van der Hagen.
voorzitter van het College voor Promoties,
in het openbaar te verdedigen op
maandag 25 maart 2019 om 15:00 uur

door

Tómas Örn ROSDAHL

Master of Science in Physics,
Universiteit van IJsland, Reykjavik, IJsland,
geboren te Reykjavik, IJsland.

Dit proefschrift is goedgekeurd door de

promotor: Dr. A. R. Akhmerov
copromotor: Dr. M. T. Wimmer

Samenstelling promotiecommissie:

Rector Magnificus,	voorzitter
Dr. A. R. Akhmerov	Technische Universiteit Delft, promotor
Dr. M. T. Wimmer	Technische Universiteit Delft, copromotor

Onafhankelijke leden:

Prof. dr. A. F. Otte	Technische Universiteit Delft
Prof. dr. F. Hassler	RWTH Aken, Duitsland
Prof. dr. G. A. Steele	Technische Universiteit Delft
Prof. dr. İ. Adagideli	Sabancı Universiteit, Turkije
Dr. J. H. Bárðarson	KTH Koninklijke Technische Hogeschool, Zweden

This work was supported by ERC Starting Grant 638760, the Netherlands Organisation for Scientific Research (NWO/OCW), as part of the Frontiers of Nanoscience program, and the US Office of Naval Research.

Printed by: Gildeprint

Cover: Momentum space representation of a superconducting order parameter with d-wave or f-wave pairing symmetry (front), and s-wave, p-wave, d-wave or f-wave pairing symmetry (back). Designed by Björn Snorri Rosdahl and Tómas Örn Rosdahl.

Casimir PhD Series, Delft-Leiden 2019-01

ISBN 978-94-6366-144-7

An electronic version of this dissertation is available at
`http://repository.tudelft.nl/`.

CONTENTS

SUMMARY

Topological materials are novel phases of quantum matter that have attracted considerable interest within condensed matter physics in recent years. In this context, topological classification applies to Hamiltonians with an energy gap, such that it is the topological classification of the bulk material Hamiltonian that distinguishes nontrivial topological phases of matter and the ordinary, trivial phase. Transitions between distinct topological phases thus always involve a closing and reopening of the energy gap. A consequence of this simple fact is that edge states appear at interfaces where the topological phase changes, including interfaces of topological materials with the vacuum, which is a trivial insulator. These topological edge states are a manifestation of nontrivial bulk topology, and therefore robust to any perturbations that do not alter the topological classification, which makes them attractive for applications.

In many cases, the topological classification only applies to Hamiltonians that respect certain symmetries, in which case the topological phase is robust to perturbations that do not alter the topological classification or break the protecting symmetries. For the edge states of symmetry-protected topological phases, the symmetry classification of the edge itself also plays a role. If the edge itself breaks any protecting symmetries, the edge states lose their topological protection, even though the bulk Hamiltonian still respects the symmetries.

The topic of this thesis is the interplay of topology, symmetry and edges, both in general theoretical terms, and applied to a few specific materials or heterostructures of contemporary relevance in condensed matter physics. This thesis starts with a brief introduction to symmetries in quantum mechanics, and a glimpse into the world of topology in condensed matter. In addition, an example is given of how topology, symmetry and edges combine in a material that at first sight seems like an unlikely candidate - graphene.

Because the proper symmetry classification of Hamiltonians is crucial to the search for new topological phases, it is useful to have general and reliable tools that automate the process. Accordingly, we describe an algorithmic approach to the problem of symmetry classification of Hamiltonians, by proposing algorithms to automatically generate all Hamiltonians compatible with given symmetries, or to find all the symmetries of a Hamiltonian. The algorithms apply to all continuous unitary symmetries, as well as spatial or nonspatial discrete symmetries that are unitary or antiunitary.

We then turn to the analysis of a particular symmetry-protected topological phase, the one-dimensional topological superconductor, which has been a popular research topic globally in recent years, including here in Delft. The standard experimental tool to detect the topological edge state of topological superconductors, namely the Majorana, is to tunnel-couple the edge of the superconductor to a normal electrode, and to search for a resonant conductance peak in the middle of the superconducting gap. Such a measurement probes the density of states near the superconductor edge and can therefore

be unreliable, because it also measures accidental low-energy states that may resemble Majoranas if they happen to be localized near the edge. We propose an alternative electrical measurement using the nonlocal two-terminal conductance, which has the advantage of probing the bulk topological phase transition instead of the Majoranas themselves.

Having seen that the detection of topological edge states can be unreliable because of effects local to the edge, we turn to an investigation of edges in more general terms through a systematic study of boundary conditions for continuum Hamiltonians. We parametrize the most general boundary conditions that conserve probability current, through a matrix parameter that is either skew-Hermitian or unitary. The parametrization allows one to easily classify boundary conditions by symmetry, and thus identify which boundary conditions are compatible with a given symmetry-protected topological phase. In addition, we show how to construct a boundary condition for a continuum model from the edge of a corresponding tight binding model, and present an algorithmic approach to computing the spectrum of a continuum Hamiltonian confined between two parallel boundaries with arbitrary boundary conditions.

We then utilize the general approaches to symmetry and edge classification in the study of a particular family of materials, and describe a previously unknown topological phase in monolayer molybdenum dichalcogenides. These materials have strong intrinsic spin-orbit coupling and can become superconducting when doped into the conduction band, with a superconducting critical in-plane magnetic field that greatly exceeds the Pauli limit. The combination of these features makes it possible to engineer a nodal topological phase that is protected by a combination of mirror and time-reversal symmetry. The topological edge states form dispersionless flat bands that extend between nodal points, and lie in the middle of the superconducting gap.

Finally, we turn to a different and well-known monolayer material, in a study of electron reflection from disordered edges in graphene. Graphene has a Dirac low-energy dispersion, similar to that of light, but with a smaller velocity. The Fermi wavelength thus diverges in the continuum limit, which by the law of reflection implies that electron reflection from graphene boundaries is largely specular, even in the presence of edge disorder. However, we identify a regime in which a disordered graphene edge never reflects specularly, thus breaking the law of reflection, and propose a magnetotransport experiment to detect this peculiar phenomenon. The origin of this breakdown of specular reflection is resonant scattering off bands of edge states, which are a generic feature of graphene boundaries, and are in fact related to topological phase of the bulk graphene Hamiltonian.

SAMENVATTING

Topologische materialen zijn nieuwe soorten quantum materialen die de afgelopen jaren erg veel aandacht hebben gekregen binnen vaste stof fysica. De topologische fase van deze materialen slaat terug op Hamiltonianen met een energiekloof, zodat de topologische staat van de Hamiltoniaan in de bulk van de materie onderscheid maakt tussen de niet triviale topologische fase en de normale triviale fase. Overgangen tussen onderscheidbare topologische fases brengt dus altijd een sluiting en heropening van de energiekloof met zich mee. Een resultaat hiervan, is dat rand niveaus verschijnen op grensvlak waar de topologische fase verandert. Inclusief raakvlakken van topologische materialen met vacuüm; wat een triviale isolator is. Deze topologische rand niveaus komen voort uit de niet-triviale bulk topologie, en zijn daarom robuust tegen alle verstoringen die niet de topologische staat veranderen, waardoor ze interessant zijn voor toepassingen.

In veel gevallen is de topologische staat alleen van toepassingen op Hamiltonianen die onderhevig zijn aan bepaalde symmetrie eigenschappen. In dat geval is de topologische fase robuust tegen versturen die niet de topologische staat veranderen of de beschermende symmetrie eigenschappen breken. Voor de rand-niveaus van de door symmetrie beschermde topologische fases, speelt de symmetrie classificering van de rand zelf ook een rol. Als de rand een van de beschermde symmetrieën breekt, verliezen de rand niveaus hun topologische bescherming, zelf als de Hamiltoniaan in de bulk van het materiaal nog wel onderhevig is aan deze symmetrie. Het onderwerp van deze thesis is een wisselwerking tussen topologie, symmetrie, en rand niveaus. Zowel in algemene theoretische zin, als toegepast op een paar specifieke materialen of heterostructuren die momenteel relevant zijn in vaste stof fysica.

Deze thesis start met een korte introductie van symmetrieën in de quantum mechanica, en een vluchtig blik in de wereld van vaste stof fysica. Daarnaast wordt een voorbeeld gegeven hoe topologie, symmetrie en rand niveaus gecombineerd kunnen worden in een materiaal wat op het eerste oog een onlogische kandidaat is – grafeen.

Omdat de goede symmetrie classificatie van de Hamiltoniaan cruciaal is voor het zoeken naar nieuwe topologische fases, is het nuttig om algemene betrouwbare hulpmiddelen te hebben om dit proces te automatiseren. We beschrijven een algoritmische aanpak voor het probleem van symmetrie classificatie van Hamiltonianen, door algoritmes te ontwikkelen die automatische alle Hamiltonianen generen die congruent zijn met de gegeven symmetrieën, of die alle symmetrieën van een Hamiltoniaan vinden. De algoritmes zijn zowel toepasbaar op alle continue unitaire symmetrieën, als op alle ruimtelijke of niet ruimtelijke symmetrieën die unitair of anti-unitair zijn.

Vervolgens analyseren we een specifieke door symmetrie beschermde fase, de een dimensionale topologische supergeleider, wat wereldwijd een populair onderzoeksonderwerp is de afgelopen jaren, inclusief hier in Delft. Het standard experimentele hulpmiddel om een topologisch rand niveau van een topologische supergeleider, namelijk een Majorana, te vinden, door de rand van de supergeleider te tunnel-koppelen aan een normale

electrode, en te zoeken naar een resonante-geleidingspiek in het midden van de supergeleidende kloof. Een dergelijke meeting onderzoekt de dichtheid van energieniveaus in de buurt van de supergeleidende kloof, en kan daarom onbetrouwbaar zijn, omdat het ook onopzettelijk lage-energieniveaus kan meten die lijken op Majoranas als deze toevallig gelokaliseerd zijn in de buurt van de rand. Wij stellen een alternatieve elektrische meting voor die gebruik maakt niet lokale tweepunts geleiding, welke het voordeel heeft dat het de bulk topologische faseovergang meet in plaats van de Majoranas zelf.

We hebben gezien dat het vinden van topologische rand niveaus onbetrouwbaar kan zijn door lokale effecten van de rand. Daarom onderzoeken we de randen op een algemenere manier door een systematische studie van randvoorwaarden van continue Hamiltonianen. We parametriseren de meest algemene randvoorwaarden die de waarschijnlijkheidsstroom behoudt, door een matrix parameter die of scheef-Hermetisch is of unitair. De parametrisatie stelt ons in staat om op een eenvoudige manier randvoorwaarden te classificeren op symmetrie, en op die manier te identificeren welke randvoorwaarden er congruent zijn met het gegeven door symmetrie beschermde topologische fase. Daarnaast, laten we zien hoe je een randvoorwaarde voor een continu model kan opstellen aan de rand van een corresponderend sterke binding model, en presenteren een algoritmische aanpak om het spectrum van een continue Hamiltoniaan te berekenen die begrensd is door twee parallel grensvlakken met arbitraire randvoorwaarden.

Vervolgens gebruiken we de algemene aanpak van symmetrie en rand classificatie in de studie van een specifieke groep materialen, en beschrijven de hieraan voorafgaand onbekende topologische fase in een enkele laag molybdeen-dichalcogenide. Deze materialen hebben een sterke interne resonante baan koppeling en kunnen supergeleidingen worden als ze gedopeerd worden ineen geleidende band, met een supergeleidende kritieke magnetisch vel in het vlak dat het Pauli limiet ver overschrijdt. De combinatie van deze eigenschapen maakt het mogelijk om een nodale topologische fase te ontwerpen die beschermd is door een combinatie van spiegel en tijd-omkering symmetrie. De topologische rand niveaus vormen dispersie loze platte banden die zich uitstrekken tussen twee nodale punten, en in het middel van de supergeleidende kloof liggen.

Uiteindelijk richten wij ons op een ander bekend enkel laags materiaal, in een studie van de elektronen reflectie op de ongeregelde randen van grafeen. Grafeen heft een Dirac lage energie dispersie die lijkt op dat van licht, maar met een lagere snelheid. De Fermi golflengte divergeert dus in de continue limiet, waarbij de wet van reflectie aangeeft dat de reflectie van elektronen van grafeen randen voornamelijk spiegelend is, zelf in de buurt van rommelige randen. Wij identificeren echter een regime waarin de ongeregelde randen van grafeen nooit spiegelend reflecteren, en dus de wet van reflectie breken, en stellen een magnetotransport experiment voor om die eigenaardige verschijnsel te detecteren. De oorzaak voor het gebrek aan spiegelende reflectie is de resonante verstrooiing van de banden bij de rand niveaus, wat een algemene eigenschap is van grafeen randen, en zijn gerelateerd aan de topologische fase van de Hamiltoniaan van de bulk van de grafeen.

1

INTRODUCTION

1.1. PREFACE

Imagine grabbing a chunk of material and manually breaking off a piece, forming a new surface on the chunk. Most likely, the surface will look rather irregular and messy, but using some method slightly more refined than your hands to break the material, you could probably obtain a surface that is rather smooth and homogenous looking to the naked eye. Go down to the atomic scale however, and you will discover a chaotic landscape. In practice, it is very challenging to create atomically pristine surfaces, and most surfaces are irregular structures of dangling electron bonds, defects and other imperfections. These irregularities frequently give rise to electronic states that are localized at the surface. Mostly, these edge states appear accidentally because of the specific microscopic details of the surface, making them sensitive to slight changes in the surface properties, and hence not very useful in practice.

In some cases, edge states form not accidentally, but rather because of an intrinsic property of the material chunk itself, namely its topological classification [1–3]. In this context, the topological classification applies to the Hamiltonian of the material, such that materials with an energy gap belong to the same topological class if their Hamiltonians can be smoothly transformed into one another without closing the energy gap. Edge states appear at the interface of materials belonging to different topological classes - including interfaces with the vacuum, which has an energy gap and therefore a topological classification. Because these edge states are a manifestation of bulk topological properties, they are robust to microscopic changes to the surface, and even to deformations of the material itself, so long as the energy gap does not close. This topological protection of the edge states makes them attractive for applications, with the most tantalizing example probably being the prospect of using the Majorana edge modes of topological superconductors [4–6] as building blocks for quantum computers [7, 8].

Most topological classes of materials are only defined if the Hamiltonian respects certain protecting symmetries. This means that the edge states are robust to deformations so long as they preserve the energy gap of the bulk Hamiltonian and the protecting

symmetries. Symmetries that can protect topological phases include spatial symmetries, such as reflection and rotation, but also time-reversal and particle-hole symmetries, which do not act in real space. Hence, unlike the spatial symmetries, particle-hole and time-reversal symmetries are not broken by scalar disorder in the material. The protecting symmetries also have consequences for the character of the edge states themselves. For example, the edge states of a quantum spin Hall insulator come in orthogonal pairs because of the protecting time-reversal symmetry, and scattering between them is thus forbidden by symmetry [9, 10]. Symmetry analysis of Hamiltonians thus plays a key role in ongoing research in symmetry-protected topological materials, and the development of suitable tools for this task is therefore paramount.

Although topologically protected edge states are a consequence of the topological classification of the Hamiltonian of the bulk material, the symmetry properties of the surface where the edge states appear may also play a subtle role. If the surface itself breaks the symmetries protecting the topological phase, then the edge states lose their protection, and may gap out in energy. Beyond hosting edge states, the specifics of its surfaces can also strongly affect the spectral properties of a material. For instance, graphene nanoribbons with zigzag or armchair edges have widely different spectra, with the former hosting a flat band of edge states but the latter not (*cf.* Figs. 1.3 and 1.5) [11]. For a general description, it is thus useful to know which boundary conditions are allowed for a given Hamiltonian, as well as the symmetry classification of the boundary conditions.

In this thesis, we investigate the interplay of topology, edges and symmetry, both from a general perspective and specifically applied to various systems. First, we focus on the symmetries of Hamiltonians, introducing an algorithmic approach to automatically generate Hamiltonians from a given symmetry group, or to find the full symmetry classification of a Hamiltonian. We then turn to a particular and well-known symmetry-protected topological phase, the one-dimensional topological superconductor. Because standard experimental tools to detect its topological edge states can be unreliable [12, 13], we propose an alternative electrical signature of the topological phase, which relies not on detecting the edge states themselves, but rather the topological phase transition of the bulk material. Our focus then shifts from the bulk to edges in a systematic study of the boundary conditions of continuum Hamiltonians, their symmetry classification, and correspondence with physical boundaries of materials. Bulk and boundary then come together when we show how to engineer a nodal topological superconducting phase in monolayer molybdenum dichalcogenides, protected by a combination of mirror and time-reversal symmetry, where the topological edge states form dispersionless flat bands in the middle of the superconducting gap. Finally, we explore the reflection of electrons off dirty edges in graphene, and find that the law of reflection comes with a subtle twist.

1.2. SYMMETRIES

Symmetry is a fundamental aspect to consider when developing physical models, and symmetries are a powerful practical tool for solving problems and generalizing conclusions between systems with similar properties. In quantum mechanics, a symmetry operation is a transformation of a system that preserves the probabilities of measurements made on the system [14]. In a Hilbert space of quantum states, symmetry operations are represented by operators which act on state vectors. The constraint of probability

conservation implies that for any $|\psi\rangle, |\phi\rangle$ in the Hilbert space, a symmetry operator S must satisfy

$$|\langle S\psi| S\phi\rangle| = |\langle\psi|\phi\rangle|, \tag{1.1}$$

namely that either $\langle S\psi| S\phi\rangle = \langle\psi|\phi\rangle$ or $\langle\psi|\phi\rangle = \langle\psi|\phi\rangle^* = \langle\phi|\psi\rangle$. Wigner's theorem states that such operators can only be of two types [15]. First of all, they can be linear and unitary $S = U$ with $U^\dagger U = 1$, satisfying

$$U\left(a|\psi\rangle + b|\phi\rangle\right) = aU|\psi\rangle + bU|\phi\rangle \tag{1.2}$$

$$\langle U\psi| U\phi\rangle = \langle\psi|U^\dagger U|\phi\rangle = \langle\psi|\phi\rangle, \tag{1.3}$$

with complex coefficients a and b. Secondly, the operators may be antiunitary $S = A$, which satisfy

$$A\left(a|\psi\rangle + b|\phi\rangle\right) = a^* A|\psi\rangle + b^* A|\phi\rangle \tag{1.4}$$

$$\langle A\psi| A\phi\rangle = \langle\psi|A^\dagger A|\phi\rangle^* = \langle\psi|\phi\rangle^*, \tag{1.5}$$

where we define the Hermitian conjugate of an antiunitary operator as

$$\langle\psi| A\phi\rangle = \left\langle A^\dagger\psi\middle|\phi\right\rangle^*. \tag{1.6}$$

Antiunitary symmetry operators must square to $A^2 = \pm 1$ [16, 17]. In addition, it is possible to express any antiunitary operator as the product $A = U\mathcal{K}$ of a unitary operator U and complex conjugation $\mathcal{K}$.

Continuous symmetry operators are a prominent class of unitary symmetry operators. In particular, they are useful to describe operations that continuously change some aspect of a system, for example propagation in time, and translation or rotation in space. In its infinitesimal form, a continuous symmetry operator is expressible as [14]

$$U_c = 1 - i\frac{\epsilon}{\hbar}G, \tag{1.7}$$

with $\epsilon \to 0$ a real parameter, and where G is called the generator of the symmetry operator in question. Here, ϵ may represent the infinitesimal change in the quantity which the symmetry operation transforms, such as real space position. We have

$$U_c^\dagger U_c = (1 + i\frac{\epsilon}{\hbar}G^\dagger)(1 - i\frac{\epsilon}{\hbar}G) = 1 + i\epsilon(G^\dagger - G) + \mathcal{O}(\epsilon^2), \tag{1.8}$$

and because U_c is unitary $U_c^\dagger U_c = 1$, the generator must be Hermitian $G^\dagger = G$, and therefore corresponds to an observable.

A Hamiltonian H is invariant under the symmetry U_c if $\langle\psi|H|\psi\rangle = \langle U_c\psi|H|U_c\psi\rangle$ for any $|\psi\rangle$ in the Hilbert space, which is equivalent to $U_c^\dagger H U_c = H$, or $HU_c = U_c H$. Substituting Eq. (1.7) shows that invariance of H under the symmetry U_c is equivalent to $[G, H] = 0$. The time evolution of G is given by the Heisenberg equation of motion [18]

$$\frac{dG}{dt} = -\frac{i}{\hbar}[G, H] = 0, \tag{1.9}$$

which shows that the observable G is a conserved quantity, and demonstrates the intimate relation between the continuous symmetries of a Hamiltonian and its conservation laws. A useful property of conservation laws is that they allow one to partition the Hamiltonian into uncoupled blocks, which may be diagonalized independent of one another. More specifically, in a basis of the eigenvectors of a conservation law, the Hamiltonian is block-diagonal with distinct blocks corresponding to different eigenvalues of the conservation law [18].

Although Eq. (1.7) only applies to infinitesimal transformations, we can build a symmetry operator that describes a transformation by a finite ϵ by combining multiple infinitesimal transformations

$$U_c = \lim_{N\to\infty} \left(1 - i\frac{\epsilon}{\hbar N} G\right)^N = e^{-i\frac{\epsilon}{\hbar}G}. \tag{1.10}$$

The operators that describe time evolution, real space translation and rotation are continuous symmetry operators. For the translation operator, ϵ corresponds to the change in the real space coordinate, and the generator for translation along the direction of the unit vector $\mathbf{n}$ is $\mathbf{n}\cdot\mathbf{p}$, with $\mathbf{p}$ the vector of momentum operators. Similarly for the rotation operator, ϵ is the angle of rotation, and the generator for rotation around the axis $\mathbf{n}$ is $\mathbf{n}\cdot\boldsymbol{J}$, where $\boldsymbol{J}$ is the vector of angular momentum operators. Finally, for the time-evolution operator, the generator is the Hamiltonian itself.

In many applications, the Hamiltonian is not invariant under continuous changes in coordinates, but rather only certain discrete transformations. For example, the Hamiltonian of a square lattice system is generally only invariant under translation by an integer multiple of a lattice vector. Similarly, the Hamiltonian is not invariant under arbitrary rotations about a lattice site, but only rotations by integer multiples of 90°. The square lattice is thus an example of a Hamiltonian that is invariant under discrete symmetry operations. Discrete symmetry operations describe changes in aspects of the system that are not continuous. Unlike rotation and translation, not all discrete symmetry operations that are useful follow from the successive application of a continuous symmetry operator, for example space inversion, which flips the sign of spatial coordinates $\mathbf{x} \to -\mathbf{x}$. Finally, there are three specific discrete symmetries which do not transform spatial coordinates, namely time-reversal symmetry, particle-hole symmetry and chiral symmetry. These symmetries, which play a crucial role in the classification of topological matter, are the topic of the following subsections.

1.2.1. TIME-REVERSAL SYMMETRY

Time reversal is an operation that flips the arrow of time, *i.e.* it maps $t \to -t$. To deduce the properties of the time-reversal operator $\mathcal{T}$, let us consider the infinitesimal time evolution of a state $|\psi\rangle$ and its time-reversed partner $\mathcal{T}|\psi\rangle$. For a state $|\psi\rangle$ that is invariant under time reversal, applying time reversal to $|\psi\rangle$ and then moving it forward in time by δt is equivalent to moving $|\psi\rangle$ backwards in time by $-\delta t$ and then applying time-reversal [14]. In terms of the infinitesimal time evolution operator (1.7), we thus have

$$\left(1 - i\frac{H}{\hbar}\delta t\right)\mathcal{T}|\psi\rangle = \mathcal{T}\left(1 + i\frac{H}{\hbar}\delta t\right)|\psi\rangle \tag{1.11}$$

which implies

$$-iH\mathcal{T} = \mathcal{T}iH. \tag{1.12}$$

Assuming that $\mathcal{T}$ is unitary and linear, this is equivalent to $H\mathcal{T} = -\mathcal{T}H$, which implies that for an eigenstate $|\psi\rangle$ with energy E, the time-reversed partner $\mathcal{T}|\psi\rangle$ is an eigenstate with energy $-E$. However, this is nonsensical, so we conclude that $\mathcal{T}$ is an antiunitary and antilinear operator, and Eq. (1.12) shows that $[\mathcal{T}, H] = 0$ or $\mathcal{T}H\mathcal{T}^{-1} = H$ for a time-reversal invariant Hamiltonian.

Because time-reversal only flips the arrow of time, it commutes with both the translation operator and the rotation operator, which by (1.7) implies that their generators anticommute with time-reversal, namely $\mathcal{T}\mathbf{p}\mathcal{T}^{-1} = -\mathbf{p}$ and $\mathcal{T}\boldsymbol{J}\mathcal{T}^{-1} = -\boldsymbol{J}$. For a translationally invariant Hamiltonian $H(\mathbf{k})$ with $\hbar\mathbf{k} = \mathbf{p}$, time-reversal invariance thus implies that if ψ is an eigenstate at momentum $\mathbf{k}$, then $\mathcal{T}\psi$ is also an eigenstate with the same energy but at the opposite momentum $-\mathbf{k}$. Furthermore, Kramer's theorem states that in systems with half integer angular momentum, ψ and $\mathcal{T}\psi$ are distinct quantum states, and therefore orthogonal [14]. This means that scattering between them is forbidden, unless time-reversal symmetry is broken, an observation which plays a crucial role in the physics of topological insulators [10].

1.2.2. PARTICLE-HOLE SYMMETRY

Particle-hole symmetry denotes an operation that flips the sign of both energy and momentum. Like time-reversal symmetry, the particle-hole symmetry operator $\mathcal{P}$ is antiunitary. Because $\mathcal{P}$ reverses energy, a Hamiltonian is invariant under particle-hole symmetry if it satisfies $\mathcal{P}H(\mathbf{k})\mathcal{P}^{-1} = -H(-\mathbf{k})$, namely if anticommutes with $\mathcal{P}$. Particle-hole symmetry of a Hamiltonian $H(\mathbf{k})$ implies that if ψ is an eigenstate at momentum $\mathbf{k}$ with energy E, then $H(-\mathbf{k})\mathcal{P}\psi = -\mathcal{P}H(\mathbf{k})\psi = -E\mathcal{P}\psi$. Hence, $\mathcal{P}\psi$ is also an eigenstate of the Hamiltonian, but with opposite energy and momentum, and particle-hole symmetry therefore implies a symmetry in the spectrum around zero energy and opposite momenta.

Particle-hole symmetry gets its name because it manifests naturally in superconductors. At the mean field level, it is convenient to describe quasiparticle excitations above the superconducting ground state with the Bogoliubov-de Gennes (BdG) Hamiltonian

$$H_{\mathrm{BdG}}(\mathbf{k}) = \begin{bmatrix} H(\mathbf{k}) & \Delta(\mathbf{k}) \\ \Delta^\dagger(\mathbf{k}) & -H^T(-\mathbf{k}) \end{bmatrix}, \tag{1.13}$$

where $H(\mathbf{k})$ is the normal state Hamiltonian, and $\Delta(\mathbf{k})$ the superconducting pairing function [19]. The BdG Hamiltonian is written in the electron-hole basis $[c_{\mathbf{k}}, c^\dagger_{-\mathbf{k}}]^T$, with $c_{\mathbf{k}}$ a vector of all electron annihilation operators in a unit cell at momentum $\mathbf{k}$. Constructing the BdG Hamiltonian thus involves introducing a redundancy in the basis, namely the hole part of the electron-hole basis, which doubles the degrees of freedom. We see that the BdG Hamiltonian has the particle-hole symmetry $\mathcal{P} = \tau_x\mathcal{K}$, with τ_x the Pauli matrix that swaps the electron and hole degrees of freedom. Particle-hole symmetry is therefore a manifestation of a redundancy in the BdG formalism.

1.2.3. CHIRAL SYMMETRY

Chiral symmetry refers to a symmetry operation that flips the sign of energy, but leaves momentum unchanged. Unlike particle-hole and time-reversal symmetry, the chiral sym-

metry operator $\mathscr{C}$ is unitary, and satisfies $\mathscr{C}^2 = 1$, such that $\mathscr{C}^\dagger = \mathscr{C} = \mathscr{C}^{-1}$. A Hamiltonian is invariant under chiral symmetry if it obeys the constraint $\mathscr{C}H(\mathbf{k})\mathscr{C}^{-1} = -H(\mathbf{k})$, *i.e.* if it anticommutes with $\mathscr{C}$, similar to particle-hole symmetry. Hence, if ψ is an eigenstate at momentum $\mathbf{k}$ and with energy E of a Hamiltonian with chiral symmetry, then $\mathscr{C}\psi$ is also an eigenstate of the Hamiltonian but with energy $-E$. Like particle-hole symmetry, chiral symmetry therefore implies that the spectrum is symmetric around zero energy. Unlike particle-hole symmetry however, this symmetry applies to each momentum separately.

Chiral symmetry for instance manifests in systems where it is possible to split the degrees of freedom into two identical groups A and B. If the Hamiltonian only couples elements of group A to group B and vice versa, but includes no coupling terms within each group, the Hamiltonian has the block off-diagonal form

$$H = \begin{bmatrix} 0 & H_{AB}(\mathbf{k}) \\ H_{AB}^\dagger(\mathbf{k}) & 0 \end{bmatrix} \tag{1.14}$$

in the basis $[c_A, c_B]^T$, with c_α the vector of all electron annihilation operators in group $\alpha = A, B$. With $\tau_{x,y,z}$ the Pauli matrices in the space of the groups A and B, we see that the Hamiltonian only includes terms proportional to τ_x and τ_y. Because $\{\tau_i, \tau_j\} = 2I\delta_{ij}$, with I the 2×2 identity, the Hamiltonian (1.14) manifestly anticommutes with τ_z, and therefore has the chiral symmetry $\mathscr{C} = \tau_z$. Lastly, we note that such grouping of degrees of freedom arises naturally in the tight binding model of graphene which only includes nearest-neighbour hopping, where the groups A and B refer to the two sublattices.

1.3. TOPOLOGY IN CONDENSED MATTER

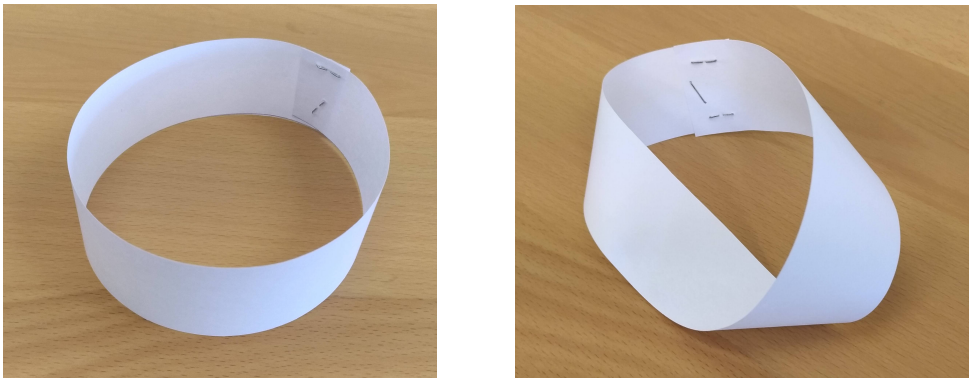

Figure 1.1: A normal band (left) and a Möbius band (right). The normal band has two surfaces, while the Möbius band only has one. Because it is impossible to change the number of surfaces that a band has without cutting and reattaching it, the normal and Möbius bands are topologically distinct.

In mathematics, topology is the study of the properties of objects that do not change under continuous deformations [20]. Continuous deformation means stretching, twisting, bending, or any other transformation that does not involve abrupt changes, such as

tearing the object or breaking it apart. If it is possible to continuously deform one object into another, then the objects are topologically the same, but if abrupt deformations are necessary, then they are topologically distinct. The Möbius band, which can be made using a paper strip, offers a glimpse into the world of topology. Gluing the two ends of the strip together forms a normal band, but if we first twist one end of the strip by 180°, we obtain a Möbius band (*cf.* Fig. 1.1). Imagine walking along the surface of the Möbius strip. Completing one full circle leaves you on the opposite side, but completing yet another circle brings you back to the starting point. The Möbius band therefore only has a single surface, unlike the normal band. In fact, it is impossible to continuously deform the Möbius band into a normal band with two surfaces - the only way to do so involves tearing the Möbius band and reattaching the ends after undoing the twist. The Möbius and normal bands are thus topologically distinct. To put it differently, we can view the number of surfaces of a band as a robust property, in the sense that it is independent of small details of the band, and deformations done to it.

In the same vein, topology in condensed matter physics is the study of the properties of Hamiltonians with an energy gap under continuous deformations. Continuous deformations are transformations that do not close the energy gap, and two Hamiltonians that continuously deform into one another without closing the energy gap are topologically the same. Much like the number of surfaces in the Möbius band above, topological phases of Hamiltonians coincide with properties that cannot change by continuous deformation. Such topological properties are thus robust to system perturbations or imperfections, such as disorder or variations in shape, so long as the energy gap does not close, which is an immensely useful characteristic. A canonical example is the Hall conductance of a two-dimensional electron gas at low temperature in a perpendicular magnetic field [21]. The Hall conductance is quantized precisely to integer multiples of e^2/h, with experimental precision greater than one part in a million routinely reported [22]. This remarkable quantization does not depend on the material, the cleanliness the sample used, or the name of the person doing the measurements, because the Hall conductance has a topological origin [23]. Lastly, we note that it is also useful to consider symmetry constraints on the topological equivalence of Hamiltonians, which means that we only take two Hamiltonians to be topologically equivalent if they continuously deform into one another without breaking certain symmetries.

1.4. CLASSIFICATION OF TOPOLOGICAL PHASES OF MATTER

Time-reversal symmetry, particle-hole symmetry and chiral symmetry, which we shall refer to as the three fundamental discrete symmetries, form the basis of a classification scheme for the topological phases of single-particle Hamiltonians. For any gapped insulating or superconducting Hamiltonian, it is possible to classify the possible topological phases in all spatial dimensions d of the bulk material, depending on which of the three fundamental discrete symmetries leave the Hamiltonian invariant [24–26]. In total, there are ten possible distinct combinations of the discrete symmetries, with each combination corresponding to a separate symmetry class. This is because $\mathscr{T}$ and $\mathscr{P}$ each comes in two distinct flavours, squaring to either $+1$ or -1, while $\mathscr{C}^2 = 1$ always. Furthermore, the product of any two of the discrete symmetries always equals the third, and it is therefore not possible for a Hamiltonian to have only two of the symmetries. This classification

Table 1.1: General classification of topological insulators and superconductors in the tenfold way. Each row represents a symmetry class, namely a distinct combination of time-reversal symmetry $\mathscr{T}$, particle-hole symmetry $\mathscr{P}$ and chiral symmetry $\mathscr{C}$. We denote the absence of a symmetry by ✗, while the presence of a symmetry is given by the square of the operator in question (± 1). In a given dimension d, a symmetry class is either always trivial (✗), or with existing topological phases, which are characterized by an integer $\mathbb{Z}$ or $\mathbb{Z}_2$ topological invariant. Although we only show the dimensions $1 \leq d \leq 4$, it is possible to extend this table to all dimensions.

Class	Symmetry			Dimension d			
	$\mathscr{T}^2$	$\mathscr{P}^2$	$\mathscr{C}^2$	1	2	3	4
A	✗	✗	✗	✗	$\mathbb{Z}$	✗	$\mathbb{Z}$
AIII	✗	✗	1	$\mathbb{Z}$	✗	$\mathbb{Z}$	✗
AI	1	✗	✗	✗	✗	✗	$\mathbb{Z}$
BDI	1	1	1	$\mathbb{Z}$	✗	✗	✗
D	✗	1	✗	$\mathbb{Z}_2$	$\mathbb{Z}$	✗	✗
DIII	-1	1	1	$\mathbb{Z}_2$	$\mathbb{Z}_2$	$\mathbb{Z}$	✗
AII	-1	✗	✗	✗	$\mathbb{Z}_2$	$\mathbb{Z}_2$	$\mathbb{Z}$
CII	-1	-1	1	$\mathbb{Z}$	✗	$\mathbb{Z}_2$	$\mathbb{Z}_2$
C	✗	-1	✗	✗	$\mathbb{Z}$	✗	$\mathbb{Z}_2$
CI	1	-1	1	✗	✗	$\mathbb{Z}$	✗

scheme is known as the tenfold way, and it is shown in Table 1.1 for the dimensions $1 \leq d \leq 4$.

If topological phases exist within a symmetry class in dimension d, we say that the class is nontrivial in the particular dimension. On the other and, if a symmetry class has no topological phases in a given dimension, we call it trivial. We see that there are five trivial and five nontrivial classes per dimension, and it can be shown that this remains true in all spatial dimensions [16]. Nontrivial symmetry classes are labelled by $\mathbb{Z}$ or $\mathbb{Z}_2$, which denotes a topological number or invariant Q that distinguishes different topological phases. A $\mathbb{Z}_2$ invariant only has two values, such as $Q = 0$ or 1, which distinguish between the nontrivial topological ($Q = 1$) and trivial ($Q = 0$) phases. On the other hand, a $\mathbb{Z}$ invariant can take any integer value, with $Q = 0$ usually denoting the trivial phase, and the remaining integers different nontrivial topological phases. The topological invariant is a bulk property, and obtaining its value typically amounts to integrating the Hamiltonian over the Brillouin zone [27], or evaluating the scattering matrix at an edge of the system [28]. Because the topological invariant reflects the topological phase of a Hamiltonian, it may only change upon closing of the bulk gap. Therefore, the value of the invariant is common to all Hamiltonians within the symmetry class that may be smoothly deformed into one another without closing the bulk gap, so long as the symmetry classification remains unchanged.

Finally, we briefly comment on the role of other symmetries in the topological classification of Hamiltonians. Conservation laws play no role in the classification, because their effect is only to reduce the Hamiltonian to uncoupled blocks, to each of which the classification of Table 1.1 applies separately. However, it is possible to extend the topological classification of Hamiltonians to include spatial symmetries, such as translation or rotation, leading to an even richer classification table [17, 29]. Topological phases of materials that are protected by spatial symmetries are called crystalline topological

insulators or superconductors [30, 31].

1.5. EDGE STATES AND BULK-BOUNDARY CORRESPONDENCE

In a system with a gapped Hamiltonian, a nontrivial value of the topological invariant has interesting consequences at its boundaries. Consider an interface between two systems, each described by a Hamiltonian that is gapped in the bulk, with one side in the trivial phase and the other a topological phase, as in Fig. 1.2(a). The two sides therefore have different values of a topological invariant. Moving from one side to the other across the interface, the topological invariant changes, and because the invariant cannot change without closing the energy gap, the bulk gap must close at the interface. States may thus exist in the gap, but because the bulk Hamiltonians on both sides remain gapped, the states are localized at the interface [32, 33]. In particular, this applies to interfaces of topological materials with the vacuum, which is a trivial insulator. This connection between the bulk topology of a material and edge states at its boundaries is called bulk-boundary correspondence [1]. Moreover, because the edge states are a manifestation of a change in bulk topology across an interface, they are topologically protected, or in other words, robust to perturbations that do not alter the topological classification of the bulk Hamiltonian, *i.e.* which do not close the energy gap or change the symmetry classification.

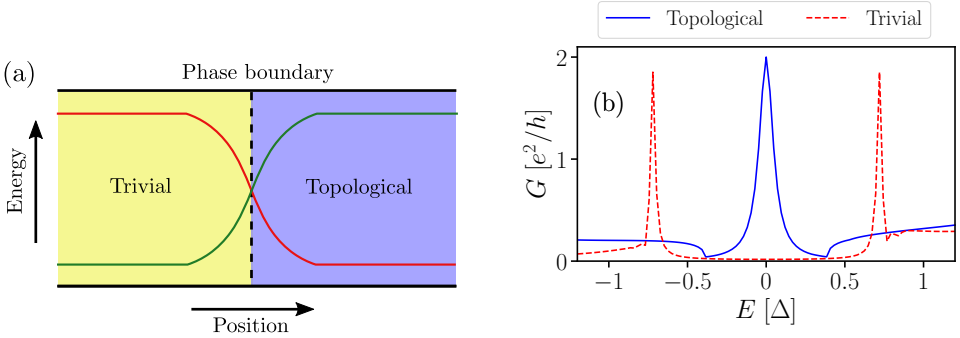

Figure 1.2: (a) Schematic of an interface, or phase boundary, between two systems with an energy gap, with one side in a topologically nontrivial phase and the other the trivial phase. The topological classification changes as we move across the phase boundary, and the gap must therefore close at the interface. As a result, topologically protected edge states manifest at the boundary. (b) A simulation of conductance tunnelling spectroscopy performed at the edge of a one-dimensional superconductor. In the trivial phase, the density of states in the superconductor vanishes at bias energies smaller than the superconducting gap. In the topological phase, the presence of the topological Majorana edge mode results in conductance peak of exactly $2e^2/h$ in the middle of the gap.

As an example, let us consider a one-dimensional superconductor, and assume that it only has particle-hole symmetry $\mathscr{P}^2 = 1$. Such a system belongs to class D of Table 1.1, and has a $\mathbb{Z}_2$ invariant, which means that only two phases are possible - a trivial phase or a topological phase. If we add an edge to the superconductor by truncating it, an edge state forms in the topological phase in the middle of the superconducting

gap Δ: the Majorana [4, 5]. Due to their potential applications in quantum information technology, Majoranas have been a hot research topic in recent years [34, 35]. Here in Delft, experimental and theoretical work on superconductor-semiconductor heterostructures that may host Majoranas continues at the time of writing of this thesis [36, 37]. We can simulate an experiment to detect the Majorana edge state by tunnel coupling the truncated superconductor to a normal electrode via an insulating barrier, forming a normal-insulator-superconductor junction, and computing the conductance of the heterostructure using Kwant [38]. The results are shown in Fig. 1.2(b). The tunnelling conductance is proportional to the density of states at the edge of the superconductor. If the superconductor is in the trivial phase, the conductance vanishes at subgap energies, because of the absence of states in the superconductor. On the other hand, there is a conductance peak in the middle of the gap if the superconductor is in the topological phase. The conductance peak is quantized to precisely $2e^2/h$ because of resonant Andreev reflection - a signature of the Majorana edge mode [39, 40]. In Chapter 3, we will introduce a different kind of transport signature of one-dimensional topological superconductivity, one which measures the topological phase transition itself rather than the Majorana edge modes.

We conclude this section with a comment on the role of the symmetry classification of the edge itself in bulk-boundary correspondence. Bulk-boundary correspondence dictates that adding an edge to a Hamiltonian which is in a nontrivial topological phase gives rise to edge states in the energy gap, so long as the bulk topology of the Hamiltonian is unchanged and any symmetries protecting the topological phase remain unbroken. However, if the edge itself has lower symmetry than the bulk Hamiltonian, the protecting symmetry may be broken locally at the edge, causing the edge states to lose their topological protection and possibly gap out in energy [17]. This is typically not an issue for topological phases protected by time-reversal or particle-hole symmetry, because these symmetries do not act on real space coordinates, and are therefore not affected by microscopic details of how a system terminates. On the other hand, chiral symmetry may be broken locally if the boundary breaks the symmetry between the two groups A and B [see Eq. (1.14)]. In graphene for example, hydrogen passivation of dangling electron bonds may lead to a potential imbalance between the two sublattices near the boundary, which breaks the chiral symmetry locally [41, 42]. Finally, the symmetry of the edge plays an important role in crystalline topological phases, which are protected by spatial symmetries, because the presence of an edge can easily break spatial symmetries. Hence, crystalline topological materials only exhibit edge states at boundaries which the protecting spatial symmetry leaves invariant.

1.6. MIXING IT ALL TOGETHER IN GRAPHENE

Graphene is a material with many exciting properties [11, 43]. A monolayer of carbon atoms, graphene is a truly flat, two-dimensional material, and was for long thought to be thermodynamically unstable. However, the group of Geim successfully isolated a single layer of graphene back in 2004, an achievement which along with their subsequent experiments on graphene earned them the Nobel prize in 2010. Graphene remains a popular topic of research to this day, and with the European Union launching the €1 billion Graphene Flagship initiative, it will likely remain in the spotlight for researchers for

years to come. In the context of this thesis, Chapter 6 presents the discovery of a peculiar electronic property of disordered graphene edges. Moreover, the interplay of topology, symmetry and edges in graphene is in many ways reminiscent of various features that appear in the subsequent chapters of this thesis. For this reason, we dedicate this section to a brief discussion of the electronic properties of graphene, and the implications of bulk-boundary correspondence.

1.6.1. LATTICE STRUCTURE AND TIGHT BINDING MODEL

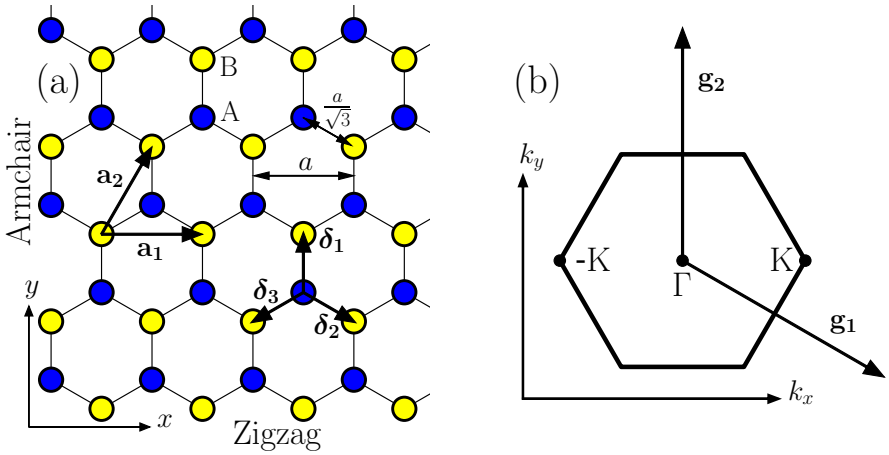

Figure 1.3: (a) Top view of the graphene honeycomb lattice with primitive Bravais lattice vectors $\mathbf{a}_1$ and $\mathbf{a}_2$ and lattice constant a. The Bravais lattice is triangular with two identical carbon atoms A (blue) and B (yellow) per unit cell. The vectors $\boldsymbol{\delta}_1$, $\boldsymbol{\delta}_2$, and $\boldsymbol{\delta}_3$ connect nearest neighbour atoms, with the interatom distance given by $a/\sqrt{3}$. Terminating the lattice along the x or y directions forms a zigzag or armchair boundary, respectively. (b) Schematic of the hexagonal first Brillouin zone of graphene, centered at the origin Γ, with the primitive reciprocal vectors $\mathbf{g}_1$ and $\mathbf{g}_2$. The six corners of the Brillouin zone are at the $\pm\mathbf{K}$ high symmetry points.

Graphene consists of a monolayer of carbon atoms forming a honeycomb structure, as is shown in Fig. 1.3(a). The Bravais lattice is triangular with two carbon atoms A and B per primitive unit cell, and primitive lattice vectors given by

$$\mathbf{a}_1 = a\hat{\mathbf{x}}, \quad \mathbf{a}_2 = \frac{a}{2}\hat{\mathbf{x}} + a\frac{\sqrt{3}}{2}\hat{\mathbf{y}}, \tag{1.15}$$

where $\hat{\mathbf{x}}$ and $\hat{\mathbf{y}}$ are unit vectors, and $a = 2.46$ Å the lattice constant. Alternatively, one may view the graphene lattice as the superposition of two triangular lattices, with one lattice consisting of the A atoms and the other the B atoms, and the groups of A and B atoms are therefore sometimes called sublattices. The reciprocal lattice is also triangular, spanned by the primitive reciprocal lattice vectors

$$\mathbf{g}_1 = \frac{2\pi}{a}(\hat{\mathbf{x}} - \frac{1}{\sqrt{3}}\hat{\mathbf{y}}), \quad \mathbf{g}_2 = \frac{4\pi}{\sqrt{3}a}\hat{\mathbf{y}}. \tag{1.16}$$

The first Brillouin zone is usually taken as the hexagon shown in Fig. 1.3(b), with corners at the six $\mathbf{K}$ points, although in principle any parallelogram spanned by $\mathbf{g}_1$ and $\mathbf{g}_2$ is a valid

choice. Of the **K** points, only two are distinct however, namely

$$\pm \mathbf{K} = \pm \frac{4\pi}{3a}\hat{\mathbf{x}}, \tag{1.17}$$

with the rest equivalent to either point up to a shift by a reciprocal lattice vector.

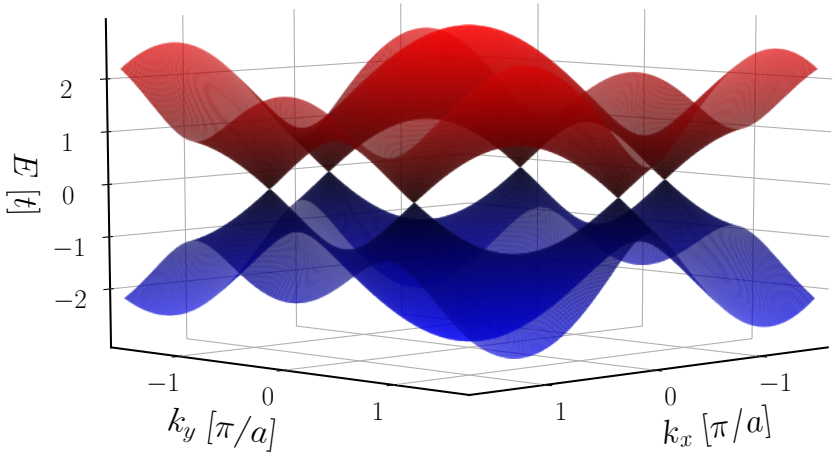

Figure 1.4: Dispersion relation of graphene within the tight binding approximation, over and around the first Brillouin zone. The dispersion relation is symmetric around zero energy and gapless, with the conduction and valence bands touching at Dirac points in the corners of the first Brillouin zone, where the energy is linear in the momenta.

A simple tight binding model, which includes one spinless orbital per carbon atom and only hoppings between nearest neighbouring atoms, provides a useful description of the low-energy electronic properties of graphene. Because the two carbon atoms that share a unit cell are identical, the labels A and B that distinguish them are arbitrary. As a result, the graphene lattice Fig. 1.3(a) has threefold rotation symmetry around the center of each carbon atom, which rotates an atom in a sublattice to another atom in the same sublattice. Equivalently, the lattice is invariant under threefold rotations around the center of a single hexagon. Furthermore, the lattice is invariant under spatial inversion around the center of a hexagon, which maps A to B and vice versa [44]. These two discrete symmetries limit the momentum-space tight binding Hamiltonian up to an overall shift in energy to the form [45]

$$\begin{aligned} H(\mathbf{k}) &= \begin{bmatrix} 0 & t(e^{i\mathbf{k}\cdot\boldsymbol{\delta}_1} + e^{i\mathbf{k}\cdot\boldsymbol{\delta}_2} + e^{i\mathbf{k}\cdot\boldsymbol{\delta}_3}) \\ t^*(e^{-i\mathbf{k}\cdot\boldsymbol{\delta}_1} + e^{-i\mathbf{k}\cdot\boldsymbol{\delta}_2} + e^{-i\mathbf{k}\cdot\boldsymbol{\delta}_3}) & 0 \end{bmatrix} \\ &\equiv \begin{bmatrix} 0 & h(\mathbf{k}) \\ h^*(\mathbf{k}) & 0 \end{bmatrix}, \end{aligned} \tag{1.18}$$

in the basis $[c_{A\mathbf{k}}, c_{B\mathbf{k}}]^T$, where t is the nearest-neighbour hopping parameter. The vectors $\boldsymbol{\delta}_i$ that connect neighbouring atoms are [see also Fig. 1.3(a)]

$$\boldsymbol{\delta}_1 = \frac{a}{\sqrt{3}}\hat{y}, \quad \boldsymbol{\delta}_2 = \frac{a}{2}(\hat{\mathbf{x}} - \frac{1}{\sqrt{3}}\hat{\mathbf{y}}), \quad \boldsymbol{\delta}_3 = -\frac{a}{2}(\hat{\mathbf{x}} + \frac{1}{\sqrt{3}}\hat{\mathbf{y}}). \tag{1.19}$$

Time-reversal invariance $\mathcal{T} H(\mathbf{k})\mathcal{T}^{-1} = H(-\mathbf{k})$ with $\mathcal{T} = I\mathcal{K}$ for spinless fermions gives the additional constraint $t \in \mathbb{R}$. We shall revisit such symmetry analysis in Chapter 2, which presents an algorithmic approach to the symmetry classification of Hamiltonians, including generating model Hamiltonians from symmetry constraints. Diagonalizing the Hamiltonian yields the tight binding dispersion [46]

$$E(\mathbf{k}) = \pm|h(\mathbf{k})|, \tag{1.20}$$

which is shown in Fig. 1.4. The band structure consists of two bands and is gapless, with the bands touching at the **K** points in the corners of the first Brillouin zone. The dispersion is furthermore linear in the momentum near the **K** points, and consequently, the **K** points at zero energy are frequently called Dirac points. In equilibrium and at zero temperature, the Fermi level of graphene lies at zero energy, and the low-energy excitations of graphene therefore happen in the vicinity of the Dirac points.

The tight binding model for graphene only couples nearest neighbouring atoms, which always belong to different sublattices A or B. Because the two sublattices are identical, the Hamiltonian (1.18) has the chiral symmetry $\mathcal{C} = \sigma_z$ as mentioned already in Section 1.2.3, where the Pauli matrix σ_z acts on the sublattice degree of freedom. The dispersion is thus symmetric around zero energy at each momentum, as is evident both from Eq. 1.20 and in Fig. 1.4. Because the graphene Hamiltonian is invariant under both time-reversal symmetry and chiral symmetry, it also has particle-hole symmetry $\mathcal{P} H(\mathbf{k})\mathcal{P}^{-1} = -H(-\mathbf{k})$, with $\mathcal{P} = \mathcal{C}\mathcal{T} = \sigma_z\mathcal{K}$ and $\mathcal{P}^2 = 1$. Finally, we note that because they invert the sign of momentum, $\mathcal{P}$ and $\mathcal{T}$ map between the two inequivalent Dirac points $\pm\mathbf{K}$.

1.6.2. DIRAC MODEL

In order to obtain a continuum Hamiltonian for the low-energy electronic excitations of graphene, we expand the Hamiltonian (1.18) around the two inequivalent Dirac points $\pm\mathbf{K}$. With $\mathbf{k} = \pm\mathbf{K} + \mathbf{q}$ and $|\mathbf{q}| \ll |\mathbf{K}|$, expanding the Hamiltonian up to linear order in $\mathbf{q}$ yields the continuum Dirac Hamiltonian [47]

$$H = \hbar v_F \tau_0 \otimes \boldsymbol{\sigma} \cdot \boldsymbol{q}, \tag{1.21}$$

written in the valley isotropic representation, such that the Hamiltonian is identical near both Dirac points. Here, τ_j and σ_j with $j = 0, x, y, z$ are the Pauli matrices with the identity in Dirac valley and sublattice space, respectively. The Fermi velocity is given by $v_F = \sqrt{3}ta/2\hbar$, and is thus independent of energy. Diagonalizing the Hamiltonian (1.21) yields the continuum dispersion

$$E(\mathbf{q}) = \pm\hbar v_F|\mathbf{q}|, \tag{1.22}$$

where there is twofold degeneracy because of the two distinct Dirac points. Because of the linear dispersion, the Fermi wavelength, which is given by

$$\lambda_F = \frac{2\pi}{q_F}, \tag{1.23}$$

diverges in the limit $E_F = \hbar v_F q_F \to 0$. As a result, one expects that electron waves in a graphene sample should reflect specularly off the sample edges due to the law of reflection, which states that smooth surfaces reflect specularly. A smooth surface here means that any surface roughness is small compared to the incident wavelength, which here diverges in the continuum limit. We shall revisit this point in Chapter 6.

1.6.3. BULK-BOUNDARY CORRESPONDENCE AT A ZIGZAG EDGE

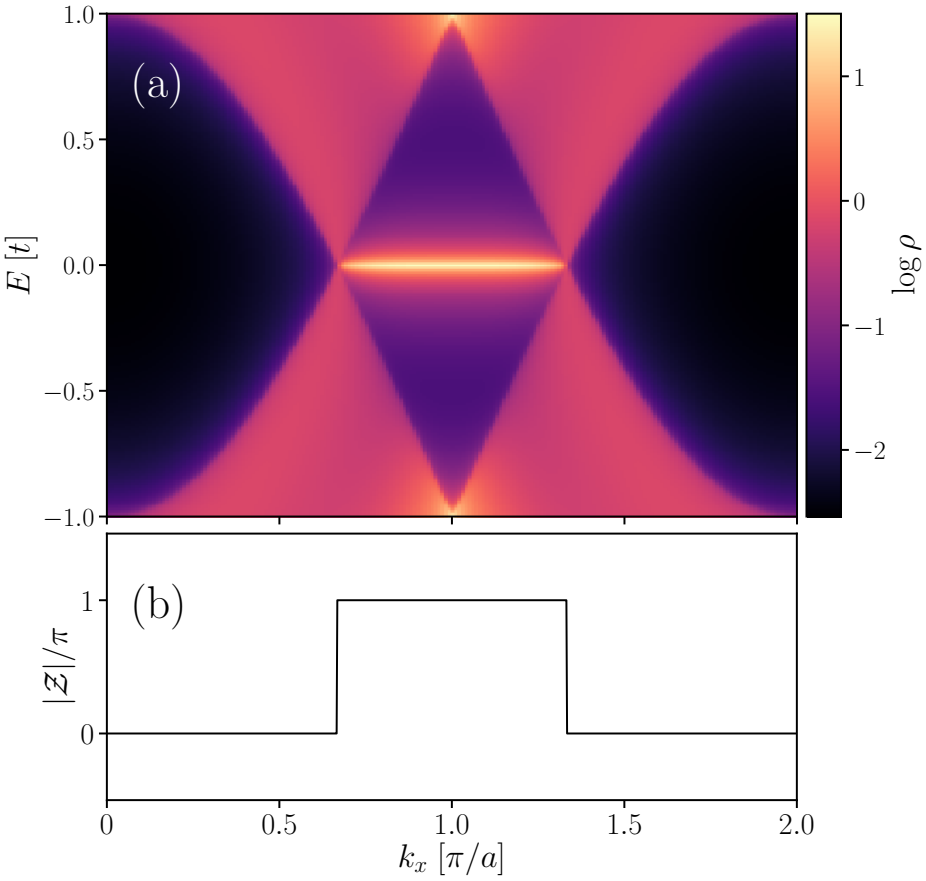

Figure 1.5: (a) Density of states at the zigzag edge of a semiinfinite graphene sheet as a function of the conserved momentum $k_\parallel = k_x$ parallel to the edge. A flat band of edge states extends between the projections of the two Dirac points on the edge Brillouin zone, *i.e.* for $\frac{2\pi}{3} < k_x < \frac{4\pi}{3}$. At these values of the parallel momentum, the graphene Hamiltonian is in a nontrivial topological phase, and the edge states therefore arise because of bulk-boundary correspondence. (b) The corresponding plot of the Zak phase for the zigzag edge of the graphene Hamiltonian as a function of the parallel momentum. A nonzero value of the Zak phase indicates a topological phase and hence the presence of edge states, while a zero value corresponds to the trivial phase.

Graphene also exhibits interesting physics at its edges. On account of the lattice structure, the shape of the edge of a graphene sheet strongly depends on the direction of

the edge cut relative to the crystallographic directions, and different edge shapes may have widely different electronic properties. The two most widely studied graphene edges are zigzag and armchair, shown in Fig. 1.3(a). It turns out that edge states are a generic feature of lattice termination boundaries in graphene, with the exception of the armchair edge orientation, which hosts no edge states [42, 48]. For instance, at a crystallographically clean zigzag boundary, a flat band of zero-energy edge states manifests, connecting the edge projections of the two distinct Dirac points, as is shown in Fig. 1.5. These edge states may be understood in terms of a topological phase of the bulk Hamiltonian of graphene, and are therefore a manifestation of bulk-boundary correspondence [27, 49, 50].

At this stage, it might seem nonsensical to invoke bulk topology in the context of graphene. The bulk Hamiltonian of graphene has a gapless spectrum as Fig. 1.4 shows, while the classification of topological phases introduced in Table 1.1 applies only to Hamiltonians with an energy gap. Aside from this conundrum, there is another problem. The graphene Hamiltonian is two dimensional, and has all of the three fundamental discrete symmetries, with $\mathscr{P}^2 = \mathscr{T}^2 = 1$. The Hamiltonian thus belongs to class BDI of Table 1.1, which is a trivial class in two dimensions, with no possible nontrivial topological phases.

The solution to this problem lies in the observation that adding an edge to a Hamiltonian only breaks translational invariance along a single direction, namely perpendicular to the edge. On the other hand, parallel to the edge, the translational symmetry remains unbroken, and the corresponding momentum $\mathbf{k}_\parallel$ thus remains conserved. Hence, instead of applying the topological classification to the full bulk Hamiltonian over the entire Brillouin zone, we can work with each Hamiltonian at a fixed $\mathbf{k}_\parallel$ separately, effectively treating $\mathbf{k}_\parallel$ as a parameter [49, 51, 52]. These Hamiltonians have one lower dimension than the full bulk Hamiltonian, and if such a lower-dimensional Hamiltonian is gapped, we an apply the topological classification of Table 1.1 to it. This simple idea allows one to study topological phases in gapless systems, and forms the basis for the analysis of a nodal topological superconducting phase in a family of monolayer transition metal dichalcogenides that is the subject of Chaper 5. In the context of graphene, the family of Hamiltonians at fixed $\mathbf{k}_\parallel$ has dimension $d = 1$, which in class BDI[1] has possible topological phases with a $\mathbb{Z}$ topological invariant.

We now demonstrate the topological origin of the edge states at zigzag graphene boundary. The bulk tight binding Hamiltonian of graphene is given in Eq. (1.18). First, we make the gauge transformation $c_{B\mathbf{k}} \to c_{B\mathbf{k}} e^{i\mathbf{k}\cdot\boldsymbol{\delta}_3}$. From Eqs. (1.15) and (1.19), we have $\boldsymbol{\delta}_1 - \boldsymbol{\delta}_3 = \mathbf{a}_2$ and $\boldsymbol{\delta}_2 - \boldsymbol{\delta}_3 = \mathbf{a}_1$, and the Hamiltonian in the new basis is thus

$$\begin{aligned} H(\mathbf{k}) &= \begin{bmatrix} 0 & t(e^{i\mathbf{k}\cdot\mathbf{a}_2} + e^{i\mathbf{k}\cdot\mathbf{a}_1} + 1) \\ t(e^{-i\mathbf{k}\cdot\mathbf{a}_2} + e^{-i\mathbf{k}\cdot\mathbf{a}_1} + 1) & 0 \end{bmatrix} \\ &= t \begin{bmatrix} 0 & e^{ik_2} + e^{ik_1} + 1 \\ e^{-ik_2} + e^{-ik_1} + 1 & 0 \end{bmatrix}, \end{aligned} \tag{1.24}$$

[1] Note that for a generic choice of $\mathbf{k}_\parallel$, time-reversal and particle-hole are generally not symmetries of the one-dimensional Hamiltonian at a fixed $\mathbf{k}_\parallel$, because these symmetries map $\mathbf{k}_\parallel \to -\mathbf{k}_\parallel$. However, for the graphene zigzag boundary with $\mathbf{k}_\parallel = k_x\hat{\mathbf{x}}$, each one-dimensional Hamiltonian at a fixed k_x still has all three discrete symmetries, and hence remains in class BDI. This is because the graphene Hamiltonian is invariant under the change $k_x \to -k_x$, as Eqs. (1.18) and (1.19) show.

with the momenta in the basis of the reciprocal lattice (1.16), $k_1 = \mathbf{k}\cdot\mathbf{a}_1$ and $k_2 = \mathbf{k}\cdot\mathbf{a}_2$. As in Fig. 1.3, we consider a zigzag edge parallel to $\mathbf{a}_1$, and identify $k_1 = k_\parallel$. The armchair direction $2\mathbf{a}_2 - \mathbf{a}_1$ is perpendicular to the edge. Introducing the normal component of the momentum $k_\perp$ with the substitution $\sqrt{3}k_\perp = \mathbf{k}\cdot(2\mathbf{a}_2 - \mathbf{a}_1) = 2k_2 - k_1$, the Hamiltonian (1.24) reads

$$\begin{aligned} H(k_\parallel, k_\perp) &= t\begin{bmatrix} 0 & e^{i(\sqrt{3}k_\perp + k_\parallel)/2} + e^{ik_\parallel} + 1 \\ e^{-i(\sqrt{3}k_\perp + k_\parallel)/2} + e^{-ik_\parallel} + 1 & 0 \end{bmatrix} \\ &= \begin{bmatrix} 0 & h(k_\parallel, k_\perp) \\ h^*(k_\parallel, k_\perp) & 0 \end{bmatrix}. \end{aligned} \tag{1.25}$$

The Hamiltonian has the form

$$H(k_\parallel, k_\perp) = \boldsymbol{\sigma}\cdot\boldsymbol{f}(k_\parallel, k_\perp), \tag{1.26}$$

with $\boldsymbol{\sigma} = (\sigma_x, \sigma_y)$ and $\boldsymbol{f}(k_\parallel, k_\perp) = (f_x, f_y)$, where

$$\begin{aligned} f_x(k_\parallel, k_\perp)/t &= \cos\left(\frac{\sqrt{3}}{2}k_\perp + \frac{1}{2}k_\parallel\right) + \cos(k_\parallel) + 1, \\ f_y(k_\parallel, k_\perp)/t &= -\sin\left(\frac{\sqrt{3}}{2}k_\perp + \frac{1}{2}k_\parallel\right) - \sin(k_\parallel). \end{aligned} \tag{1.27}$$

At a fixed $k_\parallel$, the topological properties of the Hamiltonian are encoded in loops traced out by the vector $\boldsymbol{f}(k_\parallel, k_\perp)$ as $k_\perp$ varies over the Brillouin zone [27, 50]. The loops become more apparent upon rewriting $\boldsymbol{f}(k_\parallel, k_\perp)$ as

$$\boldsymbol{f}(k_\parallel, k_\perp) = \boldsymbol{f}^0(k_\parallel) + 2\boldsymbol{f}^r(k_\parallel)\cos(\sqrt{3}k_\perp/2) + 2\boldsymbol{f}^i(k_\parallel)\sin(\sqrt{3}k_\perp/2), \tag{1.28}$$

such that

$$\begin{aligned} \boldsymbol{f}^0(k_\parallel) &= t[\cos(k_\parallel) + 1,\ -\sin(k_\parallel)]^T, \\ 2\boldsymbol{f}^r(k_\parallel) &= t[\cos(k_\parallel/2),\ \sin(k_\parallel/2)]^T, \\ 2\boldsymbol{f}^i(k_\parallel) &= t[\sin(k_\parallel/2),\ -\cos(k_\parallel/2)]^T. \end{aligned} \tag{1.29}$$

The vectors $2\boldsymbol{f}^r(k_\parallel)$ and $2\boldsymbol{f}^i(k_\parallel)$ are orthogonal, and both have the length t. Sweeping $k_\perp$ over the Brillouin zone[2] for a fixed $k_\parallel$, Eqs. (1.28) and (1.29) show that $\boldsymbol{f}(k_\parallel, k_\perp)$ traces out a circle of radius t that is centered at $\boldsymbol{f}^0(k_\parallel)$, as shown in Fig. 1.6. The Hamiltonian at $k_\parallel$ is topologically nontrivial if the circle encloses the origin, and trivial if it does not [27]. The circle encloses the origin only when the offset $\boldsymbol{f}^0$ is smaller than the radius of the circle, that is if $|\boldsymbol{f}^0| < t$, or equivalently if $2\pi/3 < k_\parallel < 4\pi/3$. By bulk-boundary correspondence, edge states should therefore appear at the zigzag edge for $2\pi/3 < k_\parallel < 4\pi/3$, which is in perfect agreement with Fig. 1.5(a).

The classification of Hamiltonians depending on whether they trace out a curve which encloses the origin or not is reminiscent of the winding number topological invariant. The winding number invariant is characteristic for the classes of Table 1.1 with chiral

[2] Note that the one-dimensional Brillouin zone of $k_\perp$ is *e.g.* $-2\pi/\sqrt{3} \le k_\perp < 2\pi/\sqrt{3}$, see Ref. [50] or Chapter 5.

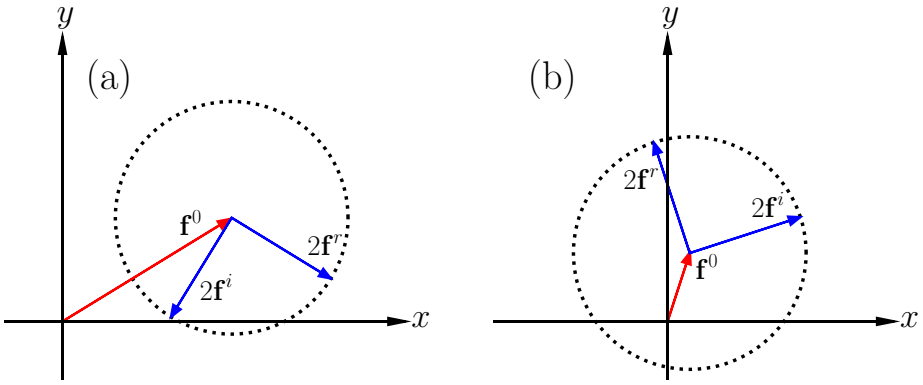

Figure 1.6: Schematic of the circles traced out by the vector $\boldsymbol{f}(k_\parallel, k_\perp)$ of Eq. (1.26) as $k_\perp$ varies over the Brillouin zone for a fixed $k_\parallel$ in (a) the trivial phase, and (b) a topological phase. The circle encloses the origin in a topological phase, but not in the trivial phase. The constituent vectors $\boldsymbol{f}^0$ (red), $\boldsymbol{f}^r$, and $\boldsymbol{f}^i$ (both in blue) of Eqs. (1.28) and (1.29) are also shown.

symmetry [16]. It counts the number of times the Hamiltonian, or a related quantity, winds around the origin. Indeed, an alternative but equivalent method to characterize the topological phases of graphene is to evaluate the Zak phase [50, 53]

$$\mathcal{Z}(k_\parallel) = \frac{1}{2}\oint dk_\perp \partial_{k_\perp}\phi(k_\parallel, k_\perp), \tag{1.30}$$

where $\phi(k_\parallel, k_\perp)$ is the phase of $h(k_\parallel, k_\perp) = |h(k_\parallel, k_\perp)|e^{i\phi(k_\parallel, k_\perp)}$ in Eq. (1.25), and the closed loop integral is taken over the one-dimensional Brillouin zone of $k_\perp$. The Zak phase counts how often the vector $\boldsymbol{f}(k_\parallel, k_\perp)$ winds around the origin, and differs from the winding number only by a prefactor of π. The Zak phase is shown in Fig. 1.5(b) for the zigzag edge, where a nonzero value at $k_\parallel$ corresponds to a topologically nontrivial phase. The winding number will surface again in the context of the gapless topological phases presented in Chapter 5.

Bulk-boundary correspondence gives rise to the flat band of zero energy edge states at a clean zigzag edge, because such an edge has the same symmetry classification as the bulk Hamiltonian. However, if the edge itself breaks the chiral symmetry, the situation changes. To see the effects of local chiral symmetry breaking at the boundary on the edge states, let us employ the Dirac equation (1.21) to compute the dispersion relations of a nanoribbon of width W. At the ribbon edges, we supplement the Dirac equation with the boundary conditions [42, 54]

$$\begin{aligned} \psi(x,0) &= -\tau_z \otimes (\sigma_z \cos\theta + \sigma_x \sin\theta)\psi(x,0), \\ \psi(x,W) &= \tau_z \otimes (\sigma_z \cos\theta + \sigma_x \sin\theta)\psi(x,W), \end{aligned} \tag{1.31}$$

for the 4-component spinor ψ on which the Dirac Hamiltonian (1.21) acts. The parameter θ interpolates between the boundary condition of a clean zigzag edge ($\theta = 0$) and the

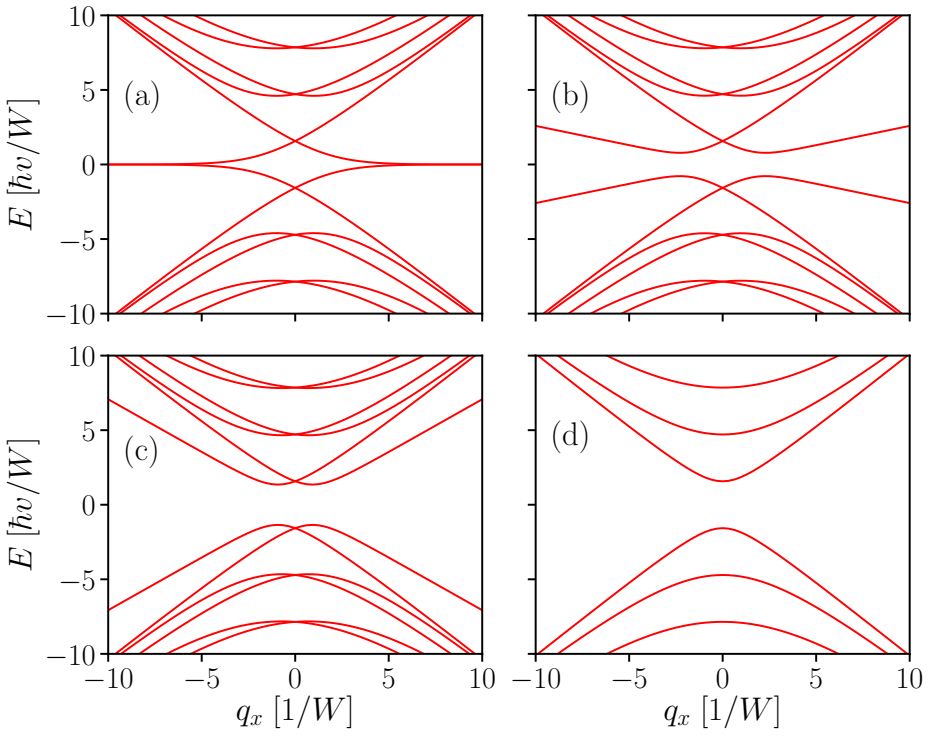

Figure 1.7: Dispersion relation of a graphene nanoribbon of width $W = 300a$ computed using the Dirac equation (1.21) with the staggered potential boundary conditions (1.31) with (a) $\theta = 0$, (b) $\theta = \pi/12$, (c) $\theta = \pi/4$, and (d) $\theta = \pi/2$. The ribbon with $\theta = 0$ (zigzag boundary conditions) has the dispersionless zero-energy edge states characteristic of zigzag boundaries. A nonzero θ violates the chiral symmetry protecting the flat bands locally at the boundary. Hence, increasing θ from zero makes the edge bands dispersive and splits them away from zero energy, until they merge completely into the bulk bands as in (d).

so-called infinite-mass boundary condition ($\theta = \pi/2$), which explicitly breaks the chiral symmetry of the boundary [42]. In practice, this boundary condition represents a staggered edge potential at a zigzag edge, *i.e.* a local potential difference between the two sublattices at the boundary. The value of θ then depends on the strength of the potential and its extent into the graphene sheet away from the edge. A staggered edge potential can occur at a zigzag edge if extra atoms bind to the outermost row of carbon atoms, which only have two neighbouring carbon atoms instead of three, and hence an unbound electron [41]. Figure 1.7 shows the dispersion relation of the ribbon for various values of θ. With the pure zigzag boundary condition $\theta = 0$, the dispersion exhibits the flat band of zero-energy edge states that is also visible in Fig. 1.5(a) [55]. A nonzero θ breaks the chiral symmetry at the boundary, and hence also the topological protection of the flat band of edge states. Indeed, increasing θ from zero splits the edge bands away from zero energy and gradually merges them into the bulk band structure of the ribbon. For the pure infinite-mass boundary condition $\theta = \pi/2$, there is no sign left of the edge bands.

Crucially, tweaking the boundary condition in this manner does not alter the topo-

logical properties of the bulk Hamiltonian. Although the bulk Hamiltonian remains in a topologically nontrivial phase in a range of momenta $k_\parallel$, the lower symmetry classification of the boundary itself removes the edge states. This example thus illustrates the importance of the symmetry classification of the boundary in bulk-boundary correspondence. Chapter 4 is devoted to a general the study of boundary conditions for continuum Hamiltonians, including the proper symmetry classification of boundary conditions.

1.7. STRUCTURE OF THIS THESIS

Here, we give a brief overview of the topics explored in the following chapters.

1.7.1. CHAPTER 2: QSYMM: ALGORITHMIC SYMMETRY FINDING AND SYMMETRIC HAMILTONIAN GENERATION.

Symmetry is a guiding principle in physics that allows to generalize conclusions between many physical systems. In the ongoing search for new topological phases of matter, symmetry plays a crucial role by protecting topological phases. We address two converse questions relevant to the symmetry classification of systems: Is it possible to generate all possible single-body Hamiltonians compatible with a given symmetry group? Is it possible to find all the symmetries of a given family of Hamiltonians? We present numerically stable, deterministic polynomial time algorithms to solve both of these problems. Our treatment extends to all continuous or discrete symmetries of non-interacting lattice or continuum Hamiltonians. We implement the algorithms in the Qsymm Python package, and demonstrate their usefulness through applications in active research areas of condensed matter physics, including Majorana wires and Kekule graphene.

1.7.2. CHAPTER 3: ANDREEV RECTIFIER: A NONLOCAL CONDUCTANCE SIGNATURE OF TOPOLOGICAL PHASE TRANSITIONS.

The proximity effect in hybrid superconductor-semiconductor structures, crucial for realizing Majorana edge modes, is complicated to control due to its dependence on many unknown microscopic parameters. In addition, defects can spoil the induced superconductivity locally in the proximitised system which complicates measuring global properties with a local probe. We show how to use the nonlocal conductance between two spatially separated leads to probe three global properties of a proximitised system: the bulk superconducting gap, the induced gap, and the induced coherence length. Unlike local conductance spectroscopy, nonlocal conductance measurements distinguish between non-topological zero-energy modes localized around potential inhomogeneities, and true Majorana edge modes that emerge in the topological phase. In addition, we find that the nonlocal conductance is an odd function of bias at the topological phase transition, acting as a current rectifier in the low-bias limit. More generally, we identify conditions for crossed Andreev reflection to dominate the nonlocal conductance and show how to design a Cooper pair splitter in the open regime.

1.7.3. CHAPTER 4: GENERAL APPROACH TO BOUNDARY CONDITIONS AND SPECTRA OF CONTINUUM HAMILTONIANS: MATCHING TO TIGHT BINDING EDGES.

In order to compute the spectrum of a confined Hamiltonian, it is necessary to impose boundary conditions at the edges. We parametrize the most general boundary conditions for a generic continuum Hamiltonian that obey current conservation at a single, isolated boundary, and show how to classify the boundary conditions by symmetry. The boundary conditions are given in terms of a matrix parameter that is either skew-Hermitian or unitary. We propose a numerically stable algorithm to compute the spectrum of a continuum Hamiltonian between two parallel confinements with arbitrary boundary conditions from the parametrization. We furthermore show how to construct a specific continuum boundary condition of the general parametrization from the boundary of a corresponding tight binding model in a numerically stable way, which makes it possible to model the tight binding boundary using a continuum model combined with an appropriate boundary condition. Finally, we apply our techniques to study the effects of scalar and magnetic edge potentials on the helical edge bands of a two-dimensional topological insulator, using both continuum and tight binding models.

1.7.4. CHAPTER 5: PLATFORM FOR NODAL TOPOLOGICAL SUPERCONDUCTORS IN MONOLAYER MOLYBDENUM DICHALCOGENIDES.

We propose a platform to realize nodal topological superconductors in a superconducting monolayer of MoX_2 (X=S, Se, Te) using an in-plane magnetic field. The bulk nodal points appear where the spin splitting due to spin-orbit coupling vanishes near the $\pm\mathbf{K}$ valleys of the Brillouin zone, and are six or twelve per valley in total. In the nodal topological superconducting phase, the nodal points are connected by flat bands of zero-energy Andreev edge states. These flat bands, which are protected by chiral symmetry, are present for all lattice-termination boundaries except zigzag.

1.7.5. CHAPTER 6: BREAKDOWN OF THE LAW OF REFLECTION AT A DISORDERED GRAPHENE EDGE.

The law of reflection states that smooth surfaces reflect waves specularly, thereby acting as a mirror. This law is insensitive to disorder as long as its length scale is smaller than the wavelength. Monolayer graphene exhibits a linear dispersion at low energies and consequently a diverging Fermi wavelength. We present proof that for a disordered graphene boundary, resonant scattering off disordered edge modes results in diffusive electron reflection even when the electron wavelength is much longer than the disorder correlation length. Using numerical quantum transport simulations, we demonstrate that this phenomenon can be observed as a nonlocal conductance dip in a magnetic focusing experiment.

REFERENCES

[1] M. Z. Hasan and C. L. Kane, *Colloquium: Topological insulators,* Rev. Mod. Phys. **82**, 3045 (2010).

[2] X.-L. Qi and S.-C. Zhang, *Topological insulators and superconductors,* Rev. Mod. Phys. **83**, 1057 (2011).

[3] M. Sato and Y. Ando, *Topological superconductors: a review,* Rep. Prog. Phys. **80**, 076501 (2017).

[4] J. Alicea, *New directions in the pursuit of majorana fermions in solid state systems,* Rep. Prog. Phys. **75**, 076501 (2012).

[5] M. Leijnse and K. Flensberg, *Introduction to topological superconductivity and majorana fermions,* Semiconductor Science and Technology **27**, 124003 (2012).

[6] C. Beenakker, *Search for majorana fermions in superconductors,* Annu. Rev. Condens. Matter Phys. **4**, 113 (2013).

[7] A. Y. Kitaev, *Unpaired majorana fermions in quantum wires,* Phys. Usp. **44**, 131 (2001).

[8] S. B. Bravyi and A. Y. Kitaev, *Fermionic quantum computation,* Annals of Physics **298**, 210 (2002).

[9] C. L. Kane and E. J. Mele, *Quantum spin hall effect in graphene,* Phys. Rev. Lett. **95**, 226801 (2005).

[10] B. A. Bernevig, T. L. Hughes, and S.-C. Zhang, *Quantum spin hall effect and topological phase transition in hgte quantum wells,* Science **314**, 1757 (2006), http://science.sciencemag.org/content/314/5806/1757.full.pdf .

[11] A. H. Castro Neto, F. Guinea, N. M. R. Peres, K. S. Novoselov, and A. K. Geim, *The electronic properties of graphene,* Rev. Mod. Phys. **81**, 109 (2009).

[12] E. Prada, P. San-Jose, and R. Aguado, *Transport spectroscopy of n s nanowire junctions with majorana fermions,* Phys. Rev. B **86**, 180503 (2012).

[13] C.-X. Liu, J. D. Sau, T. D. Stanescu, and S. Das Sarma, *Andreev bound states versus majorana bound states in quantum dot-nanowire-superconductor hybrid structures: Trivial versus topological zero-bias conductance peaks,* Phys. Rev. B **96**, 075161 (2017).

[14] J. J. Sakurai, *Modern quantum mechanics; rev. ed.* (Addison-Wesley, Reading, MA, 1994).

[15] E. Wigner and J. Griffin, *Group Theory and Its Application to the Quantum Mechanics of Atomic Spectra*, Pure and applied physics (Academic Press, 1959).

[16] S. Ryu, A. P. Schnyder, A. Furusaki, and A. W. W. Ludwig, *Topological insulators and superconductors: tenfold way and dimensional hierarchy,* New Journal of Physics **12**, 065010 (2010).

[17] C.-K. Chiu, J. C. Teo, A. P. Schnyder, and S. Ryu, *Classification of topological quantum matter with symmetries,* Reviews of Modern Physics **88** (2016), 10.1103/RevModPhys.88.035005.

[18] C. Cohen-Tannoudji, B. Diu, and F. Laloe, *Quantum Mechanics*, Quantum Mechanics No. v. 1 (Wiley, 1991).

[19] P. DE GENNES, *Superconductivity of Metals and Alloys*, Advanced Book Classics (Addison-Wesley Publishing Company, 1966).

[20] A. Hatcher, *Algebraic Topology*, Algebraic Topology (Cambridge University Press, 2002).

[21] K. v. Klitzing, G. Dorda, and M. Pepper, *New method for high-accuracy determination of the fine-structure constant based on quantized hall resistance,* Phys. Rev. Lett. **45**, 494 (1980).

[22] T. J. Witt, *Electrical resistance standards and the quantum hall effect,* Review of Scientific Instruments **69**, 2823 (1998), https://doi.org/10.1063/1.1149062 .

[23] D. J. Thouless, M. Kohmoto, M. P. Nightingale, and M. den Nijs, *Quantized hall conductance in a two-dimensional periodic potential,* Phys. Rev. Lett. **49**, 405 (1982).

[24] A. Altland and M. R. Zirnbauer, *Nonstandard symmetry classes in mesoscopic normal-superconducting hybrid structures,* Phys. Rev. B **55**, 1142 (1997).

[25] A. P. Schnyder, S. Ryu, A. Furusaki, and A. W. W. Ludwig, *Classification of topological insulators and superconductors in three spatial dimensions,* Phys. Rev. B **78**, 195125 (2008).

[26] A. Kitaev, *Periodic table for topological insulators and superconductors,* in *American Institute of Physics Conference Series*, American Institute of Physics Conference Series, Vol. 1134, edited by V. Lebedev and M. Feigel'Man (2009) pp. 22–30, arXiv:0901.2686 .

[27] R. S. K. Mong and V. Shivamoggi, *Edge states and the bulk-boundary correspondence in dirac hamiltonians,* Phys. Rev. B **83**, 125109 (2011).

[28] I. C. Fulga, F. Hassler, and A. R. Akhmerov, *Scattering theory of topological insulators and superconductors,* Phys. Rev. B **85**, 165409 (2012).

[29] B. Bradlyn, L. Elcoro, J. Cano, M. G. Vergniory, Z. Wang, C. Felser, M. I. Aroyo, and B. A. Bernevig, *Topological quantum chemistry,* Nature **547**, 298 (2017).

[30] L. Fu, *Topological crystalline insulators,* Phys. Rev. Lett. **106**, 106802 (2011).

[31] Y. Ando and L. Fu, *Topological crystalline insulators and topological superconductors: From concepts to materials,* Annu. Rev. Condens. Matter Phys. **6**, 361 (2015).

[32] R. Jackiw and C. Rebbi, *Solitons with fermion number ½,* Phys. Rev. D **13**, 3398 (1976).

[33] W. P. Su, J. R. Schrieffer, and A. J. Heeger, *Solitons in polyacetylene,* Phys. Rev. Lett. **42**, 1698 (1979).

[34] V. Mourik, K. Zuo, S. M. Frolov, S. R. Plissard, E. P. A. M. Bakkers, and L. P. Kouwenhoven, *Signatures of majorana fermions in hybrid superconductor-semiconductor nanowire devices,* Science **336**, 1003 (2012).

[35] M. T. Deng, C. L. Yu, G. Y. Huang, M. Larsson, P. Caroff, and H. Q. Xu, *Anomalous zero-bias conductance peak in a nb–insb nanowire–nb hybrid device,* Nano Letters **12**, 6414 (2012).

[36] H. Zhang, Ö. Gül, S. Conesa-Boj, M. Nowak, M. Wimmer, K. Zuo, V. Mourik, F. K. de Vries, J. van Veen, M. W. A. de Moor, J. D. S. Bommer, D. J. van Woerkom, D. Car, S. R. Plissard, E. P. A. M. Bakkers, M. Quintero-Pérez, M. C. Cassidy, S. Koelling, S. Goswami, K. Watanabe, T. Taniguchi, and L. P. Kouwenhoven, *Ballistic superconductivity in semiconductor nanowires,* **8**, 16025 EP (2017).

[37] Ö. Gül, H. Zhang, J. D. S. Bommer, M. W. A. de Moor, D. Car, S. R. Plissard, E. P. A. M. Bakkers, A. Geresdi, K. Watanabe, T. Taniguchi, and L. P. Kouwenhoven, *Ballistic majorana nanowire devices,* Nature Nanotechnology **13**, 192 (2018).

[38] C. W. Groth, M. Wimmer, A. R. Akhmerov, and X. Waintal, *Kwant: a software package for quantum transport,* New Journal of Physics **16**, 063065 (2014).

[39] K. T. Law, P. A. Lee, and T. K. Ng, *Majorana fermion induced resonant andreev reflection,* Phys. Rev. Lett. **103**, 237001 (2009).

[40] A. R. Akhmerov, J. P. Dahlhaus, F. Hassler, M. Wimmer, and C. W. J. Beenakker, *Quantized conductance at the majorana phase transition in a disordered superconducting wire,* Phys. Rev. Lett. **106**, 057001 (2011).

[41] Y.-W. Son, M. L. Cohen, and S. G. Louie, *Energy gaps in graphene nanoribbons,* Phys. Rev. Lett. **97**, 216803 (2006).

[42] A. R. Akhmerov and C. W. J. Beenakker, *Boundary conditions for Dirac fermions on a terminated honeycomb lattice,* Phys. Rev. B **77**, 085423 (2008).

[43] A. K. Geim and K. S. Novoselov, *The rise of graphene,* Nature Materials **6**, 183 (2007).

[44] B. A. Bernevig and T. L. Hughes, *Topological Insulators and Topological Superconductors*, stu - student edition ed. (Princeton University Press, 2013).

[45] D. Varjas, T. Ö. Rosdahl, and A. R. Akhmerov, *Qsymm: algorithmic symmetry finding and symmetric hamiltonian generation,* New Journal of Physics **20**, 093026 (2018).

[46] P. R. Wallace, *The band theory of graphite,* Phys. Rev. **71**, 622 (1947).

[47] G. W. Semenoff, *Condensed-matter simulation of a three-dimensional anomaly,* Phys. Rev. Lett. **53**, 2449 (1984).

[48] J. A. M. van Ostaay, A. R. Akhmerov, C. W. J. Beenakker, and M. Wimmer, *Dirac boundary condition at the reconstructed zigzag edge of graphene,* Phys. Rev. B **84**, 195434 (2011).

[49] S. Ryu and Y. Hatsugai, *Topological origin of zero-energy edge states in particle-hole symmetric systems,* Phys. Rev. Lett. **89**, 077002 (2002).

[50] P. Delplace, D. Ullmo, and G. Montambaux, *Zak phase and the existence of edge states in graphene,* Phys. Rev. B **84**, 195452 (2011).

[51] M. Sato, Y. Tanaka, K. Yada, and T. Yokoyama, *Topology of andreev bound states with flat dispersion,* Phys. Rev. B **83**, 224511 (2011).

[52] A. P. Schnyder and P. M. R. Brydon, *Topological surface states in nodal superconductors,* J. Phys.: Condens. Matter **27**, 243201 (2015).

[53] J. Zak, *Berry's phase for energy bands in solids,* Phys. Rev. Lett. **62**, 2747 (1989).

[54] E. McCann and V. I. Fal'ko, *Symmetry of boundary conditions of the Dirac equation for electrons in carbon nanotubes,* J. Phys. Condens. Matter **16**, 2371 (2004).

[55] L. Brey and H. A. Fertig, *Electronic states of graphene nanoribbons studied with the dirac equation,* Phys. Rev. B **73**, 235411 (2006).

2

QSYMM: ALGORITHMIC SYMMETRY FINDING AND SYMMETRIC HAMILTONIAN GENERATION

This chapter has been previously published as Dániel Varjas, Tómas Ö. Rosdahl, and Anton R. Akhmerov, *Qsymm: Algorithmic symmetry finding and symmetric Hamiltonian generation*, New J. Phys. **20**, 093026 (2018).

2.1. INTRODUCTION

A transformation that leaves a physical system invariant is called a symmetry, and such transformations have an ever-important role in modern physics. For example, symmetry breaking characterizes the classical theory of phase transitions, and the invariance of the speed of light between reference frames is a cornerstone of special relativity theory. In molecules and crystals, the symmetries of the constituent atomic orbitals determine the character of chemical bonds. The band theory of solids uses the translational invariance of a crystal structure to classify states into energy bands according to their crystal momentum, where the band structure is in turn constrained by the point group symmetries of the crystal. To describe such bands, model Hamiltonians based on tight-binding approximations [1–5] or $\mathbf{k}\cdot\mathbf{p}$ perturbation theory [6–8] are typically constructed by fitting a generic Hamiltonian allowed by symmetry to match experimental data or first principles-calculations.

Recent studies focused on the role of symmetry in protecting topological phases [9, 10]. Initially, analysis of time reversal and particle-hole symmetries led to the full classification of free fermionic phases in the ten Altland-Zirnbauer classes [11–13]. Later interest shifted to include symmetries involving transformations of space [14–22]. Some of these phases are stable against disorder that preserves the symmetry only on average [23], leading to a richer structure of symmetry-protected topological phases. Analysis of newly proposed symmetry-protected topological phases is often done using minimal models, such as tight-binding Hamiltonians with short-range hoppings, or continuum Hamiltonians valid near high symmetry points in the Brillouin zone. Although these models are usually easy to solve, they are prone to having higher symmetry than intended. With the plethora of available symmetry groups, it is a nontrivial task to construct models that possess the stated, but only the stated symmetries, or to decide the complete symmetry group of a given Hamiltonian.

In this chapter we present an algorithm to generate all Hamiltonians that respect given symmetries, using an approach similar to Ref. [24]. In addition, we develop a dual algorithm to find all symmetries of a family of Hamiltonians (Fig. 2.1). Our framework is applicable to all non-interacting, finite or translation invariant lattice or $\mathbf{k}\cdot\mathbf{p}$ Hamiltonians. We treat all possible symmetries, including continuous unitary symmetry groups, continuous spatial rotations, space groups, discrete onsite symmetries (such as time reversal, particle-hole and chiral symmetries), and arbitrary combinations of these. Besides static fermionic systems, our methods are also applicable to band structures in photonic crystals [25, 26], magnon spectra, classical mechanical [27, 28] and electronic systems [29], and driven Floquet systems [30].

The chapter is structured as follows: first we review the general symmetry structure of single-particle Hamiltonians. Then we present our algorithm to find Hamiltonians with such symmetries. After that we review the symmetry finding algorithm, which, by factoring out onsite unitary symmetries, makes finding all other symmetries more efficient and guaranteed. We implement our algorithms in the Qsymm Python package [31, 32]. Finally we provide a set of examples where our method was used on problems in active areas of research. We show that Majorana wire devices may be protected against band-tilting by a magnetic symmetry, and double Dirac cones in Kekule distorted graphene are protected by point group and sublattice symmetry. We also construct model Hamiltonians

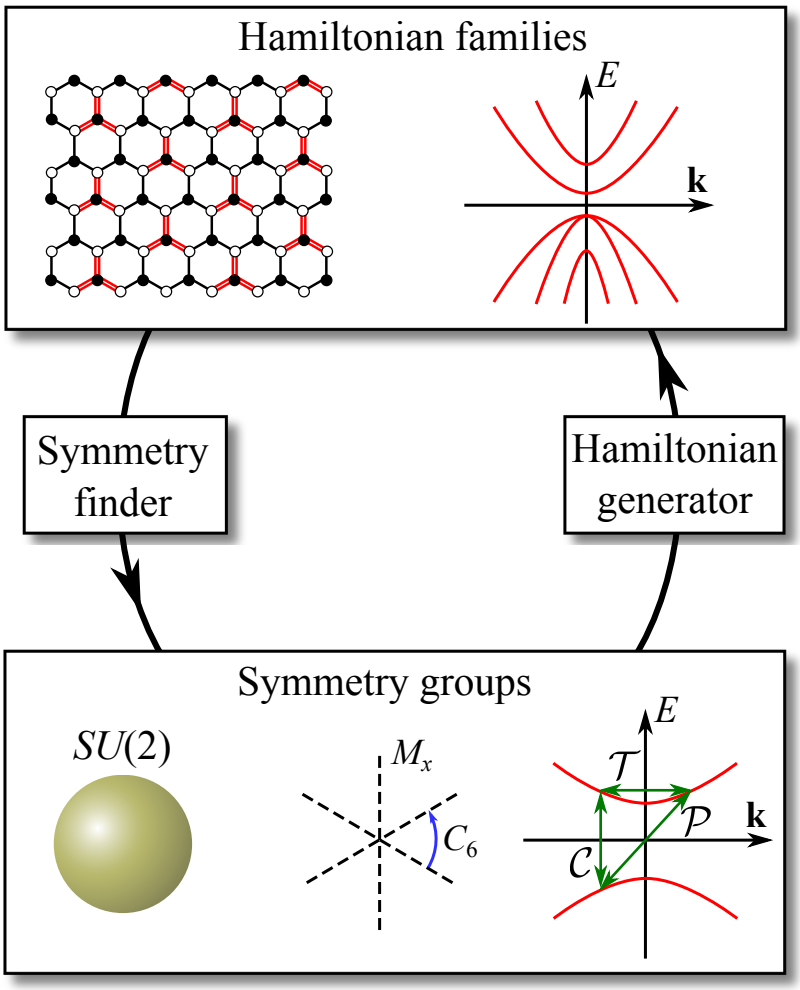

Figure 2.1: Pictorial summary of the methods studied in the chapter. The symmetry finder and Hamiltonian generator algorithms form a two-way connection between Hamiltonian families and symmetry groups.

for transition metal dichalcogenides and distorted spin-orbit coupled SnTe.

2.2. HAMILTONIAN FAMILIES AND SYMMETRIES

2.2.1. CONTINUUM AND TIGHT-BINDING HAMILTONIANS

We focus on non-interacting Hamiltonians. The quadratic Hamilton operator of a finite (zero-dimensional) system can be written as

$$\hat{H} = \sum_{ij} H_{ij} \hat{a}_i^\dagger \hat{a}_j, \tag{2.1}$$

where H is a Hermitian matrix and $\hat{a}_i$ are creation or annihilation operators. We do not make any assumptions about bosonic or fermionic nature of these operators and also allow terms with two creation or two annihilation operators, facilitating the study of superconducting Bogoliubov-de Gennes Hamiltonians. In the framework we use, all the details of the system are encoded in constraints on the matrix part H, which is the focus of our study.

Besides finite systems, we also address systems with d-dimensional translation invariance. The associated conserved quantity is the (lattice) momentum $\mathbf{k}$, which takes values in $\mathbb{R}^d$ for continuous translations, and in the d-dimensional Brillouin zone for discrete translations. Effective continuum Hamiltonians ($\mathbf{k}\cdot\mathbf{p}$ models) also arise as the long-wavelength limit of lattice Hamiltonians. The conservation of $\mathbf{k}$ allows to decompose the single-particle Hilbert space into independent sectors corresponding to each $\mathbf{k}$, such that $\hat{H}$ does not mix sectors, i.e.

$$\hat{H} = \sum_{ij}\sum_{\mathbf{k}} H_{ij}(\mathbf{k})\,\hat{a}^\dagger_{i\mathbf{k}}\hat{a}_{j\mathbf{k}}. \tag{2.2}$$

In the rest of this work we focus on analyzing the matrix-valued Hamiltonian $H(\mathbf{k})$ with matrix elements $H_{ij}(\mathbf{k})$.

A tight-binding Hamiltonian acts on a Hilbert space consisting of basis orbitals in a single translational unit cell, and has the general form

$$H(\mathbf{k}) = \sum_{\delta}\left(e^{i\mathbf{k}\cdot\delta}h_\delta + \text{h.c.}\right). \tag{2.3}$$

The hopping vectors δ connect sites on the lattice, with the matrices of hopping amplitudes h_δ. The $\mathbf{k}\cdot\mathbf{p}$ Hamiltonian provides an accurate continuum approximation near a point in the Brillouin zone, typically a high symmetry point. It is a polynomial in momenta k_i, and has the form

$$H(\mathbf{k}) = \sum_{\mathbf{n}} \mathbf{k}^{\mathbf{n}} h_{\mathbf{n}}, \tag{2.4}$$

where $\mathbf{k}^{\mathbf{n}} = \prod_i k_i^{n_i}$ is a monomial in the multi-index notation with $\mathbf{n} = (n_1, n_2, \ldots)$, and $h^\dagger_{\mathbf{n}} = h_{\mathbf{n}}$. Typical methods to construct $\mathbf{k}\cdot\mathbf{p}$ Hamiltonians start with a series expansion of a more complete lattice model from e.g. *ab initio* calculations around the high symmetry point, or by writing down all symmetry-allowed terms and fitting to experimental data or first principles calculations [2, 3, 8, 33–35].

2.2.2. HAMILTONIAN FAMILIES

A set of symmetries only defines a *Hamiltonian family*, as opposed to one single Hamiltonian. A Hamiltonian family is the linear space of Hamiltonians

$$H(\mathbf{k}) = \sum_n c_n H_n(\mathbf{k}), \tag{2.5a}$$

with arbitrary real coefficients c_n, and basis vectors

$$H_n(\mathbf{k}) = \sum_\alpha f_\alpha(\mathbf{k}) h_{\alpha n},\ H^\dagger_n(\mathbf{k}) = H_n(\mathbf{k}). \tag{2.5b}$$

Here $h_{\alpha n}$ are constant matrices of identical size, and $f_\alpha(\mathbf{k})$ are linearly independent scalar functions. In the rest of this work, whenever referring to a Hamiltonian, we mean a Hamiltonian family. A Hamiltonian family is also the only useful starting point to analyzing the symmetry content of Hamiltonians. For a zero-dimensional Hamiltonian, the symmetry group is always given by independent unitary transformations in each degenerate eigensubspace. This group, however, provides no insight beyond the degeneracies of the levels. In a family of continuum $\mathbf{k}\cdot\mathbf{p}$ Hamiltonians, $f_\alpha(\mathbf{k})$ is a monomial, and in a tight-binding Hamiltonian, a phase factor $e^{i\mathbf{k}\cdot\delta}$ with δ a hopping vector.

There is a natural inner product in the space of Hamiltonians (2.5). We define the product of $H_1(\mathbf{k}) = f_1(\mathbf{k})h_1$ and $H_2(\mathbf{k}) = f_2(\mathbf{k})h_2$ as $\langle H_1(\mathbf{k}), H_2(\mathbf{k})\rangle = \langle f_1, f_2\rangle \langle h_1, h_2\rangle_F$. On the matrix part, the Frobenius inner product is given by $\langle A, B\rangle_F = \mathrm{Tr}\left(A^\dagger B\right)$. For the inner product of the $\mathbf{k}$-dependent prefactors, we use the Bombieri inner product [36] for polynomials, $\langle \mathbf{k}^\mathbf{n}, \mathbf{k}^\mathbf{m}\rangle = \delta_{\mathbf{n},\mathbf{m}} \frac{\mathbf{n}!}{|\mathbf{n}|!}$ where $\mathbf{n}! = \prod_i n_i!$ and $|\mathbf{n}| = \sum_i n_i$, such that different monomials are orthogonal. For phase factors we use $\langle e^{i\mathbf{k}\cdot\mathbf{a}}, e^{i\mathbf{k}\cdot\mathbf{b}}\rangle = \delta_{\mathbf{a},\mathbf{b}}$. Both of these inner products on the function spaces are invariant under the isometries of $\mathbf{k}$-space, and therefore all symmetry actions we consider in this work are (anti)unitary with respect to this inner product. This structure of the space of Hamiltonians also justifies our use of single exponentials and single monomials as the expansion basis.

2.2.3. SYMMETRY CONSTRAINTS ON HAMILTONIAN FAMILIES

We adopt the active view of symmetry action g on the Hamiltonian: $g(H)$ represents a transformed Hamiltonian, such that the matrix elements between rotated wave functions $g\left(\left|\psi(\mathbf{k})\right\rangle\right)$ are identical. In other words, a Hamiltonian has a symmetry if g leaves the Hamiltonian invariant,

$$g(H) = H. \tag{2.6}$$

A general unitary symmetry g acts on a Hamiltonian $H(\mathbf{k})$ as

$$g\left(H\right)(\mathbf{k}) = \pm U_g H(R_g^{-1}\mathbf{k}) U_g^{-1}, \tag{2.7a}$$

and a general antiunitary symmetry as

$$g\left(H\right)(\mathbf{k}) = \pm U_g H^*(-R_g^{-1}\mathbf{k}) U_g^{-1}. \tag{2.7b}$$

Here the orthogonal matrix R_g is the real space action, and the unitary matrix U_g is the Hilbert space action of g. We include the overall $\pm$ sign to treat *antisymmetries*—symmetries that reverse the sign of energy—on an equal footing. We restrict our considerations to a constant U_g, however, in the real space basis (see Section 2.3.2), any space group operator may only contain an overall $\mathbf{k}$-dependent phase factor, which cancels in the previous equations.

Substituting Eq. (2.7) into (2.6), we rewrite it in a form linear in the symmetry action:

$$\mathscr{S} H(\mathbf{k}) = \pm H(R\mathbf{k})\mathscr{S}. \tag{2.8}$$

Here the symmetry action $\mathscr{S}$ is $\mathscr{S} = U$ if unitary and $\mathscr{S} = U\mathscr{K}$ if antiunitary, with $\mathscr{K}$ the real space complex conjugation operator: $\mathscr{K} H(\mathbf{k})\mathscr{K} = H^*(-\mathbf{k})$.

We apply the symmetry constraint (2.8) to the Hamiltonian family (2.5a). The spatial action of a symmetry is a rotation in the space of f_α, such that $f_\alpha(\pm R\mathbf{k}) = \sum_\beta \gamma_\alpha^\beta f_\beta(\mathbf{k})$ with γ_α^β known for given R and f_α. Substituting this yields

$$\sum_\alpha f_\alpha(\mathbf{k}) \left[\sum_n (\mathscr{S} h_{\alpha n} \mp \sum_\beta \gamma_\beta^\alpha h_{\beta n} \mathscr{S}) c_n \right] = 0. \tag{2.9}$$

Since f_α are linearly independent functions, the matrix coefficients in the parentheses must vanish for every α, resulting in the system of equations

$$\sum_n (\mathscr{S} h_{\alpha n} \mp \sum_\beta \gamma_\beta^\alpha h_{\beta n} \mathscr{S}) c_n = 0, \ \forall \alpha. \tag{2.10}$$

When symmetries form continuous Lie groups, it is advantageous to use the symmetry generators instead of the group elements. Consider a one parameter family of transformations g_ϕ which, for a fixed ϕ act as a unitary symmetry in the above, and let g_0 be the identity. We define the action of the generator g' through

$$g'(H) = \frac{d}{d\phi} g_\phi(H) \Big|_{\phi=0}. \tag{2.11}$$

Substituting (2.7) and using that $U_{g_\phi} = e^{-i\phi L}$ with $L = L^\dagger$ and $R_{g_\phi} = e^{-i\phi M}$ with $M = -M^T = M^\dagger$, we find

$$g'(H)(\mathbf{k}) = i[H(\mathbf{k}), L] + i \sum_{ij} \frac{\partial H}{\partial k_i} M_{ij} k_j. \tag{2.12}$$

$g_\phi(H) = H$ for every ϕ is equivalent to $g'(H) = 0$. Tight-binding Hamiltonians cannot be invariant under continuous rotations of space, such that $M = 0$ and the symmetry constraint simplifies to

$$\sum_n [h_{\alpha n}, L] c_n = 0, \tag{2.13}$$

where L is a local conserved quantity. Finally, if the Hamiltonian is a polynomial in $\mathbf{k}$, continuous rotation invariance is also possible. With $\sum_{ij} \frac{\partial f_\alpha}{\partial k_i} M_{ij} k_j = \sum_\beta \gamma_\alpha^\beta f_\beta(\mathbf{k})$ the symmetry constraint reads

$$\sum_n ([h_{\alpha n}, L] + \sum_\beta \gamma_\alpha^\beta h_{\beta n}) c_n = 0. \tag{2.14}$$

2.3. GENERATING HAMILTONIANS FROM SYMMETRY CONSTRAINTS

2.3.1. CONSTRAINING HAMILTONIAN FAMILIES

Given a symmetry $\mathscr{S}$ and a Hamiltonian family (2.5), we wish to find the subfamily of Hamiltonians that is invariant under the symmetry transformation (2.8). The symmetry constraint on the Hamiltonian family is a system of homogeneous linear equations for the coefficients c_n [see Eqs. (2.10), (2.13), and (2.14)]. We find the space of solutions numerically using singular value decomposition or sparse eigendecomposition, which gives the subfamily of the original Hamiltonian family (2.5) that satisfies the symmetry.

Imposing additional symmetry constraints on the family yields further linear equations that are identical to Eq. (2.10) in form. We provide an implementation of this algorithm in the Qsymm Python package.

The constraining algorithm allows to generate all possible tight-binding or $\mathbf{k}\cdot\mathbf{p}$ Hamiltonians that satisfy symmetry constraints, by applying the algorithm to the most general representative Hamiltonian family for the system at hand. As an illustration, we reproduce the family of two-band $\mathbf{k}\cdot\mathbf{p}$ Hamiltonians of Ref. [33] for the surface dispersion of the topological insulator Bi_2Te_3. Our starting point is the family of all 2×2 $\mathbf{k}\cdot\mathbf{p}$ Hamiltonians up to third order in the momentum $\mathbf{k} = (k_x, k_y)$. Expanding the matrix part in terms of the identity and Pauli matrices $\sigma_{0,x,y,z}$, the general family consists of 40 basis vectors and is given by

$$H(\mathbf{k}) = \sum_{\mathbf{n}} c_{\mathbf{n}} \sigma_j k_x^{\alpha_x} k_y^{\alpha_y},\ 0 \le |\alpha| \le 3, \tag{2.15}$$

with $\mathbf{n} = (j, \alpha_x, \alpha_y) = (j, \alpha)$. To obtain the surface dispersion Hamiltonian, we constrain (2.15) with time-reversal symmetry ($\mathcal{T} = i\sigma_y K$), and the point group symmetries of the crystal, namely three-fold rotation ($C_3 = e^{-i\pi\sigma_z/3}$), and mirror symmetry in x ($M = i\sigma_x$) [33]. Substituting the three symmetries and the family (2.15) into (2.10) yields a homogeneous system of 120 linear equations for the 40 coefficients $c_{\mathbf{n}}$. The null space of the linear system is the subfamily of Hamiltonians that satisfy the symmetry constraints:

$$\begin{aligned} H(\mathbf{k}) =& c_0 k^2 \sigma_0 + c_1 (k_x \sigma_y - k_y \sigma_x) + c_2 (k_x^3 - 3 k_x k_y^2) \\ &+ c_3 (k_x k^2 \sigma_y - k_y k^2 \sigma_x), \end{aligned} \tag{2.16}$$

with $c_n \in \mathbb{R}$, which matches the Hamiltonian of Ref. [33]. Here, $k^2 = k_x^2 + k_y^2$, and we have relabelled the coefficients c_n for clarity.

The theory of invariants also offers a systematic way to generate $\mathbf{k}\cdot\mathbf{p}$ Hamiltonians corresponding to a given point group symmetry [7]. This approach produces equivalent results in simple cases. Our methods are, however, more general, allowing to treat antiunitary and antisymmetry operators on the same footing. A possible future improvement of Qsymm is to interface with representation theory databases to make this connection more explicit.

2.3.2. GENERATING LATTICE HAMILTONIANS BY SYMMETRIZATION

Lattice models often contain multiple sites per unit cell, but only a small number of bonds. In this case the previous approach of generating all possible terms and constraining them is inefficient due to the large dimension of the null-space. On the other hand, all the hopping terms on symmetry equivalent bonds are completely determined by the hopping on one of these bonds. This allows us introduce a symmetrization strategy to generate all symmetry-constrained lattice Hamiltonians with hoppings of limited range.

To treat arbitrary space group symmetries of general crystal structures, we consider tight-binding Hamiltonians in the real space basis that preserves information on the coordinates of the basis orbitals [37, 38]. Up to a normalization factor, the Bloch basis functions are given by $\left|\chi_{\mathbf{k}}^{al}\right\rangle = \sum_{\mathbf{R}} e^{i\mathbf{k}(\mathbf{R}+\mathbf{r}_a)} \left|\phi_{\mathbf{R}}^{al}\right\rangle$, where a indexes the sites in the unit cell, $l \in [1, \ldots, n_{\text{orbs.}}^a]$ indexes the orbitals on the site, $\mathbf{r}_a$ is the real space position of the site and $\mathbf{R}$ runs over all lattice vectors. In this basis, the hopping terms in the Hamiltonian acquire

a phase factor corresponding to the true real space separation of the sites they connect, as opposed to the separation of the unit cells to which the sites belong. A hopping between site a at $\mathbf{r}_a$ and site b at $\mathbf{r}_b = \mathbf{r}_a + \delta_{ab}$ enters as a term $e^{i\mathbf{k}\delta_{ab}} h^{ab}_{\delta_{ab}} + \text{h.c.}$ where we suppressed the orbital indices of the matrix $h^{ab}_{\delta_{ab}}$. Onsite terms have $\delta_{aa} = 0$. The main advantage of using this gauge is that the form of the Hamiltonian is independent of the choice of the real space origin and the shape of the unit cell. As a consequence, nonsymmorphic symmetry operations only acquire $\mathbf{k}$-dependence in the form of an overall phase factor [38]. In the simplest case of a single site per unit cell, δ_{ab} are lattice vectors.

We start from a small set of terms for every symmetry unique bond δ_{ab} of the form

$$H_n(\mathbf{k}) = e^{i\mathbf{k}\delta_{ab}} h^{ab}_{n\delta_{ab}} + \text{h.c.}, \tag{2.17}$$

with $h^{ab}_{n\delta_{ab}}$ spanning all $n^a_{\text{orbs.}} \times n^b_{\text{orbs.}}$ matrices that are invariant under the continuous onsite symmetry group. We symmetrize these with respect to the discrete point group G, i.e.

$$H_s = \frac{1}{|G|} \sum_{g \in G} g(H), \tag{2.18}$$

where $g(H)$ is the symmetry transformed image of H under the transformation g [see Eq. (2.6)] and $|G|$ is the number of elements in G. Because the sum over $g \in G$ can be replaced by a sum over $(hg) \in G$, $h(H_s) = H_s$ for all $h \in G$. In addition, H_s is exactly the projection of H onto the space of symmetric Hamiltonians. The symmetrized terms span all symmetry allowed Hamiltonians with the prescribed hopping vectors. This space of Hamiltonians is generally overcomplete, we find a minimal set of terms spanning the space using standard linear algebra techniques.

As an example, consider graphene with one spinless orbital per site. A three-fold rotation around a site maps both sublattices onto themselves, so the unitary part of the symmetry action is $\mathbb{1}_{2\times 2}$. Let $\delta = (a_0, 0)$ be a vector connecting nearest neighbors, and the corresponding hopping term

$$H = t \begin{bmatrix} 0 & e^{i\mathbf{k}\cdot\delta} \\ e^{-i\mathbf{k}\cdot\delta} & 0 \end{bmatrix} = t \begin{bmatrix} 0 & e^{ia_0 k_x} \\ e^{-ia_0 k_x} & 0 \end{bmatrix}, \tag{2.19}$$

which is Hermitian and only connects the two sublattices. After symmetrization with respect to the full hexagonal group we obtain the well known minimal tight-binding model for graphene:

$$H_s = \frac{t}{3} \begin{bmatrix} 0 & h \\ h^\dagger & 0 \end{bmatrix} \tag{2.20}$$

with $h = e^{ia_0 k_x} + e^{ia_0\left(-\frac{1}{2}k_x + \frac{\sqrt{3}}{2}k_y\right)} + e^{ia_0\left(-\frac{1}{2}k_x - \frac{\sqrt{3}}{2}k_y\right)}$.

2.4. SYMMETRY FINDING

Unlike finding a family of symmetric Hamiltonians, that amounts to solving a linear system, finding the symmetries of a Hamiltonian family is more involved. We first focus on finite (zero-dimensional) systems and show that the unitary symmetry group generally admits a continuous Lie group structure. Next we present an algorithm to find the unitary

symmetries, and rewrite the Hamiltonian family in the symmetry-adapted basis. In this basis the Hamiltonian takes a block diagonal form, where the blocks are guaranteed to have no unitary symmetries, hence we call these blocks reduced Hamiltonians. Factoring out the unitary symmetries this way simplifies finding the discrete (anti)unitary (anti)symmetries, see Fig. 2.2. After generalizing these methods to onsite symmetries of translation invariant systems in arbitrary dimensions, we finally include real space rotation symmetries.

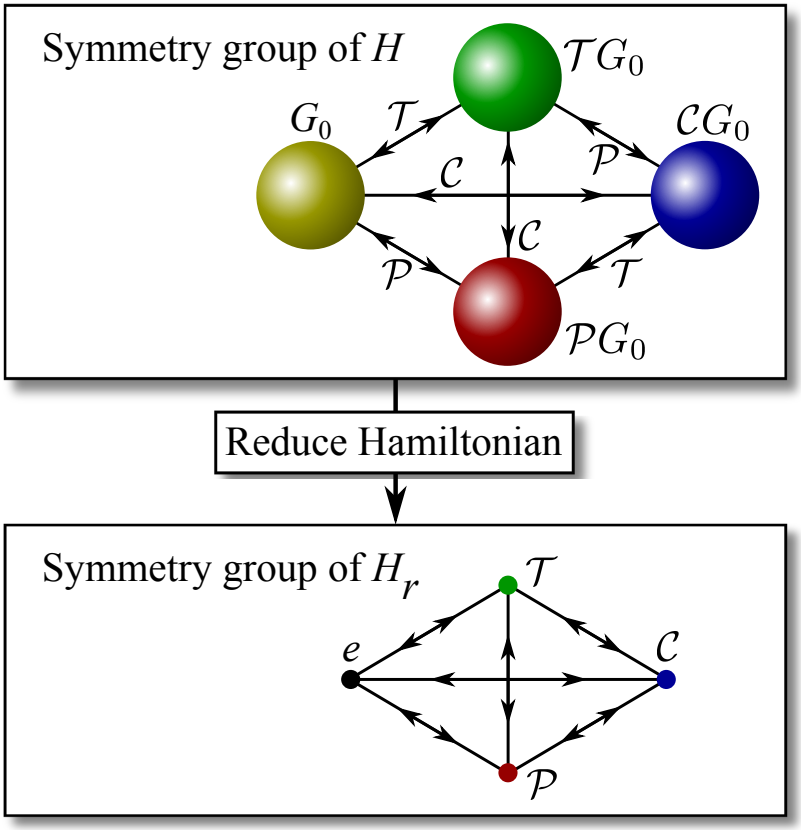

Figure 2.2: Schematic representation of the onsite symmetry group of a Hamiltonian family (top). The unitary symmetries form a continuous connected Lie group G_0. The discrete symmetries can all be combined with any unitary symmetry, forming disconnected components of the symmetry group. For example, $\mathcal{T}G_0 = \{\mathcal{T}U : U \in G_0\}$ contains all antiunitary symmetries which are combinations of the canonical time reversal $\mathcal{T}$ and some unitary U. Reducing the Hamiltonian family factors out all the unitary symmetries leaving only the identity element e, resulting in a simpler discrete group structure (bottom).

2.4.1. STRUCTURE OF THE ONSITE UNITARY SYMMETRY GROUP

Assume a unitary symmetry operator U commutes with a family of finite Hamiltonians:

$$[U, H_n] = 0. \tag{2.21}$$

Any unitary is expressible as the exponential of a Hermitian operator L

$$U = e^{-iL}, \tag{2.22}$$

which is unique if we restrict the spectrum $\sigma(L) \subset [0, 2\pi)$ (this condition is equivalent to choosing a branch cut for the logarithm in $L = i \log U$). Defining U and L this way ensures that they have exactly the same eigensubspaces. Since U and H_n commute, they also share eigensubspaces, and Eq. (2.21) is equivalent to

$$[L, H_n] = 0. \tag{2.23}$$

Therefore the Hamiltonian family has a continuous family of unitary symmetries $U(\phi) = e^{-i\phi L}$ that all commute with H_n. Because a single unitary symmetry defines a continuous family that is connected to the identity, the full group of unitary symmetries must form a single connected component G_0. This is uniquely specified by the space of conserved quantities $L \in \mathfrak{g}$, the Lie algebra of the Lie group G_0.

Consider for example a system consisting of a number of spinful orbitals, which is invariant under the set of unitary spin-flip operators $U_i = i\sigma_i \otimes \mathbb{1}$, where σ_i are the Pauli matrices and the identity acts on the space of orbitals. Taking the logarithms of these operators, we find that they are associated with the Hermitian conserved spins $L_i = \sigma_i \otimes \mathbb{1}$. The Lie group generated by these conserved quantities is $SU(2)$ acting in spin space. Therefore the generic Hamiltonian of such a system assumes the form $H = \mathbb{1}_{2\times 2} \otimes H_r$, where the reduced Hamiltonian H_r acts only on the space of orbitals and the identity acts on spin space. In the basis where spin up and spin down states are grouped together, the original Hamiltonian takes the block diagonal form with two identical blocks $H = H_r \oplus H_r$, reducing the problem to spinless fermions.

Consider the same system, but with higher spins on every site instead. Let the conserved spins be $L_i = J_i \otimes \mathbb{1}$ where J_i for $i \in [x, y, z]$ form a $2s+1$ dimensional spin representation. The generic Hamiltonian again has the form $H = \mathbb{1}_{(2s+1)\times(2s+1)} \otimes H_r$, because the J_i form an irreducible representation of the rotation group. This Hamiltonian, however, is invariant under any unitary transformation of the form $U \otimes \mathbb{1}$ with $U \in U(2s+1)$. We therefore find that the symmetry group is in fact larger than the one we started with, forming a full unitary group.

The above result may sound surprising on physical grounds, considering that many well-studied models (*e.g.* the transverse field Ising model) only have discrete onsite symmetry groups. We emphasize that this result (and much of what follows) is specific to single-particle systems, and does not directly apply to onsite symmetries on the many-particle Fock space. In the single-particle case the full Hilbert space is the direct sum of the local Hilbert spaces and therefore an onsite symmetry is the direct sum of local unitaries. The many-particle Hilbert space is a direct product, and onsite unitary symmetries take a direct product form. The associated L is generally not a sum of local terms, and does not correspond to a local conserved quantity. The above argument also fails when considering

spatial symmetries, because in general the logarithm of a locality-preserving operator (an operator that maps a state with localized support to one with localized support) mixes degrees of freedom that are far apart.

In the rest of this subsection we prove, using the theory of Lie groups, that the unitary symmetry group G_0 is a direct product of unitary groups $U(N)$ in any finite system. We then show the existence of the symmetry-adapted basis, where both the conserved quantities and the Hamiltonian take a simple form, and derive properties of reduced Hamiltonians. The reader not interested in mathematical proofs may skip to the next subsection where the algorithm for finding unitary symmetries is discussed.

The unitary symmetry group G_0 is a subgroup of the full unitary group on the Hilbert space $\mathscr{H}$, $G_0 \leq U(\dim \mathscr{H})$. G_0 is a connected and compact matrix Lie group, which means that all of its finite-dimensional representations are completely reducible [39, 40]. The Lie group G_0 is generated by all the generators in its Lie algebra $L \in \mathfrak{g}$ for which $[L, H] = 0$, the Lie algebra $\mathfrak{g}$ is also completely reducible.

Reducing the representation amounts to splitting the Hilbert space $\mathscr{H}$ into a direct sum of irreducible subspaces $\mathcal{V}_j^{(i)}$:

$$\mathscr{H} = \left(\mathcal{V}_1^{(1)} \oplus \ldots \oplus \mathcal{V}_{n_1}^{(1)}\right) \oplus \left(\mathcal{V}_1^{(2)} \oplus \ldots \oplus \mathcal{V}_{n_2}^{(2)}\right) \oplus \ldots. \tag{2.24}$$

Each of these subspaces is invariant under the symmetry action and contains no invariant subspace. $\mathcal{V}_j^{(i)}$ transforms according to irreducible representation (irrep) i, and irrep i has multiplicity n_i. We denote the union of all irreducible subspaces belonging to irrep i as $\mathcal{V}^{(i)} = \mathcal{V}_1^{(i)} \oplus \ldots \oplus \mathcal{V}_{n_i}^{(i)}$.

In a *symmetry-adapted basis*, every symmetry generator takes the same block diagonal form of irreducible representations:

$$\begin{aligned} L &= \underbrace{L^{(1)} \oplus L^{(1)} \oplus \ldots}_{n_1 \text{times}} \oplus \underbrace{L^{(2)} \oplus L^{(2)} \oplus \ldots}_{n_2 \text{times}} \oplus \ldots = \\ &= \left(L^{(1)} \otimes \mathbb{1}_{n_1 \times n_1}\right) \oplus \left(L^{(2)} \otimes \mathbb{1}_{n_2 \times n_2}\right) \oplus \ldots, \end{aligned} \tag{2.25}$$

where $L^{(i)}$ is the representation of L in the i-th irrep, each acting in a corresponding irreducible subspace $\mathcal{V}_j^{(i)}$ of dimension d_i. Irreps j and k are equivalent if there exists a unitary transformation W such that $L^{(j)} = W L^{(k)} W^{-1}\ \forall L \in \mathfrak{g}$. This guarantees that there is a basis where all operators have exactly the same representation in every equivalent irreducible subspace.

In this basis, the Hamiltonian also takes a simple block form. By Schur's Lemma, blocks of H between irreducible subspaces that transform according to different irreps are zero, and blocks between irreducible subspaces with identical irreps are proportional to the identity:

$$H = \left(\mathbb{1}_{d_1 \times d_1} \otimes H_1\right) \oplus \left(\mathbb{1}_{d_2 \times d_2} \otimes H_2\right) \oplus \ldots, \tag{2.26}$$

where the *reduced Hamiltonians* H_i are $n_i \times n_i$ Hermitian matrices. The reduced Hamiltonians H_i cannot have any nontrivial unitary symmetries. To prove that, assume that H_1 has a conserved quantity L such that $[H_1, L] = 0$. It implies that $\left(\mathbb{1}_{d_1 \times d_1} \otimes L\right) \oplus 0 \oplus \ldots$ commutes with the full Hamiltonian, which is incompatible with the unique decomposition to irreducible subspaces, except the trivial case of $L \propto \mathbb{1}$.

It is apparent from (2.26) that the symmetry group of H is a product of full unitary groups acting independently on each block

$$G_0 = U(d_1) \times U(d_2) \times \ldots, \tag{2.27}$$

where the symmetry generators have the form (2.25), with $L^{(i)} \in \mathfrak{u}(d_i)$ independently running over all $d_i \times d_i$ Hermitian matrices, and $\mathfrak{u}(d_i)$ the Lie algebra of $U(d_i)$. Because the reduction to irreducible subspaces is unique, this is the full group of unitary symmetries. The center of the group $Z(G_0)$ is formed by the abelian $U(1)$ subgroups generated by the set of projectors on each block, *i.e.* generators where one of the $L^{(i)}$ is the identity and the others vanish.

To have a basis-independent characterization of the center of the Lie algebra, we compute the structure constants $f_{\alpha\beta}{}^{\gamma}$ defined by

$$[L_\alpha, L_\beta] = i \sum_\gamma f_{\alpha\beta}{}^{\gamma} L_\gamma. \tag{2.28}$$

Using these we define the Killing form

$$K_{\alpha\beta} = \sum_{\gamma\delta} f_{\alpha\gamma}{}^{\delta} f_{\beta\delta}{}^{\gamma}. \tag{2.29}$$

It can be shown [40] that the null-space of the Killing form is exactly the center of the Lie algebra, *i.e.* if a vector l is a solution of $\sum_\beta K_{\alpha\beta} l^\beta = 0$ then $\sum_\alpha l^\alpha L_\alpha$ commutes with every operator in $\mathfrak{g}$.

2.4.2. FINDING THE UNITARY SYMMETRY GROUP

We are now ready to define the algorithm of finding the unitary symmetry group and constructing the reduced Hamiltonians for a given family of Hamiltonians. First we find all symmetry generators L_α as the linearly independent solutions of

$$[L_\alpha, H] = 0 \text{ and } L_\alpha = L_\alpha^\dagger. \tag{2.30}$$

This is a system of linear equations for the unknown components of L_α, which we solve using the same methods we used for constraining Hamiltonians. After computing the Killing form K we find all linearly independent solutions of

$$\sum_\beta K_{\alpha\beta} l^\beta = 0 \tag{2.31}$$

for l. Operators of the form $\sum_\alpha l^\alpha L_\alpha$ are the basis of conserved quantities that commute with every other conserved quantity. We simultaneously diagonalize all of these (see Appendix 2.7.1) to find the simultaneous eigensubspaces $\mathcal{V}^{(i)}$ (2.24).

We then find the generators $L^{(i)}$ of the $SU(d_i)$ symmetry group of each block. To do so, we project the Hamiltonian onto $\mathcal{V}^{(i)}$ using the projector P_i, which is an orthonormal set of column vectors, and solve

$$[L^{(i)}, P_i^\dagger H P_i] = 0 \text{ and } L^{(i)} = L^{(i)\dagger} \text{ and } \operatorname{Tr} L^{(i)} = 0, \tag{2.32}$$

to find the $d_i^2 - 1$ linearly independent solutions for $L^{(i)}$. The final step is finding a basis within $\mathcal{V}^{(i)}$ that gives the tensor product structure of (2.25) and (2.26) (see Appendix 2.7.2). We use this basis and the resulting reduced Hamiltonians in the following.

2.4.3. DISCRETE ONSITE SYMMETRIES AND ANTISYMMETRIES

Next we discuss the *discrete onsite symmetries*:

- time reversal (antiunitary symmetries),
- particle-hole (antiunititary antisymmetries),
- chiral (unitary antisymmetries).

These symmetries also form continuous families, because combining them with any onsite unitary symmetry also results in a discrete onsite symmetry of the same type. Because there is no continuous way to interpolate between unitary and antiunitary symmetries or between symmetries and antisymmetries, each type forms a disconnected component of the onsite symmetry group (see Fig. 2.2). To find one representative of each type of the discrete onsite symmetries, we utilize the symmetry-adapted basis and reduced the Hamiltonian found in the previous subsection. The reduced Hamiltonians have no residual symmetries, which makes the discrete onsite symmetries unique and allows us to efficiently find them.

We start with time reversal symmetries of finite (zero-dimensional) systems. $\mathcal{T}$ is a time reversal if

$$\mathcal{T} H = H\mathcal{T}. \tag{2.33}$$

Writing $\mathcal{T} = U\mathcal{K}$ with unitary U and complex conjugation $\mathcal{K}$, we obtain

$$UH^* = HU, \tag{2.34a}$$
$$UU^\dagger = \mathbb{1}. \tag{2.34b}$$

This is a nonlinear system of equations, and it is in general hard to solve. We show that using the reduced Hamiltonian simplifies it to a linear problem.

We first consider a Hamiltonian that has one set of identical irreducible subspaces, *i.e.* $H = \mathbb{1} \otimes H_1$. By (2.25), all conserved quantities have the form $L = L^{(1)} \otimes \mathbb{1}$, and span the full space of Hermitian matrices on the first Hilbert space of the tensor product. If L is a conserved quantity, so is $\mathcal{T} L \mathcal{T}^{-1}$, which implies $U\mathfrak{g}U^\dagger = \mathfrak{g}$. Therefore the unitary part of $\mathcal{T}$ is a direct product of two unitaries, $U = V \otimes W$ [41], with V an arbitrary unitary matrix. Because $V = \mathbb{1}$ commutes with all unitary symmetries, we call $\mathcal{T} = \mathbb{1} \otimes W\mathcal{K}$ the canonical time reversal symmetry. Due to the tensor product structure of $\mathcal{T}$, (2.34a) reduces to

$$W H_1^* = H_1 W. \tag{2.35}$$

Importantly H_1 has no unitary symmetries. Any nonzero solution W of (2.35) has $\ker W = 0$: otherwise either $\ker W$ is an invariant subspace of H_1^* or $\ker H_1^*$ is nonzero, both incompatible with H_1 having no unitary symmetries. Considering two solutions W and $\tilde{W}$ of (2.35) we find

$$W\tilde{W}^\dagger H_1 = W H_1^* \tilde{W}^\dagger = H_1 W\tilde{W}^\dagger. \tag{2.36}$$

Because H_1 has no unitary symmetries $W\tilde{W}^\dagger \propto \mathbb{1}$, which proves that any solution of (2.35) is unique and unitary up to a constant factor. In other words, any normalized solution of (2.35) automatically satisfies (2.34b).

As an example consider the reduced family of Hamiltonians

$$H = c_1\sigma_x + c_3\sigma_z. \tag{2.37}$$

This family has no residual symmetry, and solving (2.35) we find that W has to commute with both σ_x and σ_z, so $W \propto \sigma_0$. Therefore H is invariant under $\mathcal{T} = \sigma_0\mathcal{K}$, which is unique up to a phase factor. As a second example consider the reduced family

$$\begin{aligned} H = {} & c_{10}\tau_x\sigma_0 + c_{30}\tau_z\sigma_0 + c_{21}\tau_y\sigma_x + \\ & c_{22}\tau_y\sigma_y + c_{23}\tau_y\sigma_z, \end{aligned} \tag{2.38}$$

with τ_i the Pauli matrices. The condition (2.35) implies that W commutes with $\tau_x\sigma_0$, $\tau_z\sigma_0$, $\tau_y\sigma_y$ and anticommutes with $\tau_y\sigma_x$, $\tau_y\sigma_z$. The only solution is $W \propto \tau_0\sigma_y$, and $\mathcal{T} = \tau_0\sigma_y\mathcal{K}$ up to a phase factor.

In the general case of multiple irreps, we find (see Appendix 2.7.3 for details) that a time reversal can only mix subspaces $\mathcal{V}^{(i)}$ and $\mathcal{V}^{(j)}$ if they correspond to irreps of the same dimensionality and multiplicity. The block structure of U has to be symmetric, it can only exchange subspaces pairwise or leave subspaces invariant. In order to find a time reversal, we iterate over all symmetric permutations of compatible subspaces, and check if a time reversal exists with the given block structure. Specifically we consider two reduced blocks of the Hamiltonian that are interchanged

$$H_r = \begin{bmatrix} H_i & 0 \\ 0 & H_j \end{bmatrix}. \tag{2.39}$$

Because H_i and H_j have no unitary symmetry, the square of time reversal must have the form

$$\mathcal{T}_r^2 = \begin{bmatrix} e^{i\phi}\mathbb{1} & 0 \\ 0 & e^{i\phi'}\mathbb{1} \end{bmatrix}. \tag{2.40}$$

Therefore, following Appendix 2.7.3 we search for a time reversal of the form

$$\mathcal{T}_r = \begin{bmatrix} 0 & W_{ij} \\ e^{i\phi}W_{ij}^T & 0 \end{bmatrix}\mathcal{K}. \tag{2.41}$$

The relation $\mathcal{T}_r H_r = H_r\mathcal{T}_r$ then reduces to

$$W_{ij}H_j^* = H_i W_{ij}. \tag{2.42}$$

This is the key result of this section, and it is a generalization of (2.35). Following the same reasoning as before, we conclude that any nonzero solution W_{ij} of (2.42) is unique and unitary up to a constant factor.

As an example of this case consider the Hamiltonian family

$$H = \begin{bmatrix} c_{10}\tau_x + c_{30}\tau_z + c_{23}\tau_y & 0 \\ 0 & c_{10}\tau_x + c_{30}\tau_z - c_{23}\tau_y \end{bmatrix}. \tag{2.43}$$

Solving (2.42) for W_{12} we find that $[W_{12}, \tau_i] = 0$ for $i = x, y, z$, so $W_{12} \propto \tau_0$ and $\mathcal{T} = \tau_0\sigma_x\mathcal{K}$ up to a phase factor. We also confirm that (2.42) does not have any solutions for W_{11} or W_{22}, so the block form of $\mathcal{T}$ is unique.

Likewise, the canonical unitary and antiunitary antisymmetries act as a tensor product $U_{ij} = \mathbb{1} \otimes W_{ij}$ in each block, and either leave subspaces invariant or pairwise exchange compatible subspaces. The results analogous to Eq. (2.42) for unitary and antiunitary antisymmetries are respectively:

$$W_{ij} H_j = -H_i W_{ij}, \tag{2.44a}$$
$$W_{ij} H_j^* = -H_i W_{ij}. \tag{2.44b}$$

2.4.4. ONSITE SYMMETRIES OF **k**-DEPENDENT HAMILTONIANS

The above methods extend to the onsite symmetries of **k**-space Hamiltonians of arbitrary dimensions. An onsite unitary symmetry acts locally in **k**-space and is independent of **k**. Given a family of Hamiltonians $H(\mathbf{k}, \alpha)$, we treat linearly independent functions of **k** as additional free parameters and apply the methods of section 2.4.2.

We now turn to time reversal symmetry, which requires special treatment because it transforms **k** to $-\mathbf{k}$. Because $H(-\mathbf{k})$ is a reparametrization of the same Hamiltonian family, it is reduced if $H(\mathbf{k})$ is reduced. The generalization of (2.42) to the **k**-dependent case is

$$W_{ij} H_j^*(-\mathbf{k}) = H_i(\mathbf{k}) W_{ij}. \tag{2.45}$$

By the same argument as before, separating the Hamiltonian to irreducible blocks guarantees that the nonzero solutions are unique and unitary up to constant factors. The analogous results are true for particle-hole and chiral symmetry.

2.4.5. POINT GROUP SYMMETRIES

The point group of a crystal is always a subgroup of the finite point group of its Bravais lattice. Therefore we search for point group symmetries by enumerating possible real space rotations R_g, and applying methods similar to the previous subsections to find whether it is a symmetry with appropriate U_g.

Like discrete onsite symmetries, point group symmetries may be combined with onsite unitaries, forming continuous families. This ambiguity is again removed by using the reduced Hamiltonian. The analogous result to (2.42) for point group symmetries is $(U_g)_{ij} = \mathbb{1} \otimes W_{ij}$ where the blocks W_{ij} satisfy

$$W_{ij} H_j(\mathbf{k}) = H_i(R_g \mathbf{k}) W_{ij}. \tag{2.46}$$

Here W only has one nonzero block per row and column, and nonzero blocks only between compatible subspaces. If the order of the symmetry is greater than 2, permutations which are not symmetric are also possible. Because both $H_j(\mathbf{k})$ and $H_i(R_g \mathbf{k})$ are reduced, the nonzero solution for W_{ij} is unique and unitary up to normalization and a phase factor. With the knowledge of the full point group, the arbitrary phase factors appearing in W_{ij} may be fixed such that the U_g form a (double)group representation of the point group.

A similar argument applies to the case of antiunitary point group symmetries (magnetic group symmetries) and antisymmetries that involve spatial transformations. The analogous equations for unitary antisymmetries antiunitary (anti)symmetries are respec-

tively:

$$W_{ij}H_j(\mathbf{k}) = -H_i(R_g\mathbf{k})W_{ij}, \tag{2.47a}$$
$$W_{ij}H_j^*(-\mathbf{k}) = \pm H_i(R_g\mathbf{k})W_{ij}. \tag{2.47b}$$

2

2.4.6. CONTINUOUS ROTATIONS

To find continuous rotation symmetries of $\mathbf{k}\cdot\mathbf{p}$ Hamiltonians we utilize the symmetry-adapted basis of the onsite unitary symmetries again. Unlike discrete symmetries, the unitary action of a continuous symmetry cannot mix different blocks, because it continuously deforms to the identity. Therefore we treat reduced Hamiltonians H_i separately.

In order to find a continuous symmetry generator g' as defined in sec. 2.2.3, we simultaneously solve

$$g'(H_j)(\mathbf{k}) = i[H_j(\mathbf{k}), L^{(j)}] + i\sum_{lp}\frac{\partial H_j}{\partial k_l}M_{lp}k_p = 0 \tag{2.48}$$

for every j, with constraints $L^{(j)} = (L^{(j)})^\dagger$, $\mathrm{Tr}\,L^{(j)} = 0$ and $M = -M^T = M^\dagger$. We then expand $H_j(\mathbf{k})$ in a basis of monomials, and reduce (2.48) to a system of linear equations for the entries of $L^{(j)}$ and M.

2.5. APPLICATIONS

We implemented the symmetric Hamiltonian generator and symmetry finder algorithms of the previous sections in the Qsymm Python package [31, 32]. We provide an interface to define symbolic expressions of symmetries and Hamiltonian families using Sympy [42] and Kwant [43]. Efficient solving of large systems of linear equations is achieved using ARPACK [44] (bundled for Python by Scipy [45]). We provide the the source code with instructive examples as a software repository [31, 32]. The following examples illustrate how the algorithms were used to solve open research problems in condensed matter physics. We also provide the Jupyter notebooks [46] generating these results.

2.5.1. SYMMETRIES OF MAJORANA WIRE

An early version of our symmetry finding algorithm was used in Ref. [47] to find the symmetries of a superconducting nanowire in an external magnetic field. The analysis revealed unexpected symmetries of the model system in certain geometries that prevent band tilting and closing of the topological gap. Here we revisit these results.

The system under consideration is an infinite nanowire along the x axis with a semiconducting core and a superconducting shell covering some of the surface. In the presence of a magnetic field along the wire and a normal electric field, the wire undergoes a topological phase transition. This is marked by the gap closing and reopening, with Majorana zero modes appearing at each end of a finite wire segment [48]. A component of the external magnetic field normal to the wire axis breaks the symmetry of the band structure ($E(\mathbf{k}) \neq E(-\mathbf{k})$), leading to tilting of the bands and closing of the superconducting gap at finite momentum.

Reference [47] studied a tight-binding Hamiltonian of the wire and observed that depending on the geometry the band tilting may or may not occur. Applying the symmetry

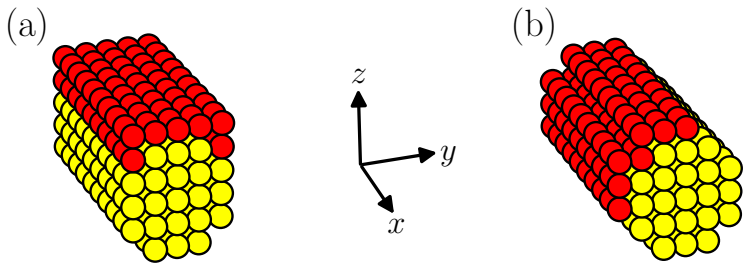

Figure 2.3: Sketch of two possible geometries for the nanowire (yellow) with a superconducting shell (red). In (a), the geometry respects the mirror symmetry M_y, which gives rise to a chiral symmetry. In (b) however, the superconducting shell breaks the mirror symmetry, and hence the chiral symmetry is also absent. Although the sketches show finite segments, the wire is translationally invariant along its axis x in both cases.

finder algorithm to wires with small cross-sections (Fig. 2.3), we identify the key difference in symmetry. If the wire geometry has a mirror plane including its axis (M_y) as in Fig. 2.3(a), with external fields $\mathbf{E} \parallel z$, and $\mathbf{B} \parallel x$, we find that the symmetry group consists of 8 elements. The three generators of this group are particle-hole symmetry ($\mathscr{P}$), a mirror plane perpendicular to the wire axis (M_x) and the combination of M_y with time reversal $\mathscr{T}$. This last symmetry $M_y\mathscr{T}$ includes both a spatial transformation and time reversal, and is easily overlooked. This operator can be further combined with particle-hole to result in a chiral symmetry $\mathscr{C}' = M_y\mathscr{T}\mathscr{P}$, as pointed out in the earlier work. A nanowire enhanced by such an effective time reversal symmetry belongs to class BDI and supports multiple Majorana modes at its end [49].

Symmetries M_x and $M_y\mathscr{T}$ require $E(k_x) = E(-k_x)$ and prevent band tilting. Adding nonzero B_z to the magnetic field breaks M_x, but preserves $M_y\mathscr{T}$, still forbidding band tilting. Further reducing the symmetry by moving the position of the superconducting cover as in Fig. 2.3(b), or by applying B_y breaks all symmetries relating k_x to $-k_x$ and enables band tilting.

2.5.2. KEKULE DISTORTION IN GRAPHENE

The Kekule distortion of graphene is a periodic pattern of weak and strong bonds tripling the size of the unit cell. In the Kekule-O pattern, weak bonds around plaquettes resemble benzene rings, and in Kekule-Y, strong bonds form Y shapes around sites (Fig. 2.4). After folding back the Brillouin zone, the K and K' points are both mapped to the Γ point. A suitable mass term can now open a gap in the band structure. A recent work [50] reported that unlike the Kekule-O distortion [51], the Kekule-Y distortion does not open a gap: instead it preserves a double Dirac cone at the Brillouin zone center. Using our algorithms we identify the symmetries protecting this double Dirac cone. First we find all

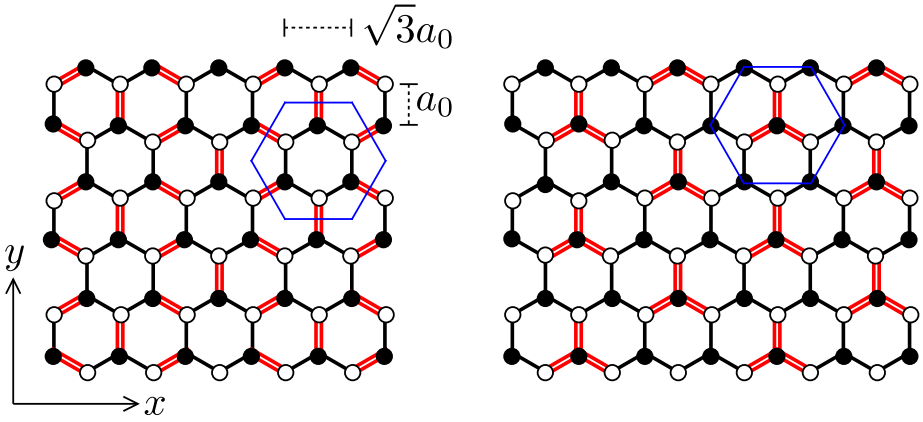

Figure 2.4: Lattice structures of Kekule-O (left) and Kekule-Y patterns (right). Weak and strong bonds are marked with single and double lines. The high symmetry unit cell is marked in blue.

the symmetries of the effective 4-band $\mathbf{k}\cdot\mathbf{p}$ model of Kekule-Y:

$$H_Y = v_1(k_x\sigma_x + k_y\sigma_y) + v_2(k_x\tau_x + k_y\tau_y), \tag{2.49}$$

with v_1, v_2 band structure parameters. We find that it is symmetric under the full hexagonal point group D_6 (in fact the linearized model has a continuous rotation symmetry), time reversal and sublattice symmetry, which results from the bipartite nature of the honeycomb lattice. Next, we systematically generate all subgroups of this symmetry group and the corresponding symmetry-allowed 4-band $\mathbf{k}\cdot\mathbf{p}$ Hamiltonians. We find that at least one antisymmetry is required to forbid a constant mass term that would open a gap at Γ. A minimal subgroup protecting the double Dirac cone is generated by sublattice symmetry and three-fold rotations. Removing sublattice symmetry, even while keeping the full D_6 point group, removes the protection of the double Dirac cone. Sublattice symmetry is broken by adding second neighbour hopping, or a staggered onsite potential compatible with the lattice symmetries in the tight-binding model.

Symmetry finding shows that the effective model of Kekule-O,

$$H_O = v(k_x\sigma_x + k_y\sigma_y) + \Delta\sigma_z\tau_x \tag{2.50}$$

with $v, \Delta \in \mathbb{R}$, has the same symmetry group structure. However, the mass term $\sigma_z\tau_x$ is allowed even in the presence of the full symmetry group. The key difference is the unitary action of rotations: the generator of continuous rotations is $\sigma_z + \tau_z$ in the Kekule-Y case, while it is σ_z in the Kekule-O case. Sublattice symmetry is $\mathscr{C} = \sigma_z\tau_z$ in both cases. Therefore no constant matrix can simultaneously anticommute with $\mathscr{C}$ and commute with the rotation generator in Kekule-Y, while a mass term is allowed in Kekule-O.

This difference in the transformation properties stems from the different Wyckoff positions of the lattice sites. In Kekule-Y the three-fold rotation centers lie on lattice sites, while in Kekule-O the three-fold rotation centers lie at centers of hexagonal plaquettes.

Using the tight-binding Hamiltonian generator, we confirm that the representation of 3-fold rotations in the low energy subspace at the center of the Brillouin zone is different for the Kekule-O and Kekule-Y systems.

2.5.3. $\mathbf{k}\cdot\mathbf{p}$ MODEL OF DISTORTED SnTe

The cubic rocksalt material SnTe is the first example of topological crystalline insulators [52]. Recently, using our method, Ref. [53] proposed that structural distortions can give rise to Weyl and nodal-line semimetal phases in the same material. Here we review these results.

The band gap of the cubic phase is smallest at the L point in the face-centered cubic Brillouin zone. We construct an effective $\mathbf{k}\cdot\mathbf{p}$ model expanded up to second order in $\mathbf{k}$ around L. The model has two orbital degrees of freedom, spanned by p orbitals on Sn and Te sites. The initial symmetry group of the L point is D_{3d} which is generated by inversion I, a three-fold rotation C_3 about the ΓL axis, and a reflection M_x about the mirror plane containing Γ and two L points. Furthermore, the model should be invariant under time reversal $\mathcal{T}$. The corresponding representations of the symmetry operators, listing the (anti)unitary action first and the $\mathbf{k}$-space action second, are as follows,

$$M_x = -is_x, \qquad k_x \to -k_x, \tag{2.51a}$$

$$C_3 = e^{i\frac{\phi}{2}s_z}, \qquad \mathbf{k} \to \begin{bmatrix} \cos\phi & -\sin\phi & 0 \\ \sin\phi & \cos\phi & 0 \\ 0 & 0 & 1 \end{bmatrix} \mathbf{k}, \tag{2.51b}$$

$$I = \sigma_z, \qquad \mathbf{k} \to -\mathbf{k}, \tag{2.51c}$$

$$\mathcal{T} = is_y\mathcal{K}, \qquad \mathbf{k} \to -\mathbf{k}, \tag{2.51d}$$

where $\phi = \frac{2\pi}{3}$, and Pauli matrices σ_i and s_i act on orbital and spin degrees of freedom respectively. $\mathbf{k}$ is the momentum vector measured from an L point in a coordinate system where the z axis is aligned with ΓL (*e.g.* [111]) and the x axis is normal to a mirror plane (*e.g.* $[1\bar{1}0]$). The σ_z in the unitary action of inversion is a result of considering an L point, because the inversion center is one of the sites in the unit cell of the rocksalt structure, the other site is translated by a lattice vector under inversion and acquires a phase factor at nonzero momentum.

Applying the $\mathbf{k}\cdot\mathbf{p}$ Hamiltonian generator algorithm we find 8 symmetry-allowed terms. Ignoring the 3 terms that are proportional to the identity and do not influence band topology, we obtain the following Hamiltonian family:

$$\begin{aligned} H_0(\mathbf{k}) = &m\sigma_z + v(k_x s_y - k_y s_x)\sigma_x + v_3 k_z \sigma_y \\ &+ ck_z^2\sigma_z + f(k_x^2 + k_y^2)\sigma_z. \end{aligned} \tag{2.52}$$

Breaking the three-fold rotational symmetry results in 8 new terms, 6 of which are not proportional to the identity:

$$\begin{aligned} H_1(\mathbf{k}) = &\delta v(k_x s_y + k_y s_x)\sigma_x + \lambda_1 k_x s_z \sigma_x + \lambda_2 k_y \sigma_y \\ &+ \lambda_3 k_z s_x \sigma_x + \delta f(k_x^2 - k_y^2)\sigma_z + g k_y k_z \sigma_z. \end{aligned} \tag{2.53}$$

Further breaking inversion symmetry produces 22 additional terms, none of which is proportional to the identity.

2.5.4. THREE-ORBITAL TIGHT-BINDING MODEL FOR MONOLAYER TRANSITION METAL DICHALCOGENIDES

Monolayers of transition metal dichalcogenides MX_2 (M = Mo, W; X = S, Se, Te) are promising materials for use in electronics and optoelectronics [54]. When doped, the MX_x monolayers also become superconducting [55]. In the $1H$ stacking, a monolayer consists of a layer of transition metal atoms M sandwiched between two layers of chalcogen atoms X. Each layer separately is a triangular Bravais lattice, with the X atoms in the top and bottom layers projecting onto the same position in the plane of M atoms, forming an overall honeycomb lattice. In the normal state, the monolayer is a semiconductor, with conduction and valence band edges at the corners of the hexagonal Brillouin zone $\pm K$. Using that the wave functions at the band edges are predominantly composed of d-orbitals on the M atoms, Liu *et al.* [4] developed a three-orbital tight-binding model with nearest neighbor hopping. This model satisfies the symmetry group of the monolayer, and has band edges near $\pm K$. Here, we reproduce their spinless tight-binding model using our algorithm for symmetric Hamiltonian generation.

The tight-binding basis consists of three d-orbitals on the M atom, namely

$$\psi = [|d_{z^2}\rangle, |d_{xy}\rangle, |d_{x^2-y^2}\rangle]^T. \tag{2.54}$$

Because the model does not include any orbitals on the X atoms, it has a triangular lattice, with lattice vectors $\mathbf{a}_1 = \hat{x}$ and $\mathbf{a}_2 = (\hat{x} + \sqrt{3}\hat{y})/2$. The symmetry generators are time reversal symmetry $\mathscr{T}$, mirror symmetry M_x, and three-fold rotation in the monolayer plane C_3 which are represented in the tight-binding basis as

$$M_x = \mathrm{diag}(1,-1,1), \qquad k_x \to -k_x, \tag{2.55a}$$

$$C_3 = \begin{bmatrix} 1 & 0 & 0 \\ 0 & \cos\phi & -\sin\phi \\ 0 & \sin\phi & \cos\phi \end{bmatrix}, \qquad \mathbf{k} \to \begin{bmatrix} \cos\phi & -\sin\phi \\ \sin\phi & \cos\phi \end{bmatrix} \mathbf{k}, \tag{2.55b}$$

$$\mathscr{T} = \mathscr{K}, \qquad \mathbf{k} \to -\mathbf{k}, \tag{2.55c}$$

with $\phi = \frac{2\pi}{3}$. Employing the symmetrization strategy for lattice Hamiltonians described in Section 2.3.2, we reproduce the tight-binding model of Ref. [4], given by

$$H(\mathbf{k}) = \begin{bmatrix} h_{00}(\mathbf{k}) & h_{01}(\mathbf{k}) & h_{02}(\mathbf{k}) \\ h_{01}^*(\mathbf{k}) & h_{11}(\mathbf{k}) & h_{12}(\mathbf{k}) \\ h_{02}^*(\mathbf{k}) & h_{12}^*(\mathbf{k}) & h_{22}(\mathbf{k}) \end{bmatrix}, \tag{2.56}$$

with the matrix elements

$$\begin{aligned}
h_{00} &= 2t_0(2\cos\xi\cos\gamma + \cos 2\xi) + \epsilon_1 \\
h_{01} &= 2it_1(\sin 2\xi + \sin\xi\cos\gamma) - 2\sqrt{3}t_2\sin\xi\sin\gamma, \\
h_{02} &= 2i\sqrt{3}t_1\cos\xi\sin\gamma + 2t_2(\cos 2\xi - \cos\xi\cos\gamma), \\
h_{11} &= t_3(\cos\xi\cos\gamma + 2\cos 2\xi) + 3t_4\cos\xi\cos\gamma + \epsilon_2, \\
h_{12} &= \sqrt{3}(t_4 - t_3)\sin\xi\sin\gamma + 4it_5\sin\xi(\cos\xi - \cos\gamma), \\
h_{22} &= 3t_3\cos\xi\cos\gamma + t_4(\cos\xi\cos\gamma + 2\cos 2\xi) + \epsilon_2,
\end{aligned} \tag{2.57}$$

where $\xi = k_x/2$ and $\gamma = \sqrt{3}k_y/2$ and the lattice constant is set to one.

2.5.5. LATTICE HAMILTONIAN OF MONOLAYER WTE_2

Monolayer $WT2_2$ was recently discovered to be a two-dimensional quantum spin Hall insulator [56–59] in accordance with previous numerical prediction [60, 61]. Transport experiments found quantized edge conductivity persisting up to 100K [58]. This suggests a much larger band gap compared to devices based on two-dimensional quantum wells [62]. It remains an open question whether a simple non-interacting lattice Hamiltonian can reproduce these findings.

We use the restricted set of orbitals in Ref. [63] to construct the spinless tight-binding Hamiltonian. The unit cell contains four sites (labeled A_d, A_p, B_d, B_p) with one orbital on each, and has a symmetry group generated by time reversal, inversion and glide reflection. We use the permutation of the sites under the symmetries and the onsite unitary action (in this case ± 1 factors) as input. The model includes hoppings of type A_p–A_p, B_d–B_d in neighboring unit cells in the x direction, and B_d–A_p, A_p–B_p and A_d–B_d within the unit cell. We reproduce the Hamiltonian family with 7 free parameters also found in the reference:

$$H(\mathbf{k}) = \begin{bmatrix} \mu_d + 2t_d \cos k_x & 0 & 2t_d^{AB} f_d(\mathbf{k}) & 2it_0^{AB} g(\mathbf{k}) \\ 0 & \mu_p + 2t_p \cos k_x & -2it_0^{AB} g(\mathbf{k}) & 2t_p^{AB} f_p(\mathbf{k}) \\ \text{h.c.} & \text{h.c.} & \mu_d + 2t_d \cos k_x & 0 \\ \text{h.c.} & \text{h.c.} & 0 & \mu_p + 2t_p \cos k_x \end{bmatrix}, \tag{2.58}$$

where

$$f_l(\mathbf{k}) = \cos(k_x x_{Al} - k_x x_{Bl}) e^{ik_y y_{Al} + ik_y y_{Bl}}, \tag{2.59}$$

$$g(\mathbf{k}) = \sin(k_x x_{Ap} - k_x x_{Bd}) e^{-ik_y y_{Ap} + ik_y y_{Bd}}, \tag{2.60}$$

for $l \in [p, d]$ and the lattice vectors are $[1, 0]$ and $[0, 1]$. This Hamiltonian is identical to the one found previously up to transformations of the Bloch basis.

Extending this analysis to include spin and possible spin-orbit coupling terms, we find that there are 7 additional terms allowed by symmetry in a tight-binding model with the same bonds. The detailed results will be published elsewhere [64].

2.6. SUMMARY

Analysis of condensed matter systems is commonly based on single-particle Hamiltonians, the symmetry properties and classification of which are crucial to understanding the physical properties. We discussed the general symmetry structure of single-particle Hamiltonian families, and presented methods to find the full symmetry group of a Hamiltonian, and to generate all Hamiltonians compatible with a given symmetry group. Our methods extend to all continuous and discrete symmetries of single-particle continuum or lattice Hamiltonians.

Although we focused on fermionic systems, the framework we presented is generally applicable whenever the form of the symmetry action and the Hamiltonians is the same, e.g. in the analysis of unconventional superconducting pairing, or even Josephson junction arrays. Our algorithms provide a powerful tool in the ongoing classification of symmetry protected topological phases in a wide variety of physical settings ranging from classical mechanics to circuit QED. The Hamiltonian generator can be extended

to search for nonlinear effective field theories and interacting lattice models respecting given symmetries. The symmetry finder may also be further generalized to facilitate more involved symmetry analysis by decomposing group representations. We leave these open questions to future work.

We implemented the algorithms in the Qsymm Python package, making them easily accessible. We demonstrated the usefulness of our approach by applying it to a number of relevant modern research topics including graphene, transition metal dichalcogenides and topological semimetals, resulting in several new insights.

2.7. APPENDIX

2.7.1. SIMULTANEOUS DIAGONALIZATION

We present an algorithm to simultaneously diagonalize a set of mutually commuting normal matrices. The key property that follows from the commutation is that the matrices share eigensubspaces. By transforming to the diagonalizing basis of one of the matrices, the rest of the matrices are guaranteed to be block diagonal with blocks corresponding to the degenerate eigensubspaces of the first. Considering this, we apply the following recursive algorithm to find the simultaneous eigenvectors spanning the simultaneous eigensubspaces of commuting matrices H_i:

- If the matrices are 1×1, return the 1×1 identity matrix.
- Diagonalize the first matrix H_0, find the orthonormal sets of eigenvectors spanning each (approximately) degenerate eigensubspace. This results in a set of projectors P_j onto the eigensubspaces, each consisting of a set of orthonormal column vectors, the number of columns equal to the degeneracy of the j'th eigensubspace.
- If there are no more matrices, return this basis.
- Project the rest of the matrices into each degenerate eigensubspace j: $\tilde{H}_{ij} = P_j^\dagger H_i P_j$ for $i > 0$.
- Perform this algorithm on the projected matrices $\tilde{H}_{ij}$ $(i > 0)$ in each eigensubspace j, this returns a set of projectors $\tilde{P}_{jk}$.
- Return the set of projectors $P_{jk} = P_j \tilde{P}_{jk}$ for every j and k.

The output is a set of projectors P_i, each consisting of a set of orthonormal column vectors spanning a simultaneous eigensubspace of the H_i's. Horizontally stacking the P_i's gives a unitary matrix U such that $U^\dagger H_i U$ is diagonal for all i. The algorithm is guaranteed to finish, as at each recursion level both the number and the size of the matrices is decreased. The main source of numerical instability is the decision whether to treat two numerically close eigenvalues as degenerate or not. The algorithm is most stable if matrices that have eigenvalues which are either well separated or degenerate to machine precision are first and those which may have accidental near-degeneracies are last. In the physical problems we consider symmetry operators and projectors are of the first kind, while Hamiltonians are of the second.

2.7.2. FINDING THE SYMMETRY-ADAPTED BASIS

Our goal in this section is to find the symmetry-adapted basis on a Hilbert space of dimension nd. We have already ensured that the algebra of conserved quantities forms a representation of $\mathfrak{su}(d)$, such that in the proper basis the generators have the tensor product structure of $L \otimes \mathbb{1}_{n\times n}$ where the matrices L span the space of all traceless $d \times d$ Hermitian matrices.

We pick a generator $L \in \mathfrak{su}(d)$. Given the tensor product structure, every eigenvalue of the generators has degenaracy which is a multiple of n. In the case when some eigenvalues of L have degeneracy higher than n, we restrict the other generators to the fn-dimensional (with $f \leq d$ integer) eigensubspace, where they span $\mathfrak{su}(f)$. By iterating over the other generators in this restricted space it is always possible to find one that has eigenvalue degeneracy lower than fn, until all degeneracies larger than n are split. This procedure results in a basis with n-dimensional subspaces grouped together, but their bases not aligned with each other.

In this basis L has the diagonal form

$$L = \begin{bmatrix} L_{11}\mathbb{1}_{n\times n} & 0 & \cdots \\ 0 & L_{22}\mathbb{1}_{n\times n} & \cdots \\ \vdots & \vdots & \ddots \end{bmatrix}. \tag{2.61}$$

We wrote the matrix in a different block form compared to (2.25), in this notation the symmetry adopted basis is characterized by every block being proportional to $\mathbb{1}_{n\times n}$ for every element M of $\mathfrak{g}$:

$$\tilde{M} = \begin{bmatrix} M_{11}\mathbb{1}_{n_i\times n_i} & M_{12}\mathbb{1}_{n_i\times n_i} & \cdots \\ M_{21}\mathbb{1}_{n_i\times n_i} & M_{22}\mathbb{1}_{n_i\times n_i} & \cdots \\ \vdots & \vdots & \ddots \end{bmatrix}. \tag{2.62}$$

We know that such basis exists with a selected generator L having the diagonal form (2.61). Every unitary basis transformation preserving (2.61) has the block diagonal form

$$U = \begin{bmatrix} U_1 & 0 & \cdots \\ 0 & U_2 & \cdots \\ \vdots & \vdots & \ddots \end{bmatrix} \tag{2.63}$$

with $n \times n$ unitaries U_k. In this transformed basis M reads

$$M = U\tilde{M}U^\dagger = \begin{bmatrix} M_{11}\mathbb{1}_{n\times n} & M_{12}U_1U_2^\dagger & \cdots \\ M_{21}U_2U_1^\dagger & M_{22}\mathbb{1}_{n\times n} & \cdots \\ \vdots & \vdots & \ddots \end{bmatrix}. \tag{2.64}$$

By fixing $U_1 = \mathbb{1}_{n\times n}$ we can iterate over the nonzero off-diagonal blocks of M and successively fix the basis for each block such that $U_iU_j^\dagger = \mathbb{1}$. It is always possible to find a generator in $\mathfrak{su}(d)$ that does not have a zero block in a given position in the diagonalizing basis of L.

By this procedure we find a symmetry-adapted basis where every generator has the tensor product structure $L \otimes \mathbb{1}_{n\times n}$ and the Hamiltonian commuting with these generators the structure $\mathbb{1}_{d\times d} \otimes H_r$ with H_r the reduced Hamiltonian. This structure is invariant under any unitary basis transformation $U \otimes V$ with $U \in U(d)$ and $V \in U(n)$, this is the ambiguity in the symmetry-adapted basis.

2.7.3. PROOF OF BLOCK STRUCTURE OF SYMMETRY OPERATORS

We consider the general case of multiple irreps and show that an antiunitary (anti)symmetry takes a simple block structure in the symmetry-adapted basis. Explicitly writing the action $UL^*U^\dagger$ of the unitary part of $\mathscr{T} = U\mathscr{K}$,

$$U = \begin{bmatrix} U_{11} & U_{12} & \cdots \\ U_{21} & U_{22} & \cdots \\ \vdots & \vdots & \ddots \end{bmatrix} \tag{2.65}$$

on the generic symmetry generator $L \in \mathfrak{g}$

$$L = \begin{bmatrix} L^{(1)} \otimes \mathbb{1}_{n_1\times n_1} & 0 & \cdots \\ 0 & L^{(2)} \otimes \mathbb{1}_{n_2\times n_2} & \cdots \\ \vdots & \vdots & \ddots \end{bmatrix} \tag{2.66}$$

and demanding $U\mathfrak{g}U^\dagger \subseteq \mathfrak{g}$ and $U^\dagger\mathfrak{g}U \subseteq \mathfrak{g}$. We find that

$$U_{ij}\mathfrak{g}_j U_{ij}^\dagger \subseteq \mathfrak{g}_i \text{ and } U_{ij}^\dagger \mathfrak{g}_i U_{ij} \subseteq \mathfrak{g}_j \tag{2.67}$$

where $\mathfrak{g}_i$ is the space of symmetry generators in block i, $\mathfrak{g}_i = \{L^{(i)} \otimes \mathbb{1}_{n_i\times n_i}\}$.

By the lemma in Appendix C of Ref. [41], $U_{ij} \neq 0$ only if $n_i = n_j$ and factorizes as $U_{ij} = V_{ij} \otimes W_{ij}$ with unitary W_{ij}. Using this we also find that $U_{ki}\mathfrak{g}_i U_{ji}^\dagger = 0$ $(k \neq j)$, which means that either U_{ki} or U_{ji} vanishes, so there can be only one nonzero block in every row or column. As $UU^\dagger = \mathbb{1}$, each block needs to be unitary and the block structure of U is restricted to that of a permutation matrix. The determinant of such a matrix is only nonzero if the nonzero off-diagonal blocks are square: $U_{ij} \neq 0$ implies $n_i = n_j$ and $d_i = d_j$. This allows $V_{ij} = \mathbb{1}$ to be chosen for all the nonzero blocks.

In the case of antiunitary (anti)symmetry $WW^* \propto \mathbb{1}$, if W_{ij} is nonzero, W_{ji} is also nonzero with $W_{ij}W_{ji}^* \propto \mathbb{1}$, the block structure of W is restricted to that of a symmetric permutation matrix. The analogous argument can be made in the case of unitary antisymmetries by dropping the complex conjugations.

2.7.4. BEAUTIFICATION OF HAMILTONIAN FAMILIES AND CONSERVED QUANTITIES

A Hamiltonian family (2.5) is a linear space of Hamiltonians, and applying symmetry constraints to a family involves mapping the constraints to a generally rectangular matrix, such that the symmetry constrained subfamily of Hamiltonians lives in its null space [see (2.10)]. Numerically obtaining a basis for the null space, namely the symmetric subfamily, is straightforward using standard linear algebra methods. However, numerical

routines generally return basis vectors that are oriented along arbitrary directions in the subspace, and the resulting subfamily thus not necessarily as easily human readable as possible, containing many nonzero elements that are redundant. To give a simple example, numerically computing a basis for a two-dimensional Euclidean plane might yield the vectors $[1/\sqrt{2}, \pm 1/\sqrt{2}]^T$, while the standard basis $\{[1,0]^T, [0,1]^T\}$ is more intuitive.

We take increased human readability of a Hamiltonian family to mean having a smaller number of nonzero elements in the matrix parts, and the span unchanged. Since a family spans a linear space, we can express each family as a full rank matrix. This is done by mapping each family member to a row vector by flattening and concatenating all the matrix coefficients, and vertically stacking these vectors. Obtaining a human readable representation of the family then amounts to finding another matrix with the same row space but with as few nonzero entries as possible. This problem is known in the literature as matrix sparsification [65], and although widely studied, to our knowledge no general algorithms for matrix sparsification exist.

To solve this problem, we sparsify the matrix representation of a Hamiltonian family by bringing it to reduced row echelon form. In reduced row echelon form, the first nonzero number from the left in a row is always equal to 1, and is located to the right of the first nonzero entry in the row above. Furthermore, the first nonzero entry per row is always the only nonzero entry in its column, and the number of nonzero entries thus minimal. In addition, bringing a matrix to reduced row echelon form preserves its row span. We obtain the reduced row echelon form by performing elementary row operations on the matrix representation of the family. In floating point precision, this generally leads to numerical instability. However, for the applications we consider, this is not a major obstacle, since the matrices we consider are typically small, and usually only contain nonzero elements that are of the order 1, such that the distinction between zero and nonzero entries is unambiguous.

Conserved quantities, which also form a linear space spanned by a set of matrices, suffer from the same ambiguity. We apply the same algorithm of bringing the matrix whose rows are the flattened generators of conserved quantities to reduced row echelon form in order to bring the generator set to a more human readable form.

REFERENCES

[1] J. C. Slater and G. F. Koster, *Simplified lcao method for the periodic potential problem,* Phys. Rev. **94**, 1498 (1954).

[2] P. Vogl, H. P. Hjalmarson, and J. D. Dow, *A semi-empirical tight-binding theory of the electronic structure of semiconductors†,* J. Phys. Chem. Solids **44**, 365 (1983).

[3] J.-M. Jancu, R. Scholz, F. Beltram, and F. Bassani, *Empirical* spds* *tight-binding calculation for cubic semiconductors: General method and material parameters,* Phys. Rev. B **57**, 6493 (1998).

[4] G.-B. Liu, W.-Y. Shan, Y. Yao, W. Yao, and D. Xiao, *Three-band tight-binding model for monolayers of group-vib transition metal dichalcogenides,* Phys. Rev. B **88**, 085433 (2013).

[5] E. Cappelluti, R. Roldán, J. A. Silva-Guillén, P. Ordejón, and F. Guinea, *Tight-binding model and direct-gap/indirect-gap transition in single-layer and multilayer mos$_2$,* Phys. Rev. B **88**, 075409 (2013).

[6] J. M. Luttinger and W. Kohn, *Motion of electrons and holes in perturbed periodic fields,* Phys. Rev. **97**, 869 (1955).

[7] G. L. Bir and G. E. Pikus, *Symmetry and strain-induced effects in semiconductors* (Wiley New York, 1974).

[8] A. Kormányos, G. Burkard, M. Gmitra, J. Fabian, V. Zólyomi, N. D. Drummond, and V. Fal'ko, *$k \cdot p$ theory for two-dimensional transition metal dichalcogenide semiconductors,* 2D Mater. **2**, 022001 (2015).

[9] M. Z. Hasan and C. L. Kane, *Colloquium: Topological insulators,* Rev. Mod. Phys. **82**, 3045 (2010).

[10] M. Sato and Y. Ando, *Topological superconductors: a review,* Rep. Prog. Phys. **80**, 076501 (2017).

[11] A. Altland and M. R. Zirnbauer, *Nonstandard symmetry classes in mesoscopic normal-superconducting hybrid structures,* Phys. Rev. B **55**, 1142 (1997).

[12] A. P. Schnyder, S. Ryu, A. Furusaki, and A. W. W. Ludwig, *Classification of topological insulators and superconductors in three spatial dimensions,* Phys. Rev. B **78**, 195125 (2008).

[13] A. Kitaev, *Periodic table for topological insulators and superconductors,* in *American Institute of Physics Conference Series,* American Institute of Physics Conference Series, Vol. 1134, edited by V. Lebedev and M. Feigel'Man (2009) pp. 22–30, arXiv:0901.2686 .

[14] L. Fu, *Topological crystalline insulators,* Phys. Rev. Lett. **106**, 106802 (2011).

[15] R.-J. Slager, A. Mesaros, V. Juričić, and J. Zaanen, *The space group classification of topological band-insulators,* Nat. Phys. **9**, 98 EP (2012).

[16] Y. Ando and L. Fu, *Topological crystalline insulators and topological superconductors: From concepts to materials,* Annu. Rev. Condens. Matter Phys. **6**, 361 (2015).

[17] H. C. Po, A. Vishwanath, and H. Watanabe, *Complete theory of symmetry-based indicators of band topology,* Nat. Commun. **8**, 50 (2017).

[18] H. Watanabe, H. C. Po, and A. Vishwanath, *Structure and Topology of Band Structures in the 1651 Magnetic Space Groups,* ArXiv e-prints (2017), arXiv:1707.01903 [cond-mat.str-el] .

[19] B. Bradlyn, L. Elcoro, J. Cano, M. G. Vergniory, Z. Wang, C. Felser, M. I. Aroyo, and B. A. Bernevig, *Topological quantum chemistry,* Nature **547**, 298 (2017).

[20] B. Bradlyn, L. Elcoro, M. G. Vergniory, J. Cano, Z. Wang, C. Felser, M. I. Aroyo, and B. A. Bernevig, *Band connectivity for topological quantum chemistry: Band structures as a graph theory problem,* Phys. Rev. B **97**, 035138 (2018).

[21] S. Murakami, M. Hirayama, R. Okugawa, and T. Miyake, *Emergence of topological semimetals in gap closing in semiconductors without inversion symmetry,* Sci. Adv. **3**, e1602680 (2017).

[22] J. Kruthoff, J. de Boer, J. van Wezel, C. L. Kane, and R.-J. Slager, *Topological classification of crystalline insulators through band structure combinatorics,* Phys. Rev. X **7**, 041069 (2017).

[23] I. C. Fulga, B. van Heck, J. M. Edge, and A. R. Akhmerov, *Statistical topological insulators,* Phys. Rev. B **89**, 155424 (2014).

[24] D. Gresch, *kdotp-symmetry,* `http://z2pack.ethz.ch/kdotp-symmetry`, Accessed: 2018-08-27.

[25] M. Notomi, *Theory of light propagation in strongly modulated photonic crystals: Refractionlike behavior in the vicinity of the photonic band gap,* Phys. Rev. B **62**, 10696 (2000).

[26] L. Lu, J. D. Joannopoulos, and M. Soljačić, *Topological photonics,* Nat. Photonics **8**, 821 EP (2014).

[27] C. L. Kane and T. C. Lubensky, *Topological boundary modes in isostatic lattices,* Nat. Phys. **10**, 39 EP (2013).

[28] R. Süsstrunk and S. D. Huber, *Observation of phononic helical edge states in a mechanical topological insulator,* Science **349**, 47 (2015).

[29] J. Ningyuan, C. Owens, A. Sommer, D. Schuster, and J. Simon, *Time- and site-resolved dynamics in a topological circuit,* Phys. Rev. X **5**, 021031 (2015).

[30] T. Kitagawa, E. Berg, M. Rudner, and E. Demler, *Topological characterization of periodically driven quantum systems,* Phys. Rev. B **82**, 235114 (2010).

[31] D. Varjas, T. O. Rosdahl, and A. Akhmerov, *Qsymm: Symmetry finder and symmetric hamiltonian generator,* (2018).

[32] Updated version of Qsymm is available at `https://gitlab.kwant-project.org/qt/qsymm`.

[33] L. Fu, *Hexagonal warping effects in the surface states of the topological insulator* bi_2te_3, Phys. Rev. Lett. **103**, 266801 (2009).

[34] D. Xiao, G.-B. Liu, W. Feng, X. Xu, and W. Yao, *Coupled spin and valley physics in monolayers of* mos_2 *and other group-vi dichalcogenides,* Phys. Rev. Lett. **108**, 196802 (2012).

[35] S. Fang, R. Kuate Defo, S. N. Shirodkar, S. Lieu, G. A. Tritsaris, and E. Kaxiras, *Ab initio,* Phys. Rev. B **92**, 205108 (2015).

[36] B. Beauzamy, E. Bombieri, P. Enflo, and H. L. Montgomery, *Products of polynomials in many variables,* Journal of Number Theory **36**, 219 (1990).

[37] R. Resta, *Manifestations of berry's phase in molecules and condensed matter,* J. Phys.: Condens. Matter **12**, R107 (2000).

[38] D. Varjas, F. de Juan, and Y.-M. Lu, *Bulk invariants and topological response in insulators and superconductors with nonsymmorphic symmetries,* Phys. Rev. B **92**, 195116 (2015).

[39] B. Hall, *Lie Groups, Lie Algebras, and Representations: An Elementary Introduction*, Graduate Texts in Mathematics (Springer International Publishing, 2015).

[40] W. Fulton, W. Harris, and J. Harris, *Representation Theory: A First Course*, Graduate Texts in Mathematics (Springer New York, 1991).

[41] D. Varjas, T. Ö. Rosdahl, and A. R. Akhmerov, *Qsymm: algorithmic symmetry finding and symmetric hamiltonian generation,* New Journal of Physics **20**, 093026 (2018).

[42] A. Meurer, C. P. Smith, M. Paprocki, O. Čertík, S. B. Kirpichev, M. Rocklin, A. Kumar, S. Ivanov, J. K. Moore, S. Singh, *et al.*, *Sympy: symbolic computing in python,* PeerJ Computer Science **3**, e103 (2017).

[43] C. W. Groth, M. Wimmer, A. R. Akhmerov, and X. Waintal, *Kwant: a software package for quantum transport,* New Journal of Physics **16**, 063065 (2014).

[44] R. Lehoucq, D. Sorensen, and C. Yang, *Arpack users' guide: Solution of large scale eigenvalue problems with implicitly restarted arnoldi methods.* Software Environ. Tools **6** (1997).

[45] E. Jones, T. Oliphant, P. Peterson, *et al.*, *SciPy: Open source scientific tools for Python,* (2001–).

[46] T. Kluyver, B. Ragan-Kelley, F. Pérez, B. E. Granger, M. Bussonnier, J. Frederic, K. Kelley, J. B. Hamrick, J. Grout, S. Corlay, *et al.*, *Jupyter notebooks-a publishing format for reproducible computational workflows.* in *ELPUB* (2016) pp. 87–90.

[47] B. Nijholt and A. R. Akhmerov, *Orbital effect of magnetic field on the majorana phase diagram,* Phys. Rev. B **93**, 235434 (2016).

[48] M. Leijnse and K. Flensberg, *Introduction to topological superconductivity and majorana fermions,* Semiconductor Science and Technology **27**, 124003 (2012).

[49] J. Li, H. Chen, I. K. Drozdov, A. Yazdani, B. A. Bernevig, and A. H. MacDonald, *Topological superconductivity induced by ferromagnetic metal chains,* Phys. Rev. B **90**, 235433 (2014).

[50] O. V. Gamayun, V. P. Ostroukh, N. V. Gnezdilov, I. Adagideli, and C. W. J. Beenakker, *Valley-momentum locking in a graphene superlattice with y-shaped kekul'e bond texture,* New J. Phys. **20**, 023016 (2018).

[51] C.-Y. Hou, C. Chamon, and C. Mudry, *Electron Fractionalization in Two-Dimensional Graphenelike Structures,* Phys. Rev. Lett. **98**, 186809 (2007).

[52] T. H. Hsieh, H. Lin, J. Liu, W. Duan, A. Bansil, and L. Fu, *Topological crystalline insulators in the snte material class,* Nat. Commun. **3**, 982 (2012).

[53] A. Lau and C. Ortix, *Topological semimetals in the SnTe material class: Nodal lines and Weyl points,* ArXiv e-prints (2018), arXiv:1804.09574 .

[54] Q. H. Wang, K. Kalantar-Zadeh, A. Kis, J. N. Coleman, and M. S. Strano, *Electronics and optoelectronics of two-dimensional transition metal dichalcogenides,* Nat. Nanotechnol. **7**, 699 EP (2012).

[55] J. T. Ye, Y. J. Zhang, R. Akashi, M. S. Bahramy, R. Arita, and Y. Iwasa, *Superconducting dome in a gate-tuned band insulator,* Science **338**, 1193 (2012).

[56] Z. Fei, T. Palomaki, S. Wu, W. Zhao, X. Cai, B. Sun, P. Nguyen, J. Finney, X. Xu, and D. H. Cobden, *Edge conduction in monolayer WTe_2,* Nat. Phys. **13**, 677 (2017).

[57] S. Tang, C. Zhang, D. Wong, Z. Pedramrazi, H.-Z. Tsai, C. Jia, B. Moritz, M. Claassen, H. Ryu, S. Kahn, J. Jiang, H. Yan, M. Hashimoto, D. Lu, R. G. Moore, C.-C. Hwang, C. Hwang, Z. Hussain, Y. Chen, M. M. Ugeda, Z. Liu, X. Xie, T. P. Devereaux, M. F. Crommie, S.-K. Mo, and Z.-X. Shen, *Quantum spin Hall state in monolayer 1T'-WTe_2,* Nat. Phys. **13**, 683 (2017).

[58] S. Wu, V. Fatemi, Q. D. Gibson, K. Watanabe, T. Taniguchi, R. J. Cava, and P. Jarillo-Herrero, *Observation of the quantum spin Hall effect up to 100 kelvin in a monolayer crystal,* Science **359**, 76 (2018).

[59] Z.-Y. Jia, Y.-H. Song, X.-B. Li, K. Ran, P. Lu, H.-J. Zheng, X.-Y. Zhu, Z.-Q. Shi, J. Sun, J. Wen, *et al.*, *Direct visualization of a two-dimensional topological insulator in the single-layer 1 t'- wt e 2,* Phys. Rev. B **96**, 041108 (2017).

[60] X. Qian, J. Liu, L. Fu, and J. Li, *Quantum spin hall effect in two-dimensional transition metal dichalcogenides,* Science , 1256815 (2014).

[61] F. Zheng, C. Cai, S. Ge, X. Zhang, X. Liu, H. Lu, Y. Zhang, J. Qiu, T. Taniguchi, K. Watanabe, *et al.*, *On the quantum spin hall gap of monolayer 1t'-wte2,* Adv. Mater. **28**, 4845 (2016).

[62] M. König, S. Wiedmann, C. Brüne, A. Roth, H. Buhmann, L. W. Molenkamp, X.-L. Qi, and S.-C. Zhang, *Quantum Spin Hall Insulator State in HgTe Quantum Wells,* Science **318**, 766 (2007).

[63] L. Muechler, A. Alexandradinata, T. Neupert, and R. Car, *Topological Nonsymmorphic Metals from Band Inversion,* Phys. Rev. X **6**, 041069 (2016).

[64] A. Lau *et al.*, (2018), unpublished.

[65] L.-A. Gottlieb and T. Neylon, *Matrix sparsification and the sparse null space problem,* in *Approximation, Randomization, and Combinatorial Optimization. Algorithms and Techniques*, edited by M. Serna, R. Shaltiel, K. Jansen, and J. Rolim (Springer Berlin Heidelberg, Berlin, Heidelberg, 2010) pp. 205–218.

3

ANDREEV RECTIFIER: A NONLOCAL CONDUCTANCE SIGNATURE OF TOPOLOGICAL PHASE TRANSITIONS

This chapter has been previously published as T. Ö. Rosdahl, A. Vuik, M. Kjaergaard, A. R. Akhmerov, *Andreev rectifier: a nonlocal conductance signature of topological phase transitions*, Phys. Rev. B 97, 045421 (2018).

3.1. INTRODUCTION

The superconducting proximity effect occurs when a normal material (metal) is placed in contact with a superconductor. The resulting transfer of superconducting properties to the normal material [1, 2] makes it possible to explore induced superconductivity in a range of materials that are not intrinsically superconducting, for example in ferromagnetic metals [3–5] and in graphene [6–8]. Another recent application of the proximity effect is the creation of the Majorana quasiparticle [9–11], which is a candidate for the realization of topological quantum computation [12], and a focus of research efforts in recent years [13–15].

The proximity effect is due to the Andreev reflection of quasiparticles at the interface with the superconductor [2], which forms correlated electron-hole pairs that induce superconductivity in the normal material. This makes the proximity effect in real systems sensitive to microscopic interface properties, such as coupling strength, charge accumulation and lattice mismatch [16, 17]. Spatial inhomogeneities in the proximitised system, such as charge defects, may furthermore spoil the induced correlations locally. In a typical proximity setup, the superconductor proximitises an extended region of a normal material, as shown in Fig. 6.1. A normal lead attached to one of the ends of the proximitised region probes the response to an applied voltage. When the coupling between the lead and the proximitised region is weak, the lead functions as a tunnel probe of the density of states in the latter. Since induced superconductivity may be inhomogeneous, and Andreev reflection happens locally, such an experiment only probes the region in direct vicinity of the normal lead, and not the overall properties of the proximitised region. For example, if the electrostatic potential is inhomogeneous, it may create accidental low-energy modes that are nearly indistinguishable from Majoranas [18–23].

We show how the *nonlocal* response between two spatially separated normal leads (see Fig. 6.1) may be used to probe both the bulk superconducting gap Δ and the induced gap Δ_{ind}, as well as the induced coherence length ξ. At subgap energies, quasiparticles propagate as evanescent waves with the decay length ξ in the proximitised system. This suppresses the nonlocal response with increasing separation L between the two normal leads [24–26]. Therefore, the length dependence of the nonlocal conductance measures when two ends of a proximitised system are effectively decoupled. When $L/\xi \gtrsim 1$, the nonlocal conductance is only possible in the energy window between the bulk superconducting gap Δ and the induced gap Δ_{ind}. The sensitivity to an induced gap allows one to use nonlocal conductance to distinguish between a induced gap closing and an Andreev level crossing at zero energy. In contrast, a local measurement may produce a similar result in both cases.

Two processes constitute the nonlocal response: direct electron transfer between the normal leads, and the crossed Andreev reflection (CAR) of an electron from one lead into a hole in the second lead [27, 28]. Experimental [29–31] and theoretical [32–37] studies of CAR-dominated signals aim at producing a Cooper pair splitter [38–40], which has potential applications in quantum information processing. We show that applying a Zeeman field in the proximitised system creates wide regions in parameter space where CAR dominates the nonlocal response. Furthermore, we demonstrate how to obtain a CAR dominated signal in the absence of a Zeeman field in the low-doping regime. Finally, we prove that at the topological phase transition and with $L/\xi \gtrsim 1$, the nonlocal conductance

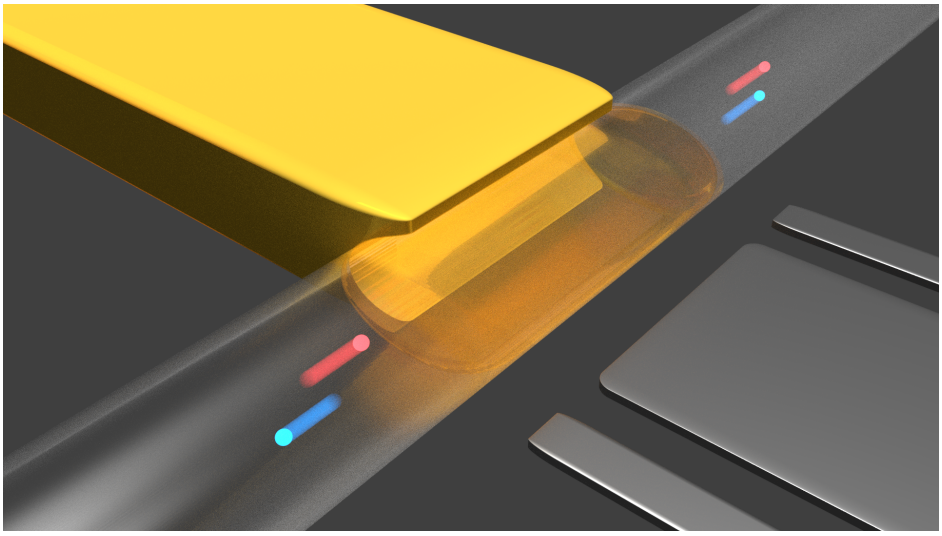

Figure 3.1: A superconductor (yellow) proximitises a semiconducting region (transparent) from the side. Narrow gates control the coupling of the proximitised scattering region with the leads, a wider gate controls the chemical potential. An incoming electron from the left (red dot) either undergoes a local process, i.e. Andreev reflection into a hole (blue outgoing dot to the left) or normal reflection (not shown), or a nonlocal process (outgoing electron or hole to the right).

is an approximately odd function of bias. This phenomenon only relies on particle-hole symmetry, and hence manifests both in clean and disordered junctions. Therefore, a proximitised system coupled to normal leads acts as a rectifier of the applied voltage bias universally at the topological phase transition.

Our method is based on probing the bulk topological phase transition in Majorana devices, instead of the Majoranas themselves. Several other works propose different methods to probe the bulk instead of the edge states in one-dimensional topological superconductors. Quantized thermal conductance and electrical shot noise measurements are predicted signatures of a bulk topological phase transition [41], and here we present a different route based on straightforward electrical conduction measurements in already available experimental systems. Further work predicts bulk signatures of a topological phase transition in the difference between the local Andreev conductances at each end of the proximitised region [42], or in the spin projection of bulk bands along the magnetic field direction [43]. In addition to probing the bulk topological phase transition, our proposed method allows to probe a number of relevant physical parameters, and can be implemented in ongoing experiments, providing a novel technique to use in the hunt for Majoranas.

This chapter is organized as follows. In Sec. 3.2, we give an overview of our model and discuss the relevant energy and length scales. In Sec. 3.3, we study how nonlocal conductance measures superconductor characteristics. We investigate the effects of a Zeeman field in homogeneous and inhomogeneous systems in Sec. 3.4. In Sec. 3.5 we consider the possible application of the proximitised system as a Cooper pair splitter. We

finish with a summary and discussion of our results in Sec. 3.6.

3.2. MODEL AND PHYSICAL PICTURE

We consider a three terminal device sketched in Fig. 3.2, with a normal central region of lateral length L and width W separating two normal leads of width W_L. The device has a grounded superconducting lead of width L attached to the central region perpendicularly to the other two leads. This geometry models the proximity effect of a lateral superconductor on a slab of normal material, with normal leads probing the transport properties, and is therefore relevant both for heterostructures based on nanowires and quantum wells.

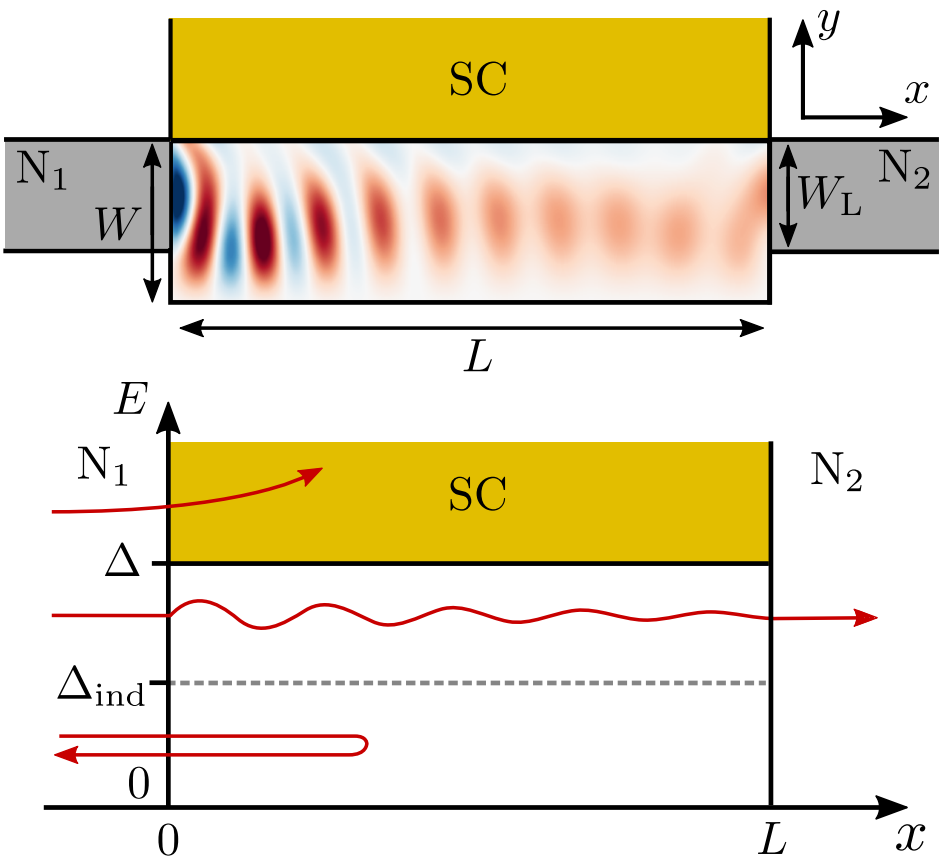

Figure 3.2: Top: schematic drawing of the device. A central region of length L and width W is connected from the sides to two normal leads N_1 (left) and N_2 (right) of width W_L, and from the top to one superconducting lead (SC) of width L. Superimposed is an example of the central region charge density, which oscillates between positive (red) and negative (blue). Bottom: illustrations of possible scattering processes in energy space in the limit $L \gg \xi$. A quasiparticle, with energy below the induced gap, $|E| < \Delta_{\text{ind}}$, is reflected back into the source lead. A quasiparticle at $\Delta_{\text{ind}} < |E| < \Delta$ is transmitted to the right lead, either as an electron (normal transmission) or as a hole (crossed Andreev reflection). At energies exceeding the bulk gap $|E| > \Delta$, the superconducting lead absorbs incoming quasiparticles.

We model the hybrid system using the Bogoliubov-de Gennes Hamiltonian. For a semiconductor electron band with effective mass m^* and Rashba spin-orbit interaction (SOI) with strength α, it reads

$$H = \left(\frac{p_x^2 + p_y^2}{2m^*} - \mu \right) \tau_z + \Delta(y)\tau_x + \frac{\alpha}{\hbar} \left(p_y \sigma_x - p_x \sigma_y \right) \tau_z + E_Z(y)\sigma_x, \tag{3.1}$$

with $p_{x,y} = -i\hbar\partial_{x,y}$, μ the equilibrium chemical potential and E_Z the Zeeman energy due to an in-plane magnetic field parallel to the interface between the central region and the superconductor. We assume a constant s-wave pairing potential that is nonzero only in the superconductor, $\Delta(y) = \Delta\theta(y - W)$ with $\theta(y)$ a step function, and choose Δ to be real since only one superconductor is present. We neglect the g-factor in the superconductor since it is much smaller than in the adjacent semiconductor, such that $E_Z(y) = E_Z\theta(W - y)$, and our conclusions are not affected by this choice. The Pauli matrices σ_i and τ_i act in spin and particle-hole space, respectively. The Hamiltonian acts on the spinor $\Psi = \left(\psi_{e\uparrow}, \psi_{e\downarrow}, \psi_{h\downarrow}, -\psi_{h\uparrow}\right)$, which represent the electron (e) or hole (h) components of spin up (↑) or down (↓).

The superconductor induces an energy gap Δ_{ind} in the heterostructure. If $L \gg W$, the larger of two energy scales, namely the bulk gap Δ and the Thouless energy E_{Th}, determines the magnitude of Δ_{ind}, with E_{Th} at low μ given by

$$E_{\text{Th}} = \gamma\delta, \quad \delta = \frac{\hbar^2\pi^2}{2m^*(2W)^2}, \tag{3.2}$$

where γ is the transparency of the interface with the superconductor and δ the level spacing. Our emphasis is on short and intermediate junctions, for which $E_{\text{Th}} \gg \Delta$ and $E_{\text{Th}} \lesssim \Delta$, respectively, such that $\Delta_{\text{ind}} \lesssim \Delta$. A brief review of normal-superconductor junctions in different limits and the relevant length and energy scales is given in App. 3.7. We keep μ constant in the entire system, but assume an anisotropic mass [44] in the superconductor with a component parallel to the interface $m_\parallel \to \infty$. This approximation results in a transparent interface $\gamma = 1$ at normal incidence and at $E_Z = 0$, and is motivated by recent advances in the fabrication of proximitised systems with a high-quality superconductor-semiconductor interface [45, 46].

We compute differential conductance using the scattering formalism. The scattering matrix relating all incident and outgoing modes in the normal leads of Fig. 3.2 is

$$S = \begin{bmatrix} S_{11} & S_{12} \\ S_{21} & S_{22} \end{bmatrix}, \quad S_{ij} = \begin{bmatrix} S_{ij}^{ee} & S_{ij}^{eh} \\ S_{ij}^{he} & S_{ij}^{hh} \end{bmatrix}. \tag{3.3}$$

Here, the $S_{ij}^{\alpha\beta}$ is the block of scattering amplitudes of incident particles of type β in lead j to particles of type α in lead i. Since quasiparticles may enter the superconducting lead for $|E| > \Delta$, the scattering matrix (3.3) is unitary only if $|E| < \Delta$. The zero-temperature differential conductance matrix equals [2, 47]

$$G_{ij}(E) \equiv \frac{\partial I_i}{\partial V_j} = \frac{e^2}{h} \left(T_{ij}^{ee} - T_{ij}^{he} - \delta_{ij} N_i^e \right), \tag{3.4}$$

with I_i the current entering terminal i from the scattering region and V_j the voltage applied to the terminal j, and N_j^e the number of electron modes at energy E in terminal j, and finally the energy-dependent transmissions are

$$T_{ij}^{\alpha\beta} = \mathrm{Tr}\left(\left[S_{ij}^{\alpha\beta}(E)\right]^\dagger S_{ij}^{\alpha\beta}\right). \tag{3.5}$$

The blocks of the conductance matrix involving the superconducting terminal are fixed by the condition that the sum of each row and column of the conductance matrix has to vanish. The finite temperature conductance is a convolution of zero-temperature conductance with a derivative of the Fermi distribution function $f(E) = (1+\exp(E/k_BT))^{-1}$:

$$G_{ij}(eV_j, T) = -\int_{-\infty}^{\infty} \mathrm{d}E \frac{\mathrm{d}f(E-eV_j, T)}{\mathrm{d}E} G_{ij}(E). \tag{3.6}$$

We discretize the Hamiltonian (3.1) on a square lattice, and use Kwant [48] to numerically obtain the scattering matrix of Eq. (3.3), see the supplementary material for source code [49]. The resulting data is available in Ref. [50]. We obtain ξ numerically by performing an eigendecomposition of the translation operator in the x-direction for a translationally invariant system and computing the decay length of the slowest decaying mode at $E = 0$ [44, 51]. We use the material parameters[1] $m^* = 0.023 m_\mathrm{e}$, $\alpha = 28$ meVnm, and unless otherwise specified $\Delta = 0.2$ meV, typical for an InAs two-dimensional electron gas with an epitaxial Al layer [45]. All transport calculations are done using $T = 30$ mK unless stated otherwise.

3.3. NONLOCAL CONDUCTANCE AS A MEASURE OF SUPERCONDUCTOR PROPERTIES

In the tunnelling regime, the local conductance in a normal lead probes the density of states in the proximitised region, which is commonly used to measure the induced gap in experiment. However, such a measurement only probes the region near the tunnel probe, but fails to give information about the density of states in the bulk of the proximitised region. The tunnelling conductance is thus not a reliable probe of the entire proximitised region if the density of states varies spatially over the proximitised region, for example due to an inhomogeneous geometry. As an illustration, Fig. 3.3 compares the local conductance G_{11} in the tunnelling limit to the nonlocal conductance G_{21} in the open regime for a proximitised system that is inhomogeneous and in a magnetic field. Inhomogeneous systems are further treated in Sec. 3.4. The combination of an inhomogeneous system and broken time-reversal symmetry creates low-energy states localized near the junctions with the normal leads, which appear as peaks in the tunnelling conductance. However, away from the junctions with the normal leads, the proximitised system remains close to fully gapped, the induced gap matching the energies at which the nonlocal conductance becomes finite in Fig. 3.3(b). Therefore, the nonlocal conductance is better than the local tunnelling conductance as a probe for the induced gap in the bulk of the proximitised region. In the following, we describe three ways in which the nonlocal conductance probes induced superconductivity.

[1] All parameters are provided per figure in a text file as supplementary material.

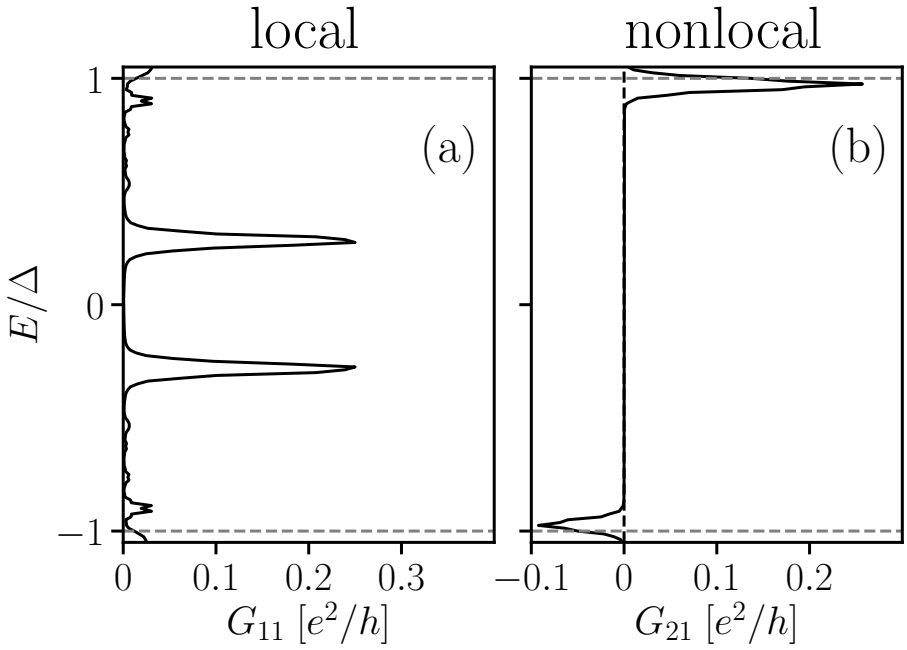

Figure 3.3: Examples of (a) the local conductance in the tunnelling regime and (b) the nonlocal conductance in the open regime, of an inhomogeneous proximitised system with broken time-reversal symmetry. Localized low-energy states are present near the junctions with the normal leads. These manifest as peaks in the tunnelling conductance, indicating $\Delta_{\text{ind}} \ll \Delta$. However, $\Delta_{\text{ind}} \approx \Delta$ still in the bulk of the proximitised system, with Δ_{ind} matching the energy at which the nonlocal conductance peaks.

First of all, the nonlocal conductance measures the induced decay length ξ in the bulk of the proximitised region between the two normal leads. To understand this, consider a nonlocal process at a subgap energy $|E| < \Delta_{\text{ind}}$. An electron injected from a normal lead must propagate as an evanescent wave $\propto e^{-x/\xi+ikx}$ through the gapped central region to the second normal lead, with ξ the decay length. Accordingly, as shown in Fig. 3.4, increasing L suppresses the nonlocal conductance at $E = 0$ exponentially [28, 38]. Therefore, the suppression of the nonlocal conductance with increasing length L at $E = 0$ is a measure of the induced decay length ξ.

Furthermore, the nonlocal conductance measures the bulk gap Δ of the superconductor. Increasing L also suppresses the nonlocal conductance G_{21} for $|E| > \Delta$, as the right column of Fig. 3.5 shows. For energies above the bulk superconducting gap Δ, the superconductor increasingly absorbs quasiparticles when the length is increased, and suppresses the nonlocal conductance to zero when $L \gg \xi$. Hence, the energy above which nonlocal conductance is suppressed at large lengths is a measure of Δ.

In addition, the nonlocal conductance measures the induced superconducting gap Δ_{ind}. When $L \gtrsim \xi$, the nonlocal conductance is suppressed at $E = 0$ but grows in a convex shape with E and peaks around $|E| \approx \Delta_{\text{ind}}$, as shown in the right column of Fig. 3.5. This is due to a divergence in ξ, since the system is no longer gapped. To illustrate the

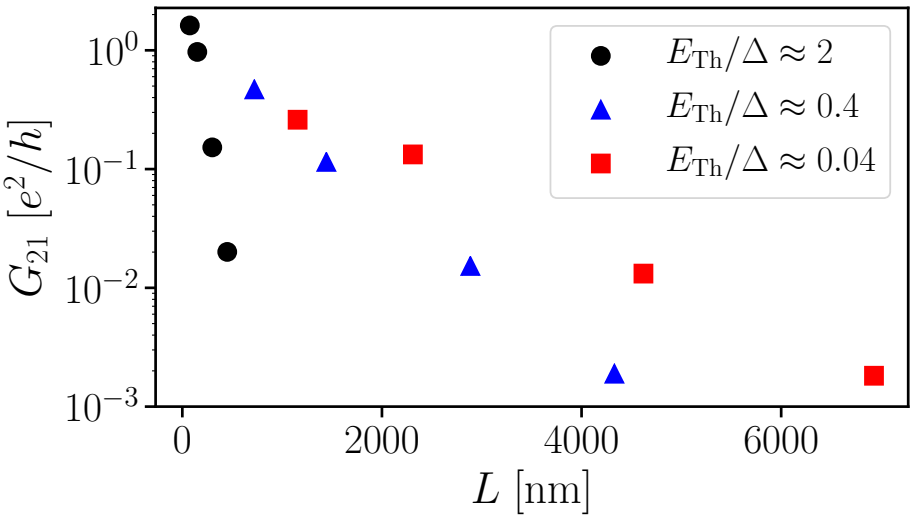

Figure 3.4: Suppression of the nonlocal conductance G_{21} at zero bias $E = 0$ as a function of length for different ratios E_{Th}/Δ. For decreasing ratio E_{Th}/Δ, the induced coherence length ξ increases. This is reflected in the larger absolute length over which the nonlocal conductance is suppressed. Data points are taken from the $E = 0$ values of the nonlocal conductance presented in Fig. 3.5.

correspondence between the nonlocal conductance and Δ_{ind}, the left column of Fig. 3.5 shows the dispersions of the corresponding proximitised systems that have the normal leads removed and are translationally invariant along the x direction, such that $k = p_x/\hbar$ is conserved. Because the system is not gapped for $|E| > \Delta_{\mathrm{ind}}$, G_{21} is generally nonzero at these energies. Note that aside from occasional dips to negative G_{21}, direct electron transfer dominates the nonlocal response (we investigate this in more detail in Sec. 3.5).

The presence of finite nonlocal conductance in the energy range $\Delta_{\mathrm{ind}} < |E| < \Delta$ depends only on density of states of the proximitised system, and therefore still holds in the presence of disorder. In Fig. 3.6, we show the effects of disorder on the transport signatures of Δ and Δ_{ind} for short and intermediate junctions when $L \gtrsim \xi$. We include onsite disorder in the central region, and vary the elastic mean free path l_e from $l_e = L$ to $l_e = 0.1L$ [52]. Even in the presence of disorder, all of the aforementioned qualities are still apparent in the nonlocal conductance (a) and (b), namely suppression for $|E| < \Delta_{\mathrm{ind}}$, a finite signal for $\Delta_{\mathrm{ind}} < |E| < \Delta$ and vanishing conductance for $|E| > \Delta$. Therefore, the nonlocal conductance remains a reliable probe of induced superconductivity even in the presence of disorder.

Lastly, in the absence of extended potential inhomogeneities, Δ and Δ_{ind} may also be inferred from the local conductance G_{11} in the open regime. As Figs. 3.6(c) and (d) show, $G_{11} \lesssim 4e^2/h$ in the ballistic case $l_e = L$ for $|E| < \Delta_{\mathrm{ind}}$, which indicates that Andreev reflection is the dominant local process. This is the expected behavior for a normal-superconductor junction with high interface transparency [2, 45], and is consistent with our results. Reducing the mean free path makes normal reflection more likely and hence lowers G_{11}, similar to an ideal normal-superconductor junction with a reduced interface

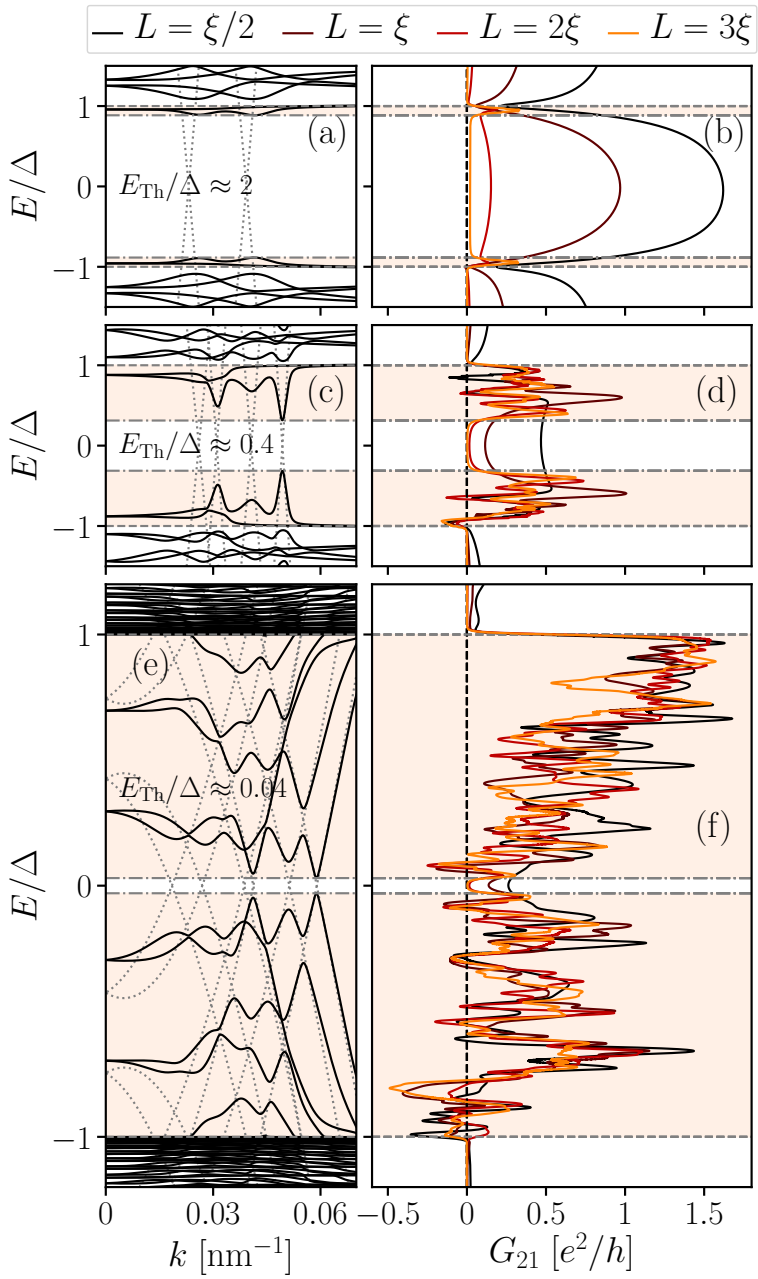

Figure 3.5: (a, c, e) Dispersions of proximitised systems that are translationally invariant along x, and (b, d, f) nonlocal conductance $G_{21}(E)$ of corresponding junctions of finite length. The latter is shown as the separation L between the two normal leads is varied, with brightening colors from black to orange denoting $L = \xi/2$, ξ, 2ξ and 3ξ, respectively. The ratio E_{Th}/Δ becomes smaller from top to bottom, such that Δ_{ind} shrinks (dash-dotted lines). For $L \gg \xi$, the nonlocal conductance is suppressed if $|E| < \Delta_{\mathrm{ind}}$, and finite only for $\Delta_{\mathrm{ind}} < |E| < \Delta$ (colored region). The solid lines in the dispersion relations show the dispersion of the normal-superconductor system, while the dotted lines show the electron and hole dispersion of the normal channel only, with the superconductor removed. We have $W = 100$ nm in (a) and (b), $W = 200$ nm in (c), (d), (e) and (f), and $W_L = 100$ nm always in the right column. $\mu = 3$ meV, $\Delta = 0.2$ meV and $T = 30$ mK in the top and middle rows, but $\mu = 4.2$ meV, $\Delta = 2$ meV and $T = 100$ mK in the bottom row. Dispersions are even in k.

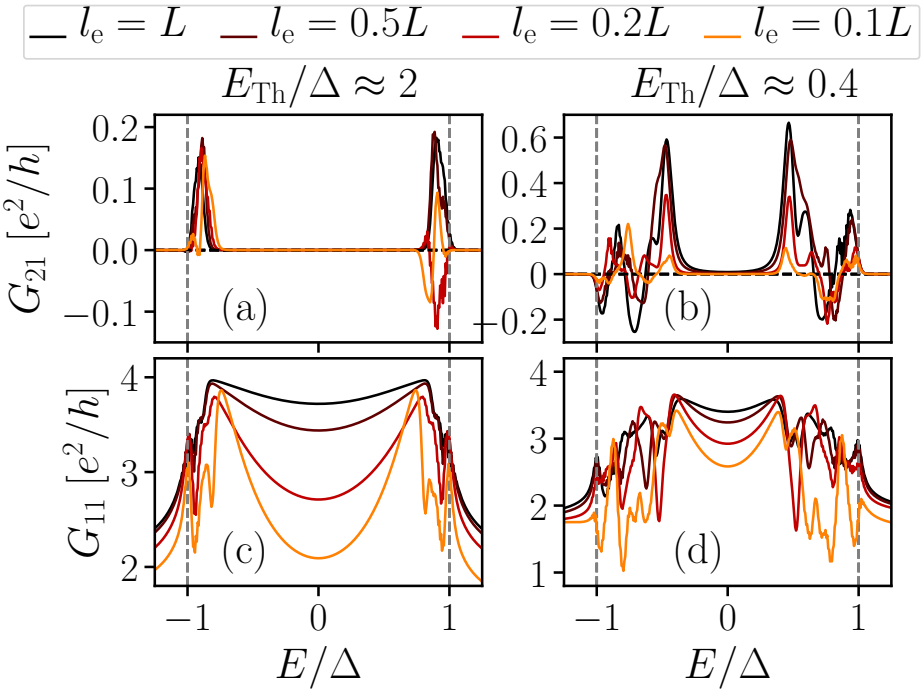

Figure 3.6: Nonlocal (a, b) and local conductance (c, d) G_{21} and G_{11} of short (left column) and intermediate (right column) junctions with $L \gtrsim \xi$, to decouple the two normal leads at $|E| < \Delta_{\text{ind}}$. The mean free path varies between curves, with brightening colors from black to light orange denoting $l_e = L,\ L/2,\ L/5$ and $L/10$ respectively. Even in the presence of disorder, signatures of Δ_{ind} and Δ are visible in the nonlocal conductance. The local conductance is Andreev enchanced at subgap energies, but normal reflection becomes more prominent with increasing disorder. We have $W = 100$ nm and $L = 8\xi$ in (a) and (c), $W = 200$ nm and $L = 2\xi$ in (b) and (d), and $W_L = 100$ nm always, with $\mu = 3$ meV.

transparency. Here, comparing G_{11} and G_{21} shows that Δ_{ind} and Δ may also be inferred from the local conductance, because it changes smoothly with bias only outside the interval $\Delta_{\text{ind}} < |E| < \Delta$. However, the signatures are clearer in G_{21}, where it is a transition between finite and vanishing conductance that indicates the gaps. Furthermore, the induced gap observed in the local and nonlocal conductances coincide here only due to the absence of extended potential inhomogeneities. For the case of an inhomogeneous geometry as in Fig. 3.3, only the nonlocal conductance correctly measures Δ_{ind} in the bulk of the proximitised system.

3.4. ANDREEV RECTIFIER AT THE TOPOLOGICAL PHASE TRANSITION

3.4.1. ANDREEV RECTIFICATION AS A MEASURE OF THE TOPOLOGICAL PHASE

In order to study nonlocal conductance at the topological phase transition, we apply an in-plane Zeeman field along the x-direction of the proximitised system. Figure 3.7 shows

the nonlocal conductance G_{21} as a function of bias E and Zeeman energy E_Z, for short and intermediate junctions in (a) and (b) with $L = 10\xi$ and $L = 3\xi$, respectively, such that the two normal leads are well decoupled, and the nonlocal conductance is exponentially suppressed at subgap energies. Increasing the magnetic field closes the induced gap and the system is driven into a topological phase. The line cuts of Fig. 3.7(c), taken at the critical magnetic field $E_Z = E_Z^c$, show that at the topological phase transition the nonlocal conductance is a linear function of energy, $G_{21}(E) \propto E$ around $E = 0$. At the topological phase transition, the current $I \propto V^2$ with V the voltage bias, and the system functions as a current rectifier due to crossed Andreev reflection.

This Andreev rectifier manifests due to the topology and symmetry of the proximitised system. The system only has particle-hole symmetry and is therefore in class D [53, 54]. Expanding $G_{21}(E, E_Z) = c_0(E_Z) + c_1(E_Z)E + O(E^2)$ around $E = 0$, the exponential suppression of G_{21} at subgap energies means that the coefficients c_0 and c_1 are exponentially suppressed at magnetic fields before the topological phase transition. In class D systems, if G_{21} is exponentially suppressed at subgap energies, it is guaranteed to remain exponentially suppressed across the topological phase transition [41, 55]. At the critical magnetic field $E_Z = E_Z^c$, $G_{21}(E = 0, E_Z^c) = c_0(E_Z^c)$ is therefore also exponentially suppressed. However, the system is gapless at the topological phase transition, such that G_{21} is generally finite at any nonzero E, and $c_1(E_Z^c)$ thus not exponentially suppressed. At the topological phase transition, we therefore have $G_{21} \propto E$ in the limit $E \to 0$, where higher order contributions are negligible. Consequently, rectifying behavior in the nonlocal conductance is an indication of a topological phase transition. This makes the nonlocal conductance not only a probe of the bulk properties of induced superconductivity as discussed in Sec. 3.3, but also makes it selectively sensitive to topological phase transitions.

The rectifying behavior $G_{21} \propto E$ at the topological phase transition in Fig. 3.7 is grounded in the symmetry classification of the channel. As a result, we expect it to be robust to the presence of onsite disorder, so long as it does not alter the symmetry class. Figure 3.8 shows G_{21} as a function of E and E_Z for systems with the same widths as in Fig. 3.7. In the left column, parameters are chosen identical to those in Fig. 3.7, with the addition of onsite disorder to give an elastic mean free path $l_e = 0.2L$ [52], bringing the systems well into the quasiballistic regime. In the right column of Fig. 3.8, we investigate G_{21} when the central region is in the diffusive limit, with $l_e = 0.2W$. The widths are the same as in the quasiballistic (and clean) case, but μ is increased such that several modes are active. We gate the leads into the single mode regime using quantum point contacts at the junctions with the scattering region. In each case we pick $L \gtrsim \tilde{\xi}$, since in the diffusive limit $\tilde{\xi} = \sqrt{\xi l_e}$ governs the range of the coupling between the two normal terminals at subgap energies [56]. In both quasiballistic and diffusive cases, G_{21} remains an approximately odd function of E around the gap closing, and the proximitised system therefore acts as a rectifier even in the presence of disorder.

3.4.2. DISTINGUISHING THE TOPOLOGICAL PHASE TRANSITION IN SPATIALLY INHOMOGENEOUS DEVICES

Several works [18–23] discuss the emergence of zero-energy modes in the trivial phase of a hybrid semiconductor-superconductor device with an extended, spatially inhomogeneous potential. Local conductance measurements do not distinguish between these

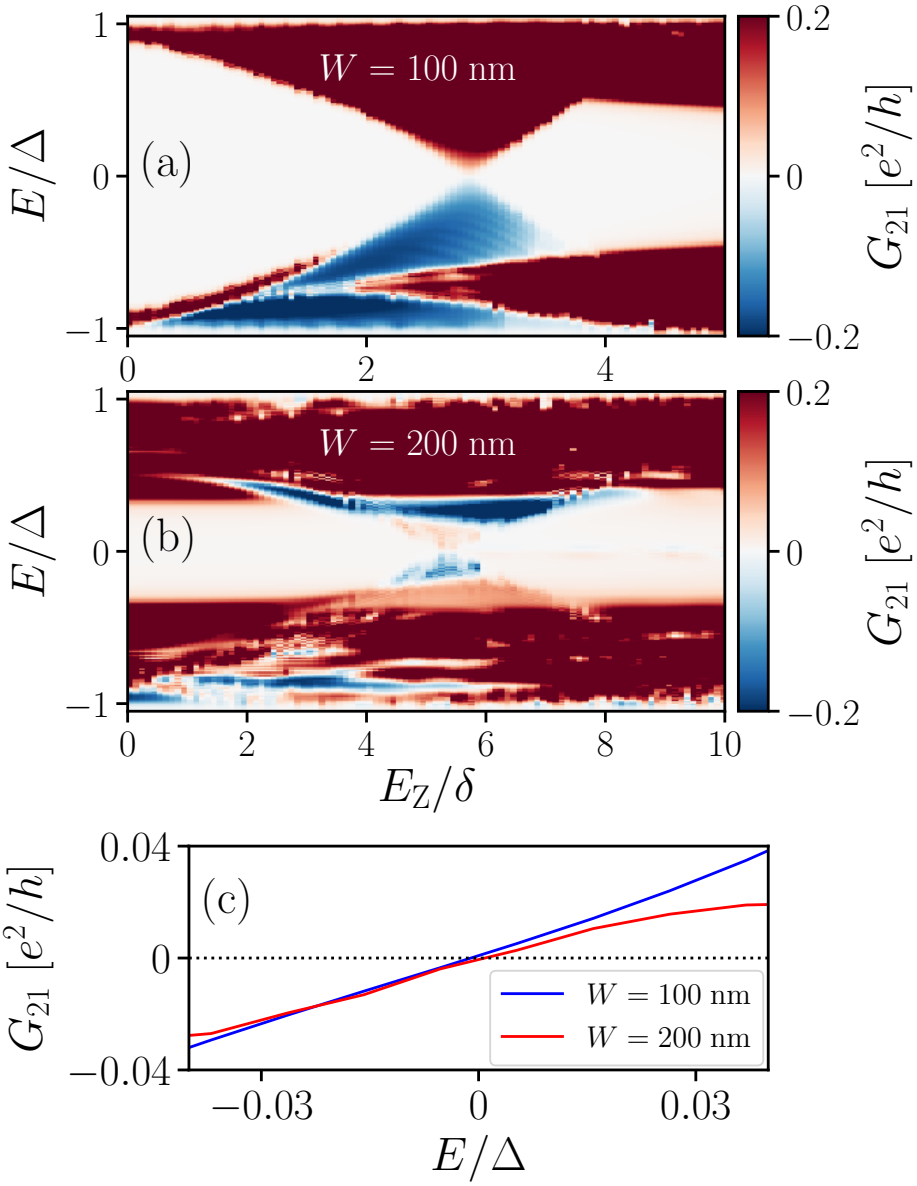

Figure 3.7: (a, b) Nonlocal conductance G_{21} in the single-mode regime as a function of E and E_Z in the absence of disorder. We have $W = 100$ and 200 nm in (a) and (b), respectively. The Zeeman field closes the induced gap and the system undergoes a topological phase transition. At the transition, G_{21} vanishes and changes sign as a function of bias. There are prominent regions where the nonlocal conductance is negative, i.e. where CAR dominates. The color scale is saturated for clarity. (c) Line cuts of G_{21} as a function of bias at the topological phase transition, taken at $E_Z \approx 2.9\delta$ for $W = 100$ nm and $E_Z \approx 5.4\delta$ for $W = 200$ nm, showing that the nonlocal conductance is an approximately odd function of bias.

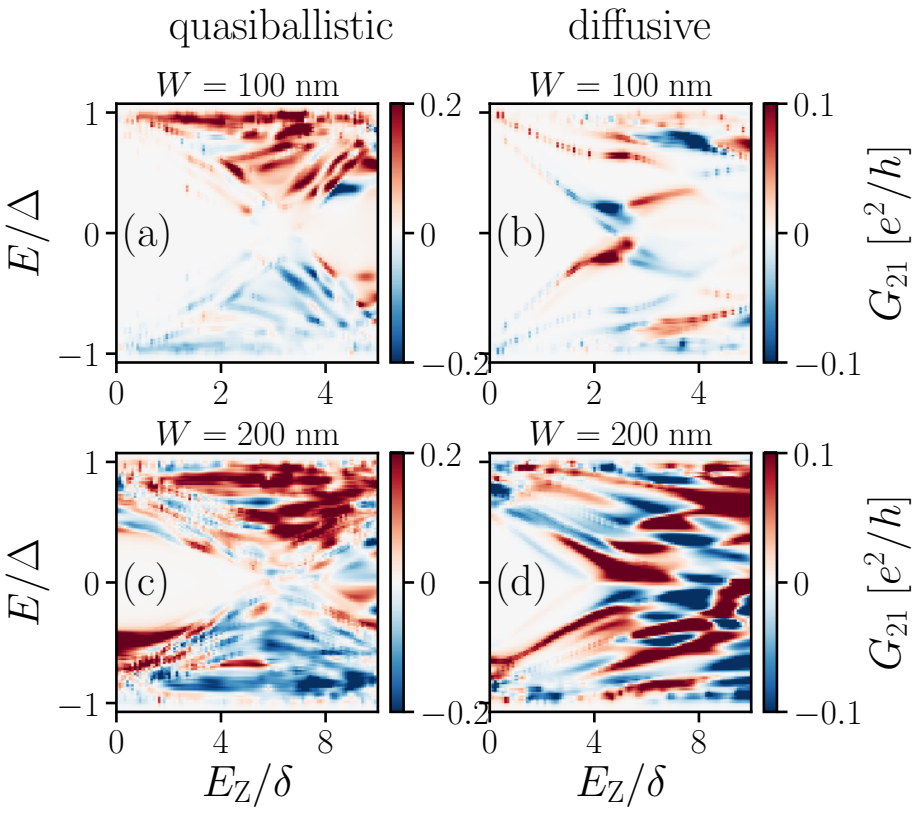

Figure 3.8: The nonlocal conductance G_{21} as a function of E and E_Z for a proximitised system that is quasiballisic (a, c with $\mu = 3$ meV) and diffusive (b, d with $\mu = 16$ meV). For the diffusive junction, the leads are gated into the single-mode regime using quantum point contacts at the junctions with the channel. Top and bottom row present results for $W = 100$ and 200 nm respectively. For the quasiballistic junction, $L/\xi = 8$ and 2 for $W = 100$ nm and 200 nm respectively, and the mean free path is $l_e = 0.2L$ in each case. In the diffusive system, we have $l_e = 0.2W$ and $L/\tilde{\xi} = 5$ and 2 for the widths respectively, where $\tilde{\xi} = \sqrt{l_e \xi}$. The color scale is saturated in both cases for clarity.

modes and well-separated Majorana modes at the endpoints of the proximitised region in the topological phase, since both give rise to zero-bias conductance features.

To study this problem, we include an extended inhomogeneous potential

$$\phi(x,y) = V_0 \exp\left[-\frac{1}{2}\left(\frac{x-x_0}{d_x}\right)^2\right] \exp\left[-\frac{1}{2}\left(\frac{y-y_0}{d_y}\right)^2\right], \tag{3.7}$$

in the setup shown in Fig. 3.2, with V_0 the potential amplitude, x_0 and y_0 the coordinates of the potential center, and d_x and d_y parameters to control the smoothness in x- and y-direction, respectively. We compare conductance for an amplitude $V_0 = -4.5$ mV to conductance in a homogeneous system $V_0 = 0$ V. We calculate the local conductance in the tunneling regime, with tunnel barriers at both wire ends $x = 0$ and $x = L$, and the

nonlocal conductance in the open regime, with the system length fixed to $L = 8\xi$ and the width to $W = 100$ nm.

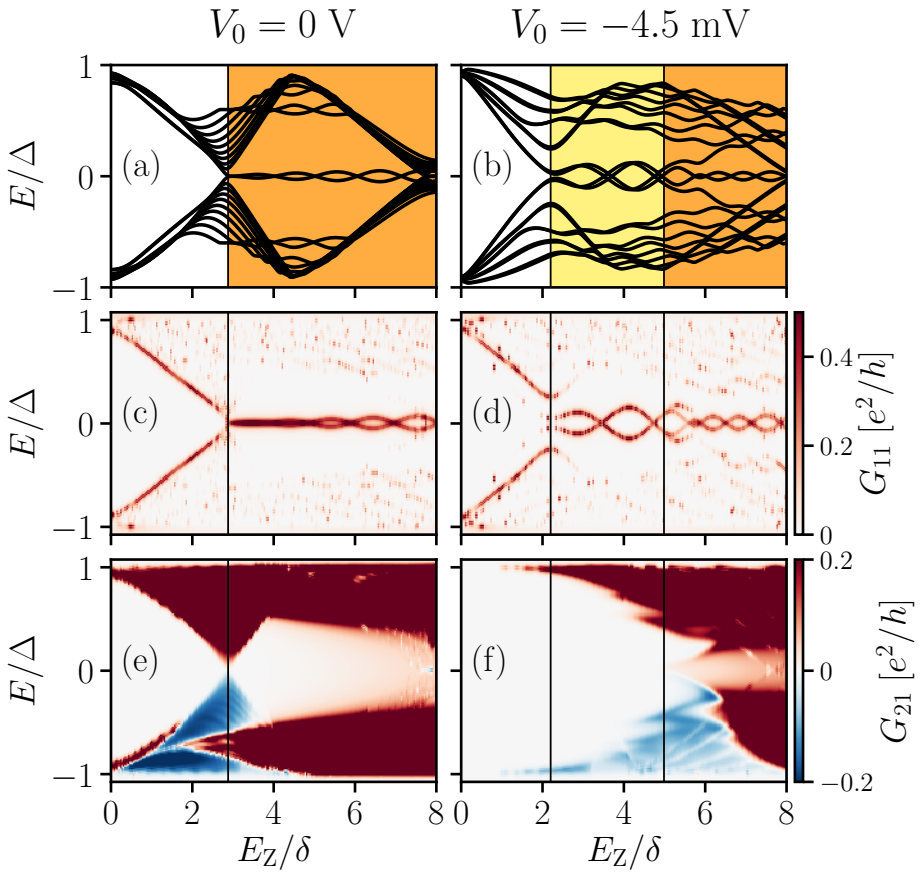

Figure 3.9: Spectrum (a, b), local conductance G_{11} (c, d) and nonlocal conductance G_{21} (e, f) of a system without potential variations (left column) and a system with a long-range Gaussian potential of amplitude $V_0 = -4.5$ mV (right column). The orange region in (a) and (b) denotes the topological phase, yellow the trivial phase with a state around zero energy. G_{11} is calculated in presence of two tunnel barriers at both wire ends, G_{21} in the single mode regime. The color scale is saturated for clarity. For the potential inhomogeneity, we set $V_0 = -4.5$ meV, $x_0 = L/2$, $y_0 = W/2$, $d_x = L/5$ and $d_y = 2W/3$.

To confirm that such a spatially inhomogeneous system can indeed exhibit trivial zero-energy modes, we calculate the low-energy spectrum of our system when decoupled from the leads, forming a closed superconductor-semiconductor system. The phase transition is computed from the absolute value of the determinant of the reflection matrix in the open system at $E = 0$, with $|\det(r)| = 1$ everywhere for $L \gg \xi$, except at the phase transition, where it drops to zero [57]. Figure 3.9(a) shows the spectrum as a function of E_Z in the homogeneous case ($V_0 = 0$), Fig. 3.9(b) for the inhomogeneous case ($V_0 = -4.5$ mV). While in the first case the closing of the induced superconducting gap coincides with the

topological phase transition, in the second case an extended topologically trivial region exists with states around zero energy (yellow region).

Comparing the local conductance with and without an inhomogeneous potential, we find that zero-energy modes appear regardless of whether they are topological or trivial. Panels (c) and (d) of Fig. 3.9 show the local response as a function of bias and Zeeman energy when leads are connected to the central region via tunnel barriers. Since the system is ballistic and long ($L \gg \xi$), the local conductance agrees well with the spectra presented in panels (a) and (b). Accordingly, the local conductance in panel (d) for $V_0 = -4.5$ mV shows zero-energy modes in the topologically trivial regime. Therefore, a gap closing and the emergence of zero-energy modes in the local conductance is not a sufficient sign of a topological phase transition.

On the other hand, nonlocal conductance has a much clearer signature of the topological transition than the local conductance. To demonstrate this, in panels (e) and (f) of Fig. 3.9 we show the nonlocal conductance as a function of bias and Zeeman energy. Both for the homogeneous and the inhomogeous case, the appearance of nonlocal conductance around $E = 0$ coincides with the change of the topological invariant. In other words, the appearance of finite nonlocal conductance around $E = 0$ implies a global closing of the induced gap. Additionally, the nonlocal conductance shows rectifying behavior around $E = 0$ at the gap closing. These two features of the nonlocal conductance are strong evidence of a topological phase transition. Therefore, due to its insensitivity to spatial inhomogeneities in the potential and the additional feature of Andreev rectification, nonlocal conductance is a more reliable measure of a topological phase transition.

3.5. COOPER PAIR SPLITTER

A negative nonlocal conductance, dominated by CAR, is of fundamental interest, since the proximitised system then functions as a Cooper pair splitter [38–40, 58, 59]. In Sec. 3.3, we observed that the nonlocal conductance in clean systems at zero magnetic field is generally positive, and a CAR-dominated signal ($G_{21} < 0$) is rare. The reason for this is shown schematically in Fig. 3.10: an electron entering the proximitised region usually converts into an electron-like quasiparticle. Andreev reflection changes both the quasiparticle charge and velocity, so that the resulting hole-like quasiparticle returns to the source. Therefore under normal circumstances Andreev reflection alone is insufficient to generate a negative nonlocal current.

Despite G_{21} stays predominantly positive in clean systems, in Sec. 3.4 we found that a magnetic field can make the nonlocal conductance negative in large regions of parameter space. We identify these regions with the presence of only hole-like bands in the proximitized region at the relevant energy, as shown in Fig. 3.10. If only hole-like states are present in the proximitized region, the incoming electron may only convert into a right-moving hole-like quasiparticle, which in turn converts predominantly into a hole when exiting the proximitized region. To confirm this argument, we compare the energy ranges where only hole-like quasiparticles are present with the regions of negative G_{21}. Our results are shown in Fig. 3.11, and they exhibit a very good agreement. Since the only required property to get a negative nonlocal conductance is a hole-like dispersion relation, this phenomenon does not require SOI, or even Zeeman field. Indeed, our calculations (not shown here) reveal that it is possible to extend the energy ranges

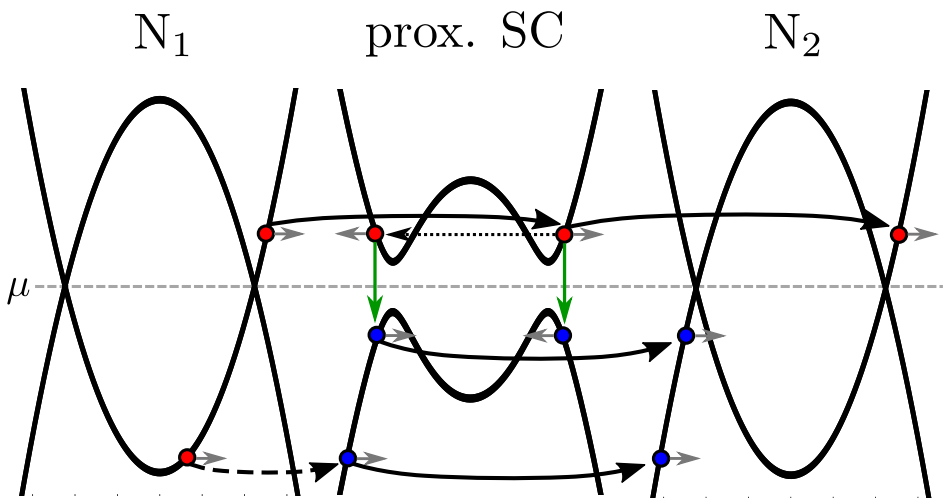

Figure 3.10: Schematic of the quasiparticle transport properties from the normal lead N_1, to the lead N_2 through the proximitised region. Quasiparticles transferring to a neighboring region (solid black arrows) predominantly preserve the quasiparticle type: electron-like (red dots) or hole-like (blue dots). Andreev reflection (green vertical arrows) changes the quasiparticle type, and the direction of propagation (grey arrows). Disorder scattering (black dotted arrow) changes the propagation direction. Finally, if no quasiparticles of the same type are available, quasiparticle transmission between regions may also result in the change of the quasiparticle type (black dashed arrow).

over which CAR dominates by filtering the nonlocal conductance by spin, e.g. by using magnetically-polarized contacts [27].

It is possible to systematically obtain a negative nonlocal conductance in the low-doping regime without using a Zeeman field if $\Delta > \Delta_{\text{ind}}$. This is shown in Fig. 3.11(c) and (d), where we have also neglected SOI for simplicity. By choosing μ comparable to the band offset of the lowest mode in the proximitised channel, at negative energies we obtain an energy range in which the band structure is only hole-like [Fig. 3.11(c)]. However, the small μ implies that no electron modes are active in the normal leads in this energy range. To observe negative nonlocal conductance here, it is therefore necessary to have a larger chemical potential in the normal leads than in the proximitised region, which ensures the presence of propagating electron modes at the relevant energies. Doing so, we indeed observe a negative nonlocal conductance in the expected energy range of Fig. 3.11(d).

Disorder provides an alternative mechanism to obtain negative nonlocal conductance. Unlike direct electron transfer, which generally conserves the sign of quasiparticle momentum, CAR often requires a sign change of the quasiparticle momentum. Since disorder breaks momentum conservation, the probabilities of CAR and direct electron transfer become comparable once the system length exceeds the mean free path, and CAR thus more prominent than in a clean system. Indeed, as shown in Fig. 3.8, in disordered systems the nonlocal conductance becomes positive or negative with approximately equal probability.

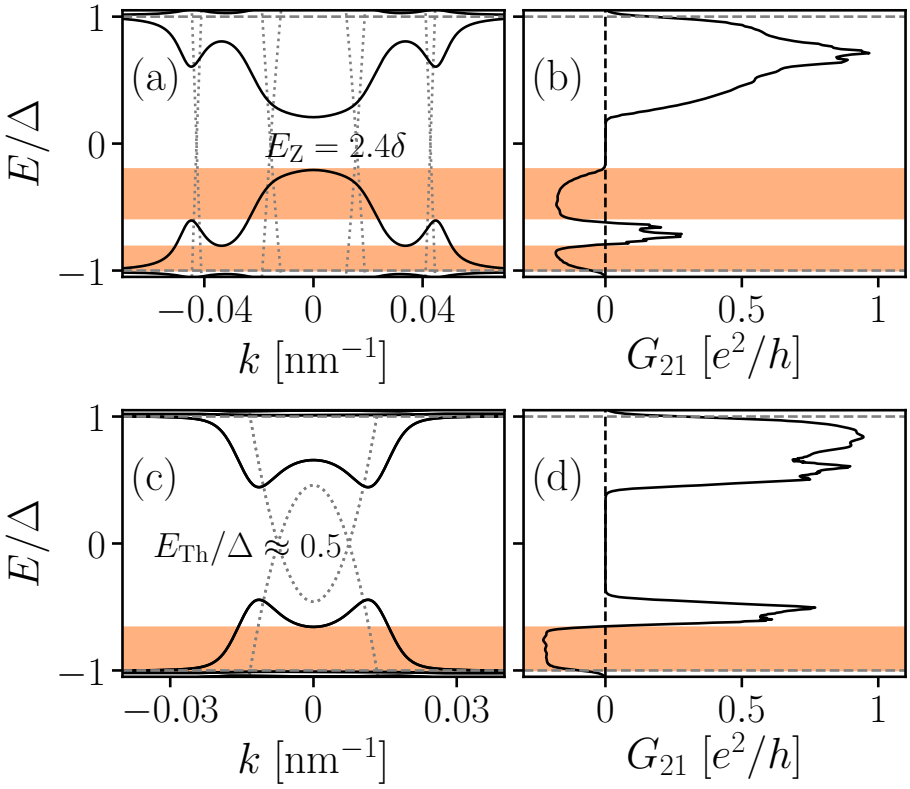

Figure 3.11: Dispersions (left column) and nonlocal conductance with $L \gg \xi$ (right column) of proximitised channels of width $W = 100$ nm (a, b) and $W = 200$ nm (c, d). Dotted lines show the electron and hole dispersions of the channels with the superconductor removed. In both cases, the induced gap is smaller than Δ, due to a Zeeman field in (a), and due to $E_{Th} \lesssim \Delta$ in (c). There are energy ranges in which only hole-like bands are present, and these correspond to regions of negative G_{21}. Here, (c) is in a low-doping regime $\mu = 0.5$ meV, such that electron modes are absent for $E/\Delta \lesssim -0.5$, producing the hole-like dispersion. As a result, a larger chemical potential $\mu = 0.8$ meV is needed in the normal leads to observe $G_{21} < 0$ at the corresponding energies in (d). In (a) and (b), we have $\mu = 3$ meV.

3.6. SUMMARY AND OUTLOOK

The standard experimental tool for probing induced superconductivity in a Majorana device is a tunnelling conductance measurement using an attached normal lead. While this approach detects the density of states, its usefulness is limited because it cannot distinguish the properties in close vicinity of the lead from the properties of the bulk system. We studied how the *nonlocal* conductance between two spatially separated normal leads attached to the proximitised region overcomes this limitation. We find that the nonlocal conductance is selectively sensitive to the bulk properties of a proximity superconductor, and allows to directly measure the induced and the bulk superconducting gaps as well as the induced coherence length of the proximitised region. While we focused on the quasi 1D-systems suitable for the creation of Majorana states, our conclusions are applicable to

general proximity superconductors, including 2D materials like graphene covered by a bulk superconductor.

When the probability of CAR is larger than that of electron transmission, the nonlocal conductance turns negative. While this does not happen normally, we identified conditions that allow CAR to dominate. This may happen due to disorder, which breaks the relation between quasiparticle charge, velocity and momentum and makes the nonlocal conductance zero on average. We identified another, systematic way of obtaining dominant CAR by ensuring that the only available states in the proximitised region are hole-like. A special case of this behaviour is the vicinity of the topological phase transition, where the nonlocal conductance becomes proportional to voltage, resulting in a linear relation between the differential conductance and voltage, or in other words a positive nonlocal current regardless of the sign of the voltage. This behavior is specific to

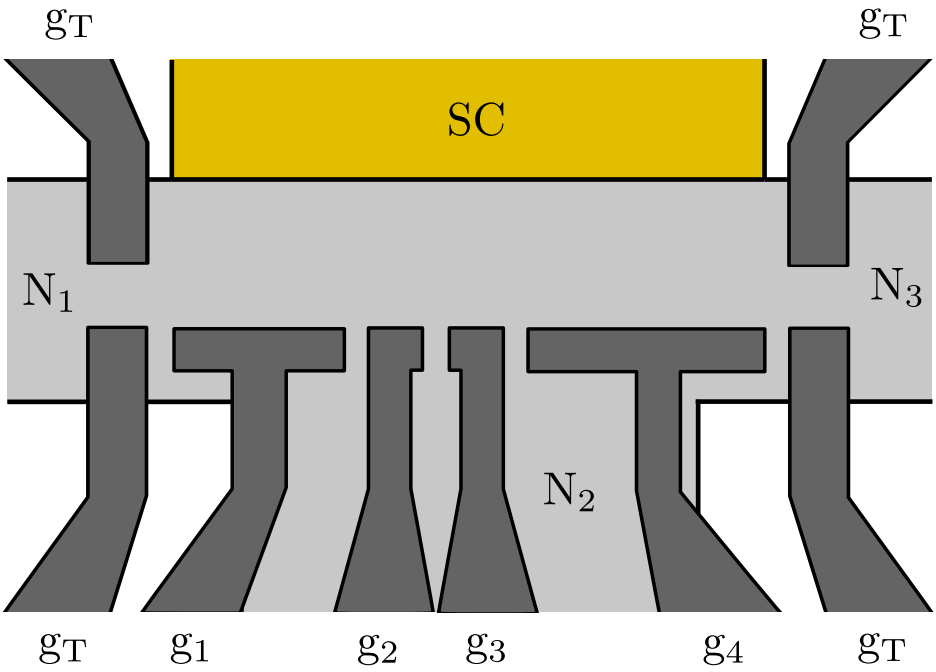

Figure 3.12: A possible experimental realization of a multiterminal proximitized device suited for nonlocal conductance measurements. Electrostatic gates g_i, $i \in \{1,2,3,4\}$, pattern out a quasi-one dimensional region in a two-dimensional electron gas, which is proximitised from the side by a superconductor. Gates g_T create tunnel barriers at the endpoints of the proximised region. Changing the potentials applied to the gates allows for changing the effective device length.

topological phase transitions, and we showed how it can be used to distinguish accidental low energy states from Majorana states, resolving a potential shortcoming of Majorana tunneling experiments identified in Refs. [19–23].

Our setup can be used with trivial adjustments to probe the properties of Josephson junctions, proposed as a promising alternative platform for the creation of Majorana states [53, 54]. Further work could investigate interaction effects on the the nonlocal

response [60]. An alternative promising avenue of follow-up work is to consider a multiterminal generalization of a nonlocal setup in order to combine local and global sensitivity within the same device. In Fig. 3.12 we show a possible experimental realization of such a multiterminal device, where the effective length can be adjusted with gates. Finally, our results regarding control of the CAR dominance can be used to design devices with a large electron-hole conversion efficiency.

3.7. APPENDIX

3.7.1. SHORT, INTERMEDIATE AND LONG JUNCTION LIMITS FOR HYBRID STRUCTURES

In this appendix, we briefly discuss the subgap spectral characteristics of normal-superconductor junctions in different limits, using heuristic arguments to highlight the essential physics. For a more rigorous study, we refer the interested reader to e.g. Refs. [61–65]. Consider a quasi-one dimensional channel of length $L \to \infty$ that consists of a junction between a normal part of width W and a superconductor of width $W_{sc} \gg W$. The Hamiltonian is the same as in Eq. (3.1), but with $p_x \to \hbar k$ and as before $\Delta \neq 0$ only in the superconductor. Furthermore, we consider only $E_Z = 0$ and neglect SOI ($\alpha = 0$) and disorder for simplicity.

The hybrid structure generally has an energy gap Δ_{ind}, the size of which is determined by two competing energy scales, namely the bulk gap Δ and the Thouless energy $E_{Th} \approx \hbar/\tau$, with τ the quasiparticle dwell time in the normal part of the junction. A short junction has $\Delta \ll E_{Th}$ and a long junction $\Delta \gg E_{Th}$, while $\Delta \gtrsim E_{Th}$ for an intermediate junction. Alternatively, these conditions are expressed in terms of W and the BCS coherence length $\xi_0 = \hbar v_F/\Delta$, where v_F is the Fermi velocity. For a quasiparticle incident perpendicularly from the normal part to the interface with the superconductor and assuming perfect interface transparency, we have $\tau \propto W/v_F$ and thus $E_{Th} \propto \hbar v_F/W$. The conditions for short, intermediate and long junctions then become $W \ll \xi_0$, $W \gtrsim \xi_0$ and $W \gg \xi_0$, respectively. In the short junction limit, we have $\Delta_{ind} \approx \Delta$, while for long and intermediate junctions $\Delta_{ind} \propto E_{Th}$.

We now derive a lower bound for E_{Th} in terms of the level spacing δ in the normal part of the junction. A quasiparticle exiting the superconductor has the dwell time $\tau \propto 2W/\gamma v_\perp(k)$ in the normal part. Here, $v_\perp(k) = \hbar k_\perp(k)/m^*$ and $k_\perp = \sqrt{k_F^2 - k^2}$ are respectively the velocity and momentum projections perpendicular to the interface with the superconductor at the parallel momentum k, with k_F the Fermi momentum, and $2W$ is the distance the quasiparticle travels before colliding with the superconductor again. The dwell time scales inversely with the transparency γ of the interface between the normal part and the superconductor. In practice, the transparency is determined by interface properties, such as the presence of a barrier or velocity mismatch, which we parametrize with $0 \leq \gamma \leq 1$ for simplicity. We thus obtain $E_{Th}(k) \propto \gamma\hbar^2\sqrt{k_F^2 - k^2}/2m^*W$. Observe that E_{Th} decreases with k and tends to vanish as $k \to k_F$ since then $v_\perp \to 0$. However, $v_\perp$ is bounded from below in a finite geometry by the momentum uncertainty associated with the band offset, which corresponds to the velocity $\mathrm{d}v_\perp \approx \hbar\pi/m^*W$ in a square-well approximation. Using $v_\perp = \mathrm{d}v_\perp$ gives the lower bound for the Thouless energy $E_{Th} \propto \gamma\hbar^2\pi/2m^*W^2$. The preceding discussion implies that in the absence of

magnetic fields, the gap in the spectrum of such a junction decreases with momentum to a minimum $\propto 1/m^* W^2$ at $k = k_F$ [see left column Fig. 3.13]. Since Δ_{ind} is the energy of the lowest Andreev bound state in the junction, we define

$$E_{\text{Th}} = \gamma\delta, \quad \delta = \frac{\hbar^2\pi^2}{2m^*(2W)^2} \tag{3.8}$$

as the Thouless energy of the junction. Observe that we use $2W$ in the denominator, since that is the distance normal to the interface a quasiparticle travels between successive Andreev reflections [44].

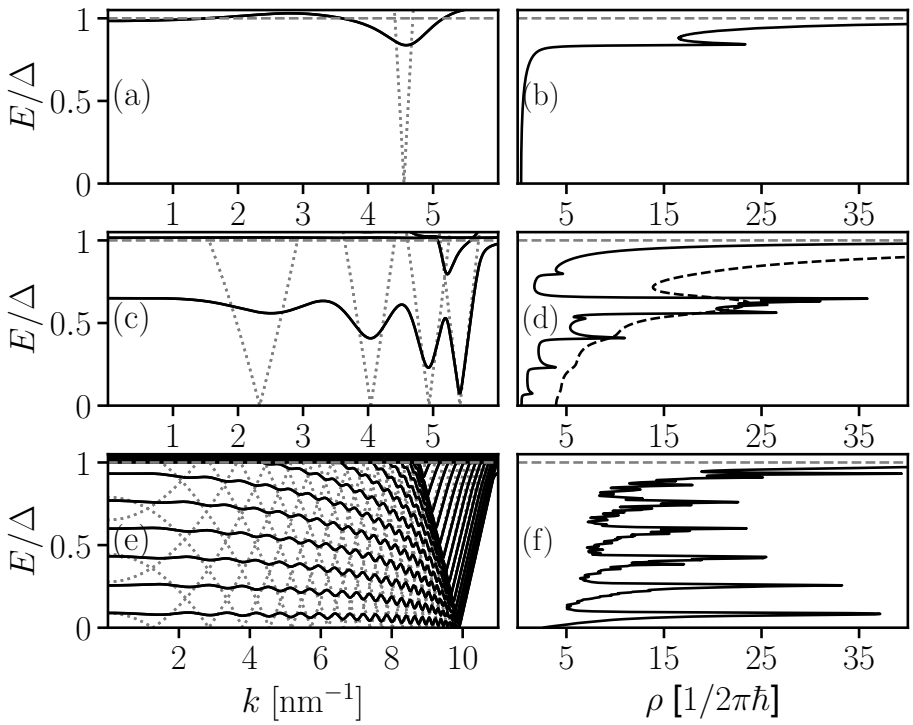

Figure 3.13: Dispersion (left column) and density of states (right column) of a quasi one-dimensional normal-superconductor junction in different regimes: a short junction (top), an intermediate junction (middle) and a long junction (bottom). In the left column, the dotted curves show the electron and hole dispersions of the corresponding normal channel with the superconductor removed. In all cases, a small broadening $\Gamma \ll \Delta$ has been added to the density of states. For the intermediate junction (d), the density of states with larger broadening is also shown (dashed curve). The curves are symmetric under $(k, E) \to (\pm k, \pm E)$.

The spectral characteristics of a proximitised system strongly depend on which regime the system is in. Figure 3.13 shows the dispersion $\epsilon_n(k)$ and density of states ρ per unit length for junctions in the short, intermediate and long regimes. The density of states is given by

$$\rho(E) = \frac{1}{2\pi\hbar}\sum_n \int \delta\left[E - \epsilon_n(k)\right] \frac{\mathrm{d}E}{|v(E)|} = \frac{1}{2\pi\hbar}\sum_n \left|\frac{\mathrm{d}\epsilon_n(k)}{\mathrm{d}k}\right|^{-1}. \tag{3.9}$$

Here, n is the subband index including spin and we have used $\hbar v = \mathrm{d}E/\mathrm{d}k$ for the velocity v. In the left column, the solid lines give the dispersion of the hybrid structure, while the dotted lines show the electron and hole dispersions of the normal channel only (with $W_{\mathrm{sc}} = 0$ or $\gamma = 0$). In all cases, $\mu \gg \Delta$, and ρ has been broadened by convolution with a Lorentzian of full width at half maximum $\Gamma \ll \Delta$. For the short junction, we indeed have $\Delta_{\mathrm{ind}} \approx \Delta$, which manifests as an essentially hard superconducting gap for $|E| < \Delta_{\mathrm{ind}}$. We have verified that ρ vanishes identically in this regime with $\Gamma \to 0$. In the intermediate and long regimes, subgap states exist at energies smaller than Δ, which manifests as a nonzero subgap ρ (soft gap). The difference between the two regimes is the number of these states: in an intermediate junction, they are few, but multiple in the long junction limit, as the conditions $\Delta \gtrsim E_{\mathrm{Th}}$ and $\Delta \gg E_{\mathrm{Th}}$ indicate. Observe that in both cases, the subgap bands are flat around $k = 0$ and drop towards a minimum in energy as k increases before rising sharply again [66]. Superimposed on this are intraband oscillations that happen on a smaller energy scale. In principle, oscillations thus manifest in ρ on two energy scales: the larger energy scale is the interband spacing around $k = 0$ ($\propto 1/W^2$), and the smaller the scale of intraband oscillations. Overall, the former has a larger contribution to ρ due to the small curvature in the dispersion. Oscillations on both scales are clearly visible for the intermediate junction. However, increasing Γ further (dashed curve) washes out the fine structure due to intraband oscillations. As a result, ρ gradually increases towards a maximum, when E aligns with the energy of the subgap state around $k = 0$. On the other hand, in the long junction there are multiple states at subgap energies, and the most prominent feature in ρ is the peaks associated with the flat parts of those bands. The fine structure due to intraband oscillations is superimposed, but masked by the broadening.

REFERENCES

[1] P. G. De Gennes, *Boundary effects in superconductors,* Rev. Mod. Phys. **36**, 225 (1964).

[2] G. E. Blonder, M. Tinkham, and T. M. Klapwijk, *Transition from metallic to tunneling regimes in superconducting microconstrictions: Excess current, charge imbalance, and supercurrent conversion,* Phys. Rev. B **25**, 4515 (1982).

[3] T. Tokuyasu, J. A. Sauls, and D. Rainer, *Proximity effect of a ferromagnetic insulator in contact with a superconductor,* Phys. Rev. B **38**, 8823 (1988).

[4] E. A. Demler, G. B. Arnold, and M. R. Beasley, *Superconducting proximity effects in magnetic metals,* Phys. Rev. B **55**, 15174 (1997).

[5] E. C. Gingrich, B. M. Niedzielski, J. A. Glick, Y. Wang, D. L. Miller, R. Loloee, W. P. Pratt Jr, and N. O. Birge, *Controllable 0-[pi] josephson junctions containing a ferromagnetic spin valve,* Nat Phys **12**, 564 (2016).

[6] M. Titov and C. W. J. Beenakker, *Josephson effect in ballistic graphene,* Phys. Rev. B **74**, 041401 (2006).

[7] H. B. Heersche, P. Jarillo-Herrero, J. B. Oostinga, L. M. K. Vandersypen, and A. F. Morpurgo, *Bipolar supercurrent in graphene,* Nature **446**, 56 (2007).

[8] V. E. Calado, S. Goswami, G. Nanda, M. Diez, A. R. Akhmerov, K. Watanabe, T. Taniguchi, T. M. Klapwijk, and L. M. K. Vandersypen, *Ballistic josephson junctions in edge-contacted graphene,* Nat. Nano. **10**, 761 (2015).

[9] J. Alicea, *New directions in the pursuit of majorana fermions in solid state systems,* Rep. Prog. Phys. **75**, 076501 (2012).

[10] M. Leijnse and K. Flensberg, *Introduction to topological superconductivity and majorana fermions,* Semiconductor Science and Technology **27**, 124003 (2012).

[11] C. Beenakker, *Search for majorana fermions in superconductors,* Annu. Rev. Condens. Matter Phys. **4**, 113 (2013).

[12] S. B. Bravyi and A. Y. Kitaev, *Fermionic quantum computation,* Annals of Physics **298**, 210 (2002).

[13] V. Mourik, K. Zuo, S. M. Frolov, S. R. Plissard, E. P. A. M. Bakkers, and L. P. Kouwenhoven, *Signatures of majorana fermions in hybrid superconductor-semiconductor nanowire devices,* Science **336**, 1003 (2012).

[14] A. Das, Y. Ronen, Y. Most, Y. Oreg, M. Heiblum, and H. Shtrikman, *Zero-bias peaks and splitting in an al-inas nanowire topological superconductor as a signature of majorana fermions,* Nat Phys **8**, 887 (2012).

[15] M. T. Deng, C. L. Yu, G. Y. Huang, M. Larsson, P. Caroff, and H. Q. Xu, *Anomalous zero-bias conductance peak in a nb–insb nanowire–nb hybrid device,* Nano Letters **12**, 6414 (2012).

[16] T. M. Klapwijk, *Proximity effect from an andreev perspective,* Journal of Superconductivity **17**, 593 (2004).

[17] S. Guéron, H. Pothier, N. O. Birge, D. Esteve, and M. H. Devoret, *Superconducting proximity effect probed on a mesoscopic length scale,* Phys. Rev. Lett. **77**, 3025 (1996).

[18] D. I. Pikulin and Y. V. Nazarov, *Topological properties of superconducting junctions,* JETP Letters **94**, 693 (2012).

[19] G. Kells, D. Meidan, and P. W. Brouwer, *Near-zero-energy end states in topologically trivial spin-orbit coupled superconducting nanowires with a smooth confinement,* Phys. Rev. B **86**, 100503 (2012).

[20] S. Mi, D. I. Pikulin, M. Marciani, and C. W. J. Beenakker, *X-shaped and y-shaped andreev resonance profiles in a superconducting quantum dot,* Journal of Experimental and Theoretical Physics **119**, 1018 (2014).

[21] E. Prada, P. San-Jose, and R. Aguado, *Transport spectroscopy of ns nanowire junctions with majorana fermions,* Phys. Rev. B **86**, 180503 (2012).

[22] C. Moore, T. D. Stanescu, and S. Tewari, *Majorana bound states in non-homogeneous semiconductor nanowires,* ArXiv e-prints (2016), arXiv:1611.07058 [cond-mat.mes-hall] .

[23] C.-X. Liu, J. D. Sau, T. D. Stanescu, and S. Das Sarma, *Andreev bound states versus majorana bound states in quantum dot-nanowire-superconductor hybrid structures: Trivial versus topological zero-bias conductance peaks,* Phys. Rev. B **96**, 075161 (2017).

[24] J. M. Byers and M. E. Flatté, *Probing spatial correlations with nanoscale two-contact tunneling,* Phys. Rev. Lett. **74**, 306 (1995).

[25] S. Russo, M. Kroug, T. M. Klapwijk, and A. F. Morpurgo, *Experimental observation of bias-dependent nonlocal andreev reflection,* Phys. Rev. Lett. **95**, 027002 (2005).

[26] R. W. Reinthaler, P. Recher, and E. M. Hankiewicz, *Proposal for an all-electrical detection of crossed andreev reflection in topological insulators,* Phys. Rev. Lett. **110**, 226802 (2013).

[27] Falci, G., Feinberg, D., and Hekking, F. W. J., *Correlated tunneling into a superconductor in a multiprobe hybrid structure,* Europhys. Lett. **54**, 255 (2001).

[28] R. Mélin and D. Feinberg, *Transport theory of multiterminal hybrid structures,* The European Physical Journal B - Condensed Matter and Complex Systems **26**, 101 (2002).

[29] D. Beckmann, H. B. Weber, and H. v. Löhneysen, *Evidence for crossed andreev reflection in superconductor-ferromagnet hybrid structures,* Phys. Rev. Lett. **93**, 197003 (2004).

[30] J. Brauer, F. Hübler, M. Smetanin, D. Beckmann, and H. v. Löhneysen, *Nonlocal transport in normal-metal/superconductor hybrid structures: Role of interference and interaction,* Phys. Rev. B **81**, 024515 (2010).

[31] J. Schindele, A. Baumgartner, R. Maurand, M. Weiss, and C. Schönenberger, *Nonlocal spectroscopy of andreev bound states,* Phys. Rev. B **89**, 045422 (2014).

[32] P. Recher, E. V. Sukhorukov, and D. Loss, *Andreev tunneling, coulomb blockade, and resonant transport of nonlocal spin-entangled electrons,* Phys. Rev. B **63**, 165314 (2001).

[33] J. P. Morten, A. Brataas, and W. Belzig, *Circuit theory of crossed andreev reflection,* Phys. Rev. B **74**, 214510 (2006).

[34] H. Haugen, D. Huertas-Hernando, A. Brataas, and X. Waintal, *Crossed andreev reflection versus electron transfer in three-terminal graphene devices,* Phys. Rev. B **81**, 174523 (2010).

[35] F. Crépin, P. Burset, and B. Trauzettel, *Odd-frequency triplet superconductivity at the helical edge of a topological insulator,* Phys. Rev. B **92**, 100507 (2015).

[36] Y.-T. Zhang, Z. Hou, X. C. Xie, and Q.-F. Sun, *Quantum perfect crossed andreev reflection in top-gated quantum anomalous hall insulator–superconductor junctions,* Phys. Rev. B **95**, 245433 (2017).

[37] J. Liu, J. Song, Q.-F. Sun, and X. C. Xie, *Even-odd interference effect in a topological superconducting wire,* Phys. Rev. B **96**, 195307 (2017).

[38] G. Deutscher and D. Feinberg, *Coupling superconducting-ferromagnetic point contacts by andreev reflections,* Applied Physics Letters **76**, 487 (2000).

[39] L. Hofstetter, S. Csonka, J. Nygard, and C. Schonenberger, *Cooper pair splitter realized in a two-quantum-dot y-junction,* Nature **461**, 960 (2009).

[40] L. G. Herrmann, F. Portier, P. Roche, A. L. Yeyati, T. Kontos, and C. Strunk, *Carbon nanotubes as cooper-pair beam splitters,* Phys. Rev. Lett. **104**, 026801 (2010).

[41] A. R. Akhmerov, J. P. Dahlhaus, F. Hassler, M. Wimmer, and C. W. J. Beenakker, *Quantized conductance at the majorana phase transition in a disordered superconducting wire,* Phys. Rev. Lett. **106**, 057001 (2011).

[42] B. M. Fregoso, A. M. Lobos, and S. Das Sarma, *Electrical detection of topological quantum phase transitions in disordered majorana nanowires,* Phys. Rev. B **88**, 180507 (2013).

[43] P. Szumniak, D. Chevallier, D. Loss, and J. Klinovaja, *Spin and charge signatures of topological superconductivity in rashba nanowires,* Phys. Rev. B **96**, 041401 (2017).

[44] D. Sticlet, B. Nijholt, and A. Akhmerov, *Robustness of majorana bound states in the short-junction limit,* Phys. Rev. B **95**, 115421 (2017).

[45] M. Kjaergaard, F. Nichele, H. J. Suominen, M. P. Nowak, M. Wimmer, A. R. Akhmerov, J. A. Folk, K. Flensberg, J. Shabani, C. J. Palmstrøm, and C. M. Marcus, *Quantized conductance doubling and hard gap in a two-dimensional semiconductor–superconductor heterostructure,* Nature Communications **7**, 12841 EP (2016).

[46] H. Zhang, Ö. Gül, S. Conesa-Boj, M. Nowak, M. Wimmer, K. Zuo, V. Mourik, F. K. de Vries, J. van Veen, M. W. A. de Moor, J. D. S. Bommer, D. J. van Woerkom, D. Car, S. R. Plissard, E. P. A. M. Bakkers, M. Quintero-Pérez, M. C. Cassidy, S. Koelling, S. Goswami, K. Watanabe, T. Taniguchi, and L. P. Kouwenhoven, *Ballistic superconductivity in semiconductor nanowires,* **8**, 16025 EP (2017).

[47] M. P. Anantram and S. Datta, *Current fluctuations in mesoscopic systems with andreev scattering,* Phys. Rev. B **53**, 16390 (1996).

[48] C. W. Groth, M. Wimmer, A. R. Akhmerov, and X. Waintal, *Kwant: a software package for quantum transport,* New Journal of Physics **16**, 063065 (2014).

[49] See supplementary files available with this manuscript.

[50] T. O. Rosdahl, A. Vuik, M. Kjaergaard, and A. R. Akhmerov, *The Andreev rectifier: a nonlocal conductance signature of topological phase transitions,* (2017).

[51] B. Nijholt and A. R. Akhmerov, *Orbital effect of magnetic field on the majorana phase diagram,* Phys. Rev. B **93**, 235434 (2016).

[52] T. Ando, *Quantum point contacts in magnetic fields,* Phys. Rev. B **44**, 8017 (1991).

[53] M. Hell, M. Leijnse, and K. Flensberg, *Two-dimensional platform for networks of majorana bound states,* Phys. Rev. Lett. **118**, 107701 (2017).

[54] F. Pientka, A. Keselman, E. Berg, A. Yacoby, A. Stern, and B. I. Halperin, *Topological superconductivity in a planar josephson junction,* Phys. Rev. X **7**, 021032 (2017).

[55] B. J. Wieder, F. Zhang, and C. L. Kane, *Signatures of majorana fermions in topological insulator josephson junction devices,* Phys. Rev. B **89**, 075106 (2014).

[56] Feinberg, D., *Andreev scattering and cotunneling between two superconductor-normal metal interfaces: the dirty limit,* Eur. Phys. J. B **36**, 419 (2003).

[57] I. C. Fulga, F. Hassler, A. R. Akhmerov, and C. W. J. Beenakker, *Scattering formula for the topological quantum number of a disordered multimode wire,* Phys. Rev. B **83**, 155429 (2011).

[58] J. J. He, J. Wu, T.-P. Choy, X.-J. Liu, Y. Tanaka, and K. T. Law, *Correlated spin currents generated by resonant-crossed andreev reflections in topological superconductors,* **5**, 3232 EP (2014).

[59] W. Chen, D. N. Shi, and D. Y. Xing, *Long-range cooper pair splitter with high entanglement production rate,* **5**, 7607 EP (2015).

[60] D. Aasen, S.-P. Lee, T. Karzig, and J. Alicea, *Interaction effects in superconductor/quantum spin hall devices: Universal transport signatures and fractional coulomb blockade,* Phys. Rev. B **94**, 165113 (2016).

[61] C. W. J. Beenakker, *Three "universal" mesoscopic josephson effects,* in *Transport Phenomena in Mesoscopic Systems: Proceedings of the 14th Taniguchi Symposium, Shima, Japan, November 10–14, 1991*, edited by H. Fukuyama and T. Ando (Springer Berlin Heidelberg, Berlin, Heidelberg, 1992) pp. 235–253.

[62] A. Volkov, P. Magnée, B. van Wees, and T. Klapwijk, *Proximity and josephson effects in superconductor-two-dimensional electron gas planar junctions,* Physica C: Superconductivity **242**, 261 (1995).

[63] S. Pilgram, W. Belzig, and C. Bruder, *Excitation spectrum of mesoscopic proximity structures,* Phys. Rev. B **62**, 12462 (2000).

[64] G. Tkachov, *Nonmetallic thermal transport in low-dimensional proximity structures with partially preserved time-reversal symmetry in a magnetic field,* Physica C: Superconductivity **417**, 127 (2005).

[65] C. R. Reeg and D. L. Maslov, *Hard gap in a normal layer coupled to a superconductor,* Phys. Rev. B **94**, 020501 (2016).

[66] M. Titov, A. Ossipov, and C. W. J. Beenakker, *Excitation gap of a graphene channel with superconducting boundaries,* Phys. Rev. B **75**, 045417 (2007).

4

General approach to boundary conditions and spectra of continuum Hamiltonians: matching to tight binding edges

4.1. INTRODUCTION

Edges of materials can exhibit fascinating physics, and may furthermore strongly affect the electronic properties of materials. In graphene for example, zigzag and armchair edges have widely different character, with the former hosting a flat band of edge states but the latter not [1]. In recent years, edges have been in the spotlight for researchers in the context of topological materials [2–4]. Bulk-boundary correspondence dictates that topological edge states manifest at the boundaries of a material in a topologically nontrivial phase [5]. These edge states are robust to perturbations that do not alter the topological classification of the bulk material, or, if present, break symmetries protecting the topological phase, which makes topological edge states attractive for applications in e.g. spintronics and quantum computing [6–8].

Analysis of materials and their edges is often done using either tight binding or continuum Hamiltonians. A continuum Hamiltonian is a polynomial approximation in momenta valid near a high symmetry point of the Brillouin zone, tailored to accurately capture the low-energy excitations at small momenta near the high symmetry point. Continuum models thus usually present a more compact and intuitive physical picture of electronic dispersion than tight binding models, and are sometimes solvable analytically. Indeed, it is possible to describe all single-particle topologically nontrivial phases using continuum Dirac Hamiltonians [9, 10]. In principle, it is trivial to map a continuum model to a lattice model using finite difference methods, but in practice this is not always feasible, because it can lead to the appearance of spurious, unphysical solutions, for example in the doubling of a single time-reversal invariant Dirac cone that is discretized on a lattice [2, 11]. It can be advantageous to use continuum models to simulate confinements such as nanoribbons, because the size of the Hamiltonian does not scale up with the dimensions of the confinement, in contrast with lattice Hamiltonians, which grow with the number of sites.

In order to use a continuum Hamiltonian to model a bounded system, it is necessary to supplement the Hamiltonian with boundary conditions. The most well-known boundary conditions are arguably hard-wall, or Dirichlet type, which force the wave function to vanish at the edge. However, they are not the only conceivable boundary conditions [12–16], and depending e.g. on the underlying lattice or the specifics of the confinement, more complex boundary conditions mixing wave function amplitudes and derivatives may be necessary [17–23], which can make an exact analytical solution difficult to obtain. Although the edge of a topologically nontrivial bulk hosts protected edge states due to bulk-boundary correspondence, if the boundary itself breaks any protecting symmetries, the edge states lose their protection and may gap out in energy [24]. It is therefore useful to have a general description of which boundary conditions the basic principle of current conservation allows, and to be able to sort the boundary conditions by symmetry classification.

The aim of this chapter is an analysis of boundary conditions for continuum Hamiltonians, and to present tools to compute the spectra of confinements. First of all, we parametrize all boundary conditions that conserve current at a single, isolated boundary for a generic continuum Hamiltonian up to second order in the momentum orthogonal to the boundary, and show how to classify the boundary conditions by symmetry. The general boundary conditions are given in terms of a skew-Hermitian matrix parameter, whose

eigenvalues can take any values on the complex axis, or in terms of a more stable unitary matrix parametrization. Secondly, we develop an algorithm to compute the spectra of generic continuum Hamiltonians in a confinement formed by two parallel boundaries, each with arbitrary boundary conditions from the parametrization. The algorithm is numerically stable and capable of finding both edge and bulk states of the confinement. Thirdly, we show how to map the edge of a tight binding Hamiltonian to a boundary condition from the parametrization for the corresponding continuum Hamiltonian, making it possible to simulate effects local to the tight binding edge using the continuum model in combination with specific boundary conditions. Finally, we demonstrate the use of our results and methods by applying them to compute the dispersion of topological insulator nanoribbons. We study the effects of scalar or magnetic edge potentials on the topological edge states, using both a tight binding model with edge potentials, and a continuum model with boundary conditions matching the edge potentials.

The outline of the chapter is as follows. In Sec. 4.2, we formulate the general boundary conditions and their symmetry constraints. In Sec. 4.3, we present the algorithm to compute the spectra of continuum Hamiltonians in confinements. In Sec. 4.4, we show how to match a tight binding lattice boundary to a boundary condition for the corresponding continuum model. In Sec. 4.5, we compute the dispersions of topological insulator nanoribbons, comparing tight binding calculations with the continuum model supplemented with corresponding boundary conditions. We conclude with a summary in Sec. 4.6.

4.2. GENERAL CURRENT-CONSERVING BOUNDARY CONDITIONS

We consider a continuum Hamiltonian of the form

$$H(k_\perp, k_\parallel) = h_0(k_\parallel) + h_1(k_\parallel)k_\perp + h_2(k_\parallel)k_\perp^2, \tag{4.1}$$

which acts on the N_c-component spinor wave function ψ, with $N_c \times N_c$ Hermitian matrices $h_i(k_\parallel)$ for $i = 0, 1, 2$. Here, $k_\parallel$ and $k_\perp$ are wave vector components along the orthogonal directions $x_\parallel$ and $x_\perp$. We add a boundary to the domain of the Hamiltonian by confining the $x_\perp$-axis to the half-plane $x_\perp < x_\perp^B$, such that translational invariance along $x_\perp$ is broken, and therefore interpret $k_\perp$ in (4.1) as the operator $\hat{k}_\perp = -i\partial_{x_\perp}$. Because the boundary does not break translational invariance along $x_\parallel$, $k_\parallel$ is a conserved continuous quantum number that describes propagation along the boundary. Note that (4.1) also applies in the case of more than one translationally invariant directions along the boundary, in which case $x_\parallel$ and $k_\parallel$ are vectors.

4.2.1. SKEW-HERMITIAN PARAMETRIZATION OF BOUNDARY CONDITIONS

In the presence of a boundary, it is necessary to supplement the Hamiltonian with boundary conditions to compute its spectrum. For a general description of a single, isolated boundary, we wish to know which boundary conditions are allowed by the principle of probability current conservation for the Hamiltonian (4.1), independent of any additional microscopic input. The operator for the probability current density normal to the boundary at the coordinate $\mathbf{x}$ is

$$j_\perp(\mathbf{x}) = \frac{1}{2}(v_\perp |\mathbf{x}\rangle \langle \mathbf{x}| + |\mathbf{x}\rangle \langle \mathbf{x}| v_\perp). \tag{4.2}$$

The real space projector $|\mathbf{x}\rangle\langle\mathbf{x}|$ acts as the identity in the Hilbert space of basis orbitals of the Hamiltonian (4.1), i.e. if $|\psi\rangle = [|\psi_1\rangle, |\psi_2\rangle, \ldots, |\psi_{N_c}\rangle]^T$ and $\langle\mathbf{x}|\,\psi_j\rangle = \psi_j(\mathbf{x})$, then $\langle\mathbf{x}|\,\psi\rangle = [\psi_1(\mathbf{x}), \psi_1(\mathbf{x}), \ldots, \psi_{N_c}(\mathbf{x})]^T$. With $\mathbf{n}_B$ the unit vector pointing outward from the boundary, the outward projection of the velocity operator $\hbar\mathbf{v} = \nabla_{\mathbf{k}} H$ is given by $v_\perp = \mathbf{n}_B \cdot \mathbf{v}$, namely

$$\begin{aligned} v_\perp(k_\parallel) &= \frac{1}{\hbar}\frac{\partial H(k_\perp, k_\parallel)}{\partial k_\perp} = \frac{1}{\hbar}\left[h_1(k_\parallel) + 2h_2(k_\parallel)k_\perp\right] \\ &\equiv v_1 + v_2 k_\perp. \end{aligned} \tag{4.3}$$

At the boundary $\mathbf{x}_B = (x_\perp^B, x_\parallel)$, probability current conservation requires that the normal projection of the current vanishes $\langle\psi|\, j_\perp(\mathbf{x}_B)\,|\psi\rangle = 0$, i.e.

$$\langle\psi|\, v_\perp\,|\mathbf{x}_B\rangle\langle\mathbf{x}_B|\,\psi\rangle + \langle\psi|\,\mathbf{x}_B\rangle\langle\mathbf{x}_B|\, v_\perp\,|\psi\rangle = 0. \tag{4.4}$$

A parametrization of the space of solutions to the vanishing-current constraint (4.4) gives a general description of the boundary conditions which conserve current at a single boundary. The local linear constraint

$$\begin{aligned} &\langle\mathbf{x}_B|\,\psi\rangle = \langle\mathbf{x}_B|\,\alpha\, v_\perp\,|\psi\rangle \\ \Leftrightarrow\ &\psi(\mathbf{x}_B) = \alpha\, v_\perp \psi(\mathbf{x}_B) \end{aligned} \tag{4.5}$$

with an $N_c \times N_c$ skew-Hermitian matrix $\alpha^\dagger = -\alpha$ ensures that the normal projection of the current vanishes, i.e.

$$\begin{aligned} &\langle\psi|\, v_\perp\,|\mathbf{x}_B\rangle\langle\mathbf{x}_B|\,\psi\rangle + \langle\psi|\,\mathbf{x}_B\rangle\langle\mathbf{x}_B|\, v_\perp\,|\psi\rangle \\ =&\langle\psi|\, v_\perp\,|\mathbf{x}_B\rangle\langle\mathbf{x}_B|\,\alpha\, v_\perp\,|\psi\rangle + \langle\psi|\, v_\perp \alpha^\dagger\,|\mathbf{x}_B\rangle\langle\mathbf{x}_B|\, v_\perp\,|\psi\rangle \\ =&\langle\psi|\, v_\perp\,|\mathbf{x}_B\rangle\langle\mathbf{x}_B|\,\alpha\, v_\perp\,|\psi\rangle - \langle\psi|\, v_\perp\,|\mathbf{x}_B\rangle\langle\mathbf{x}_B|\,\alpha\, v_\perp\,|\psi\rangle \\ =&\,0, \end{aligned} \tag{4.6}$$

because α commutes with $|\mathbf{x}_B\rangle\langle\mathbf{x}_B|$. This parametrization for the boundary conditions also arises in the context of a variational calculation of the self-adjoint extensions [25, 26] to the Hamiltonian with a boundary [27]. The completeness of the parametrization is proven in Appendix 4.7.1. Analogous parametrizations exist for various specific Hamiltonians [17, 19], e.g. the free-particle Hamiltonian $H = -\partial_x^2$ [13], or topological insulators in two or three dimensions [21]. That the boundary conditions (4.5) ensure that the Hamiltonian with the boundary is self-adjoint is shown in Appendix 4.7.2.

4.2.2. SYMMETRIES OF BOUNDARY CONDITIONS

In addition to current conservation, it is useful to classify boundary conditions depending on whether they preserve or break symmetries. For example, in a symmetry-protected topological phase, edge states lose their topological protection if the boundary conditions break the protecting symmetry. A boundary condition α for the state $\psi(\mathbf{x}_B)$ preserves a symmetry $\mathcal{S}$ if the boundary condition applies equally to $\psi(\mathbf{x}_B)$ and its symmetry-partner $\mathcal{S}\psi(\mathbf{x}_B)$, namely if

$$\psi(\mathbf{x}_B) = \alpha\, v_\perp \psi(\mathbf{x}_B), \tag{4.7a}$$

$$\mathcal{S}\psi(\mathbf{x}_B) = \alpha\, v_\perp \mathcal{S}\psi(\mathbf{x}_B). \tag{4.7b}$$

Here, we assume that $\mathscr{S}$ either has no real space action, or if it does, that it transforms each point at the boundary to another point at the boundary. Otherwise, the boundary breaks the symmetry. Applying $\mathscr{S}$ from the left to (4.7a) and subtracting (4.7b) yields

$$(\mathscr{S}\alpha v_\perp - \alpha v_\perp \mathscr{S})\psi(\mathbf{x}_B) = 0, \tag{4.8}$$

and the boundary condition thus preserves the symmetry if

$$[\mathscr{S}, \alpha v_\perp] = 0. \tag{4.9}$$

Because $v_\perp$ and its transformation by the symmetry are known for a given Hamiltonian, Eq. (4.9) is a constraint on the matrix parameter α.

4.2.3. EXAMPLES

As an example, we consider the boundary conditions for the continuum Dirac model of graphene. The Hamiltonian that describes the low-energy excitations in graphene is [28]

$$H = v\tau_0 \otimes (\sigma_x p_x + \sigma_y p_y), \tag{4.10}$$

with v the Fermi velocity, and the Pauli matrices and identity in valley and sublattice space τ_j and σ_j, respectively, where $j = x, y, z, 0$. The boundary conditions for the Dirac equation that give vanishing current normal to the boundary are [14, 18]

$$\psi = M\psi, \quad \{M, v_\perp\} = 0, \quad M^\dagger = M = M^{-1}, \tag{4.11}$$

with $v_\perp = \mathbf{n}_B \cdot \mathbf{v}$, where $\mathbf{v} = v\tau_0 \otimes \boldsymbol{\sigma}$ is the velocity operator, and $\mathbf{n}_B$ the outward pointing unit vector normal to the boundary. We now show that (4.11) is consistent with the parametrization (4.5). Comparing (4.11) and (4.5), we identify

$$M = \alpha v_\perp, \tag{4.12}$$

or equivalently, because $v_\perp^2 = v^2$,

$$\alpha = M v_\perp / v^2. \tag{4.13}$$

Hence

$$\alpha^\dagger = (M v_\perp)^\dagger / v^2 = v_\perp^\dagger M^\dagger / v^2 = v_\perp M / v^2, \tag{4.14}$$

and because $\{M, v_\perp\} = 0$,

$$\alpha^\dagger = v_\perp M / v^2 = -M v_\perp / v^2 = -\alpha, \tag{4.15}$$

which shows that the two parametrizations are consistent.

As a second example, consider the Hamiltonian of a spinful free particle in one dimension

$$H = \frac{p_x^2}{2m}\sigma_0, \tag{4.16}$$

which acts on the spinor $\psi(x) = [\psi_\uparrow(x), \psi_\downarrow(x)]^T$, with σ_0 the identity in spin space. The velocity operator is $v_x = \sigma_0 p_x / m$, and all current-conserving boundary conditions at $x = x_B$ for the half-line $x \leq x_B$ of the form $\psi(x_B) = \alpha v_x \psi(x_B)$, with α a 2×2 skew-Hermitian

matrix. With $\alpha = 0$, we recover the hard-wall boundary condition $\psi_\uparrow(x_B) = \psi_\downarrow(x_B) = 0$. Choosing $\alpha = \mathrm{diag}(i\lambda, i\lambda)$ on the other hand, we obtain the Neumann boundary condition $\partial_x\psi_\uparrow(x_B) = \partial_x\psi_\downarrow(x_B) = 0$ by inverting α and setting $\lambda \to \infty$: $v_x\psi(x_B) = -i\hbar\sigma_0\partial_x\psi(x_B) = \alpha^{-1}\psi(x_B) \to 0$ as $\lambda \to \infty$, because $\alpha^{-1} = -\mathrm{diag}(i/\lambda, i/\lambda)$. The space of boundary conditions α that preserve time-reversal symmetry $\mathcal{T} = i\sigma_y$ satisfies $[\mathcal{T}, \alpha v_x] = 0$. Now, α is skew-Hermitian, so we can express it as the linear combination $\alpha = i\sum_n c_n\sigma_n$ with $n = x, y, z, 0$ for the Pauli matrices plus identity and c_n real parameters. Because $\{\mathcal{T}, v_x\} = 0$, a boundary condition is time-reversal invariant if $\{\alpha, \mathcal{T}\} = 0$. This condition is only met if $\alpha = ic_0\sigma_0$, i.e. if the boundary condition is independent of spin, and shows that any boundary condition that splits or couples the spin projections breaks time-reversal symmetry. The hard-wall and Neumann boundary conditions above both respect time-reversal symmetry.

The above example highlights a drawback of the boundary conditions parametrization. The only general constraint on α is that it is skew-Hermitian, $\alpha^\dagger = -\alpha$, which means that the eigenvalues of α can vary greatly, taking values on the entire imaginary axis, but still correspond to physical boundary conditions. This situation arises naturally in the example above: a vanishing α gives hard-wall boundary conditions, but a diverging α the equally physically relevant Neumann boundary conditions. Because working with diverging quantities is hard in practice, especially numerically, where it easily leads to instability, it is useful to reformulate the boundary conditions to remove any divergences.

4.2.4. Unitary parametrization of boundary conditions - Cayley transformation

Applying the Cayley transformation [29] parametrizes the boundary conditions in terms of a unitary matrix, removing any divergences. The Cayley transformation is a one-to-one matrix map between the space of $N \times N$ skew-Hermitian matrices and the unitary group $U(N)$, by which we obtain a unitary matrix Q from the skew-Hermitian matrix A:

$$Q = (I - A)(I + A)^{-1}. \tag{4.17}$$

Because A is skew-Hermitian, its eigenvalues are purely imaginary numbers. The matrix $I + A$ is therefore always invertible, and Q is well defined for any A. Solving Eq. (4.17) for A yields

$$A = (I + Q)^{-1}(I - Q). \tag{4.18}$$

Morally speaking, (4.18) is only valid if $I + Q$ is nonsingular, that is if Q does not have an eigenvalue equal to -1. However, an eigenvalue -1 of Q means that A has a diverging eigenvalue, which as we know represents a physically acceptable boundary condition, and we therefore interpret Eq. (4.18) as always valid, even when A has diverging eigenvalues. Anticipating the results of Section 4.4, we choose to invert the boundary conditions, and apply the Cayley transformation to α^{-1} instead of α. With $A = \alpha^{-1}$ in (4.17), we thus obtain an alternative but equivalent parametrization for the boundary conditions in terms of the unitary matrix Q:

$$\psi(\mathbf{x}_B) = \alpha v_\perp \psi(\mathbf{x}_B) \tag{4.19a}$$

$$\Leftrightarrow \quad \alpha^{-1}\psi(\mathbf{x}_B) = v_\perp\psi(\mathbf{x}_B) \tag{4.19b}$$

$$\Leftrightarrow \quad (I - Q)\psi(\mathbf{x}_B) = (I + Q)\, v_\perp\psi(\mathbf{x}_B). \tag{4.19c}$$

The advantage of this unitary formulation is that it removes the need to deal with divergences. Because Q is unitary, all of its eigenvalues live on the unit circle, instead of taking potentially any value on the complex axis (including infinity) as is the case with α. For example, with $Q = I$ we obtain the Neumann-like boundary conditions $v_\perp \psi = 0$, instead of using $\alpha = \text{diag}(i\lambda)$ with $\lambda \to \infty$ in (4.5). On the other hand, $Q = -I$ reproduces the Dirichlet boundary conditions $\psi = 0$ for $\alpha = 0$.

4.3. ALGORITHM TO FIND SPECTRA OF CONFINEMENTS WITH ARBITRARY BOUNDARY CONDITIONS

The spectrum of a Hamiltonian in a confinement strongly depends on the boundary conditions at the edges, and generally computing the spectrum with arbitrary boundary conditions by hand is a difficult task. In this section, we present a numerically stable algorithm to compute the bound states of a continuum Hamiltonian of the form (4.1) when the direction $x_\perp$ is confined between two parallel boundaries, each with arbitrary current-conserving boundary conditions.

4.3.1. MODE DECOMPOSITION

We begin by analyzing the eigenstates of the Hamiltonian H (4.1) in the absence of confinements. Because the Hamiltonian commutes with the translation operator along $x_\perp$, we can construct simultaneous eigenstates of $\hat{k}_\perp = -i\partial_{x_\perp}$ and H. These eigenstates are the modes of the Hamiltonian, and they have the form $\psi(x_\perp, k_\parallel) = \phi(k_\parallel) e^{ik_\perp x_\perp}$ with $k_\perp$ the eigenvalue of $\hat{k}_\perp$. To compute the modes at a specific energy E, we transform the Schrödinger equation $H\psi = E\psi$ into the generalized eigenproblem [30, 31]

$$\begin{bmatrix} E - h_0 & 0 \\ 0 & I \end{bmatrix} \begin{bmatrix} \phi \\ k_\perp \phi \end{bmatrix} = k_\perp \begin{bmatrix} h_1 & h_2 \\ I & 0 \end{bmatrix} \begin{bmatrix} \phi \\ k_\perp \phi \end{bmatrix}, \tag{4.20}$$

or, if $h_2 = 0$ such that the Hamiltonian is linear in $k_\perp$,

$$(E - h_0)\phi = k_\perp h_1 \phi, \tag{4.21}$$

with implicit dependence on $k_\parallel$. The solutions ϕ_n are the modes and corresponding eigenvalues $k_{\perp,n}$. In total, there are pN_c modes, where p is the maximum degree of $k_\perp$ in the Hamiltonian, and with each ϕ_n an N_c-dimensional vector. Modes with $k_{n,\perp} \in \mathbb{R}$ are propagating, while those with $\text{Im}\{k_{\perp,n}\} \neq 0$ are evanescent. Evanescent modes with $\text{Im}\{k_{\perp,n}\} > 0$ are right-moving, because they decay with increasing $x_\perp$ but diverge as $x_\perp \to -\infty$. Similarly, evanescent modes with $\text{Im}\{k_{\perp,n}\} < 0$ are left-moving. We classify the propagating modes into right- and left-movers based on their velocity along $x_\perp$, i.e. $\langle v_\perp \rangle = \langle \phi_n | v_\perp | \phi_n \rangle$ with $v_\perp$ in (4.3), where ϕ_n is right moving if $\langle v_\perp \rangle > 0$ and left moving if $\langle v_\perp \rangle < 0$. We denote the sorted modes by ϕ_n^γ, with $\gamma = +$ and $\gamma = -$ for right- and left-movers, respectively, and corresponding eigenvalues $k_{\perp,n}^\gamma$.

At a given energy, any solution to the Schrödinger equation can be decomposed in terms of the modes [32, 33]. Gathering the left- and right-moving modes into the matrices U_γ, such that column n of U_γ is ϕ_n^γ, and with $\Lambda_\gamma(x_\perp) = \text{diag}[e^{ik_{\perp,1}^\gamma}, e^{ik_{\perp,2}^\gamma}, \ldots]$, we have

$$\psi(x_\perp, k_\parallel) = U_+ \Lambda_+(x_\perp) \mathbf{D}_+ + U_- \Lambda_-(x_\perp) \mathbf{D}_-, \tag{4.22}$$

with $\mathbf{D}_\gamma$ vectors of expansion coefficients. In the absence of confinements, any linear combination of the form (4.22) is a solution to the Schrödinger equation. Confining the $x_\perp$-direction by imposing boundary conditions at $x_\perp = x_L$ and $x_\perp = x_R = x_L + W > x_L$ constrains the space of coefficients $\mathbf{D}_\gamma$ to solutions that solve the Schrödinger equation and obey the boundary conditions.

4.3.2. SPECTRUM OF A CONFINEMENT

We now formulate a matrix equation for the eigenstates of the Hamiltonian with the boundary conditions. At the boundary $x_\perp = x_j$ with $j = L, R$, the boundary condition in unitary form (4.19c) is

$$\begin{aligned}(I - Q_L)\psi(x_L) &= -(I + Q_L)\,v_\perp \psi(x_L),\\ (I - Q_R)\psi(x_R) &= (I + Q_R)\,v_\perp \psi(x_R),\end{aligned} \tag{4.23}$$

with $v_\perp$ given in (4.3), and the extra minus in the top equation due to the sign of the outward pointing velocity projection. Applying $v_\perp$ to the mode decomposition (4.22) yields

$$\begin{aligned}v_\perp \psi(x_j) &= \sum_{\gamma=+,-} (v_1 U_\gamma + v_2 U_\gamma \hat{k}_\perp)\Lambda_\gamma(x_j)\mathbf{D}_\gamma\\ &= \sum_{\gamma=+,-} (v_1 U_\gamma + v_2 U_\gamma K_\gamma)\Lambda_\gamma(x_j)\mathbf{D}_\gamma\\ &= \sum_{\gamma=+,-} V_\gamma \Lambda_\gamma(x_j)\mathbf{D}_\gamma,\end{aligned} \tag{4.24}$$

with the matrices $K_\gamma = \mathrm{diag}(k^\gamma_{\perp,1}, k^\gamma_{\perp,2}, \ldots)$, and $V_\gamma = v_1 U_\gamma + v_2 U_\gamma K_\gamma$. Substituting into the boundary conditions (4.23) gives the system of equations

$$\begin{aligned}(I - Q_L)\,[U_+\Lambda_+(x_L)\mathbf{D}_+ + U_-\Lambda_-(x_L)\mathbf{D}_-] &= -(I + Q_L)\,[V_+\Lambda_+(x_L)\mathbf{D}_+ + V_-\Lambda_-(x_L)\mathbf{D}_-]\\ (I - Q_R)\,[U_+\Lambda_+(x_R)\mathbf{D}_+ + U_-\Lambda_-(x_R)\mathbf{D}_-] &= (I + Q_R)\,[V_+\Lambda_+(x_R)\mathbf{D}_+ + V_-\Lambda_-(x_R)\mathbf{D}_-],\end{aligned} \tag{4.25}$$

which a state at a fixed energy must satisfy.

In practice, the equations (4.25) are prone to numerical instability, because of the presence of evanescent modes. Each of the matrices $\Lambda_+(x)$ and $\Lambda_-(x)$ is evaluated at both boundaries x_L and x_R, and therefore contribute both exponentially small and diverging terms to Eq. (4.25). We stabilize the equations using the property

$$\Lambda_\gamma(x_j) = \Lambda_\gamma(x_j - x_i)\Lambda_\gamma(x_i), \tag{4.26}$$

along with $x_R = x_L + W$ to rewrite

$$\begin{aligned}\Lambda_+(x_R)\mathbf{D}_+ &= \Lambda_+(W)\Lambda_+(x_L)\mathbf{D}_+\\ \Lambda_-(x_L)\mathbf{D}_- &= \Lambda_-(-W)\Lambda_-(x_R)\mathbf{D}_-,\end{aligned} \tag{4.27}$$

such that all evanescent exponentials in both $\Lambda_+(W)$ and $\Lambda_-(-W)$ are exponentially suppressed, and not diverging. Substituting into Eq. (4.25), we obtain the homogeneous matrix equation

$$B(E, k_\parallel)\begin{bmatrix}\Lambda_+(x_L)\mathbf{D}_+\\ \Lambda_-(x_R)\mathbf{D}_-\end{bmatrix} = 0, \tag{4.28}$$

with the matrix

$$B = \begin{bmatrix} (I-Q_L)U_+ + (I+Q_L)V_+ & (I-Q_L)U_-\Lambda_-(-W) + (I+Q_L)V_-\Lambda_-(-W) \\ (I-Q_R)U_+\Lambda_+(W) - (I+Q_R)V_+\Lambda_+(W) & (I-Q_R)U_- - (I+Q_R)V_- \end{bmatrix}. \tag{4.29}$$

Note that B implicitly depends on E through the modes. States of the confinement are elements of the kernel of B, and searching for the solutions amounts to searching for values of E (and $k_\parallel$ if appropriate) for which the kernel of B is nontrivial. Because of the stabilization (4.27), the matrix B contains no diverging quantities, and (4.28) is therefore numerically stable. The analogous matrix using the skew-Hermitian parametrization (4.5) is

$$B = \begin{bmatrix} U_+ + \alpha_L V_+ & U_-\Lambda_-(-W) + \alpha_L V_-\Lambda_-(-W) \\ U_+\Lambda_+(W) - \alpha_R V_+\Lambda_+(W) & U_- - \alpha_R V_- \end{bmatrix}. \tag{4.30}$$

A nontrivial element of the kernel of B is a solution to the Schrödinger equation that satisfies the boundary conditions of the confinement. However, such a solution may be a false-positive if it does not correspond to a physical state. For example, in an infinite square well with normal hard-wall boundary conditions at both ends, the kernel of B is nontrivial at the energies $E = k_\parallel^2$. The corresponding wave function with boundary conditions imposed vanishes over the well, and is therefore not normalizable. We filter out such false-positives by bringing the solution to real space, and rejecting those that are not normalizable while simultaneously obeying the boundary conditions.

4.3.3. EXAMPLES

As an illustration, we apply the algorithm to compute the dispersion of nanoribbons. First, consider a semiconductor ribbon in a longitudinal magnetic field with Rashba spin-orbit coupling. The Hamiltonian is

$$H = \frac{\hbar^2}{2m}(k_x^2 + k_y^2)\sigma_0 + \beta(k_x\sigma_y - k_y\sigma_x) + E_Z\sigma_y, \tag{4.31}$$

where m is the electron effective mass, β the spin-orbit coupling strength, and E_Z the Zeeman energy due to the longitudinal magnetic field. Here, $\sigma_{x,y,z}$ are the Pauli matrices in spin space, and the Hamiltonian acts on the spinor $\psi = [\psi_\uparrow, \psi_\downarrow]$. We form a ribbon that is translationally invariant along y by imposing hard-wall boundary conditions $\psi(0,y) = \psi(W,y) = 0$ at the left and right edges $x = 0$ and $x = W$, respectively, which in terms of the parametrization (4.19c) means $Q_L = Q_R = -I$. To compute the dispersion, we set $W = 50a$ with a a unit of length, and apply the algorithm with $h_2 = \sigma_0\hbar^2/2ma^2$, $h_1 = \beta a\sigma_y$ and $h_0 = \sigma_0\hbar^2k_y^2/2m + E_Z\sigma_y$ to search for solutions of (4.28) as a function of k_y and energy E. The results are shown in Fig. 4.1(a), where the helical gap manifests at $k_y = 0$ due to the interplay of the spin-orbit coupling with the Zeeman field [34]. In addition, we superimpose the result of a tight binding calculation, obtained with Kwant[35] by discretizing the Hamiltonian (4.31) over the width of the ribbon. The two methods agree perfectly.

As a second example, we consider a graphene nanoribbon with zigzag boundaries. The Dirac Hamiltonian that governs the low-energy excitations of graphene in the continuum limit near the high symmetry points $\pm\mathbf{K}$ is given in Eq. (4.10), and acts on a

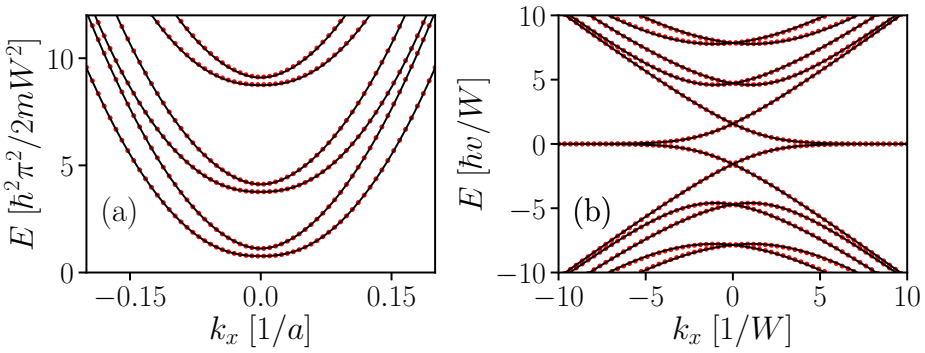

Figure 4.1: (a) Dispersion of a ribbon with Rashba spin-orbit coupling in a longitudinal Zeeman field with hard-wall boundary conditions at its edges, computed using the continuum spectrum-finding algorithm (red dots), and by discretizing the Hamiltonian over the ribbon width (solid lines). The two methods are in perfect agreement. Parameters are $W = 50a$, $\beta a/t = 0.03$, and $E_Z/t = 7\times10^{-4}$, where $t = \hbar^2/2ma^2$. (b) Dispersion of graphene nanoribbon of width $W = 300a$ with zigzag boundaries, with a the graphene lattice constant, computed using the continuum dispersion algorithm (red dots) and the tight binding model of graphene (solid lines). The two methods agree perfectly.

four-component spinor ψ. We take the ribbon as translationally invariant along y, and impose boundary conditions at the edges $x = 0$ and $x = W$. The zigzag boundary conditions are $\psi(0,y) = -M\psi(0,y)$ and $\psi(W,y) = M\psi(W,y)$, with $M = \tau_z\otimes\sigma_z$ [14, 18, 36]. Using (4.13), in terms of the parametrization (4.5) we thus have $\alpha_L = \alpha_R = Mv_x/v^2$ at the left and right boundaries, where $v_x = \hbar v\tau_0\otimes\sigma_x$. With $h_2 = 0$, $h_1 = \hbar v\tau_0\otimes\sigma_x$ and $h_0 = \hbar v\tau_0\otimes\sigma_y k_y$, we search for solutions of (4.28) as a function of k_y and energy E to compute the dispersion. The results are shown in Fig. 4.1(b), where we superimpose the dispersion computed near $\pm\mathbf{K}$ with Kwant[35] using the tight binding model for graphene with nearest neighbour hopping, showing that the two methods are in perfect agreement. The spectrum exhibits the dispersionless zero-energy edge states characteristic of zigzag graphene boundaries.

4.4. CONTINUUM BOUNDARY CONDITIONS FROM TIGHT BINDING EDGES

The space of current conserving boundary conditions (4.5) includes infinitely many boundary conditions, but gives no direct correspondence between a physical boundary and a particular boundary condition in the parametrization. In this section, we show how to construct a boundary condition for a continuum Hamiltonian from the edge of a corresponding tight binding model.

4.4.1. TIGHT BINDING DESCRIPTION OF A BOUNDARY

We consider tight binding equations of the form

$$H_{j,j-1}\boldsymbol{C}_{j-1} + (H_j - E)\boldsymbol{C}_j + H_{j,j+1}\boldsymbol{C}_{j+1} = 0, \tag{4.32}$$

where j is a real space index, $H_j = H_j^\dagger$ are onsite matrices which act on the vectors of tight binding amplitudes $\mathbf{C}_j$, $H_{i,j}$ is the hopping matrix from cell j to i, and E is the energy. In the following, we absorb the energy E into the onsite matrix to simplify notation, $H_j - E \equiv H_j$, with the energy dependence implicit. Equation (4.32) applies equally to systems that are finite or translationally invariant in the plane perpendicular to the direction of the real space index j. In the latter case, the tight binding matrices become functions of the corresponding lateral wave vector $\mathbf{k}_\parallel$, and (4.32) applies to each $\mathbf{k}_\parallel$ separately [37, 38].

In order to describe a homogeneous material with a boundary, we take Eq. (4.32) to describe a bulk system that couples to an edge region, beyond which the system terminates. In the homogeneous bulk, the hoppings and onsites are independent of j, which numbers the translational unit cells. The corresponding tight binding equations are

$$T_L \boldsymbol{C}_{j-1} + H_L \boldsymbol{C}_j + T_L^\dagger \boldsymbol{C}_{j+1} = 0, \tag{4.33}$$

where $H_j = H_L$ and $H_{j,j-1} = T_L$ for all j, and $H_{j,j+1} = T_L^\dagger$ due to Hermiticity. With M_L orbitals per translational unit cell, H_L and T_L are $M_L \times M_L$ matrices. To include a boundary, we truncate the bulk equations (4.33) at the cell $j = 0$, and couple the last bulk cell to an edge. The tight binding equations for the boundary and adjacent bulk cells are

$$H_S \boldsymbol{C}_S + T_S^\dagger \boldsymbol{C}_0 = 0, \tag{4.34a}$$
$$T_S \boldsymbol{C}_S + H_L \boldsymbol{C}_0 + T_L^\dagger \boldsymbol{C}_1 = 0, \tag{4.34b}$$
$$T_L \boldsymbol{C}_0 + H_L \boldsymbol{C}_1 + T_L^\dagger \boldsymbol{C}_2 = 0, \tag{4.34c}$$
$$T_L \boldsymbol{C}_1 + H_L \boldsymbol{C}_2 + T_L^\dagger \boldsymbol{C}_3 = 0, \tag{4.34d}$$
$$\vdots$$

with H_S the onsite matrix of the edge, $\boldsymbol{C}_S$ the corresponding tight binding amplitudes, and T_S the hopping from the boundary region to the adjacent bulk unit cell $j = 0$. The edge describes deviations from the bulk material that are local to the system boundary, such as surface potentials, and is therefore generally different from the bulk translational unit cell. If there are M_S orbitals in the boundary region, the matrices H_S and T_S are $M_S \times M_S$ and $M_L \times M_S$, respectively.

4.4.2. MATCHING A TIGHT BINDING BOUNDARY TO A BOUNDARY CONDITION

We begin by showing how to fold the boundary region (4.34) into an effective boundary condition for the bulk tight binding Hamiltonian (4.33) that is consistent with the parametrization (4.5). In other words, our goal is to remove the boundary region $j = S$ from (4.34), and replace it with a boundary condition at the last bulk cell $j = 0$ adjacent to the boundary. Solving for $\mathbf{C}_S$ in (4.34a),

$$\mathbf{C}_S = -H_S^{-1} T_S^\dagger \mathbf{C}_0, \tag{4.35}$$

and substituting into (4.34b) yields

$$-T_S H_S^{-1} T_S^\dagger \mathbf{C}_0 + H_L \mathbf{C}_0 + T_L^\dagger \mathbf{C}_1 = 0. \tag{4.36}$$

This expression is ill-defined if H_S is singular, i.e. if H_S has zero eigenvalues, and hence not invertible. Because H_S is Hermitian, it is diagonalizable $H_S = U_S \times \mathrm{diag}[\epsilon_1, \epsilon_2, \ldots, \epsilon_{M_S}] \times U_S^\dagger$, with $U_S^\dagger = U_S^{-1}$ and eigenvalues ϵ_n. The inverse is then $H_S^{-1} = U_S \times \mathrm{diag}[\epsilon_1^{-1}, \epsilon_2^{-1}, \ldots, \epsilon_{M_S}^{-1}] \times U_S^\dagger$, so we can imagine that any zero eigenvalues become divergences in the inverse. In the context of the parametrization (4.5), divergences indeed correspond to physically acceptable boundary conditions. With this in mind, we for now freely invert matrices with no regard to whether this causes divergences, but address this point later on. In the final bulk cell $j = 0$, the projection of the tight binding velocity operator outwards from the boundary $V_\perp$ is (see Appendix 4.7.3)

$$(V_\perp \mathbf{C})_0 = -i[T_L^\dagger \mathbf{C}_1 - T_S \mathbf{C}_S]. \tag{4.37}$$

4

Solving for $T_L^\dagger \mathbf{C}_1$ and substituting in (4.36) results in

$$-T_S H_S^{-1} T_S^\dagger \mathbf{C}_0 + H_L \mathbf{C}_0 + T_S \mathbf{C}_S + i(V_\perp \mathbf{C})_0 = 0. \tag{4.38}$$

Using Eq. (4.35) yields

$$\begin{aligned} & -2T_S H_S^{-1} T_S^\dagger \mathbf{C}_0 + H_L \mathbf{C}_0 + i(V_\perp \mathbf{C})_0 = 0 \\ \Leftrightarrow \quad & [H_L - 2T_S H_S^{-1} T_S^\dagger]\mathbf{C}_0 = -i(V_\perp \mathbf{C})_0 \\ \Leftrightarrow \quad & \mathbf{C}_0 = -i[H_L - 2T_S H_S^{-1} T_S^\dagger]^{-1}(V_\perp \mathbf{C})_0 \end{aligned} \tag{4.39}$$

or

$$\mathbf{C}_0 = \alpha_{\mathrm{TB}} (V_\perp \mathbf{C})_0, \tag{4.40}$$

where by analogy with (4.5), we identify the tight binding boundary condition matrix

$$\alpha_{\mathrm{TB}} = -i(H_L - 2T_S H_S^{-1} T_S^\dagger)^{-1}. \tag{4.41}$$

The matrix α_{TB} is $M_L \times M_L$, and acts in the space of tight binding orbitals within a single translational unit cell of the bulk model (4.33). Crucially, we have $\alpha_{\mathrm{TB}}^\dagger = -\alpha_{\mathrm{TB}}$, such that the boundary condition is current conserving.

4.4.3. CONTINUUM LIMIT OF THE BOUNDARY CONDITION

The matrix (4.41) is a boundary condition for the tight binding model (4.33), while our goal is a boundary condition for a corresponding continuum model. To obtain the continuum model for the homogenous bulk, we invoke Bloch's theorem with the ansatz $\mathbf{C}_j = (e^{ik_\perp})^j \mathbf{C}$ where $k_\perp$ is the wave number along the direction of the index j [32], and obtain the Schrödinger equation

$$(T_L e^{-ik_\perp} + H_L + T_L^\dagger e^{ik_\perp})\boldsymbol{C} = E\boldsymbol{C}, \tag{4.42}$$

with $\mathbf{C}$ a vector of tight binding amplitudes in a bulk translational unit cell, and where we have written out the energy E again explicitly. Expanding up to second order in $k_\perp$ in the limit $k_\perp \to 0$ gives

$$H_c(k_\perp)\mathbf{C} = E\mathbf{C}, \tag{4.43}$$

with

$$H_c(k_\perp) = H_L + T_L + T_L^\dagger + ik_\perp(T_L - T_L^\dagger) - \frac{k_\perp^2}{2}(T_L^\dagger + T_L). \tag{4.44}$$

A continuum model acts in a basis of continuum orbitals, which may in general differ from the basis orbitals of a single translational unit cell in the parent tight binding model. In order to obtain the final continuum Hamiltonian, we project (4.43) down to the subspace spanned by the continuum orbitals. We assume that there are $M_c \leq M_L$ continuum orbitals in the continuum model, and that we know their representations ϕ_m in the tight binding basis, for $1 \leq m \leq M_c$. With $\Phi_c = [\phi_1, \phi_2, \ldots, \phi_{M_c}]$, the matrix $\Phi_c \Phi_c^\dagger$ is the projector from the tight binding basis into the basis of continuum orbitals. The projection of the tight binding vector $\mathbf{C}$ into the subspace of continuum orbitals is $\psi = \Phi_c^\dagger \mathbf{C} = [\phi_1^\dagger \mathbf{C}, \phi_2^\dagger \mathbf{C}, \ldots, \phi_{M_c}^\dagger \mathbf{C}]^T$, where ψ is the vector of wave function amplitudes in the continuum basis. Inserting $\Phi_c \Phi_c^\dagger$ between H_c and $\mathbf{C}$ in (4.43) and multiplying from the left with $\Phi_c^\dagger$, we obtain

$$\begin{aligned} & \Phi_c^\dagger H_c(k_\perp) \Phi_c \Phi_c^\dagger \mathbf{C} = E \Phi_c^\dagger \mathbf{C} \\ \Leftrightarrow\ & h_c(k_\perp)\psi = E\psi, \end{aligned} \tag{4.45}$$

with the $M_c \times M_c$ continuum Hamiltonian $h_c = \Phi_c^\dagger H_c \Phi_c$, which acts in the basis of continuum orbitals.

We now extract a boundary condition for the continuum Hamiltonian h_c in (4.45) from the tight binding boundary condition (4.41). In the limit $k_\perp \to 0$, the bulk tight binding velocity operator is (see Appendix 4.7.3)

$$V_\perp^c \mathbf{C} = i \left[T_L^\dagger - T_L + i k_\perp (T_L^\dagger + T_L) \right] \mathbf{C}, \tag{4.46}$$

which as Eq. (4.44) shows is equivalent to $V_\perp^c = \partial H_c(k_\perp)/\partial k_\perp$. Substituting (4.46) for the velocity operator in (4.40), we obtain

$$\mathbf{C}_0 = \alpha_{\mathrm{TB}} V_\perp^c \mathbf{C}_0. \tag{4.47}$$

To finish taking the continuum limit, we project to the continuum subspace by inserting projectors between all tight binding quantities and applying $\Phi_c^\dagger$ from the left:

$$\Phi_c^\dagger \mathbf{C}_0 = \Phi_c^\dagger \alpha_{\mathrm{TB}} \Phi_c \Phi_c^\dagger V_\perp^c \Phi_c \Phi_c^\dagger \mathbf{C}_0. \tag{4.48}$$

Because $\Phi_c^\dagger V_\perp^c \Phi_c = \partial h_c(k_\perp)/\partial k_\perp = v_\perp$ is the continuum velocity operator [see Eq. (4.45)], and $\Phi_c^\dagger \mathbf{C}_0 = \psi_0$ the continuum wave function amplitudes in the last bulk cell adjacent to the edge, Eq. (4.48) is equivalent to

$$\psi_0 = \alpha_c v_\perp \psi_0 \tag{4.49}$$

where

$$\alpha_c = -i \Phi_c^\dagger (H_L - 2 T_S H_S^{-1} T_S^\dagger)^{-1} \Phi_c \tag{4.50}$$

is an $M_c \times M_c$ matrix that satisfies $\alpha_c^\dagger = -\alpha_c$, and acts in the continuum basis. By supplementing the continuum Hamiltonian (4.45) with the boundary condition matrix α_c in the parametrization (4.5), we are thus able to simulate the effects of the tight binding boundary (4.34) on the spectrum at the level of the continuum Hamiltonian.

4.4.4. STABILIZATION OF THE MATCHING PROCEDURE

Although Eq. (4.50) is manifestly a current conserving boundary condition, it contains inverses which potentially make it unsuitable for numerical evaluation. In this section, we derive a stabilized expression for the boundary condition as a function of the tight binding parameters using the Cayley transformation of Sec. 4.2.4.

Because α_{TB} of Eq. (4.41) contains an overall inverse, instead of the boundary condition (4.40), it is easier to apply the Cayley transformation to the equivalent boundary condition $\alpha_{\mathrm{TB}}^{-1}\mathbf{C}_0 = (v_\perp \mathbf{C})_0$. Including the projection to the continuum limit, we thus stabilize the boundary condition by applying the Cayley transformation [see Eq. (4.17)]

$$Q_c = \frac{I - \Phi_c^\dagger \alpha_{\mathrm{TB}}^{-1} \Phi_c}{I + \Phi_c^\dagger \alpha_{\mathrm{TB}}^{-1} \Phi_c}, \tag{4.51}$$

where the $M_c \times M_c$ matrix Q_c is unitary, and acts in the basis of continuum orbitals. Using α_{TB} in (4.41), we obtain (see Appendix 4.7.4)

$$\begin{aligned} Q_c = -I - 2i(\Phi_c^\dagger H_L \Phi_c - i)^{-1} \{ I + \Phi_c^\dagger T_S [\frac{1}{2} H_S - \Phi_c T_S^\dagger (\Phi_c^\dagger H_L \Phi_c - i)^{-1} T_S \Phi_c]^{-1} \\ \times T_S^\dagger \Phi_c (\Phi_c^\dagger H_L \Phi_c - i)^{-1} \}, \end{aligned} \tag{4.52}$$

which is compatible with the boundary condition parametrization given in Eq. (4.19c).

Although the expression for Q_c in (4.52) looks cumbersome, it has a number of useful properties. First of all, we avoid the intermediate step of constructing α_{TB}, and hence avoid dealing with potentially diverging quantities. Instead, we obtain a unitary boundary condition matrix directly from the tight binding parameters that characterize the boundary. Secondly, although (4.52) contains a number of inverses, they are regularized. Because the matrix $\Phi_c^\dagger H_L \Phi_c$ is Hermitian, its eigenvalues are real. The eigenvalues of $(\Phi_c^\dagger H_L \Phi_c - i)$ thus always have a finite imaginary component $-i$, and the matrix is therefore always invertible. Similarly, the original bare inverse of H_S in (4.41) obtains the regularization term $\Phi_c T_S^\dagger (\Phi_c^\dagger H_L \Phi_c - i)^{-1} T_S \Phi_c$, which resembles a self-energy [39].

4.5. APPLICATION TO THE QUANTUM SPIN HALL EFFECT

In this section, we apply the boundary condition matching procedure to investigate the effects of different boundary conditions on the edge states in a two-dimensional topological insulator [2]. Topological insulators are materials that have a bulk energy gap, but exhibit metallic edge states in the topological phase which are protected by time-reversal symmetry. In a two-dimensional topological insulator, an edge hosts a pair of counterpropagating bands of edge states which are Kramers partners [cf. Fig. 4.2(a)], forbidding scattering between them as long as time-reversal symmetry is unbroken. Because of their localization at an edge, the edge states are more responsive to edge effects than the bulk states, which in combination with their inherent dependence on symmetry makes them an ideal subject to investigate boundary conditions.

4.5.1. BHZ MODEL

To model a two-dimensional topological insulator, we use the Bernevig-Hughes-Zhang (BHZ) Hamiltonian [40]. The tight binding Hamiltonian consists of a square lattice with

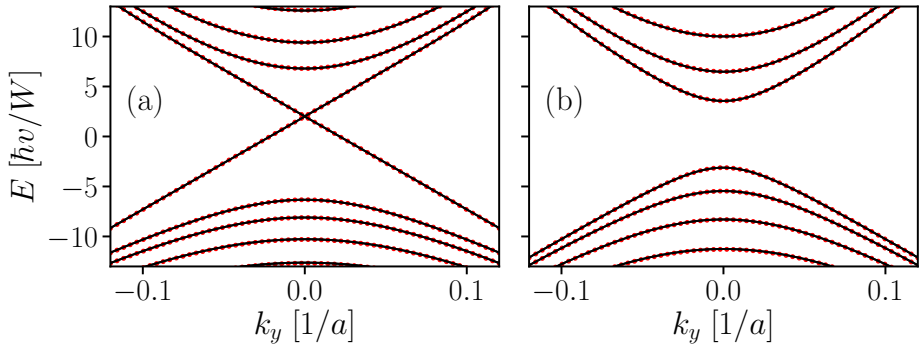

Figure 4.2: Dispersion relations of a topological insulator nanoribbon of width W in the (a) topological and (b) trivial phase. The dispersions are computed with a tight binding model that simply terminates at the ribbon edges (solid lines), and using the continuum dispersion finding algorithm of Section 4.3 with corresponding normal hard-wall boundary conditions (red dots). Although the system is gapped in the trivial phase, helical bands of edge states manifest in the gap in the topological phase. Parameters are $A \equiv \hbar v = 0.09$, $B/A = -2$, $C = 0$ and $D/A = -0.72$, with $M/A = -0.056$ in (a) and $M/A = 0.022$ in (b).

four electron- (E) or hole-like (H) orbitals $[|E,{}^1\!/_2\rangle, |H,{}^3\!/_2\rangle, |E,-{}^1\!/_2\rangle, |H,-{}^3\!/_2\rangle]^T$ per primitive unit cell, where the second index is the magnetic quantum number. The tight binding Hamiltonian is

$$H(\mathbf{k}) = \begin{bmatrix} h(\mathbf{k}) & 0 \\ 0 & h^*(-\mathbf{k}) \end{bmatrix}, \tag{4.53}$$

with

$$h(\mathbf{k}) = \mathbf{d}(\mathbf{k}) \cdot \boldsymbol{\tau}, \tag{4.54}$$

where $\boldsymbol{\tau} = (\tau_0, \tau_x, \tau_y, \tau_z)$ is the vector of Pauli matrices in electron-hole space including also the identity, and $\mathbf{d}(\mathbf{k}) = (d_0, d_x, d_y, d_z)$ with

$$\begin{aligned} d_0(\mathbf{k}) &= C - 4D + 2D(\cos k_x + \cos k_y) \\ d_x(\mathbf{k}) &= A \sin k_x \\ d_y(\mathbf{k}) &= A \sin k_y \\ d_z(\mathbf{k}) &= M - 4B + 2B(\cos k_x + \cos k_y), \end{aligned} \tag{4.55}$$

where A, B, C and D are material parameters. We scale all lengths and wave numbers in terms of the lattice constant a. The tight binding onsite Hamiltonian is thus

$$H_0 = M\sigma_0\tau_z + C\sigma_0\tau_0 - 4B\sigma_0\tau_z - 4D\sigma_0\tau_0, \tag{4.56}$$

and the hoppings along the x and y directions

$$\begin{aligned} T_x &= i\frac{A}{2}\sigma_z\tau_x + B\sigma_0\tau_z + D\sigma_0\tau_0, \\ T_y &= i\frac{A}{2}\sigma_0\tau_y + B\sigma_0\tau_z + D\sigma_0\tau_0, \end{aligned} \tag{4.57}$$

with σ_i the Pauli matrices and identity acting in spin space.

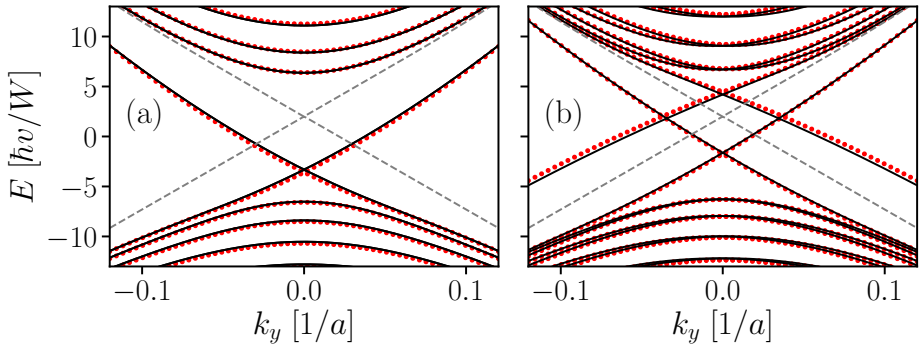

Figure 4.3: (solid lines) Tight binding dispersions of the quantum spin Hall nanoribbon with edge potentials V_L and V_R that are (a) symmetric ($V_L/A = V_R/A = -2.22$), and (b) asymmetric ($V_L/A = -1.78$, $V_R/A = 0.89$). (Dots) Ribbon dispersions computed using the continuum model supplemented with boundary conditions (4.52) that match the tight binding boundaries. For comparison, the dispersion of the edge states with no edge potentials is shown with dashed lines, illustrating the shift in the edge bands caused by the edge potentials. Asymmetric edge potentials split the edge bands belong to opposite edges. Parameters are the same as in Fig. 4.2(b).

We obtain the continuum BHZ Hamiltonian by expanding the tight binding Hamiltonian around the Γ point. It has the same form as the tight binding Hamiltonian given in Eqs. (4.53) and (4.54), but with

$$\begin{aligned} d_0(\mathbf{k}) &= C - D(k_x^2 + k_y^2) \\ d_x(\mathbf{k}) &= Ak_x \\ d_y(\mathbf{k}) &= Ak_y \\ d_z(\mathbf{k}) &= M - B(k_x^2 + k_y^2). \end{aligned} \tag{4.58}$$

4.5.2. DISPERSION RELATION OF A RIBBON

We now investigate the dispersion relations of nanoribbons with different boundary conditions. Using the tight binding BHZ model, we compute the dispersion of ribbons with various edge perturbations, and by applying the methods of Sections 4.3 and 4.4, compare the results with a corresponding calculation employing the continuum BHZ model supplemented with the appropriate boundary conditions. The nanoribbon is translationally invariant along the y-direction, and confined to a width $W = 100$ along the x-direction. For the tight binding model, we invoke Bloch's theorem along the y-direction to obtain an effective quasi-one dimensional system at each momentum k_y, such that the onsite and hopping along x in the notation of Section 4.4 are

$$\begin{aligned} H_L &= H_0 + T_y e^{-ik_y} + T_y^\dagger e^{ik_y}, \\ T_L &= T_x. \end{aligned} \tag{4.59}$$

Figure 4.2 shows the dispersion of the ribbon in the topological [(a)] and trivial [(b)] phase, computed using both the tight binding model, and the continuum model with the dispersion solver of Section 4.3. Here, the tight binding model simply terminates

at the ribbon edges, which in the continuum model corresponds the normal hard-wall boundary conditions $Q_j = -I$ in Eq. (4.19c) for the left ($j = L$) and right ($j = R$) boundaries, respectively. The continuum and tight binding computations of the dispersion agree perfectly. While the system is gapped in the trivial phase, helical edge bands appear in the gap in the topological phase.

Because the edge states are localized near the ribbon edges, they are strongly affected by potentials that are local to the edge [41]. In contrast, edge potentials couple only weakly to the bulk states, which are primarily localized in the interior of the ribbon. Using the tight binding model, we include extra scalar edge potentials V_L and V_R in the final cell adjacent to the left and right boundary, respectively. In order to map the left and right boundaries with edge potentials to boundary conditions Q_L and Q_R for the continuum BHZ model, we use Eq. (4.52) with Φ_c the 4×4 identity, and

$$\begin{aligned} H_S &= H_L + V_L \sigma_0 \tau_0,\ T_S = T_L \text{ for } Q_L, \\ H_S &= H_L + V_R \sigma_0 \tau_0,\ T_S = T_L^\dagger \text{ for } Q_R. \end{aligned} \tag{4.60}$$

Here, H_L and T_L are given in (4.59), and we solve for the boundary condition in the continuum limit $E = 0$ and $k_y = 0$. Imposing the boundary conditions (4.19c) at the left and right boundaries, we then compute the dispersion of the ribbon using the continuum algorithm of Section 4.3. Figure 4.3 compares the results of the tight binding computation with the calculation using the continuum model supplemented with the boundary conditions, with symmetric edge potentials $V_L = V_R$ in (a) and asymmetric potentials $V_L \neq V_R$ in (b). The agreement between the continuum and tight binding calculations is reasonably good. Comparing with Fig. 4.2, the edge potentials indeed shift the edge states more prominently than the bulk bands, a feature which the boundary conditions capture. At a given edge, the edge states couples mostly to the potential local to the edge, such that applying different potentials to the two boundaries splits the edge bands belonging opposite edges. Such asymmetric edge potentials break the inversion symmetry of the ribbon, causing energy splitting of the bulk bands at finite momentum, which is captured by the boundary conditions.

The counterpropagating edge bands at a ribbon boundary are Kramers partners, and backscattering between them is thus forbidden so long as time-reversal symmetry $\mathcal{T} = i\sigma_y \tau_0$ is unbroken. Hence, the ribbon remains gapless even in the presence of edge potentials which preserve time-reversal symmetry, as Fig. 4.3 shows. On the other hand, adding a magnetic edge potential breaks time-reversal symmetry locally, which couples the edge bands and opens up an energy gap. In the tight binding model, we include magnetic edge potentials U_L and U_R in the final cell adjacent to the left and right boundary, respectively. The corresponding continuum boundary conditions Q_L and Q_R follow from (4.52) with

$$\begin{aligned} H_S &= H_L + U_L \sigma_x \tau_0,\ T_S = T_L \text{ for } Q_L, \\ H_S &= H_L + U_R \sigma_x \tau_0,\ T_S = T_L^\dagger \text{ for } Q_R. \end{aligned} \tag{4.61}$$

In Fig. 4.4, we compare the dispersion from tight binding with the calculation using the continuum model with boundary conditions using the algorithm of Section 4.3, with symmetric magnetic edge potentials $U_L = U_R$ in (a) and asymmetric $U_L \neq U_R$ in (b),

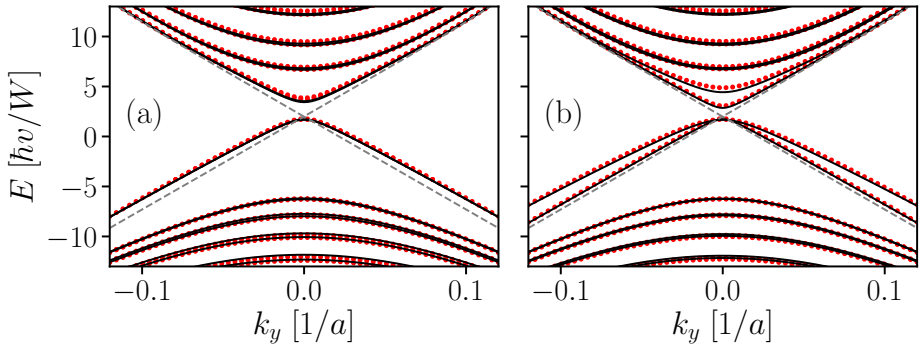

Figure 4.4: (solid lines) Tight binding dispersions of the quantum spin Hall nanoribbon with magnetic edge potentials U_L and U_R that are (a) symmetric ($U_L/A = U_R/A = -0.89$), and (b) asymmetric ($U_L/A = -0.67$, $U_R/A = 1.11$). (Dots) Ribbon dispersions computed using the continuum model supplemented with boundary conditions (4.52) that match the tight binding boundaries. The magnetic edge potentials break time-reversal symmetry locally at the edges, which couples the edge bands and opens up an energy gap. For comparison, the dashed lines show the edge bands in the absence of magnetic edge potentials. If the magnetic potentials are asymmetric, the splitting of the edge bands differs between the two edges, revealing all four edge bands. Parameters are the same as in Fig. 4.2(b).

and see that the results match reasonably well. The magnetic edge potentials break time-reversal symmetry because $[\mathcal{T}, \sigma_x\tau_0] \neq 0$, such that the edge states couple and a gap opens. The potential local to a boundary mostly governs the coupling between the edge bands at the boundary in question, and hence their energy splitting. If the magnetic potentials are symmetric, the edge states belonging to each edge therefore gap out in equal measure, such that the edge bands remain doubly degenerate. With asymmetric potentials, different coupling at each edge splits the edge bands of the two edges differently, showing all four edge bands. The continuum boundary conditions capture these features, in addition to small spin-splitting in the bulk bands, by mixing opposite spin projections.

If we map a boundary condition matrix Q including a magnetic edge potential back to the skew-Hermitian parametrization (4.5) by inverting the transformation (4.19c), we find that the boundary conditions have the form

$$\alpha = \alpha_0 + \alpha', \tag{4.62a}$$

$$\alpha_0 = i\sigma_0(c_0\tau_0 + c_1\tau_z) + ic_3\sigma_z\tau_y, \tag{4.62b}$$

$$\alpha' = i\sigma_x(c_4\tau_0 + c_5\tau_z) + ic_6\sigma_y\tau_x, \tag{4.62c}$$

with real parameters c_n. Here, α' is the component of the boundary conditions due to the magnetic edge potential, i.e. $\alpha = \alpha_0$ in the absence of a magnetic edge potential. The boundary condition preserves time-reversal symmetry if $[\mathcal{T}, \alpha v_x] = 0$ [see Eq. (4.9)], where the normal projection of the continuum BHZ velocity operator $v_x = \partial H/\partial k_x$ is

$$v_x = -2\sigma_0(D\tau_0 + B\tau_z)k_x + A\sigma_z\tau_x. \tag{4.63}$$

We have $\{v_x, \mathcal{T}\} = 0$, and therefore the boundary condition preserves time-reversal if $\{\mathcal{T}, \alpha\} = 0$. Indeed, we have $\{\mathcal{T}, \alpha_0\} = 0$ but $\{\mathcal{T}, \alpha'\} \neq 0$, and the contribution from the

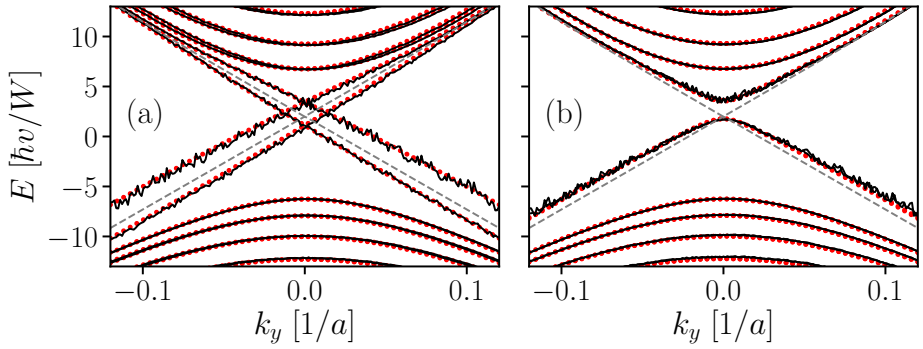

Figure 4.5: (solid lines) Tight binding dispersions of a quantum spin Hall nanoribbon with a translation unit cell of lateral width $L = 20$ along y, and random onsite potentials added to the outermost sites that are (a) scalar, or (b) magnetic. (Dots) Dispersion of a ribbon computed using the continuum model combined with boundary conditions (4.52) matching the tight binding boundaries. The dashed lines are the dispersion of a ribbon in the absence of edge disorder. The continuum calculation captures the main features of the tight binding dispersion, shifts or gap openings in the edge dispersion, but does not capture the fluctuations in the edge band dispersion which are caused by disorder. Parameters are the same as in Fig. 4.2(b).

magnetic edge potential therefore breaks the symmetry, which leads to the mixing of opposite spin projections in the boundary condition. Finally, we note that with an edge potential that is scalar instead of magnetic, as in the preceding paragraph, the boundary condition has the form α_0, and therefore preserves time-reversal symmetry, as expected.

In the preceding paragraphs, the translation unit cell of the tight binding model is identical to the primitive unit cell, and the use of the projectors Φ_c when matching the tight binding boundary to a continuum boundary condition therefore unnecessary. To demonstrate their use, we consider a tight binding translation unit cell of lateral width $L = 20$ primitive unit cells along the y-direction, and compute the dispersion of ribbons with edge disorder at the outermost sites, which is either scalar or magnetic. Because the continuum basis orbitals are the orbitals in a single primitive unit cell of the tight binding model, the projector is proportional to the identity in each primitive unit cell, and is given by

$$\Phi_c = \frac{1}{\sqrt{L}}[\overbrace{I_{4\times4}, I_{4\times4}, \ldots, I_{4\times4}}^{L \text{ times}}]^T. \tag{4.64}$$

The projector thus averages the boundary condition over the lateral width of the unit cell. As before, we map the disordered edges to continuum boundary conditions Q_L and Q_R using Eq. (4.52). Figure 4.5 compares the tight binding and continuum computations for a ribbon with random potentials added to the outermost sites that are scalar in (a) and magnetic in (b). Although scalar disorder shifts the edge bands, the system remains gapless, while magnetic disorder opens an energy gap. The edge disorder causes fluctuations in the dispersion of the edge bands, which the continuum boundary condition does not capture. Aside from these oscillations however, the continuum calculation with the boundary condition matches the structure of the tight binding dispersion, and captures the overall shift and gap opening in the edge dispersion.

4.6. SUMMARY

In summary, we have shown that general boundary conditions for a continuum Hamiltonian that conserve probability current are given in terms of a skew-Hermitian matrix parameter. With the parametrization, it is straightforward to classify boundary conditions depending on which symmetries they preserve or break, which is useful in the context of symmetry protected topological phases. An alternative parametrization in terms of a unitary matrix using the Cayley transformation may be more useful in practice, because it avoids dealing with diverging elements of the skew-Hermitian parametrization, which are still physically acceptable boundary conditions. We derived a numerically stable algorithm to compute the spectrum of a continuum Hamiltonian confined between two parallel boundaries with arbitrary boundary conditions, and have shown that it can calculate both bulk and edge states of confinements. Furthermore, we have derived equations which allow one to fold a tight binding boundary into an effective boundary condition for the corresponding continuum model, with the boundary condition a function of the boundary tight binding parameters. This makes it possible to simulate a specific tight binding boundary using the continuum Hamiltonian in combination with a boundary condition. Finally, we have applied our techniques to the edges of a two-dimensional topological insulator with the BHZ model, to study the effects of edge potentials on the topological edge bands. We have shown that it is possible to approximate the effects of scalar or magnetic tight binding edge potentials on the dispersion of nanoribbons by using a boundary condition for the continuum BHZ model.

4.7. APPENDIX

4.7.1. PROOF OF THE COMPLETENESS OF THE BOUNDARY CONDITIONS PARAMETRIZATION

We show that the parametrization Eq. (4.5) is equivalent to the condition of vanishing normal current at the boundary (4.4), and hence a complete parametrization of all solutions to the vanishing normal current constraint. Our strategy is to consider an alternative parametrization with built-in redundancies, which makes the equivalence simpler to prove, and then show that it reduces to the original parametrization (4.5).

Motivated by (4.5), we define an extended vector at the boundary $\boldsymbol{x} = \boldsymbol{x}_B$ by stacking $\psi(\boldsymbol{x}_B)$ and $v_\perp\psi(\boldsymbol{x}_B)$

$$\Psi(\boldsymbol{x}_B) = \left[\psi, v_\perp\psi\right]^T = \left[\langle \boldsymbol{x}_B|\,\psi\rangle, \langle \boldsymbol{x}_B|\,v_\perp\psi\rangle\right]^T. \tag{4.65}$$

For the boundary condition, we assume a linear constraint on the extended spinor

$$B\Psi = \Psi, \tag{4.66}$$

with B a complex matrix. The spinor Ψ has $2N_c$ elements, and B is $2N_c \times 2N_c$. The Hamiltonian (4.1) is an ordinary differential equation in $k_\perp$ of order 2 (quadratic), or 1 (linear) if $h_2 = 0$, and must thus be supplemented with a total of $2N_c$ boundary conditions to be well-posed if it is quadratic, or N_c boundary conditions if it is linear. Assuming that the total confinement is formed by two parallel and independent boundaries, as is the case in quantum wells or ribbons, we impose half of the boundary conditions at

each boundary, and thus require N_c (quadratic) or $N_c/2$ (linear) boundary conditions at a single boundary. As a result, (4.66) implies that B has eigenvalue 1 in a subspace that is at most N_c-dimensional and contains Ψ, with the remaining degrees of freedom redundant. Without loss of generality, we may thus pick B such that it has the eigenvalue -1 in the orthogonal subspace, which is at least N_c-dimensional, such that B is both Hermitian and unitary [18]:

$$B^\dagger = B^{-1} = B. \tag{4.67}$$

In the extended representation, the vanishing normal current constraint (4.4) is

$$j_\perp(\boldsymbol{x}_B) = \Psi^\dagger(\boldsymbol{x}_B) J_\perp \Psi(\boldsymbol{x}_B) = 0, \tag{4.68}$$

where $J_\perp = \sigma_x \otimes I_{N_c}$, with I_{N_c} the N_c-dimensional identity matrix, is the current density operator in the extended representation.

We now prove that the requirement of vanishing current normal to the boundary (4.68) is equivalent to the anticommutation relation

$$\{B, J_\perp\} = 0. \tag{4.69}$$

To see that (4.69) implies (4.68), observe that

$$\begin{aligned} j_\perp(\boldsymbol{x}_B) &= \Psi^\dagger(\boldsymbol{x}_B) J_\perp \Psi(\boldsymbol{x}_B) \\ &= \Psi^\dagger(\boldsymbol{x}_B) B J_\perp B \Psi(\boldsymbol{x}_B) \\ &= -\Psi^\dagger(\boldsymbol{x}_B) J_\perp \Psi(\boldsymbol{x}_B) \\ &= -j_\perp(\boldsymbol{x}_B) \\ &\Rightarrow j_\perp(\boldsymbol{x}_B) = 0, \end{aligned} \tag{4.70}$$

where we used Eq. (4.66) and its Hermitian conjugate, and that $B^\dagger = B = B^{-1}$. To see that Eq. (4.68) implies Eq. (4.69), recall that vectors $\Psi(\boldsymbol{x}_B)$ which satisfy the boundary conditions live in the eigensubspace of B with eigenvalue 1 of dimension N', where $N' = N_c$ or $N_c/2$, and that the orthogonal $2N_c - N'$ dimensional eigensubspace has the eigenvalue -1. In terms of an eigenbasis of B, the matrices B and $J_\perp$ are thus

$$B = \begin{bmatrix} I_{N'} & 0 \\ 0 & -I_{2N_c - N'} \end{bmatrix}, \quad J_\perp = \begin{bmatrix} A & D \\ D^\dagger & C \end{bmatrix}, \tag{4.71}$$

where the matrices A, D and C are $N' \times N'$, $N' \times (2N_c - N')$ and $(2N_c - N') \times (2N_c - N')$, respectively. Because the vanishing current constraint $j_\perp(\boldsymbol{x}_B) = \Psi^\dagger J_\perp \Psi = 0$ holds for any extended spinor Ψ satisfying the boundary conditions, i.e. for any Ψ in the N'-dimensional subspace of eigenvectors of B with eigenvalue 1, we have $A = 0$. Furthermore,

$$\begin{aligned} J_\perp^2 &= \begin{bmatrix} 0 & I_{N_c} \\ I_{N_c} & 0 \end{bmatrix} \begin{bmatrix} 0 & I_{N_c} \\ I_{N_c} & 0 \end{bmatrix} = \begin{bmatrix} I_{N_c} & 0 \\ 0 & I_{N_c} \end{bmatrix} \\ &= \begin{bmatrix} DD^\dagger & DC \\ CD^\dagger & D^\dagger D + C^2 \end{bmatrix}, \end{aligned} \tag{4.72}$$

and therefore $DD^\dagger = I_{N'}$, $D^\dagger D = I_{2N_c-N'}$ and $C = 0$. Hence,

$$\begin{aligned}\{B, J_\perp\} &= \begin{bmatrix} I_{N'} & 0 \\ 0 & -I_{2N_c-N'} \end{bmatrix} \begin{bmatrix} 0 & D \\ D^\dagger & 0 \end{bmatrix} + \\ &\quad \begin{bmatrix} 0 & D \\ D^\dagger & 0 \end{bmatrix} \begin{bmatrix} I_{N'} & 0 \\ 0 & -I_{2N_c-N'} \end{bmatrix} \\ &= \begin{bmatrix} 0 & D \\ -D^\dagger & 0 \end{bmatrix} + \begin{bmatrix} 0 & -D \\ D^\dagger & 0 \end{bmatrix} \\ &= 0,\end{aligned} \tag{4.73}$$

which concludes the proof.

We have shown that with the parametrization Eq. (4.66), the vanishing normal current condition (4.68) is equivalent to the anticommutation relation (4.69). We now show that with the anticommutation relation (4.69), the boundary condition parametrization (4.66) is equivalent to the parametrization (4.5) with $\alpha^\dagger = -\alpha$. Because B is Hermitian, it has the block structure

$$B = \begin{bmatrix} X & Y \\ Y^\dagger & Z \end{bmatrix}. \tag{4.74}$$

where X, Y and Z are $N_c \times N_c$ matrices, $X^\dagger = X$ and $Z^\dagger = Z$. Anticommutation with $J_\perp = \sigma_x \otimes I_{N_c}$ gives

$$\begin{aligned}\{B, J_\perp\} &= \begin{bmatrix} Y + Y^\dagger & X + Z \\ Z + X & Y^\dagger + Y \end{bmatrix} = 0 \\ &\Rightarrow X = -Z, \quad Y = -Y^\dagger,\end{aligned} \tag{4.75}$$

and therefore

$$B = \begin{bmatrix} X & Y \\ -Y & -X \end{bmatrix}. \tag{4.76}$$

Because $B^\dagger = B = B^{-1}$, we furthermore have

$$B^2 = \begin{bmatrix} X^2 - Y^2 & XY - YX \\ XY - YX & X^2 - Y^2 \end{bmatrix} = \begin{bmatrix} I_{N_c} & 0 \\ 0 & I_{N_c} \end{bmatrix} \tag{4.77}$$

which shows that

$$X^2 - Y^2 = I_{N_c}, \quad [X, Y] = 0. \tag{4.78}$$

To summarize, the boundary conditions that give vanishing normal current at the boundary are given by

$$\begin{bmatrix} X & Y \\ -Y & -X \end{bmatrix} \begin{bmatrix} \psi \\ v_\perp \psi \end{bmatrix} = \begin{bmatrix} \psi \\ v_\perp \psi \end{bmatrix}, \tag{4.79a}$$

$$X^2 - Y^2 = I_{N_c}, \quad [X, Y] = 0, \tag{4.79b}$$

$$X^\dagger = X, \quad Y^\dagger = -Y. \tag{4.79c}$$

Because Y is skew-Hermitian, it is diagonalizable with a unitary transformation V, i.e.

$$Y = iV\Lambda_y V^\dagger, \quad V^\dagger = V^{-1}, \quad \Lambda_y = \mathrm{diag}(\lambda_{1y}, \lambda_{2y}, ..., \lambda_{N_c y}), \tag{4.80}$$

where $\lambda_{jy} \in \mathbb{R}$, and $i\lambda_{jy}$ are the purely complex eigenvalues of Y. It follows that

$$Y^2 = -V\Lambda_y V^\dagger V\Lambda_y V^\dagger = -V\Lambda_y^2 V^\dagger, \tag{4.81}$$

where $\Lambda_y^2 = \mathrm{diag}(\lambda_{1y}^2, \lambda_{2y}^2, ..., \lambda_{N_c y}^2)$. Because $X^2 - Y^2 = I_{N_c}$, we have

$$X^2 = I_{N_c} + Y^2 = V\left(I_{N_c} - \Lambda_y^2\right)V^\dagger, \tag{4.82}$$

which shows that V also diagonalizes X^2, and therefore also X, which is not surprising because $[X, Y] = 0$. Denoting the eigenvalues of X by λ_{jx}, we thus have $X = V\Lambda_x V^\dagger$ with $\Lambda_x = \mathrm{diag}(\lambda_{jx})$ for $0 \leq j \leq N_c$, where

$$\Lambda_x^2 = I_{N_c} - \Lambda_y^2 \Leftrightarrow \lambda_{jx}^2 + \lambda_{jy}^2 = 1, \quad i = 1, 2, .., N_c. \tag{4.83}$$

Because $X^\dagger = X$ and $Y^\dagger = -Y$, X^2 is positive semidefinite and Y^2 negative semidefinite, i.e. the eigenvalues λ_{jx}^2 of X^2 are strictly positive, and the eigenvalues $-\lambda_{jy}^2$ of Y^2 strictly negative [42]. Therefore, $\lambda_{jx}^2, \lambda_{jy}^2 \geq 0\ \forall j$, and because $\lambda_{ix}^2 + \lambda_{iy}^2 = 1$, we have

$$0 \leq \lambda_{jx}^2, \lambda_{jy}^2 \leq 1 \Leftrightarrow 0 \leq |\lambda_{ix}|, \left|\lambda_{iy}\right| \leq 1, \quad \forall j. \tag{4.84}$$

Writing out the matrix equation (4.79a) explicitly gives

$$\begin{aligned} & X\psi + Y\nu_\perp\psi = \psi \ \text{ and } \ -Y\psi - X\nu_\perp\psi = \nu_\perp\psi \\ \Leftrightarrow\ & (1-X)\psi = Y\nu_\perp\psi \ \text{ and } \ Y\psi = -(1+X)\nu_\perp\psi \\ \Leftrightarrow\ & \psi = (1-X)^{-1}Y\nu_\perp\psi \ \text{ and } \ \psi = -Y^{-1}(1+X)\nu_\perp\psi. \end{aligned} \tag{4.85}$$

In the last step, we have assumed that the matrices $(1-X)$ and Y are invertible, i.e. that neither has a vanishing eigenvalue. Because of Eqs. (4.83) and (4.84), we have

$$\lambda_{jx} = \mp\sqrt{1-\lambda_{jy}^2}, \quad -1 \leq \lambda_{jy} \leq 1 \qquad \forall j, \tag{4.86}$$

which shows that the matrices are invertible if $\lambda_{iy} \neq 0\ \forall j$. We will make this assumption for now, and examine the limit $\lambda_{jy} \to 0$ at a later stage. We then also have

$$\begin{aligned} Y^2 &= X^2 - 1 = (X+1)(X-1) \\ &= -(X+1)(1-X) \\ \Leftrightarrow\ & Y(1-X)^{-1} = -Y^{-1}(X+1). \end{aligned} \tag{4.87}$$

Plugging this into the last line of Eq. (4.85) yields

$$\begin{aligned} & \psi = (1-X)^{-1}Y\nu_\perp\psi \ \text{ and } \ \psi = -Y^{-1}(1+X)\nu_\perp\psi \\ \Leftrightarrow\ & \psi = (1-X)^{-1}Y\nu_\perp\psi \ \text{ and } \ \psi = Y(1-X)^{-1}\nu_\perp\psi. \end{aligned} \tag{4.88}$$

Because $\lambda_{jy} \neq 0$, we have $\left|\lambda_{jx}\right| < 1$ and can expand $(1-X)^{-1}$ as a power series in X. Using also $[X, Y] = 0$, one obtains

$$(1-X)^{-1} = 1 + X + X^2 + ... \Rightarrow [(1-X)^{-1}, Y] = 0. \tag{4.89}$$

The two equations in the second line of Eq. (4.88) are thus equivalent, so the boundary conditions are fully contained in the single matrix equation

$$\psi = (1-X)^{-1} Y v_\perp \psi \equiv \alpha v_\perp \psi, \tag{4.90}$$

where the $N_c \times N_c$ matrix α satisfies

$$\begin{aligned} \alpha^\dagger &= \left[(1-X)^{-1}Y\right]^\dagger = Y^\dagger (1-X^\dagger)^{-1} \\ &= -Y(1-X)^{-1} = -(1-X)^{-1}Y \\ &= -\alpha, \end{aligned} \tag{4.91}$$

and is therefore skew-Hermitian.

Equations (4.79b) and (4.79c) show that there are constraints on the matrices X and Y. To see if they constrain the form of α in any other way than making it skew-Hermitian, let us look at the spectrum of α. That α is skew-Hermitian means that its eigenvalues are all purely complex numbers, living on the imaginary axis $i\mathbb{R}$. We have

$$\begin{aligned} \alpha &= (1-X)^{-1}Y \\ &= iV(1-D_x)^{-1}D_y V^\dagger \\ &= iVD_\alpha V^\dagger, \end{aligned} \tag{4.92}$$

where iD_α is the diagonal matrix of eigenvalues of α, all of which are purely imaginary, with

$$\begin{aligned} D_\alpha &= \mathrm{diag}\left(\frac{\lambda_{1y}}{1-\lambda_{1x}}, \frac{\lambda_{2y}}{1-\lambda_{2x}}, ..., \frac{\lambda_{N_c y}}{1-\lambda_{N_c x}}\right) \\ &= \mathrm{diag}\left(\frac{\lambda_{1y}}{1 \mp \sqrt{1-\lambda_{1y}^2}}, ..., \frac{\lambda_{N_c y}}{1 \mp \sqrt{1-\lambda_{N_c y}^2}}\right), \end{aligned} \tag{4.93}$$

see also Eq. (4.86). To understand the spectrum of α, we thus look at the functions

$$F_\mp(\lambda_{jy}) = \frac{\lambda_{jy}}{1 \mp \sqrt{1-\lambda_{jy}^2}}, \qquad \lambda_{jy} \in [-1,1], \tag{4.94}$$

taking special care around the point $\lambda_{jy} = 0$. The functions $F_\mp$ are continuous in the intervals $[-1,0[$ and $]0,1]$. Furthermore,

$$F_+(-1) = -1,\ F_+(1) = 1, \tag{4.95a}$$

$$F_+(0) \to 0, \text{ as } \lambda_{iy} \to 0, \tag{4.95b}$$

$$F_-(-1) = -1,\ F_-(1) = 1, \tag{4.95c}$$

$$F_-(\lambda_{jy}) \to \pm\infty, \text{ as } \lambda_{jy} \to 0^\pm. \tag{4.95d}$$

which shows that the combined range of the functions $F_\mp$ is $\mathbb{R}$, and therefore the eigenvalues of α can generally take any value on the axis $i\mathbb{R}$. We thus conclude that in the general case, the only thing assertible about α is that it is skew-Hermitian.

To sum up, we have shown that at a single, isolated boundary, the boundary condition parametrization

$$\psi(\boldsymbol{x}_B) = \alpha\, \nu_\perp \psi(\boldsymbol{x}_B),\ \alpha^\dagger = -\alpha, \tag{4.96}$$

is equivalent to the requirement of vanishing current density normal to the boundary.

4.7.2. SELF-ADJOINT EXTENSION OF A HAMILTONIAN BOUNDED BY A SINGLE BOUNDARY

Because it is an observable, a Hamiltonian must be self-adjoint, which means that it must be Hermitian $H^\dagger = H$, and satisfy

$$\langle \phi | H\psi \rangle = \langle H\phi | \psi \rangle \tag{4.97}$$

for any ϕ, ψ in the Hilbert space [25, 26]. In an unbounded space, any Hermitian Hamiltonian is self-adjoint, because elements of the Hilbert space are square integrable, and therefore vanish at $\pm\infty$. As a result, the boundary terms at $\pm\infty$ vanish in the integration by parts to show that (4.97) holds. In a bounded system however, the integration by parts gives rise to surface terms that have to cancel or vanish for (4.97) to hold, resulting in extra constraints at the boundaries that the self-adjoint Hamiltonian must obey. In this Appendix, we show that imposing boundary conditions from the parametrization (4.5) on the wave functions automatically gives a self-adjoint Hamiltonian.

As in the main text, we consider the Hamiltonian (4.1) confined to the half-plane $x_\perp \leq x_\perp^B$. To check the self-adjointness condition (4.97), we take the left hand side

$$\langle \phi | H\psi \rangle = \int_{-\infty}^{x_\perp^B} \phi^\dagger(x_\perp) \left[h_0 + h_1 \hat{k}_\perp + h_2 \hat{k}_\perp^2 \right] \psi(x_\perp) \mathrm{d}x_\perp, \tag{4.98}$$

and integrate by parts, neglecting the direction $x_\parallel$ to simplify notation, but without loss of generality. The zeroth order term in $k_\perp$ is manifestly self-adjoint, because $\phi^\dagger h_0 \psi = (h_0\phi)^\dagger \psi$. Using $\hat{k}_\perp = -i\partial_{x_\perp}$ and integrating the first order term by parts gives

$$\langle h_1 k_\perp \phi | \psi \rangle - \langle \phi | h_1 k_\perp \psi \rangle = i \{h_1 \phi(x_\perp^B)\}^\dagger \psi(x_\perp^B), \tag{4.99}$$

where the right hand side is equivalent to

$$\begin{aligned} & i\{h_1\phi(x_\perp^B)\}^\dagger \psi(x_\perp^B) \\ =& \frac{i}{2}[\{h_1\phi(x_\perp^B)\}^\dagger \psi(x_\perp^B) + \phi^\dagger(x_\perp^B) h_1 \psi(x_\perp^B)] \\ =& \frac{i}{2}(\langle\phi| h_1 |x_\perp^B\rangle\langle x_\perp^B|\psi\rangle + \langle\phi| x_\perp^B\rangle\langle x_\perp^B| h_1 |\psi\rangle) \\ =& \frac{i\hbar}{2}(\langle\phi| v_1 |x_\perp^B\rangle\langle x_\perp^B|\psi\rangle + \langle\phi| x_\perp^B\rangle\langle x_\perp^B| v_1 |\psi\rangle), \end{aligned} \tag{4.100}$$

using the velocity operator in Eq. (4.3). Evaluating the second order term gives

$$\begin{aligned}
&\langle h_2 k_\perp^2 \phi|\psi\rangle - \langle\phi|h_2 k_\perp^2 \psi\rangle \\
&= i\phi^\dagger(x_\perp^B) h_2 \frac{\partial_{x_\perp}}{i}\psi(x_\perp^B) + i\{h_2 \frac{\partial_{x_\perp}}{i}\phi(x_\perp^B)\}^\dagger \psi(x_\perp^B) \\
&= i(\langle\phi| h_2 \hat{k}_\perp |x_\perp^B\rangle\langle x_\perp^B|\,\psi\rangle + \langle\phi|\,x_\perp^B\rangle\langle x_\perp^B| h_2 \hat{k}_\perp |\psi\rangle) \\
&= \frac{i\hbar}{2}(\langle\phi|\, v_2 \hat{k}_\perp |x_\perp^B\rangle\langle x_\perp^B|\,\psi\rangle + \langle\phi|\,x_\perp^B\rangle\langle x_\perp^B|\, v_2 \hat{k}_\perp |\psi\rangle).
\end{aligned} \tag{4.101}$$

Gathering terms and identifying the current operator of Eq. (4.2), we obtain

$$\langle H\phi|\psi\rangle - \langle\phi|H\psi\rangle = i\hbar\langle\phi|\, j_\perp(x_\perp^B)\,|\psi\rangle, \tag{4.102}$$

and the condition for a self-adjoint Hamiltonian is therefore

$$\langle\phi|\, j_\perp(x_\perp^B)\,|\psi\rangle = 0. \tag{4.103}$$

To see that supplementing the Hamiltonian with the boundary conditions (4.5) fulfills (4.103), we expand $|\phi\rangle$ and $|\psi\rangle$ in a basis of eigenfunctions $|\xi_n\rangle$ of the Hamiltonian with boundary conditions, i.e. $|\phi\rangle = \sum_n c_n|\xi_n\rangle$ and $|\psi\rangle = \sum_m d_m|\xi_n\rangle$. Inserting into (4.103), the Hamiltonian is self-adjoint if $\langle\xi_n|\, j_\perp(x_\perp^B)\,|\xi_m\rangle$ vanishes for all m, n. The eigenfunctions $|\xi_n\rangle$ are all solutions with the same boundary condition α, i.e. $\xi_n(x_\perp^B) = \alpha v_\perp \xi_n(x_\perp^B)$ for all n, such that

$$\begin{aligned}
&2\langle\xi_n|\, j_\perp(x_\perp^B)\,|\xi_m\rangle \\
&= \langle\xi_n|\, v_\perp |x_\perp^B\rangle\langle x_\perp^B|\,\xi_m\rangle + \langle\xi_n|\,x_\perp^B\rangle\langle x_\perp^B|\, v_\perp |\xi_m\rangle \\
&= \langle\xi_n|\, v_\perp |x_\perp^B\rangle\langle x_\perp^B|\,\alpha v_\perp|\xi_m\rangle - \langle\xi_n|\, v_\perp \alpha\,|x_\perp^B\rangle\langle x_\perp^B|\, v_\perp|\xi_m\rangle \\
&= 0,
\end{aligned} \tag{4.104}$$

for all m, n. Supplementing the bounded Hamiltonian with the boundary conditions (4.5) therefore ensures that the Hamiltonian is self-adjoint.

4.7.3. THE TIGHT BINDING VELOCITY OPERATOR

In this Appendix, we introduce the tight binding velocity operator. The Hamiltonian operator of the tight binding model in (4.32) is

$$\hat{H} = \sum_j (\hat{H}_{j,j-1} + \hat{H}_{j,j} + \hat{H}_{j,j+1},) \tag{4.105}$$

with j a real space index along the direction $x_\perp$, and where $\hat{H}_{i,j} = P_i H P_j$, with P_j the projector onto block j. The velocity operator along $x_\perp$ is

$$\hat{V}_\perp = \frac{i}{\hbar}[\hat{H}, \hat{x}_\perp], \tag{4.106}$$

where the tight binding coordinate operator is $\hat{x}_\perp = \sum_j \hat{x}_j = \sum_j P_j \hat{x}_\perp P_j$ [43]. The projectors are orthogonal, satisfying $P_i P_j = P_j \delta_{ij}$, so we have

$$\begin{aligned}\hat{V}_\perp &= \frac{i}{\hbar}\sum_{jk}[(\hat{H}_{j,j-1}+\hat{H}_{j,j}+\hat{H}_{j,j+1})\hat{x}_k \\ &\qquad -\hat{x}_k(\hat{H}_{j,j-1}+\hat{H}_{j,j}+\hat{H}_{j,j+1})] \\ &= \frac{i}{\hbar}\sum_j[P_j\hat{H}P_{j-1}\hat{x}_\perp P_{j-1}+P_j\hat{H}P_j\hat{x}_\perp P_j \\ &\qquad +P_j\hat{H}P_{j+1}\hat{x}_\perp P_{j+1}-P_j\hat{x}_\perp P_j\hat{H}P_{j-1} \\ &\qquad -P_j\hat{x}_\perp P_j\hat{H}P_j-P_j\hat{x}_\perp P_j\hat{H}P_{j+1}].\end{aligned} \tag{4.107}$$

If we assume that the position of individual sites in the unit cell is not important, only the coordinate of the unit cell itself matters. Assuming a lattice constant a and that cell j is at $x_\perp = ja$, we then have $P_j\hat{x}_\perp P_k = jaP_j$. Using $P_iP_j = P_j\delta_{ij}$, we then obtain

$$\begin{aligned}\hat{V}_\perp &= \frac{i}{\hbar}\sum_j[\hat{H}_{j,j-1}a(j-1)+\hat{H}_{j,j}aj+\hat{H}_{j,j+1}a(j+1) \\ &\qquad -aj\hat{H}_{j,j-1}-aj\hat{H}_{j,j}-aj\hat{H}_{j,j+1}] \\ &= \frac{ia}{\hbar}\sum_j[\hat{H}_{j,j+1}-\hat{H}_{j,j-1}].\end{aligned} \tag{4.108}$$

With $\mathbf{C} = \sum_j P_j\mathbf{C} = \sum_j \mathbf{C}_j$ containing the tight binding amplitudes in all the cells, we have

$$\begin{aligned}\hat{V}_\perp\mathbf{C} &= \frac{ia}{\hbar}\sum_{jk}[\hat{H}_{k,k+1}-\hat{H}_{k,k-1}]P_j\mathbf{C} \\ &= \frac{ia}{\hbar}\sum_k[\hat{H}_{k,k+1}\mathbf{C}_{k+1}-\hat{H}_{k,k-1}\mathbf{C}_{k-1}],\end{aligned} \tag{4.109}$$

The velocity at cell j is the projection onto the cell, i.e.

$$(V_\perp\mathbf{C})_j = \frac{ia}{\hbar}[\hat{H}_{j,j+1}\mathbf{C}_{j+1}-\hat{H}_{j,j-1}\mathbf{C}_{j-1}]. \tag{4.110}$$

In the following and in the main text, we scale the velocity operator with $a/\hbar$.

For the Hamiltonian of the translationally invariant bulk (4.33), Bloch's theorem gives $\mathbf{C}_{j+1} = e^{ik_\perp}\mathbf{C}_j$, such that the velocity projection (4.110) becomes

$$\begin{aligned}(V_\perp\mathbf{C})_j &= i[T_L^\dagger e^{ik_\perp}-T_L e^{-ik_\perp}]\mathbf{C} \\ &\approx i[T_L^\dagger - T_L + ik_\perp(T_L^\dagger+T_L)]\mathbf{C},\end{aligned} \tag{4.111}$$

where we have expanded the exponentials to first order in $k_\perp$ in the continuum limit $k_\perp \to 0$, and identify the continuum velocity operator

$$V_\perp^c = i[T_L^\dagger - T_L + ik_\perp(T_L^\dagger+T_L)]. \tag{4.112}$$

For the system with the boundary (4.34), in the cell $j = 0$ adjacent to the boundary, Eq. (4.110) gives

$$\begin{aligned} (V_\perp \mathbf{C})_0 &= -i[T_L^\dagger \mathbf{C}_1 - T_S \mathbf{C}_S] \\ \Leftrightarrow\ T_L^\dagger \mathbf{C}_1 &= T_S \mathbf{C}_S + i(V_\perp \mathbf{C})_0, \end{aligned} \tag{4.113}$$

with the extra minus because we take the projection along the negative $x_\perp$-direction, pointing outwards towards the boundary region.

4.7.4. CAYLEY TRANSFORMATION OF THE TIGHT BINDING BOUNDARY CONDITION.

To derive an expression for the unitary continuum boundary condition matrix $Q_c$in terms of the boundary tight binding matrices, we take the expression for α_{TB} in (4.41) and plug it into the Cayley transformation (4.51). We obtain

$$\begin{aligned} Q_c &= \frac{I - \Phi_c^\dagger \alpha_{\mathrm{TB}}^{-1} \Phi_c}{I + \Phi_c^\dagger \alpha_{\mathrm{TB}}^{-1} \Phi_c} \\ &= \frac{I - i\Phi_c^\dagger \left[H_L - 2T_S H_S^{-1} T_S^\dagger \right] \Phi_c}{I + i\Phi_c^\dagger \left[H_L - 2T_S H_S^{-1} T_S^\dagger \right] \Phi_c} \\ &= -I - \frac{2i}{\Phi_c^\dagger H_L \Phi_c - i - 2\Phi_c^\dagger T_S H_S^{-1} T_S^\dagger \Phi_c}, \end{aligned} \tag{4.114}$$

with the hidden energy dependence $H_L \to H_L - E$ and $H_S \to H_S - E$. We see that on the level of the tight binding matrices, the continuum projection amounts to substituting $H_L \to \Phi_c^\dagger H_L \Phi_c$ and $T_S \to \Phi_c^\dagger T_S$. Invoking the Woodbury matrix identity [44],

$$(A + UCV)^{-1} = A^{-1} - A^{-1} U \left(C^{-1} + VA^{-1}U \right)^{-1} VA^{-1}, \tag{4.115}$$

with $A = H_L - i$, $C = -2H_S^{-1}$, $U = \Phi_c^\dagger T_S$, and $V = T_S^\dagger \Phi_c$, we obtain the desired result

$$\begin{aligned} Q_c &= -I - 2i \left[\Phi_c^\dagger H_L \Phi_c - i - 2\Phi_c^\dagger T_S H_S^{-1} T_S^\dagger \Phi_c \right]^{-1} \\ &= -I - 2i \left(\Phi_c^\dagger H_L \Phi_c - i \right)^{-1} \left\{ I + \Phi_c^\dagger T_S \left[\frac{1}{2} H_S - \Phi_c T_S^\dagger \left(\Phi_c^\dagger H_L \Phi_c - i \right)^{-1} T_S \Phi_c \right]^{-1} \right. \\ &\qquad \left. \times T_S^\dagger \Phi_c \left(\Phi_c^\dagger H_L \Phi_c - i \right)^{-1} \right\}. \end{aligned} \tag{4.116}$$

REFERENCES

[1] A. H. Castro Neto, F. Guinea, N. M. R. Peres, K. S. Novoselov, and A. K. Geim, *The electronic properties of graphene,* Rev. Mod. Phys. **81**, 109 (2009).

[2] M. Z. Hasan and C. L. Kane, *Colloquium: Topological insulators,* Rev. Mod. Phys. **82**, 3045 (2010).

[3] X.-L. Qi and S.-C. Zhang, *Topological insulators and superconductors,* Rev. Mod. Phys. **83**, 1057 (2011).

[4] M. Sato and Y. Ando, *Topological superconductors: a review,* Rep. Prog. Phys. **80**, 076501 (2017).

[5] R. S. K. Mong and V. Shivamoggi, *Edge states and the bulk-boundary correspondence in dirac hamiltonians,* Phys. Rev. B **83**, 125109 (2011).

[6] A. Y. Kitaev, *Unpaired majorana fermions in quantum wires,* Phys. Usp. **44**, 131 (2001).

[7] S. B. Bravyi and A. Y. Kitaev, *Fermionic quantum computation,* Annals of Physics **298**, 210 (2002).

[8] J. E. Moore, *The birth of topological insulators,* Nature **464**, 194 EP (2010).

[9] A. Kitaev, *Periodic table for topological insulators and superconductors,* in *American Institute of Physics Conference Series*, American Institute of Physics Conference Series, Vol. 1134, edited by V. Lebedev and M. Feigel'Man (2009) pp. 22–30, arXiv:0901.2686 .

[10] S. Ryu, A. P. Schnyder, A. Furusaki, and A. W. W. Ludwig, *Topological insulators and superconductors: tenfold way and dimensional hierarchy,* New Journal of Physics **12**, 065010 (2010).

[11] H. Nielsen and M. Ninomiya, *The adler-bell-jackiw anomaly and weyl fermions in a crystal,* Physics Letters B **130**, 389 (1983).

[12] T. E. Clark, R. Menikoff, and D. H. Sharp, *Quantum mechanics on the half-line using path integrals,* Phys. Rev. D **22**, 3012 (1980).

[13] M. Carreau, E. Farhi, and S. Gutmann, *Functional integral for a free particle in a box,* Phys. Rev. D **42**, 1194 (1990).

[14] E. McCann and V. I. Fal'ko, *Symmetry of boundary conditions of the Dirac equation for electrons in carbon nanotubes,* J. Phys. Condens. Matter **16**, 2371 (2004).

[15] M. Kharitonov, J.-B. Mayer, and E. M. Hankiewicz, *Universality and stability of the edge states of chiral-symmetric topological semimetals and surface states of the luttinger semimetal,* Phys. Rev. Lett. **119**, 266402 (2017).

[16] K. Hashimoto, T. Kimura, and X. Wu, *Boundary conditions of weyl semimetals,* Progress of Theoretical and Experimental Physics **2017**, 053I01 (2017).

[17] A. V. Rodina, A. Y. Alekseev, A. L. Efros, M. Rosen, and B. K. Meyer, *General boundary conditions for the envelope function in the multiband k·p model,* Phys. Rev. B **65**, 125302 (2002).

[18] A. R. Akhmerov and C. W. J. Beenakker, *Boundary conditions for Dirac fermions on a terminated honeycomb lattice,* Phys. Rev. B **77**, 085423 (2008).

[19] A. Medhi and V. B. Shenoy, *Continuum theory of edge states of topological insulators: variational principle and boundary conditions,* Journal of Physics: Condensed Matter **24**, 355001 (2012).

[20] V. N. Men'shov, V. V. Tugushev, T. V. Menshchikova, S. V. Eremeev, P. M. Echenique, and E. V. Chulkov, *Modelling near-surface bound electron states in a 3d topological insulator: analytical and numerical approaches,* Journal of Physics: Condensed Matter **26**, 485003 (2014).

[21] V. V. Enaldiev, I. V. Zagorodnev, and V. A. Volkov, *Boundary conditions and surface state spectra in topological insulators,* JETP Letters **101**, 89 (2015).

[22] C. G. Péterfalvi, A. Kormányos, and G. Burkard, *Boundary conditions for transition-metal dichalcogenide monolayers in the continuum model,* Phys. Rev. B **92**, 245443 (2015).

[23] D. J. P. de Sousa, L. V. de Castro, D. R. da Costa, and J. M. Pereira, *Boundary conditions for phosphorene nanoribbons in the continuum approach,* Phys. Rev. B **94**, 235415 (2016).

[24] C.-K. Chiu, J. C. Teo, A. P. Schnyder, and S. Ryu, *Classification of topological quantum matter with symmetries,* Reviews of Modern Physics **88** (2016), 10.1103/RevModPhys.88.035005.

[25] G. Bonneau, J. Faraut, and G. Valent, *Self-adjoint extensions of operators and the teaching of quantum mechanics,* American Journal of Physics **69**, 322 (2001), https://doi.org/10.1119/1.1328351 .

[26] M. Tanhayi Ahari, G. Ortiz, and B. Seradjeh, *On the role of self-adjointness in the continuum formulation of topological quantum phases,* American Journal of Physics **84**, 858 (2016), https://doi.org/10.1119/1.4961500 .

[27] F. Kirtschig, *Topological* $\mathbf{k}\cdot\mathbf{p}$ *Hamiltonians and their applications to uniaxially strained Mercury telluride*, Ph.D. thesis, Dresden University of Technology (2017).

[28] A. R. Akhmerov and C. W. J. Beenakker, *Detection of valley polarization in graphene by a superconducting contact,* Phys. Rev. Lett. **98**, 157003 (2007).

[29] G. Golub and C. Van Loan, *Matrix Computations*, Matrix Computations (Johns Hopkins University Press, 2012).

[30] G. Peters and J. Wilkinson, $ax = \lambda bx$ *and the generalized eigenproblem,* SIAM Journal on Numerical Analysis **7**, 479 (1970), https://doi.org/10.1137/0707039 .

[31] F. Tisseur and K. Meerbergen, *The quadratic eigenvalue problem,* SIAM Review **43**, 235 (2001), https://doi.org/10.1137/S0036144500381988 .

[32] T. Ando, *Quantum point contacts in magnetic fields,* Phys. Rev. B **44**, 8017 (1991).

[33] H. Wu and D. W. L. Sprung, *Validity of the transfer-matrix method for a two-dimensional electron waveguide,* Applied Physics A **58**, 581 (1994).

[34] P. Středa and P. Šeba, *Antisymmetric spin filtering in one-dimensional electron systems with uniform spin-orbit coupling,* Phys. Rev. Lett. **90**, 256601 (2003).

[35] C. W. Groth, M. Wimmer, A. R. Akhmerov, and X. Waintal, *Kwant: a software package for quantum transport,* New Journal of Physics **16**, 063065 (2014).

[36] L. Brey and H. A. Fertig, *Electronic states of graphene nanoribbons studied with the dirac equation,* Phys. Rev. B **73**, 235411 (2006).

[37] D. H. Lee and J. D. Joannopoulos, *Simple scheme for surface-band calculations. i,* Phys. Rev. B **23**, 4988 (1981).

[38] P. A. Khomyakov, G. Brocks, V. Karpan, M. Zwierzycki, and P. J. Kelly, *Conductance calculations for quantum wires and interfaces: Mode matching and green's functions,* Phys. Rev. B **72**, 035450 (2005).

[39] S. Datta, *Electronic Transport in Mesoscopic Systems*, Cambridge Studies in Semiconductor Physics and Microelectronic Engineering (Cambridge University Press, 1995).

[40] B. A. Bernevig, T. L. Hughes, and S.-C. Zhang, *Quantum spin hall effect and topological phase transition in hgte quantum wells,* Science **314**, 1757 (2006), http://science.sciencemag.org/content/314/5806/1757.full.pdf .

[41] R. Skolasinski, D. I. Pikulin, J. Alicea, and M. Wimmer, *Robust Helical Edge Transport in Quantum Spin Hall Quantum Wells,* ArXiv e-prints (2017), arXiv:1709.04830 [cond-mat.mes-hall] .

[42] R. A. Horn and C. R. Johnson, eds., *Matrix Analysis* (Cambridge University Press, New York, NY, USA, 1986).

[43] J. Kudrnovský, V. Drchal, C. Blaas, P. Weinberger, I. Turek, and P. Bruno, *Ab initio theory of perpendicular magnetotransport in metallic multilayers,* Phys. Rev. B **62**, 15084 (2000).

[44] N. J. Higham, *Accuracy and Stability of Numerical Algorithms* (Society for Industrial and Applied Mathematics, Philadelphia, PA, USA, 1996).

5

PLATFORM FOR NODAL TOPOLOGICAL SUPERCONDUCTORS IN MONOLAYER MOLYBDENUM DICHALCOGENIDES

This chapter has been previously published as Lin Wang, Tomas Orn Rosdahl, and Doru Sticlet, *Platform for nodal topological superconductors in monolayer molybdenum dichalcogenides*, Phys. Rev. B **98**, 205411 (2018).

5.1. INTRODUCTION

Fully gapped topological superconductors (TSCs), characterized by a global topological invariant in the Brillouin zone, have been the subject of intense investigation in recent years. They provide a platform for the creation of the Majorana quasiparticle [1–3], which has promising applications in quantum information [4–6]. Nodal superconductors, *i.e.*, superconductors with nodal points or lines at the Fermi surface where the bulk gap vanishes, can also display nontrivial topological properties, becoming nodal TSCs [7–9]. Their topological invariants are only defined locally in the Brillouin zone, giving rise to flat bands or arcs of surface states in the nontrivial phase [10–12].

Intrinsic nodal TSCs are predicted to exist in unconventional superconductors, such as high-temperature d-wave superconductors [13], the heavy fermion systems [14–16], noncentrosymmetric superconductors [17, 18], and Weyl superconductors [19]. However, intrinsic unconventional pairing is complex and ambiguous, and is furthermore not robust to disorder, making intrinsic nodal TSCs challenging experimentally. It is therefore desirable to engineer nodal TSCs using simpler components [20–22], such as conventional s-wave spin-singlet superconductors, similar to efforts in realizing fully gapped TSCs using proximity-induced s-wave pairing [23, 24].

Two-dimensional monolayers of transition metal dichalcogenides (TMDs) [25] offer an opportunity to engineer nodal TSCs. Recent experiments show that several monolayer TMDs, such as MoS_2, $MoSe_2$, $MoTe_2$, WS_2, and $NbSe_2$, become superconducting [26–34], with a critical temperature *e.g.* as large as 10 K observed in MoS_2 [28]. These superconductors possess an extremely high critical in-plane magnetic field, several times larger than the Pauli limit, due to a special type of Ising spin-orbit coupling (SOC) [28, 30, 35, 36]. The Ising SOC results from the heavy atoms and the absence of inversion symmetry, and acts as an effective Zeeman term perpendicular to the TMD plane, with opposite orientation at opposite momenta, pinning electron spins to the out-of-plane direction [37, 38]. Previous work predicts that hole-doped monolayer $NbSe_2$ with s-wave superconductivity near $\mathbf{\Gamma}$ becomes a nodal TSC in an in-plane magnetic field [39]. In their proposal, the bulk nodal points appear along $\Gamma - M$ lines where the Ising SOC vanishes because of the in-plane mirror symmetry $M_x : x \to -x$. However, the potential of TMD materials such as MoS_2, $MoSe_2$, $MoTe_2$, and WS_2, which are superconducting at electron doping near the **K** valleys, to become nodal TSC, is currently not known. Note that M_x does not guarantee the vanishing of SOC near the **K** valleys.

In this chapter, we show that s-wave superconducting monolayers of molybdenum dichalcogenides (MoX_2, X=S, Se, Te) become nodal TSCs in the presence of an in-plane magnetic field. In this previously unknown topological phase, the bulk nodal points appear near the **K** valleys at special momenta where the SOC splitting vanishes. We find two regimes in the nodal topological phase, with six or twelve nodal points appearing near each valley respectively. In the nodal topological phase, nodal points are connected by zero-energy Andreev flat band edge states, which are protected by a chiral symmetry originating from mirror symmetry in the MoX_2 plane, and present for all edges except zigzag. Finally, we discuss possible experimental verification of the nodal topological phase.

5.2. MODEL

A monolayer MX_2 (MoS_2, $MoSe_2$, $MoTe_2$, or WS_2) consists of a triangular lattice of M atoms sandwiched between two layers of X atoms, each also forming a triangular lattice. The top and bottom X atoms project onto the same position in the layer of M atoms, such that when viewed from above, the monolayer has the hexagonal lattice structure shown in Fig. 5.1(a), with primitive lattice vectors $\mathbf{a}_1$ and $\mathbf{a}_2$. In the normal state, the monolayer MX_2 has a direct band gap at the $\pm\mathbf{K}$ points. Near the $\eta\mathbf{K}$ ($\eta = \pm$) points, the point group is C_{3h}, and the effective Hamiltonian of the lowest conduction band up to the third order in momentum $\mathbf{k} = (k_x, k_y)$ is

$$H_e^\eta(\mathbf{k}) = \frac{k^2}{2m^*} + [\lambda\eta + A_1 k^2 \eta + A_2(k_x^3 - 3k_x k_y^2)]\sigma_z, \tag{5.1}$$

in the basis $[c_{\eta\mathbf{k}\uparrow}, c_{\eta\mathbf{k}\downarrow}]$, with $c_{\eta\mathbf{k}s}$ the annihilation operator for an electron in valley η at momentum $\mathbf{k}$ with spin $s = \uparrow, \downarrow$. We obtain this effective Hamiltonian from the $\mathbf{k}\cdot\mathbf{p}$ Hamiltonian near the $\pm\mathbf{K}$ valleys in Ref. [40] by the Löwdin partition method [41, 42]. Here, the x (y)-axis points along the zigzag (armchair) direction as in Fig. 5.1(a), m^* denotes the effective mass, λ and $A_{1,2}$ are SOC strengths, and $\sigma_{x,y,z}$ are the Pauli matrices in spin space. Material parameters are provided as Supplementary Material 5.8.1.

Including superconductivity with s-wave pairing and an in-plane magnetic field, the Bogoliubov-de Gennes (BdG) Hamiltonian in the basis $[c_{\eta\mathbf{k}\uparrow}, c_{\eta\mathbf{k}\downarrow}, c^\dagger_{-\eta-\mathbf{k}\uparrow}, c^\dagger_{-\eta-\mathbf{k}\downarrow}]$ is

$$\begin{aligned} H_{\mathrm{BdG}}^\eta(\mathbf{k}) =& (\frac{k^2}{2m^*} - \mu)\tau_z + [\lambda\eta + A_1 k^2\eta + A_2(k_x^3 - 3k_x k_y^2)]\sigma_z \\ &+ V_x\sigma_x\tau_z + V_y\sigma_y + \Delta\sigma_y\tau_y, \end{aligned} \tag{5.2}$$

where μ, $\tau_{x,y,z}$, Δ, and $V_{x,y}$ are the chemical potential, Pauli matrices in particle-hole space, the superconducting gap, and the Zeeman energy terms due to the magnetic field, respectively.

The BdG Hamiltonian $H_{\mathrm{BdG}}^\eta(\mathbf{k})$ has a particle-hole symmetry (PHS) $\mathscr{P}H_{\mathrm{BdG}}^\eta(\mathbf{k})\mathscr{P}^{-1} = -H_{\mathrm{BdG}}^{-\eta}(-\mathbf{k})$ where $\mathscr{P} = \tau_x\mathscr{K}$, with $\mathscr{K}$ being the complex conjugation operator. Although time-reversal symmetry (TRS) $\mathscr{T} = i\sigma_y\mathscr{K}$ is broken by the magnetic field, $H_{\mathrm{BdG}}^\eta(\mathbf{k})$ respects an effective TRS $\tilde{\mathscr{T}}H_{\mathrm{BdG}}^\eta(\mathbf{k})\tilde{\mathscr{T}}^{-1} = H_{\mathrm{BdG}}^{-\eta}(-\mathbf{k})$ where $\tilde{\mathscr{T}} = M_{xy}\mathscr{T}$, with $M_{xy} = -i\sigma_z\tau_z$ the mirror symmetry in the monolayer plane. Therefore, $H_{\mathrm{BdG}}^\eta(\mathbf{k})$ has the chiral symmetry $\mathscr{C}H_{\mathrm{BdG}}^\eta(\mathbf{k})\mathscr{C}^{-1} = -H_{\mathrm{BdG}}^\eta(\mathbf{k})$ with $\mathscr{C} = \mathscr{P}\tilde{\mathscr{T}} = \sigma_x\tau_y$. As a result, $H_{\mathrm{BdG}}^\eta(\mathbf{k})$ is in class BDI, which is trivial in two dimensions for gapped systems [43, 44], but can be nontrivial for nodal systems. We reduce the dimension to one by fixing two orthogonal directions $\mathbf{k}_\parallel$ and $\mathbf{k}_\perp$ in momentum space, and considering each $H_{\mathrm{BdG}}^\eta(\mathbf{k}_\perp, \mathbf{k}_\parallel)$ at a fixed $\mathbf{k}_\parallel$ separately [11]. Although $\mathscr{P}$ and $\tilde{\mathscr{T}}$ are in general not symmetries of the one-dimensional (1D) Hamiltonian $H_{\mathrm{BdG}}^\eta(\mathbf{k}_\perp, \mathbf{k}_\parallel)$ at a fixed $\mathbf{k}_\parallel$ [45], because they flip the sign of both $\mathbf{k}_\parallel$ and $\mathbf{k}_\perp$ [1], $\mathscr{C}$ is a symmetry for any choice of $\mathbf{k}_\parallel$. Therefore the 1D Hamiltonians $H_{\mathrm{BdG}}^\eta(\mathbf{k}_\perp, \mathbf{k}_\parallel)$ at a fixed $\mathbf{k}_\parallel$ belong to class AIII [2], and are thus characterized by an integer topological invariant: the winding number [43].

[1] The 1D PHS or TRS that only flip $\mathbf{k}_\perp$ require an extra unitary symmetry that maps $\mathbf{k}_\parallel \to -\mathbf{k}_\parallel$, but we find that

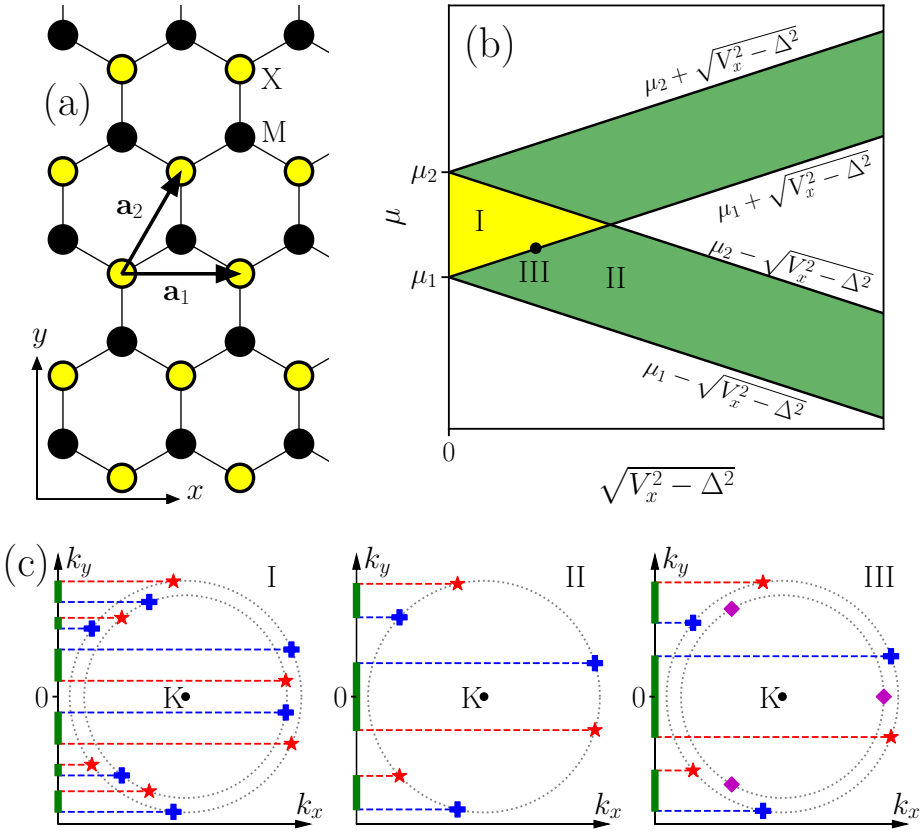

Figure 5.1: (a) Top view of monolayer MX_2 lattice structure with primitive lattice vectors $\mathbf{a}_1$ and $\mathbf{a}_2$. (b) Phase diagram of the gap-closing condition as a function of μ and $\sqrt{V_x^2 - \Delta^2}$. Nodal points appear in regions where the gap closes, colored yellow (regime I) and green (regime II), with the phase boundaries given by $\mu = \mu_{1,2} \pm \sqrt{V_x^2 - \Delta^2}$. III represents the boundary between regimes I and II. (c) Sketch of nodal points near $\mathbf{K}$ valley. The chirality of nodal points with $+(\star)$ is $1(-1)$, and diamond denotes two overlapping nodal points of opposite chirality. Nodal point projections on the k_y-axis determine topologically nontrivial phases with nonzero winding number (solid green lines).

5.3. BULK NODAL POINTS

We begin investigating the topological phases of $H^{\eta}_{\mathrm{BdG}}(\mathbf{k})$ by finding the gap-closing conditions, which determine the bulk nodal points. Due to chiral symmetry, $H^{\eta}_{\mathrm{BdG}}(\mathbf{k})$ can

no such symmetry exists for generic $(\mathbf{k}_\perp, \mathbf{k}_\parallel)$.

[2] For the armchair direction $\mathbf{k}_\parallel = k_y\hat{\mathbf{y}}$, although the 1D Hamiltonian of the continuum model belongs to class BDI, it turns out to be in class AIII in the tight-binding models, due to the absence of a point group symmetry that maps $y \to -y$.

be brought to a block off-diagonal form [11, 46], with the upper off-diagonal element

$$\begin{aligned} A_\eta(\mathbf{k}) &= -(\frac{k^2}{2m^*}-\mu)+[\lambda\eta+A_1k^2\eta+A_2(k_x^3-3k_xk_y^2)]\sigma_z \\ &\quad -V_x\sigma_x+V_y\sigma_y+i\Delta\sigma_z. \end{aligned} \tag{5.3}$$

The gap-closing condition $\det[A_\eta(\mathbf{k})]=0$ gives rise to two requirements:

$$\lambda\eta+A_1k^2\eta+A_2(k_x^3-3k_xk_y^2)=0, \tag{5.4a}$$

$$\mu\pm\sqrt{V_x^2+V_y^2-\Delta^2}=\frac{k^2}{2m^*}. \tag{5.4b}$$

The first is the vanishing of spin splitting due to SOC [see Eq. (5.1)], and the second is the magnetic field closing the bulk gap at the Fermi circle without SOC. These two conditions arise because closing the gap with the magnetic field brings together bands that are coupled by SOC. The bands thus repulse, except at points in momentum space where the SOC vanishes and the gap closes. Such points manifest as crossings between the spin-split conduction bands in the normal-state dispersion, which are present near $\pm\mathbf{K}$ valleys in monolayer MoX_2 (X=S, Se, Te) but not WS_2, due to the relative strengths of SOC contributions from the d orbitals on the transition metal atoms and the p orbitals on the chalcogen atoms [47–49]. Therefore, the requirement (5.4a) is not met in WS_2, and we focus on MoX_2 in the following. The gap-closing requirements (5.4) are independent of the in-plane magnetic field orientation, so we set $V_y=0$ in the following. Solving Eq. (5.4a) limits k to $k_{c1}\le k\le k_{c2}$ with $k_{c1,c2}=k_0\pm k_0^2/(2A_0)$, $k_0=\sqrt{-\lambda/A_1}$ and $A_0=A_1/A_2$ [see Supplementary Material 5.8.1]. Figure 5.1(b) shows a phase diagram of the gap-closing conditions as a function of μ and $\sqrt{V_x^2-\Delta^2}$. The four phase boundaries $\mu=\mu_{1,2}\pm\sqrt{V_x^2-\Delta^2}$ with $\mu_{1,2}=k_{c1,c2}^2/(2m^*)$ divide the diagram into regimes, with nodal points and therefore possible nontrivial phases in the colored regions (I and II).

5.4. TOPOLOGICAL PHASES

In the gapless regimes of the phase diagram, Fig. 5.1(c) sketches the nodal points near the $\mathbf{K}$ valley along with their chirality $w(\mathbf{k}^i)$. The chirality of the nodal point at $\mathbf{k}^i=(k_\perp^i,k_\parallel^i)$ is the winding number around it, and is ±1 [11, 18, 46]. The nodal point chirality relates to the winding number W of the 1D Hamiltonian at a fixed $k_\parallel$ through $W(k_\parallel)=\sum_{k_\parallel^i<k_\parallel}w(\mathbf{k}^i)$, which means that we can obtain $W(k_\parallel)$ by counting the nodal point projections onto the $k_\parallel$-axis and keeping track of their chirality. For the zigzag direction $\mathbf{k}_\parallel=k_x\hat{\mathbf{x}}$, the nodal point projections cancel exactly, because the nodal points come in pairs with opposite chirality at each k_x, and hence $W(k_x)=0$ always. For any other direction, the nodal points do not cancel, and nontrivial phases thus exist for all directions $\mathbf{k}_\parallel$ other than zigzag. We show the projections of the nodal points on the armchair direction $\mathbf{k}_\parallel=k_y\hat{\mathbf{y}}$, and the corresponding segments of the k_y-axis where $W(k_y)\neq0$(solid green lines). In regime I, there are two momentum circles (5.4b) near the $\mathbf{K}$ valley, with six nodal points each for a total of twelve. The nodal points divide the k_y-axis into thirteen segments, with six segments topologically nontrivial. In regime II, there is only one momentum circle with

six nodal points, such that the k_y-axis separates into seven parts, with three nontrivial. At the boundary between regimes I and II (marked as III in the figure), pairs of nodal points of opposite chirality overlap on one momentum circle, such that only the other circle contributes to the winding number W, similar to regime II. The nodal points near the $-\mathbf{K}$ valley are symmetric to the ones near $\mathbf{K}$ in k_x [see also Fig. 5.4(a)]. The preceding analysis applies equally to all three MoX_2 monolayers. In the following, we explore further details of the topological phases, focusing on nodal point projections on the armchair direction. Although we show examples for specific materials, we have verified that the physics is qualitatively the same for all three [see Supplementary Material 5.8.4].

To complement the analysis of nodal point projections, Figs. 5.2(a) and (b) show computed phase diagrams of the winding number as a function of k_y and $\sqrt{V_x^2-\Delta^2}$ at two chemical potentials, $\mu_1 < \mu < (\mu_1+\mu_2)/2$ in (a) and $\mu < \mu_1$ in (b), respectively representative of regimes I and II of Fig. 5.1. The phase diagrams are even in k_y, and the winding number is ± 2 due to equal contributions from the $\pm\mathbf{K}$ valleys. The phase boundaries in Fig. 5.1(b) determine the range of the nontrivial regions in $\sqrt{V_x^2-\Delta^2}$, while the maximum extent along k_y is bounded from above by $|k_y| \leq k_0$, independent of μ and $\sqrt{V_x^2-\Delta^2}$ [see Supplementary Material 5.8.1]. Sweeping over $\sqrt{V_x^2-\Delta^2}$ in (a), the phase diagram transitions from regime I to II indicated by the vertical dashed line, such that the number of topologically nontrivial segments along k_y changes from six to three (also counting $-k_y$). In contrast, (b) is exclusively in regime II.

5.5. EXCITATION GAP AND EDGE STATES

Topologically nontrivial phases are protected by the topological excitation gap, which we define as $E_{\text{gap}}(\mathbf{k}_\parallel) = \min_{n,\mathbf{k}_\perp} |E_n(\mathbf{k}_\parallel, \mathbf{k}_\perp)|$, where $E_n(\mathbf{k})$ is the spectrum of $H^\eta_{\text{BdG}}(\mathbf{k})$, with n a band index. Figures 5.2(c) and (d) show maps of the topological excitation gap corresponding to the phase diagrams (a) and (b), respectively. In the nontrivial phase, we see that $E_{\text{gap}} \lesssim 0.1\Delta$ for $MoSe_2$, and similarly find $E_{\text{gap}} \lesssim 0.04\Delta$ for MoS_2, and $E_{\text{gap}} \lesssim 0.2\Delta$ for $MoTe_2$ [see Supplementary Material 5.8.4]. Here, we emphasize that Δ may represent intrinsic superconductivity, which means that no proximity effect is required, and interface effects that tend to reduce the gap further are thus absent.

In a topologically nontrivial phase, edge states manifest at a monolayer lattice termination boundary. We investigate the edge states at an armchair edge by calculating the local density of states at the boundary, $\rho(E, x_B, k_y) = -\frac{1}{\pi}\text{Tr}[\text{Im}G(E, x_B, k_y)]$, with E the energy, x_B the coordinate of the armchair edge, and G the surface Green's function [50]. Figure 5.3(a) shows the local density of states obtained using parameters from regime I of Fig. 5.1(b), *i.e.* with 12 nodal points per valley. At zero energy, there are six sections of Andreev flat bands connecting nodal points, which exactly match the topologically nontrivial phases with nonzero winding number, marked by the vertical dotted lines, and the shaded regions in Fig. 5.3(b). In Fig. 5.3(b), we also present the decay length of the topologically nontrivial edge states, and see that it is of the order 1 μm here.

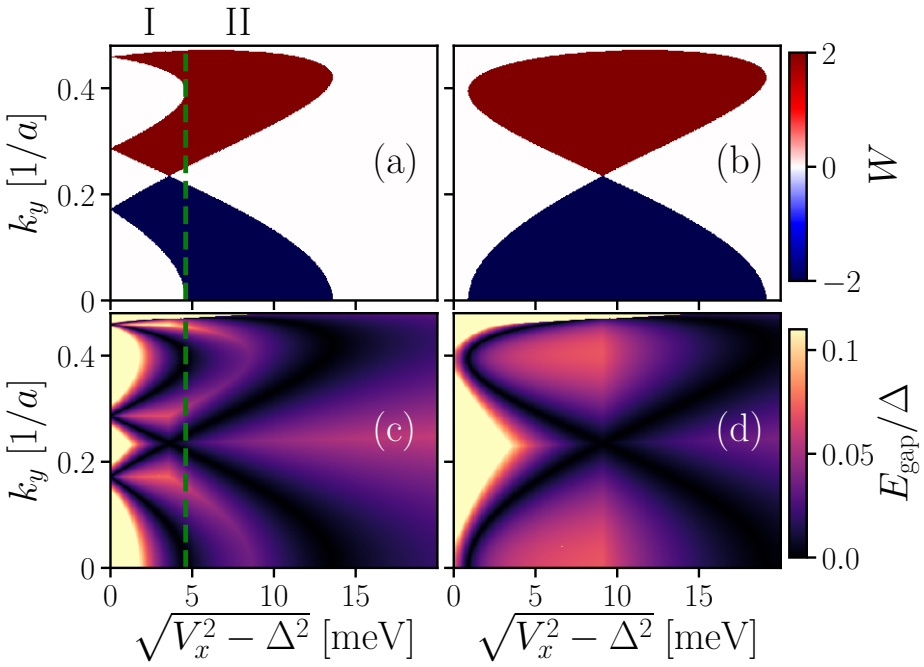

Figure 5.2: Topological phase diagrams for the armchair direction $\mathbf{k}_\parallel = k_y\hat{\mathbf{y}}$ of monolayer $MoSe_2$. The winding number as a function of k_y and $\sqrt{V_x^2-\Delta^2}$ with (a) $\mu_1 < \mu < (\mu_1+\mu_2)/2$ and (b) $\mu < \mu_1$, in regimes I and II of Fig. 5.1. The phase diagrams for $(\mu_1+\mu_2)/2 < \mu < \mu_2$ and $\mu > \mu_2$ are similar to (a) and (b) respectively, but with opposite winding numbers. (c, d) The corresponding topological excitation gap E_{gap} to (a) and (b) separately. Data is obtained using the continuum model (5.2), and a is the lattice constant of the MX_2 lattice.

5.6. ARBITRARY EDGE DIRECTIONS

Although we have so far focused on an armchair edge, topologically nontrivial regimes exist for all lattice termination edges except zigzag. Using tight-binding models to simulate the MX_2 lattice [Fig. 5.1(a)] with Kwant [51], we characterize a lattice termination edge with a superlattice vector $\mathbf{T}$ at the angle ϕ relative to the armchair direction [see Supplementary Material 5.8.5]. To investigate topological phases, we deform the hexagonal first Brillouin zone into the rectangle spanned by primitive reciprocal vectors $\hat{\mathbf{k}}_\parallel$ and $\hat{\mathbf{k}}_\perp$, which are parallel and, respectively, transverse to $\mathbf{T}$ [52], and project the nodal points onto the $k_\parallel$-axis [Fig. 5.4(a)]. As before, flat bands exist in segments of the $k_\parallel$-axis where the winding number is nonzero. Unlike an armchair edge, the nodal points near $\pm\mathbf{K}$ generally do not project pairwise onto the same $k_\parallel$ at a generic boundary, and the winding number can take other values than ±2, e.g., ±1 (green lines). Figure 5.4(b) is an example of a phase diagram for an edge direction with $\phi \approx 1.2°$, and shows that the winding number can be ±1, ±3, and even ±4. For generic lattice terminations other than armchair, nodal topological phases are thus not only present, but also manifest in rich phase diagrams with large winding numbers.

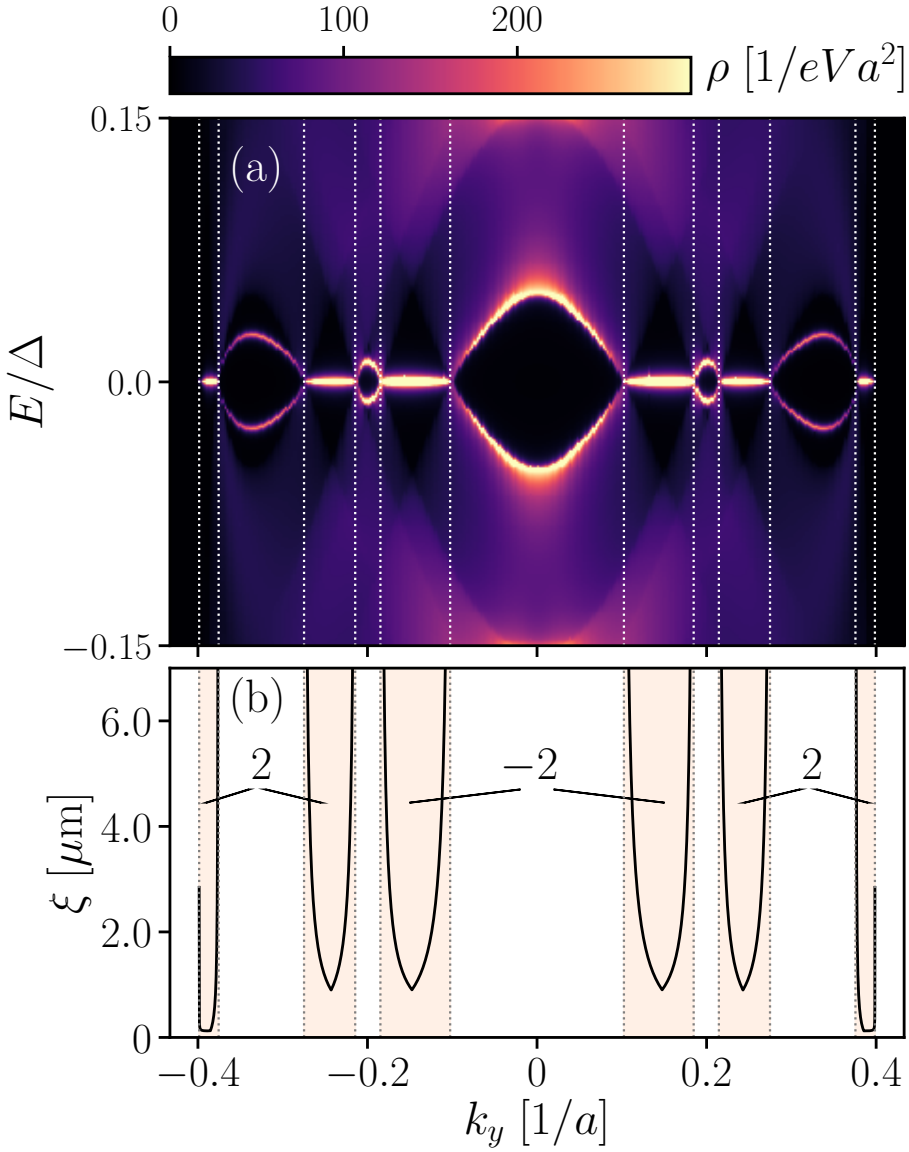

Figure 5.3: (a) Density of states at the armchair edge as a function of k_y for monolayer MoS_2, with parameters in regime I of Fig. 5.1(b). Flat bands of zero-energy Andreev edge states where the winding number is nonzero between nodal point projections. (b) Decay length of the edge states in the topologically nontrivial phase. The nontrivial phases are marked by the shaded regions with the nonzero winding numbers in the insets. Data is obtained using an 11-orbital tight-binding model with $\mu = 1.8337$ eV, $\sqrt{V_x^2 - \Delta^2} = 1.5$ meV, and $\Delta = 0.8$ meV, [see Supplementary Material 5.8.2].

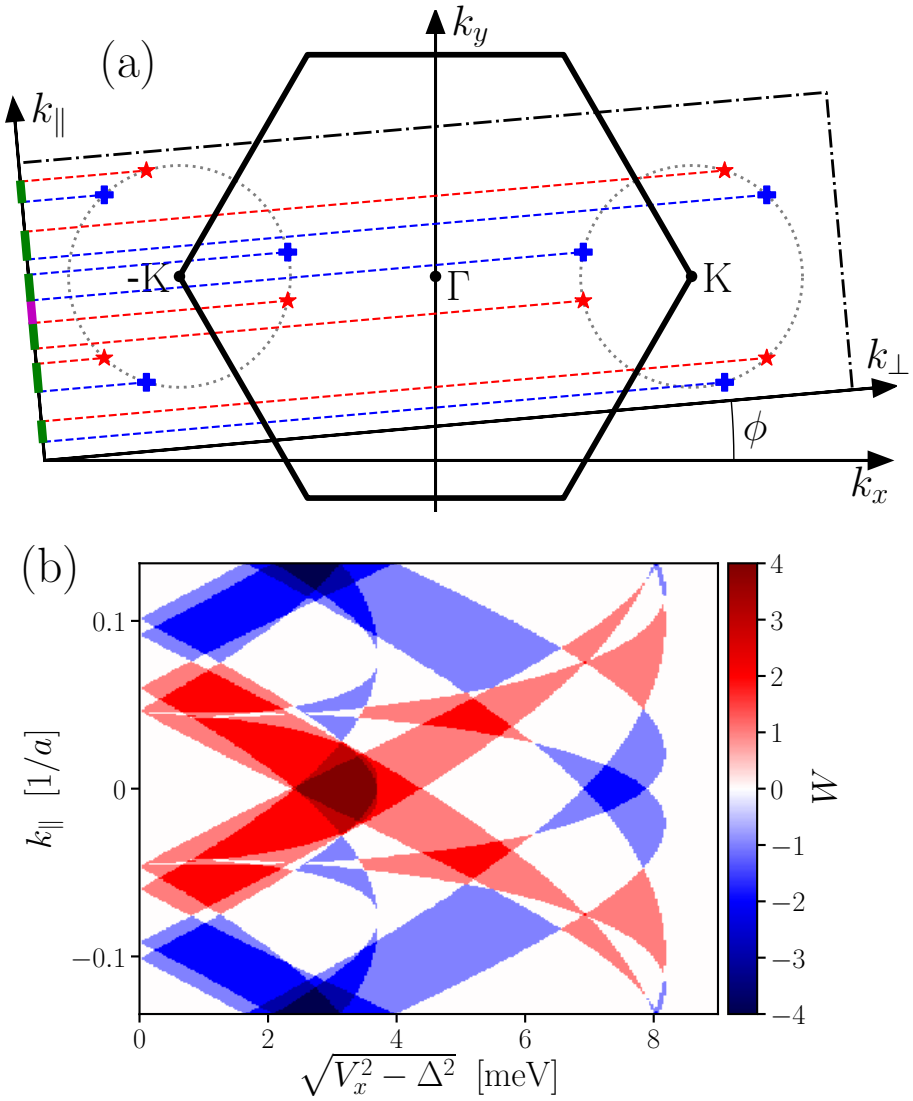

Figure 5.4: (a) Schematic of the hexagonal first Brillouin zone of the monolayer lattice, with nodal points around the high symmetric points ±**K**. For arbitrary edge cuts, we deform the Brillouin zone into a rectangle, illustrated by the dash-dotted lines and the $k_\parallel$ and $k_\perp$ axes, and project the nodal points onto $k_\parallel$. Flat bands of Andreev bound states exist for $k_\parallel$ where the winding number is nonzero (bold colored lines). For a generic edge cut, each nodal point generally projects onto a distinct $k_\parallel$, such that the winding number may take various values, *e.g.* ±1 (green) or ±2 (purple) in the sketch. (b) Phase diagram of the winding number for an edge with $\phi \approx 1.2°$. The phase diagram is rich with the winding number ±1, ±2, ±3 or ±4. Data is obtained from an 11-orbital tight-binding model for MoS_2 with $\mu = 1.8390$ eV and $\Delta = 0.8$ meV, [see Supplementary Material 5.8.2].

5.7. SUMMARY AND DISCUSSION

We have shown that a superconducting monolayer MoX_2 (X=S, Se, Te) can become a nodal TSC in the presence of an in-plane magnetic field. The bulk nodal points occur at

Table 5.1: Chemical potentials $\mu_{1,2}$ in meV for MoS_2, $MoSe_2$ and $MoTe_2$ [see also Fig. 5.1(b)], obtained from the continuum model.

	MoS_2	$MoSe_2$	$MoTe_2$
μ_1	32.6	126.7	136.1
μ_2	34.5	143.0	184.5

special momenta near $\pm\mathbf{K}$ valleys in the Brillouin zone where the spin splitting due to SOC vanishes, and can be 6 or 12 in each valley. For all lattice termination edges except zigzag, the edge projections of the nodal points are connected by flat bands of zero-energy Andreev edge states. These flat bands are protected by chiral symmetry. Our conclusions are based on a study of both continuum and atomic tight-binding models.

Finally, we address experimental feasibility. It is possible to produce high-quality monolayer MoX_2 crystals with low impurity densities, and sizes in the tens of microns or even millimeters [53–56]. Such large samples may guarantee that the topological Andreev edge states at opposing edges are well separated. In addition, recent experiments show that thin films even down to monolayers of MoX_2 become superconducting in the conduction band at carrier densities $\gtrsim 6\times10^{13}$ cm^{-2} [26, 28, 29], which translates to a minimum chemical potential μ_0 for superconductivity of 153 meV (MoS_2), 120 meV ($MoSe_2$) and 117 meV ($MoTe_2$). The mismatch of μ_0 and $\mu_{1,2}$ in MoS_2 implies that intrinsic superconductivity is not suitable to realize the nodal topological phase in MoS_2, but this can potentially be overcome using the proximity effect. In addition, a recent experiment indicates possible intrinsic unconventional pairing in MoS_2 at very large doping [57]. For monolayer $MoSe_2$ and $MoTe_2$, μ_0 is close to $\mu_{1,2}$ in Fig. 5.1(b) [see Table 5.1], and therefore these two materials are promising candidates for realizing nodal TSCs. For experimental detection, aside from tunnelling measurements, the character of bulk nodal points could be probed using quasiparticle interference or local pair-breaking measurements [15, 16, 58]. Because the flat bands manifest as a zero-energy density of states peak in the nontrivial parts of the phase diagram Fig. 5.1(b), it is possible to discern them from other edge states [59], which generally don't stick to zero energy, by tuning the magnetic field and/or chemical potential. If the chiral symmetry is broken, the flat bands may split from zero energy. Two possible causes are a perpendicular electric field due to asymmetric electrostatic gating, and an out-of-plane Zeeman field. The electric field can be avoided by chemical doping [26, 28] and it is possible to align the magnetic field along the in-plane direction to a precision of $\lesssim 0.02°$, such that the out-of-plane projection is negligible [30].

5.8. SUPPLEMENTARY INFORMATION

5.8.1. VANISHING OF SPIN SPLITTING DUE TO SPIN-ORBIT COUPLING IN CONTINUUM MODEL FOR MONOLAYER MoX_2

The condition for vanishing of spin splitting due to spin-orbit coupling (SOC) in the continuum model is given by Eq. (4a) of the main text:

$$\lambda\eta + A_1 k^2\eta + A_2(k_x^3 - 3k_x k_y^2) = 0. \tag{5.5}$$

With $\eta = 1$, we perform an analytic derivation near **K** valley. By defining $k_0 = \sqrt{-\lambda/A_1}$ and $A_0 = A_1/A_2$, Eq. (5.5) becomes

$$k_x^3 + A_0 k_x^2 - 3k_x k_y^2 + A_0(k_y^2 - k_0^2) = 0, \tag{5.6}$$

which is a cubic equation in k_x for a fixed k_y. By considering that $|k_y|$ and k_0 are much smaller than $|A_0|$, this equation has three real solutions approximately, $k_{x1,x2} = \frac{4k_y^2 - k_0^2}{2A_0} \pm \sqrt{k_0^2 - k_y^2}$ and $k_{x3} = -A_0$ for $|k_y| \leq k_0$ whereas only one real solution approximately, $k_x = -A_0$ for $|k_y| > k_0$. Note that the solution $k_x = -A_0$ is unphysically large in the continuum model, and we therefore reject it. As a result, the cubic equation has two physical solutions $k_{x1,x2}$ only when $|k_y| \leq k_0$, and no solutions otherwise. This gives rise to an upper limit of $|k_y|$ in the topologically nontrivial phase for armchair direction.

The magnitude of the momentum where the spin splitting due to SOC vanishes is calculated by $k^2 = k_{x1,x2}^2 + k_y^2 \approx \pm\frac{\sqrt{k_0^2 - k_y^2}}{A_0}[4(k_0^2 - k_y^2) - 3k_0^2] + k_0^2$. Due to $|k_y| \leq k_0$, we have the maximum of k, $k_{c2} = \sqrt{k_0^2 - k_0^3/A_0} \approx k_0 - k_0^2/(2A_0)$ and the minimum of k, $k_{c1} = \sqrt{k_0^2 + k_0^3/A_0} \approx k_0 + k_0^2/(2A_0)$.

Note that the results near $-\mathbf{K}$ valley can be easily obtained by replacing k_x by $-k_x$.

Table 5.2: Material parameters for the continuum model of the monolayer MoX_2 family [see Eq. (1) of the main text]. They are obtained from $\mathbf{k}\cdot\mathbf{p}$ Hamiltonians near $\pm\mathbf{K}$ valleys in Ref. [40] (MoS_2 and $MoSe_2$) and in Ref. [49] ($MoTe_2$) by the Löwdin partition method [41, 42]. Here, a is the lattice constant of the monolayer lattice.

	a [Å]	m^*/m_0	λ [meV]	A_1/a^2 [meV]	A_2/a^3 [meV]
MoS_2	3.18	0.47	-1.5	36	-4.88
$MoSe_2$	3.32	0.60	-10.6	45.5	-6.23
$MoTe_2$	3.516	0.62	18	-56.33	15.13

5.8.2. TIGHT-BINDING HAMILTONIANS FOR MONOLAYER MoX_2

In this section, we introduce the crystal structure symmetries of the monolayer MoX_2 lattice, and the monolayer tight-binding Hamiltonians that we have adopted in our analysis. The monolayer MoX_2 crystal consists of a two-dimensional triangular lattice of Mo atoms, sandwiched between two equidistant layers of X atoms X_A above and X_B below, each also forming a triangular lattice, such that the X_A and X_B atoms project onto the same position in the layer of Mo atoms [see Fig. 1(a) of the main text]. The primitive Bravais lattice vectors are

$$\mathbf{a}_1 = a\hat{\mathbf{x}}, \quad \mathbf{a}_2 = a(\frac{1}{2}\hat{\mathbf{x}} + \frac{\sqrt{3}}{2}\hat{\mathbf{y}}). \tag{5.7}$$

The Mo atoms lie in the xy-plane, with the planes of X_A and X_B atoms above and below at distances $\pm d/2$, such that d is the separation between the two planes of X atoms. The monolayer has threefold rotational symmetry, a mirror symmetry in the yz-plane $M_{yz} : x \to -x$, and the xy mirror symmetry $M_{xy} : z \to -z$.

THE THREE-ORBITAL MODEL

In Ref. [47] a simple tight-binding model was proposed to reproduce the low-energy spectrum near the $\pm\mathbf{K}$ point where only $d_0 \equiv d_{z^2}, d_{xy}$, and $d_{x^2-y^2}$ orbitals of the Mo atom are considered due to them having the largest contribution to the electronic band. The detailed structure of the spinless three-orbital Hamiltonian H_0 in the basis $(d_0, d_{xy}, d_{x^2-y^2})$ in Bloch form reads

$$H_0 = \begin{pmatrix} h_0 & h_1 & h_2 \\ h_1^* & h_{11} & h_{12} \\ h_2^* & h_{12}^* & h_{22} \end{pmatrix}, \tag{5.8}$$

with the following matrix elements for nearest-neighbor hopping:

$$\begin{aligned} h_0 &= 2t_0(2\cos\xi\cos\gamma + \cos 2\xi) + \varepsilon_1 - \mu \\ h_1 &= 2it_1(\sin 2\xi + \sin\xi\cos\gamma) - 2\sqrt{3}t_2\sin\xi\sin\gamma, \\ h_2 &= 2i\sqrt{3}t_1\cos\xi\sin\gamma + 2t_2(\cos 2\xi - \cos\xi\cos\gamma), \\ h_{11} &= t_{11}(\cos\xi\cos\gamma + 2\cos 2\xi) + 3t_{22}\cos\xi\cos\gamma + \varepsilon_2 - \mu, \\ h_{22} &= 3t_{11}\cos\xi\cos\gamma + t_{22}(\cos\xi\cos\gamma + 2\cos 2\xi) + \varepsilon_2 - \mu, \\ h_{12} &= \sqrt{3}(t_{22} - t_{11})\sin\xi\sin\gamma + 4it_{12}\sin\xi(\cos\xi - \cos\gamma), \end{aligned} \tag{5.9}$$

where $\xi = k_x a/2$ and $\gamma = \sqrt{3}k_y a/2$.

Due to the heavy Mo atoms, there is a large SOC of strength λ, such that the spinful Hamiltonian reads

$$H_1 = \sigma_0 \otimes H_0 + \frac{\lambda}{2}\sigma_z \otimes L_z \tag{5.10}$$

with σ the Pauli matrices acting on the spin degree of freedom, and $(L_z)_{kl} = 2i\varepsilon_{1kl}$, the matrix elements of L_z in the basis $(d_0, d_{xy}, d_{x^2-y^2})$, with ϵ the Levi-Civita symbol. The starting tight-binding parameters are displayed in Table 5.3, obtained from the nearest-neighbor model in Ref. [47]. In addition we consider a chemical potential μ tuned into the lowest conduction band.

Table 5.3: Tight-binding parameters for the family of MoX_2 materials in eV from a generalized-gradient approximation fit of first-principle data [47].

	ε_1	ε_2	t_0	t_1	t_2	t_{11}	t_{12}	t_{22}	λ
MoS_2	1.046	2.104	−0.184	0.401	0.507	0.218	0.338	0.057	0.073
$MoSe_2$	0.919	2.065	−0.188	0.317	0.456	0.211	0.290	0.130	0.091
$MoTe_2$	0.605	1.972	−0.169	0.228	0.390	0.390	0.207	0.239	0.107

As observed in Ref. [47] from first-principle calculations, the MoX_2 materials have crossings between the spin-split conduction bands near $\pm\mathbf{K}$ valleys. As mentioned in the main text, these crossings are crucial to realize topological nodal superconductivity, because the spin splitting due to SOC vanishes at the crossing points. Unfortunately, the three-orbital model in Eq. (5.10) (even if extended to next-nearest hopping) does not reproduce the expected spin-orbit crossings of the conductance bands. This is due to the model not properly including the effect of p orbitals from the X atoms. Extended models

with a larger basis containing orbitals from X atoms correctly reproduce the crossings present in the first-principle data [40].

To solve this problem, we extend here the three-orbital model to include the effects of p_x and p_y orbitals near the $\pm\mathbf{K}$ points by renormalizing the tight-binding parameters to include virtual hoppings to these orbitals. Since we are interested only in physics near the $\pm\mathbf{K}$ points, where the physics is largely dominated by d_0, we neglect the renormalization of the other orbitals. Thus, the hopping integrals between d_0 orbitals are renormalized by virtual hoppings on the $p_{x,y}$ orbitals from the X atoms.

The wave functions for the spinless p_x and p_y orbitals read

$$p_x = -\frac{1}{\sqrt{2}}(|1,1\rangle - |1,-1\rangle), \quad p_y = \frac{i}{\sqrt{2}}(|1,1\rangle + |1,-1\rangle), \tag{5.11}$$

in terms of the orbital angular momentum eigenstates. Therefore

$$\langle p_y|\boldsymbol{L}\cdot\boldsymbol{S}|p_x\rangle = \langle p_y|\big[\frac{1}{2}(L^+S^- + L^-S^+) + L_zS_z\big]|p_x\rangle, \tag{5.12}$$

with $\boldsymbol{L}$ and $\boldsymbol{S}$ the vectors of orbital and spin angular momentum operators, respectively, and $\mathcal{O}^\pm = \mathcal{O}_x \pm i\mathcal{O}_y$, $\mathcal{O} \in \{L, S\}$. We keep only the energetically most important contribution due to the spin-conserving term

$$\langle p_y|L_zS_z|p_x\rangle = \frac{i}{2}\sigma_z. \tag{5.13}$$

The spin-flip terms are energetically more expensive, involving transitions to higher energy states, and may be neglected to a first order approximation [60].

The tight-binding equations for the jth unit cell of MoX_2 read:

$$(E-\varepsilon_p)c_{x,j} = \sum_k t_{x0}(\boldsymbol{n}_k)g_k - \frac{i}{2}\sigma_z c_{y,j} \tag{5.14}$$

$$(E-\varepsilon_p)c_{y,j} = \sum_k t_{y0}(\boldsymbol{n}_k)g_k + \frac{i}{2}\sigma_z c_{x,j} \tag{5.15}$$

$$(E-\varepsilon_d)g_j = \sum_k [t_{0x}(\boldsymbol{n}_k)c_{x,k} + t_{0y}(\boldsymbol{n}_k)c_{y,k}], \tag{5.16}$$

with the sums running over all cells k available through nearest-neighbor hopping. We denote with $c_{x/y,k}$ the amplitude of an electron in orbital p_x or p_y in cell k, and g_k the amplitude of an electron in the d_0 orbital in cell k. The onsite energy for being in the $p_{x/y}$ or d_0 orbitals is ε_p and, respectively, ε_d. The nearest-neighbor hopping from orbital β to α from the current cell j to nearby cell k is denoted by $t_{\alpha\beta}(\boldsymbol{n}_k)$, with orbitals $\alpha, \beta \in \{0 \equiv d_0, x \equiv p_x, y \equiv p_y\}$. The unit vector $\boldsymbol{n}_k$ points in the hopping direction along the bond.

We solve the equations at energy E close to the conduction band minimum at $\pm\mathbf{K}$. Eliminating the equations involving the p orbitals, we obtain the renormalization of the

hopping integrals between d_0 orbitals:

$$(E-\varepsilon_d)g_j = \sum_{kl}\Big\{\big[t_{0x}(\boldsymbol{n}_k)t_{x0}(\boldsymbol{n}_l)+t_{0y}(\boldsymbol{n}_k)t_{y0}(\boldsymbol{n}_l)\big] - \frac{i\sigma_z}{2(E-\varepsilon_p)}\big[t_{0x}(\boldsymbol{n}_k)t_{y0}(\boldsymbol{n}_l)-t_{0y}(\boldsymbol{n}_k)t_{x0}(\boldsymbol{n}_l)\big]\Big\}F(E)g_l, \tag{5.17a}$$

$$F(E) = \Big[E-\varepsilon_p-\frac{1}{4(E-\varepsilon_p)}\Big]^{-1}. \tag{5.17b}$$

The first term in Eq. (5.17a) is just a tuning of the existing parameters in the model. Most importantly, the second term in Eq. (5.17a) complements the three-orbital model with a spin-obit term which is qualitatively different from the current model. The structure of the new term recalls the Kane-Mele spin-orbit term in graphene [61]. In graphene, such a spin-orbit term is produced for next-nearest neighbor hopping between p_z orbitals due to virtual transitions to nearest neighbor p_z orbitals.

The hopping terms t_{0x} and t_{0y} depend on $V_{pd\sigma}$, the LCAO (linear combination of atomic orbitals) two-center integrals for σ bonds. They are determined for the lattice orientation in Fig. 1(a) of the main text by the direction cosines $(l,m,0)$, with the aid of Koster-Slater tables [62]:

$$t_{0x}=-\frac{l}{2}V_{pd\sigma} \quad t_{0y}=-\frac{m}{2}V_{pd\sigma}. \tag{5.18}$$

Therefore the spin-orbit interaction contribution due to virtual hopping on p orbitals may be abbreviated from Eq. (5.17a) to:

$$i\nu_{ij}\beta_{\rm so}\sigma_z, \tag{5.19}$$

with $\nu_{ij}=\pm1$, depending whether the hopping between two Mo atoms passes the closest X atom to the right or, respectively, to the left. The amplitude for the interaction at the conduction band bottom ε_c reads:

$$\beta_{\rm so}=\frac{\sqrt{3}}{16}\frac{F(\varepsilon_c)}{(\varepsilon_c-\varepsilon_p)(\varepsilon_c-\varepsilon_d)}. \tag{5.20}$$

Going back to momentum space, we find the final Bloch Hamiltonian:

$$H=H_1+2\beta_{so}[\sin(2\xi)-2\sin(\xi)\cos(\gamma)]\sigma_z\otimes L_{d_0}+V_x\sigma_x\otimes I_3+V_y\sigma_y\otimes I_3, \tag{5.21}$$

where we have also included Zeeman energy terms V_x and V_y due to an in-plane magnetic field, with I_3 the 3×3 identity. The orbital momentum matrix $L_{d_0}=\mathrm{diag}(1,0,0)$ ensures that only the hopping term between d_0 orbitals is renormalized by virtual hopping to p_x and p_y orbitals of X atoms. In fact virtual hoppings will also contribute to renormalize all d orbitals. Since we are interested in the low-energy physics at $\pm\mathbf{K}$ points close to the bottom of conduction band, we neglect further effects.

The result (5.20) for the coupling strength overestimates the strength of spin-orbit interaction required to obtain the observed conduction-band spin-orbit splitting. Instead

we perform an additional fit to obtain β_{so}. The lowest conduction bands in the tight-binding model are fitted at $\pm\mathbf{K}$ to the continuum model in the main text. The value extracted from the fits and used in our simulations for MoS_2 is $\beta_{\mathrm{so}} \approx 0.35\,\mathrm{meV}$, which reproduces the crossings of the spin-split lowest conduction band. Similarly, the coupling for $MoSe_2$ and $MoTe_2$ are approximately 2.04 meV and, respectively, $-3.46\,\mathrm{meV}$.

THE 11-ORBITAL MODEL

To further verify our conclusions, we adopt the *ab initio* tight-binding Hamiltonian for MoX_2 developed by Fang *et al.* in Ref. [40]. In this tight-binding model, the lowest conduction and topmost valence bands are in good agreement with the band structure obtained from first-principles calculations over the entire Brillouin zone. Unlike the three-orbital model, which only includes electron orbitals on the transition metal (Mo) atom, this tight-binding model includes orbitals on both the transition metal and chalcogen (X) atoms. Therefore, the model captures the real three-layer structure of the MoX_2 unit cell, making it possible to investigate effects that rely on the position of individual atoms, such as the orbital effects of a magnetic field. Furthermore, spin-orbit interaction is naturally included in this model by means of atomic SOC, which reproduces the expected crossings of the spin-split lowest conduction band.

The spinless tight-binding model includes five d orbitals on the Mo atom and six p orbitals on the X atoms per primitive unit cell. In Ref. [40], the basis of tight-binding orbitals is chosen to embody the mirror symmetry M_{xy} by forming linear combinations of the p orbitals from X_A and X_B atoms that are eigenstates of M_{xy}, effectively treating stacked X_A and X_B as a single composite atom. To recover a basis that reflects the three-layer structure of the MoX_2, we disentangle this symmetric basis into its constituent atomic orbitals with a unitary transformation, and use the atomic tight-binding basis

$$\begin{aligned}\psi = [&d_{xz}, d_{yz}, d_{z^2}, d_{xy}, d_{x^2-y^2},\\ &p_z^A, p_x^A, p_y^A, p_z^B, p_x^B, p_y^B]^T\\ = [&\psi_M, \psi_{X_A}, \psi_{X_B}]^T,\end{aligned} \tag{5.22}$$

where in the last line we have grouped the orbitals into vectors by atom.

The tight-binding Hamiltonian includes diagonal atomic onsite terms, and hoppings between various neighboring atoms. In terms of the atomic blocks (5.22), the spinless Bloch Hamiltonian is given by

$$H_0(\mathbf{k}) = \begin{bmatrix} H_{\mathrm{MoMo}} & H^\dagger_{\mathrm{X}_A\mathrm{Mo}} & H^\dagger_{\mathrm{X}_B\mathrm{Mo}} \\ H_{\mathrm{X}_A\mathrm{Mo}} & H_{\mathrm{X}_A\mathrm{X}_A} & H^\dagger_{\mathrm{X}_B\mathrm{X}_A} \\ H_{\mathrm{X}_B\mathrm{Mo}} & H_{\mathrm{X}_B\mathrm{X}_A} & H_{\mathrm{X}_B\mathrm{X}_B} \end{bmatrix}. \tag{5.23}$$

On the diagonal are blocks that consist of onsite terms h_α and intralayer hoppings between nearest neighbor atoms of the same type. These blocks are given by

$$H_{\alpha\alpha}(\mathbf{k}) = h_\alpha + \sum_{j\in\{1,2,3\}} \left[T^{(j)}_{\alpha\alpha} e^{-i\mathbf{k}\cdot\boldsymbol{\delta}_j} + \mathrm{h.c.} \right], \tag{5.24}$$

where $\alpha \in \{\mathrm{Mo}, \mathrm{X}_A, \mathrm{X}_B\}$. Here, $T^{(j)}_{\alpha\beta}$ is the matrix of hopping amplitudes from atom β to atom α along $\boldsymbol{\delta}_j$ (see Table 5.4). Off the diagonal, hoppings from Mo atoms to nearest

neighbor and next-nearest neighbor X atoms contribute terms of the form

$$H_{\alpha\mathrm{Mo}}(\mathbf{k}) = \sum_{j\in\{4,5,6,7\}} T^{(j)}_{\alpha\mathrm{Mo}} e^{i\mathbf{k}\cdot\boldsymbol{\delta}_j}, \tag{5.25}$$

with $\alpha \in \{\mathrm{X}_A, \mathrm{X}_B\}$. Finally, interlayer hoppings between X atoms are given by

$$H_{\mathrm{X}_B\mathrm{X}_A}(\mathbf{k}) = T^{(0)}_{\mathrm{X}_B\mathrm{X}_A} + \sum_{j\in\{1,2,3\}} \left[T^{(j)}_{\mathrm{X}_B\mathrm{X}_A} e^{-i\mathbf{k}\cdot\boldsymbol{\delta}_j} + \left(T^{(j)}_{\mathrm{X}_A\mathrm{X}_B}\right)^{\dagger} e^{i\mathbf{k}\cdot\boldsymbol{\delta}_j} \right]. \tag{5.26}$$

All the matrices h_α and $T^{(j)}_{\beta\gamma}$ for MoS_2 are provided as supplementary material to the manuscript. Note that tight-binding parameters for $MoSe_2$ are also available in Ref. [40], but not for $MoTe_2$.

5

Table 5.4: Hopping vectors $\boldsymbol{\delta}_j = \alpha_1\mathbf{a}_1 + \alpha_2\mathbf{a}_2$ in the tight-binding Hamiltonian, with the lattice vectors given in (5.7). Adapted from Ref. [40].

	$\boldsymbol{\delta}_1$	$\boldsymbol{\delta}_2$	$\boldsymbol{\delta}_3$	$\boldsymbol{\delta}_4$	$\boldsymbol{\delta}_5$	$\boldsymbol{\delta}_6$	$\boldsymbol{\delta}_7$	$\boldsymbol{\delta}_8$	$\boldsymbol{\delta}_9$
α_1	1	0	−1	1/3	−1/3	2/3	2/3	2/3	−4/3
α_2	0	1	1	−1	2/3	−1/3	−4/3	2/3	2/3

Spin-orbit coupling is incorporated in the tight-binding model by adding the atomic spin-orbit interaction terms $\lambda_\alpha \boldsymbol{L}\cdot\boldsymbol{S}$, with λ_α the strength of spin-orbit interaction for atom $\alpha \in \{\mathrm{Mo}, \mathrm{X}_A, \mathrm{X}_B\}$. Although the lowest conduction band at $\pm\mathbf{K}$ is dominated by the d orbitals of Mo atoms, the contribution of X atoms to SOC is necessary to produce the crossings between the lowest spin-split conduction band at $\pm\mathbf{K}$ (see Fig. 5.5), which are essential to realize nodal topological superconductivity. Including spin, the Bloch Hamiltonian in the basis $[\psi^{\uparrow}_{\mathrm{Mo}}, \psi^{\uparrow}_{\mathrm{X}_A}, \psi^{\uparrow}_{\mathrm{X}_B}, \psi^{\downarrow}_{\mathrm{Mo}}, \psi^{\downarrow}_{\mathrm{X}_A}, \psi^{\downarrow}_{\mathrm{X}_B}]^T$ in the presence of an in-plane magnetic field is given by

$$H(\mathbf{k}) = \sigma_0 \otimes H_0(\mathbf{k}) + H_{\mathrm{SOI}} + V_x\sigma_x \otimes I_{11} + V_y\sigma_y \otimes I_{11}, \tag{5.27}$$

with I_N the $N\times N$ identity matrix. The spin-orbit interaction matrix H_{SOI} has the block structure $h_{\alpha\beta}$ with $\alpha,\beta \in \{\mathrm{Mo}, \mathrm{X}_A, \mathrm{X}_B\}$, and nonzero blocks only for $\alpha = \beta$. Furthermore, $h_{\mathrm{X}_A\mathrm{X}_A} = h_{\mathrm{X}_B\mathrm{X}_B}$ since the atoms are identical. For SOC on the X atoms, the nonzero matrix elements of $h_{\mathrm{X}_\alpha\mathrm{X}_\alpha}$ with $\alpha = A, B$ are

$$\langle p^\alpha_x\downarrow|H_{\mathrm{SOI}}|p^\alpha_z\uparrow\rangle = -\lambda_{\mathrm{X}_\alpha}/2,\ \langle p^\alpha_y\downarrow|H_{\mathrm{SOI}}|p^\alpha_z\uparrow\rangle = -i\lambda_{\mathrm{X}_\alpha}/2,\ \langle p^\alpha_y\uparrow|H_{\mathrm{SOI}}|p^\alpha_x\uparrow\rangle = i\lambda_{\mathrm{X}_\alpha}/2,$$
$$\langle p^\alpha_x\downarrow|H_{\mathrm{SOI}}|p^\alpha_x\uparrow\rangle = \lambda_{\mathrm{X}_\alpha}/2,\ \langle p^\alpha_z\downarrow|H_{\mathrm{SOI}}|p^\alpha_y\uparrow\rangle = i\lambda_{\mathrm{X}_\alpha}/2,\ \langle p^\alpha_y\downarrow|H_{\mathrm{SOI}}|p^\alpha_x\downarrow\rangle = -i\lambda_{\mathrm{X}_\alpha}/2,$$

along with their Hermitian conjugates. Similarly, the nonzero spin-orbit matrix elements

of h_{MoMo} for the Mo atom are

$\langle d_{yz}\uparrow|H_{\mathrm{SOI}}|d_{xz}\uparrow\rangle = i\lambda_{\mathrm{Mo}}/2$, $\langle d_{z^2}\downarrow|H_{\mathrm{SOI}}|d_{xz}\uparrow\rangle = \sqrt{3}\lambda_{\mathrm{Mo}}/2$, $\langle d_{xy}\downarrow|H_{\mathrm{SOI}}|d_{xz}\uparrow\rangle = -i\lambda_{\mathrm{Mo}}/2$,
$\langle d_{x^2-y^2}\downarrow|H_{\mathrm{SOI}}|d_{xz}\uparrow\rangle = -\lambda_{\mathrm{Mo}}/2$, $\langle d_{z^2}\downarrow|H_{\mathrm{SOI}}|d_{yz}\uparrow\rangle = i\sqrt{3}\lambda_{\mathrm{Mo}}/2$, $\langle d_{xy}\downarrow|H_{\mathrm{SOI}}|d_{yz}\uparrow\rangle = -\lambda_{\mathrm{Mo}}/2$,
$\langle d_{x^2-y^2}\downarrow|H_{\mathrm{SOI}}|d_{yz}\uparrow\rangle = i\lambda_{\mathrm{Mo}}/2$, $\langle d_{xz}\downarrow|H_{\mathrm{SOI}}|d_{z^2}\uparrow\rangle = -\sqrt{3}\lambda_{\mathrm{Mo}}/2$, $\langle d_{yz}\downarrow|H_{\mathrm{SOI}}|d_{z^2}\uparrow\rangle = -i\sqrt{3}\lambda_{\mathrm{Mo}}/2$,
$\langle d_{x^2-y^2}\uparrow|H_{\mathrm{SOI}}|d_{xy}\uparrow\rangle = -i\lambda_{\mathrm{Mo}}$, $\langle d_{xz}\downarrow|H_{\mathrm{SOI}}|d_{xy}\uparrow\rangle = i\lambda_{\mathrm{Mo}}/2$, $\langle d_{yz}\downarrow|H_{\mathrm{SOI}}|d_{xy}\uparrow\rangle = \lambda_{\mathrm{Mo}}/2$,
$\langle d_{xz}\downarrow|H_{\mathrm{SOI}}|d_{x^2-y^2}\uparrow\rangle = \lambda_{\mathrm{Mo}}/2$, $\langle d_{yz}\downarrow|H_{\mathrm{SOI}}|d_{x^2-y^2}\uparrow\rangle = -i\lambda_{\mathrm{Mo}}/2$, $\langle d_{yz}\downarrow|H_{\mathrm{SOI}}|d_{xz}\downarrow\rangle = -i\lambda_{\mathrm{Mo}}/2$,
$\langle d_{x^2-y^2}\downarrow|H_{\mathrm{SOI}}|d_{xy}\downarrow\rangle = i\lambda_{\mathrm{Mo}}$.

The strength of the atomic SOC is $\lambda_{\mathrm{X}_A} = \lambda_{\mathrm{X}_B} = 0.0556$ eV for X = S, 0.2470 eV for X = Se, and $\lambda_{\mathrm{Mo}} = 0.0836$ eV [40].

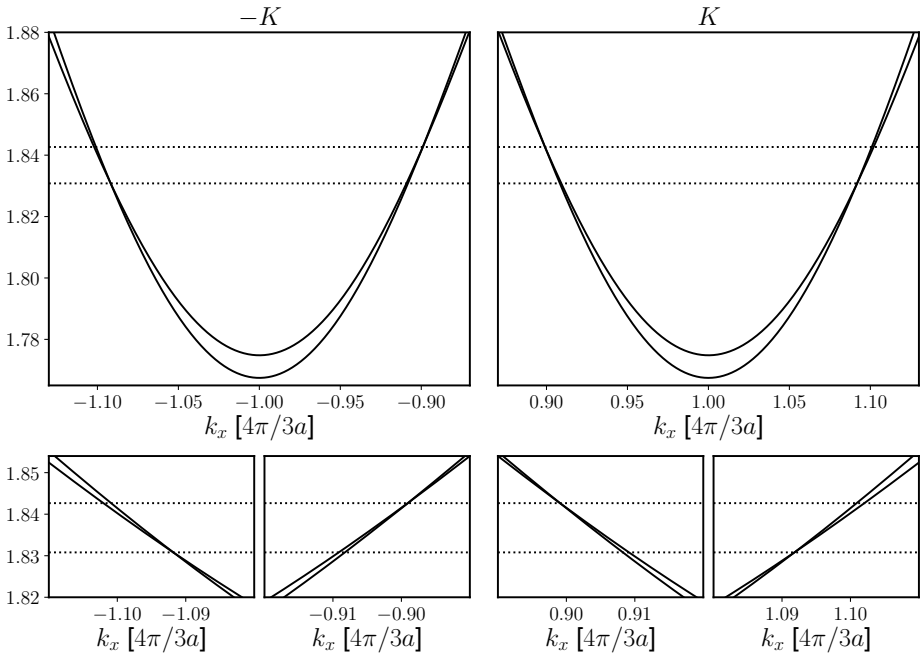

Figure 5.5: Band structure of the normal-state spin-split lowest conduction band in monolayer MoS_2 near the $\pm\mathbf{K}$ valleys along the line $k_y = 0$. The bands are split by spin-orbit interaction, but cross at finite k_x at points in momentum space where the spin splitting due to SOC vanishes, at energies indicated by the horizontal dotted lines. The bottom panels show a zoom in on the crossings in each valley. Such conduction band crossings near $\pm\mathbf{K}$ are present in the MoX_2 family of materials.

The physics of nodal topological superconductivity in monolayer MoX_2 materials is governed by the low-energy dispersion of the spin-split lowest conduction band around the high symmetry points $\pm\mathbf{K}$. The 11-orbital tight-binding model captures the orbital

character and symmetry of the monolayer bands and reproduces the main features of band structure over the entire Brillouin zone. However, at the small energy scales close to the the conduction band minimum at **K**, there are deviations in the 11-orbital model from the first-principles calculations. This is because the model is optimized to reflect the band structure over the entire Brillouin zone, but not to accurately capture nuances in the low-energy dispersion of individual bands near high-symmetry points, for which $\mathbf{k}\cdot\mathbf{p}$ Hamiltonians are generally more suitable. Unlike the 11-orbital model, the three-orbital model and the continuum model in the main part of this manuscript are both optimized to capture the relevant low-energy physics. As a result, there are quantitative differences in the low-energy dispersion of the spin-split conduction band between the 11-orbital model and the other two models, such as conduction band crossings that occur further away from the high-symmetry points **K**. This difference is intrinsic to the design of the 11-orbital model [40], and that despite the quantitative differences, all results obtained with the 11-orbital model are in qualitative agreement with the continuum and three-orbital models.

5

5.8.3. TIGHT-BINDING MODELS FOR NODAL TOPOLOGICAL SUPERCONDUCTIVITY IN MoX_2

We model a superconducting monolayer MoX_2 at the mean-field level with the Bogoliubov-de Gennes (BdG) Hamiltonian

$$H_{\mathrm{BdG}}(\mathbf{k}) = \begin{bmatrix} H(\mathbf{k}) - \mu I_{2N} & -i\Delta\sigma_y \otimes I_N \\ i\Delta\sigma_y \otimes I_N & -H^*(-\mathbf{k}) + \mu I_{2N} \end{bmatrix}, \tag{5.28}$$

with μ the chemical potential, Δ the s-wave pairing, and where the normal-state Hamiltonian $H(\mathbf{k})$ refers to either the three-orbital model (5.21) or the 11-orbital model (5.27), for which $N = 3$ and $N = 11$, respectively. In this work, we only consider values of μ that lie in the conduction band.

The BdG Hamiltonian Eq. (5.28) has the intrinsic particle-hole symmetry

$$\mathscr{P} = \tau_x \otimes I_{2N}\mathscr{K}, \quad \mathscr{P}H_{\mathrm{BdG}}(\mathbf{k})\mathscr{P}^{-1} = -H_{\mathrm{BdG}}(-\mathbf{k}), \tag{5.29}$$

such that $\mathscr{P}^2 = 1$, where $\mathscr{K}$ is the complex conjugation operator and $\tau_{x,y,z}$ are Pauli matrices that act in particle-hole space. In the absence of magnetic fields, the BdG Hamiltonian furthermore has time-reversal symmetry $\mathscr{T}H_{\mathrm{BdG}}(\mathbf{k})\mathscr{T}^{-1} = H_{\mathrm{BdG}}(-\mathbf{k})$, with $\mathscr{T} = i\tau_0\sigma_y \otimes I_N\mathscr{K}$. Although a nonzero in-plane magnetic field breaks both $\mathscr{T}$ and the mirror symmetry M_{xy} individually, the BdG Hamiltonian nevertheless remains symmetric to their product, and we can therefore define the effective time-reversal operator $\tilde{\mathscr{T}}$ that leaves the BdG Hamiltonian invariant, namely

$$\tilde{\mathscr{T}} = M_{xy}\mathscr{T}, \quad \tilde{\mathscr{T}}H_{\mathrm{BdG}}(\mathbf{k})\tilde{\mathscr{T}}^{-1} = H_{\mathrm{BdG}}(-\mathbf{k}), \tag{5.30}$$

such that $\tilde{\mathscr{T}}^2 = 1$. Combining $\mathscr{P}$ and $\tilde{\mathscr{T}}$, we therefore find that the BdG Hamiltonian Eq. (5.28) has the chiral symmetry

$$\mathscr{C} = \tilde{\mathscr{T}}\mathscr{P}, \quad \mathscr{C}H_{\mathrm{BdG}}(\mathbf{k})\mathscr{C}^{-1} = -H_{\mathrm{BdG}}(\mathbf{k}), \quad \mathscr{C}^2 = 1. \tag{5.31}$$

Since $\tilde{\mathscr{T}}^2 = \mathscr{P}^2 = 1$, the BdG Hamiltonian (5.28) describes a superconductor in class BDI, which in two-dimensions is a topologically trivial class. Nevertheless, topologically protected flat bands of Andreev bound states may exist at the edges of such systems [11]. To demonstrate this, we separate $\mathbf{k} = (\mathbf{k}_\parallel, \mathbf{k}_\perp)$ into two orthogonal projections, parallel $\mathbf{k}_\parallel$ and perpendicular $\mathbf{k}_\perp$ to a monolayer edge, respectively. For example, an armchair edge of MoX_2 is parallel to the y direction and perpendicular to x, such that $\mathbf{k}_\parallel = k_y\hat{\mathbf{y}}$ and $\mathbf{k}_\perp = k_x\hat{\mathbf{x}}$. Instead of applying the symmetry classification to the full two-dimensional BdG Hamiltonian $H_{\mathrm{BdG}}(\mathbf{k})$, we reduce the dimension to one by treating $\mathbf{k}_\parallel$ as a parameter, and consider each one-dimensional Hamiltonian $H_{\mathrm{BdG}}(\mathbf{k}) = H^{\mathbf{k}_\parallel}_{\mathrm{BdG}}(\mathbf{k}_\perp)$ at a fixed $\mathbf{k}_\parallel$ separately. Now, $\mathscr{P}$ and $\tilde{\mathscr{T}}$ are in general not symmetries of the one-dimensional Hamiltonian $H^{\mathbf{k}_\parallel}_{\mathrm{BdG}}(\mathbf{k}_\perp)$ at a fixed $\mathbf{k}_\parallel$, because they flip the sign of both $\mathbf{k}_\parallel$ and $\mathbf{k}_\perp$. Indeed, we generally find that no one-dimensional particle-hole $\mathscr{P}_{1\mathrm{D}}$ or time-reversal $\mathscr{T}_{1\mathrm{D}}$ type symmetries that satisfy $\mathscr{P}_{1\mathrm{D}} H^{\mathbf{k}_\parallel}_{\mathrm{BdG}}(\mathbf{k}_\perp)\mathscr{P}^{-1}_{1\mathrm{D}} = -H^{\mathbf{k}_\parallel}_{\mathrm{BdG}}(-\mathbf{k}_\perp)$ or $\mathscr{T}_{1\mathrm{D}} H^{\mathbf{k}_\parallel}_{\mathrm{BdG}}(\mathbf{k}_\perp)\mathscr{T}^{-1}_{1\mathrm{D}} = H^{\mathbf{k}_\parallel}_{\mathrm{BdG}}(-\mathbf{k}_\perp)$ exist in the tight-binding BdG models, even after performing a systematic search for such symmetries [45]. The reason is that for the one-dimensional symmetries $\mathscr{P}_{1\mathrm{D}}$ and $\mathscr{T}_{1\mathrm{D}}$ to exist, there should be an extra unitary symmetry $V_\parallel$ commuting with the Hamiltonian that maps $\mathbf{k}_\parallel \to -\mathbf{k}_\parallel$. We could then construct a 1D symmetry $\mathscr{P}_{1\mathrm{D}}$ or $\mathscr{T}_{1\mathrm{D}}$ with the product of $V_\parallel$ and the corresponding 2D symmetry. However, for generic $(\mathbf{k}_\perp, \mathbf{k}_\parallel)$, we find that no such symmetry $V_\parallel$ exists, and hence $\mathscr{P}_{1\mathrm{D}}$ and $\mathscr{T}_{1\mathrm{D}}$ are generally non-existent. Regardless, the chiral symmetry (5.31) is valid for any choice of directions in the Brillouin zone since $\mathscr{C}$ always leaves the momentum unchanged, *i.e.* $\mathscr{C} H^{k_\parallel}_{\mathrm{BdG}}(\mathbf{k}_\perp)\mathscr{C}^{-1} = -H^{k_\parallel}_{\mathrm{BdG}}(\mathbf{k}_\perp)$. We therefore conclude that the one-dimensional Hamiltonians $H^{\mathbf{k}_\parallel}_{\mathrm{BdG}}(\mathbf{k}_\perp)$ at a fixed $\mathbf{k}_\parallel$ belong to symmetry class AIII.

The topological number relevant for one-dimensional systems in class AIII is the winding number [11, 43], which at the parallel momentum $\mathbf{k}_\parallel$ is given by

$$W(\mathbf{k}_\parallel) = \frac{1}{2\pi i}\int_{\mathrm{BZ}} \frac{dz(\mathbf{k}_\perp)}{z(\mathbf{k}_\perp)}. \tag{5.32}$$

The integration is performed for a fixed value of $\mathbf{k}_\parallel$ over the one-dimensional Brillouin zone along the direction of $\mathbf{k}_\perp$, which is a closed loop. Here, $z(\mathbf{k}_\perp) = \det\{A(\mathbf{k}_\perp)\}/|\det\{A(\mathbf{k}_\perp)\}|$ with

$$U^\dagger_{\mathscr{C}} H_{\mathrm{BdG}}(\mathbf{k}) U_{\mathscr{C}} = \begin{bmatrix} 0 & A(\mathbf{k}) \\ A^\dagger(\mathbf{k}) & 0 \end{bmatrix}, \tag{5.33}$$

and $U_{\mathscr{C}}$ the unitary matrix that diagonalizes $\mathscr{C}$, $U^\dagger_{\mathscr{C}}\mathscr{C}U_{\mathscr{C}} = \tau_z \otimes I_{2N}$. The winding number is quantized to $W(\mathbf{k}_\parallel) \in \mathbb{Z}$, and changes only when the integration path over $\mathbf{k}_\perp$ intersects a nodal point [11, 46], where the system is gapless such that $\det[A(\mathbf{k})] = 0$. When $W(\mathbf{k}_\parallel)$ is nonzero, zero-energy states exist at the edge of the monolayer at the parallel momentum $\mathbf{k}_\parallel$. Since $W(\mathbf{k}_\parallel)$ only changes at values of $\mathbf{k}_\parallel$ where the integration path over $\mathbf{k}_\perp$ crosses a nodal point, $W(\mathbf{k}_\parallel)$ is generally nonzero in finite intervals of $\mathbf{k}_\parallel$, forming flat bands of Andreev bound states in the dispersion that are localized at the monolayer edge.

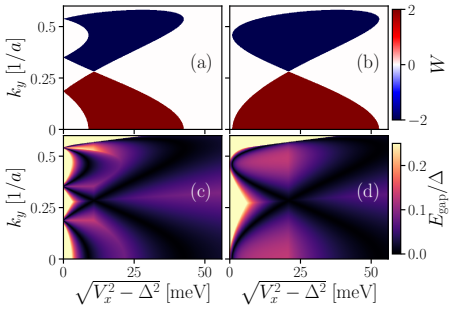

(i) $MoTe_2$ $\mathbf{k}\cdot\mathbf{p}$ model.

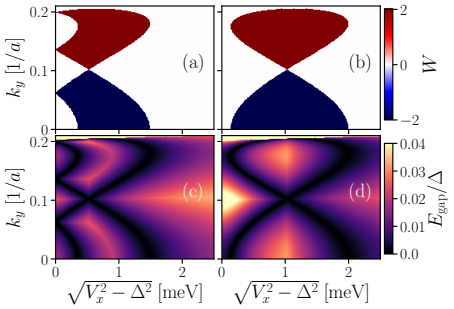

(ii) MoS_2 $\mathbf{k}\cdot\mathbf{p}$ model.

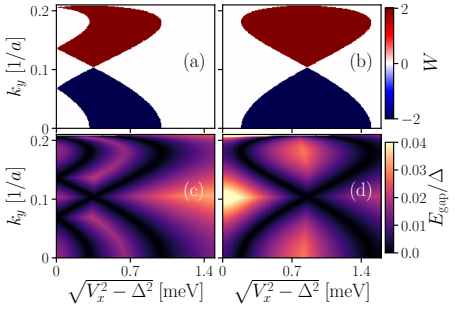

(iii) MoS_2 3-orbital tight-binding model.

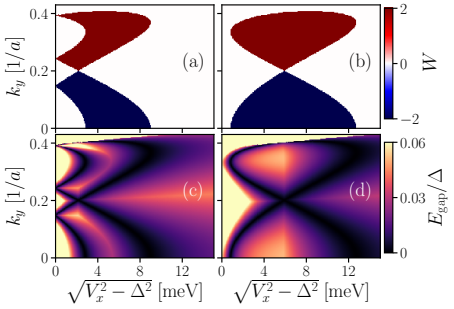

(iv) MoS_2 11-orbital tight-binding model.

Figure 5.6: Topological phase diagrams and excitation gaps along the armchair direction $\mathbf{k}_\parallel = k_y\hat{\mathbf{y}}$ for (i) $MoTe_2$ from the continuum $\mathbf{k}\cdot\mathbf{p}$ model, and (ii-iv) MoS2, comparing the $\mathbf{k}\cdot\mathbf{p}$ and three- and 11-orbital tight-binding models. In all cases, panels (a) and (b) show the winding number W computed using Eq. (5.32) as a function of k_y and $\sqrt{V_x^2-\Delta^2}$ for (a) $\mu<\mu_1$ and (b) $\mu_1<\mu<(\mu_1+\mu_2)/2$, representative of regimes I and II of Fig. 1(b) of the main text. For $(\mu_1+\mu_2)/2<\mu<\mu_2$ and $\mu>\mu_2$, the phase diagrams are similar to (a) and (b) respectively, but with opposite winding numbers. In all cases, panels (c) and (d) show the topological excitation gap E_{gap} corresponding to (a) and (b) separately.

5.8.4. PHASE DIAGRAMS FOR MoX_2 MONOLAYERS AND COMPARISON WITH TIGHT-BINDING CALCULATIONS

In Fig. 5.6 (i) and (ii), we show examples of (a, b) topological phase diagrams and (c, d) maps of the corresponding topological excitation gap for superconducting monolayers of $MoTe_2$ and MoS_2, respectively, obtained using the continuum $\mathbf{k}\cdot\mathbf{p}$ Hamiltonian. Analogous data for monolayer $MoSe_2$ is shown in Fig. 2 of the main text. We see that the phase diagrams of all three MoX_2 materials are qualitatively similar, but with some quantitative differences, for instance a much larger excitation gap in $MoTe_2$ than in MoS_2. This is because the continuum Hamiltonians for all three materials are identical in form and have the same symmetries, see Eq. (1) of the main text. Crucially, despite the differences in material parameters between the three types of monolayer, they all exhibit crossings between the spin-split conduction band where the SOC vanishes, as illustrated in Fig. 5.5, which makes the realization of the nodal topological phase possible. The sign of the wind-

ing number for $MoTe_2$ in (i) is opposite to that of MoS_2 in (ii) because spin-polarization of the conduction bands is inverted [see Table 5.2]. Figures 5.6 (iii) and (iv) show analogous results for MoS_2 obtained using (iii) the three-orbital tight-binding model, and (iv) the 11-orbital tight-binding model. The three-orbital tight-binding model agrees well with the continuum model, but there are more prominent quantitative differences with the 11-orbital model, because the latter is not optimized to accurately describe the low-energy physics near the **K** valleys [40]. Nonetheless, all three models are in qualitative agreement.

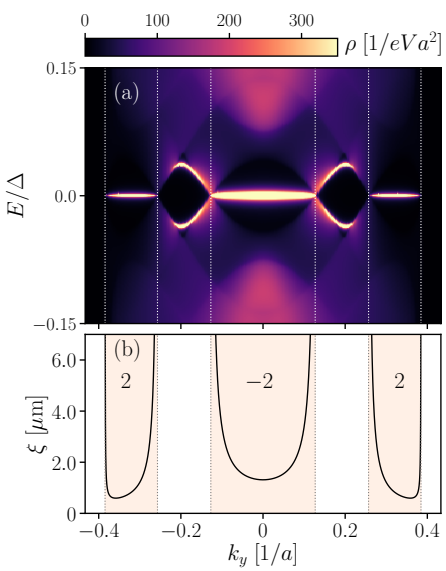

(i) 11-orbital tight-binding model.

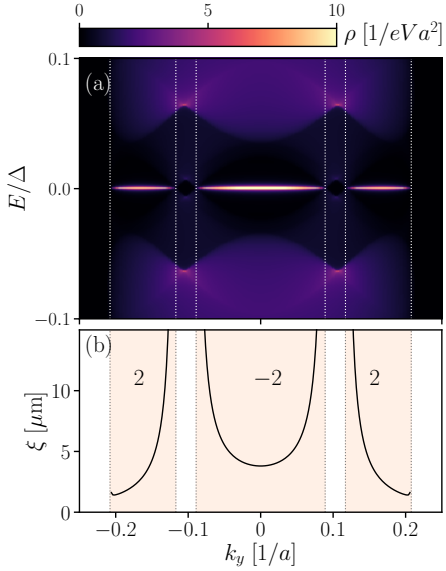

(ii) 3-orbital tight-binding model.

Figure 5.7: (a) Local density of states and (b) decay length of the nontrivial edge states at an armchair edge of a monolayer MoS_2 obtained using the (i) 11-orbital tight-binding model, and (ii) the three-orbital tight-binding model. In both cases $\Delta = 0.8$ meV, with other parameters in regime II of of Fig. 1(b) of the main text. When the winding number is nonzero, flat bands of zero-energy Andreev edge states connecting the edge projections of the nodal points appear at the armchair edge. The nontrivial phases are marked by the shaded regions in (b) with the nonzero winding numbers in the insets. We have $\mu = 1.830$ eV and $V_x = 3.105$ meV in (i), and $\mu = 1.709$ eV, $V_x = 1.131$ meV in (ii).

Figure 5.7 shows the local density of states at an armchair edge of a superconducting monolayer MoS_2 using parameters within regime II of Fig. 1(b) of the main text, obtained from the (i) 11-orbital tight-binding model, and the (ii) three-orbital tight-binding model. We see flat bands of zero-energy Andreev bound states that are localized at the edge manifest in regions where the winding number $W(k_y)$ is nonzero. In the parameter regime II we consider here, there are 6 nodal points near each inequivalent K valley. The projections of the nodal points onto the armchair edge partition the one-dimensional Brillouin zone of the armchair edge into 7 segments, with the flat bands appearing in segments where the winding number is nonzero. Despite quantitative differences between the two models, the figures are in qualitative agreement.

We conclude this section with a brief comparison of the two tight-binding models. Both models agree with our analysis of the nodal topological phase based on the continuum Hamiltonian in the main text. Since it contains fewer basis orbitals per unit cell, the three-orbital model is less cumbersome to work with than the 11-orbital model. This also makes the three-orbital model more suitable for performing large-scale simulations of finite systems with multiple unit cells, as the size of the Hamiltonian will scale better than using the 11-orbital model. In addition, the three-orbital model is more accurate than the 11-orbital model near the high symmetry points $\pm\mathbf{K}$ which are most relevant in our study, since the 11-orbital model is designed to approximate the band structure in the entire Brillouin zone instead of only near $\pm\mathbf{K}$. However, the three-orbital model only includes orbitals on the M atoms but not the X atoms, while the 11-orbital model includes orbitals on all the atoms in the monolayer unit cell. This makes the 11-orbital model better suited than the three-orbital model to simulate effects that depend on the three dimensional structure of the monolayer, such as the orbital effects of a magnetic field. Similarly, atomic SOC terms are sufficient to reproduce the crossings in the conduction band necessary for the nodal topological phase within the 11-orbital model. In the three-orbital model however, it is necessary to supplement the SOC on the M atom with an extra term due to virtual hoppings to orbitals on the X atoms, as shown in Section 5.8.2.

5.8.5. TOPOLOGICAL PHASES FOR ARBITRARY EDGE CUTS

The presence of zero-energy flat bands for ribbons with different edge orientation can be predicted due to bulk-edge correspondence from the knowledge of the bulk topological invariant. The usual way to probe the topological phase diagram is to write effective Hamiltonians for specific edge orientation. Zero-energy states exist whenever the effective edge Hamiltonian has a non-trivial winding number. This procedure is cumbersome since it requires redefining for each edge a different Hamiltonian, which depending of the edge orientation, might be represented by an unwieldy large matrix.

An alternative method developed in Ref. [52], allows us to keep the bulk Hamiltonian unchanged, but instead vary an effective Brillouin zone. As described in the main text, we assume that the lattice termination edge forms a one-dimensional superlattice, with a translation period given by the superlattice vector

$$\mathbf{T} = m\mathbf{a}_1 + n\mathbf{a}_2, \tag{5.34}$$

which is parallel to the lattice termination edge. Here, m and n are coprime integers, and the Bravais lattice vectors are given in (5.7).

Along the edge, parallel to $\mathbf{T}$, we define the conserved momentum $k_\parallel$, with values in the 1D Brillouin zone of size $\Delta k_\parallel = 2\pi/|\mathbf{T}|$, namely

$$k_\parallel \in \Delta k_\parallel = \frac{\pi}{a}\left[-\frac{1}{\sqrt{m^2+n^2+mn}}, \frac{1}{\sqrt{m^2+n^2+mn}}\right). \tag{5.35}$$

The momentum span $\Delta k_\perp$ in the direction perpendicular to the edge is constrained such that the area of Brillouin zone is conserved,

$$k_\perp \in \Delta k_\perp = \frac{2\pi}{\sqrt{3}a}\left[-\sqrt{m^2+n^2+mn}, \sqrt{m^2+n^2+mn}\right), \tag{5.36}$$

with the momentum $k_\perp$ perpendicular to the edge. For a given lattice termination boundary characterized by **T**, the winding number at the momentum $k_\parallel$ in the 1D Brillouin zone (5.35) follows from Eq. (5.32) by integrating over all $k_\perp$ in (5.36). Note that (5.36) is exactly one period in reciprocal space, and the integral over $k_\perp$ to compute the winding number is therefore over a closed loop.

5.8.6. ORBITAL EFFECT OF THE IN-PLANE MAGNETIC FIELD

In this section, we discuss the orbital effects of the in-plane magnetic field on the nodal topological superconducting phase in the monolayer MoX_2. For simplicity, we assume a magnetic field $\boldsymbol{B} = B\hat{\mathbf{x}}$ along x only. To preserve translational invariance in the monolayer plane, we pick the vector potential $\boldsymbol{A} = -Bz\hat{\mathbf{y}}$.

Including the orbital effect of the magnetic field does not alter the symmetry classification of the BdG Hamiltonian (5.28). To demonstrate this, we include the magnetic field in the normal state continuum model with the kinetic momentum substitution $k_y \to \hbar k_y + eA = k_y - eBz$, with e the unit charge. Since $M_{xy} : z \to -z$ and $\mathcal{T} : \mathbf{k} \to -\mathbf{k}$, we see that the new kinetic momentum transforms identically under the product $M_{xy}\mathcal{T}$ with and without the orbital effects of the magnetic field. Thus, the normal-state Hamiltonian with orbital effects included remains invariant to the generalized time-reversal symmetry $\tilde{\mathcal{T}} = M_{xy}\mathcal{T}$, and the BdG Hamiltonian therefore also to the chiral symmetry $\mathscr{C}$. We have verified this numerically by including the orbital effects of the magnetic field in the 11-orbital tight-binding model, with a Peierls substitution for the hopping matrices $T^{(j)}_{\alpha\beta} \to T^{(j)}_{\alpha\beta} \exp(-i\frac{e}{\hbar}\int \boldsymbol{A}\cdot d\mathbf{r})$ [63–65]. We find negligible quantitative differences in our numerical results with and without the orbital effects included and no qualitative differences, and therefore neglect the orbital effects in our calculations. This is reasonable, because the magnetic length $l_B = \sqrt{\hbar/eB}$ with $\hbar$ the reduced Planck's constant is in the nanometers even up to extremely large fields $\lesssim 100$ T, and thus always much larger than the separation $d \approx 3$ Å between the top and bottom layers of X atoms in the monolayer.

REFERENCES

[1] J. Alicea, *New directions in the pursuit of majorana fermions in solid state systems,* Rep. Prog. Phys. **75**, 076501 (2012).

[2] M. Leijnse and K. Flensberg, *Introduction to topological superconductivity and majorana fermions,* Semiconductor Science and Technology **27**, 124003 (2012).

[3] C. Beenakker, *Search for majorana fermions in superconductors,* Annu. Rev. Condens. Matter Phys. **4**, 113 (2013).

[4] A. Y. Kitaev, *Unpaired majorana fermions in quantum wires,* Phys. Usp. **44**, 131 (2001).

[5] S. B. Bravyi and A. Y. Kitaev, *Fermionic quantum computation,* Annals of Physics **298**, 210 (2002).

[6] C. Nayak, S. H. Simon, A. Stern, M. Freedman, and S. Das Sarma, *Non-Abelian anyons and topological quantum computation,* Reviews of Modern Physics **80**, 1083 (2008).

[7] S. Kashiwaya and Y. Tanaka, *Tunnelling effects on surface bound states in unconventional superconductors,* Rep. Prog. Phys. **63**, 1641 (2000).

[8] T. Löfwander, V. S. Shumeiko, and G. Wendin, *Andreev bound states in high- t c superconducting junctions,* Supercond. Sci. Technol. **14**, R53 (2001).

[9] A. P. Schnyder and P. M. R. Brydon, *Topological surface states in nodal superconductors,* J. Phys.: Condens. Matter **27**, 243201 (2015).

[10] S. Ryu and Y. Hatsugai, *Topological origin of zero-energy edge states in particle-hole symmetric systems,* Phys. Rev. Lett. **89**, 077002 (2002).

[11] M. Sato, Y. Tanaka, K. Yada, and T. Yokoyama, *Topology of andreev bound states with flat dispersion,* Phys. Rev. B **83**, 224511 (2011).

[12] A. P. Schnyder, P. M. R. Brydon, and C. Timm, *Types of topological surface states in nodal noncentrosymmetric superconductors,* Phys. Rev. B **85**, 024522 (2012).

[13] C. C. Tsuei and J. R. Kirtley, *Pairing symmetry in cuprate superconductors,* Rev. Mod. Phys. **72**, 969 (2000).

[14] Y. Kasahara, T. Iwasawa, H. Shishido, T. Shibauchi, K. Behnia, Y. Haga, T. D. Matsuda, Y. Onuki, M. Sigrist, and Y. Matsuda, *Exotic superconducting properties in the electron-hole-compensated heavy-fermion "semimetal"* uru_2si_2, Phys. Rev. Lett. **99**, 116402 (2007).

[15] B. B. Zhou, S. Misra, E. H. da Silva Neto, P. Aynajian, R. E. Baumbach, J. D. Thompson, E. D. Bauer, and A. Yazdani, *Visualizing nodal heavy fermion superconductivity in cecoin5,* Nat. Phys. **9**, 474 EP (2013).

[16] M. P. Allan, F. Massee, D. K. Morr, J. Van Dyke, A. W. Rost, A. P. Mackenzie, C. Petrovic, and J. C. Davis, *Imaging cooper pairing of heavy fermions in cecoin5,* Nat. Phys. **9**, 468 EP (2013).

[17] K. Yada, M. Sato, Y. Tanaka, and T. Yokoyama, *Surface density of states and topological edge states in noncentrosymmetric superconductors,* Phys. Rev. B **83**, 064505 (2011).

[18] A. P. Schnyder and S. Ryu, *Topological phases and surface flat bands in superconductors without inversion symmetry,* Phys. Rev. B **84**, 060504 (2011).

[19] M. H. Fischer, T. Neupert, C. Platt, A. P. Schnyder, W. Hanke, J. Goryo, R. Thomale, and M. Sigrist, *Chiral d-wave superconductivity in srptas,* Phys. Rev. B **89**, 020509 (2014).

[20] T. Meng and L. Balents, *Weyl superconductors,* Phys. Rev. B **86**, 054504 (2012).

[21] C. L. M. Wong, J. Liu, K. T. Law, and P. A. Lee, *Majorana flat bands and unidirectional majorana edge states in gapless topological superconductors,* Phys. Rev. B **88**, 060504 (2013).

[22] B. Huang, X. Yang, N. Xu, and M. Gong, *Type-i and type-ii topological nodal superconductors with s-wave interaction,* Phys. Rev. B **97**, 045142 (2018).

[23] L. Fu and C. L. Kane, *Superconducting proximity effect and majorana fermions at the surface of a topological insulator,* Phys. Rev. Lett. **100**, 096407 (2008).

[24] J. D. Sau, R. M. Lutchyn, S. Tewari, and S. Das Sarma, *Generic new platform for topological quantum computation using semiconductor heterostructures,* Phys. Rev. Lett. **104**, 040502 (2010).

[25] Q. H. Wang, K. Kalantar-Zadeh, A. Kis, J. N. Coleman, and M. S. Strano, *Electronics and optoelectronics of two-dimensional transition metal dichalcogenides,* Nat. Nanotechnol. **7**, 699 EP (2012).

[26] J. T. Ye, Y. J. Zhang, R. Akashi, M. S. Bahramy, R. Arita, and Y. Iwasa, *Superconducting dome in a gate-tuned band insulator,* Science **338**, 1193 (2012).

[27] K. Taniguchi, A. Matsumoto, H. Shimotani, and H. Takagi, *Electric-field-induced superconductivity at 9.4 k in a layered transition metal disulphide mos2,* Appl. Phys. Lett. **101**, 042603 (2012).

[28] J. M. Lu, O. Zheliuk, I. Leermakers, N. F. Q. Yuan, U. Zeitler, K. T. Law, and J. T. Ye, *Evidence for two-dimensional ising superconductivity in gated mos2,* Science **350**, 1353 (2015).

[29] W. Shi, J. Ye, Y. Zhang, R. Suzuki, M. Yoshida, J. Miyazaki, N. Inoue, Y. Saito, and Y. Iwasa, *Superconductivity series in transition metal dichalcogenides by ionic gating,* Sci. Rep. **5**, 12534 (2015).

[30] Y. Saito, Y. Nakamura, M. S. Bahramy, Y. Kohama, J. Ye, Y. Kasahara, Y. Nakagawa, M. Onga, M. Tokunaga, T. Nojima, Y. Yanase, and Y. Iwasa, *Superconductivity protected by spin–valley locking in ion-gated mos2,* Nat. Phys. **12**, 144 (2016).

[31] D. Costanzo, S. Jo, H. Berger, and A. F. Morpurgo, *Gate-induced superconductivity in atomically thin mos2 crystals,* Nat. Nanotech. **11**, 339 EP (2016).

[32] X. Xi, Z. Wang, W. Zhao, J.-H. Park, K. T. Law, H. Berger, L. Forró, J. Shan, and K. F. Mak, *Ising pairing in superconducting nbse2 atomic layers,* Nat. Physics **12**, 139 (2016).

[33] O. Zheliuk, J. Lu, J. Yang, and J. Ye, *Monolayer superconductivity in ws2,* Phys. Status Solidi RRL **11**, 1700245 (2017).

[34] S. C. de la Barrera, M. R. Sinko, D. P. Gopalan, N. Sivadas, K. L. Seyler, K. Watanabe, T. Taniguchi, A. W. Tsen, X. Xu, D. Xiao, and B. M. Hunt, *Tuning ising superconductivity with layer and spin–orbit coupling in two-dimensional transition-metal dichalcogenides,* Nat. Commun. **9**, 1427 (2018).

[35] B. T. Zhou, N. F. Q. Yuan, H.-L. Jiang, and K. T. Law, *Ising superconductivity and majorana fermions in transition-metal dichalcogenides,* Phys. Rev. B **93**, 180501 (2016).

[36] S. Ilić, J. S. Meyer, and M. Houzet, *Enhancement of the Upper Critical Field in Disordered Transition Metal Dichalcogenide Monolayers,* Physical Review Letters **119** (2017), 10.1103/PhysRevLett.119.117001.

[37] Z. Y. Zhu, Y. C. Cheng, and U. Schwingenschlögl, *Giant spin-orbit-induced spin splitting in two-dimensional transition-metal dichalcogenide semiconductors,* Phys. Rev. B **84**, 153402 (2011).

[38] D. Xiao, G.-B. Liu, W. Feng, X. Xu, and W. Yao, *Coupled spin and valley physics in monolayers of* mos_2 *and other group-vi dichalcogenides,* Phys. Rev. Lett. **108**, 196802 (2012).

[39] W.-Y. He, B. T. Zhou, J. J. He, N. F. Q. Yuan, T. Zhang, and K. T. Law, *Magnetic field driven nodal topological superconductivity in monolayer transition metal dichalcogenides,* Communications Physics **1** (2018), 10.1038/s42005-018-0041-4.

[40] S. Fang, R. Kuate Defo, S. N. Shirodkar, S. Lieu, G. A. Tritsaris, and E. Kaxiras, *Ab initio,* Phys. Rev. B **92**, 205108 (2015).

[41] P. Löwdin, *A note on the quantum-mechanical perturbation theory,* J. Chem. Phys. **19**, 1396 (1951).

[42] L. Wang and M. W. Wu, *Electron spin relaxation due to dyakonov-perel and elliot-yafet mechanisms in monolayer mos2 : Role of intravalley and intervalley processes,* Phys. Rev. B **89**, 115302 (2014).

[43] A. P. Schnyder, S. Ryu, A. Furusaki, and A. W. W. Ludwig, *Classification of topological insulators and superconductors in three spatial dimensions,* Phys. Rev. B **78**, 195125 (2008).

[44] C.-K. Chiu, J. C. Teo, A. P. Schnyder, and S. Ryu, *Classification of topological quantum matter with symmetries,* Reviews of Modern Physics **88** (2016), 10.1103/RevModPhys.88.035005.

[45] D. Varjas, T. Ö. Rosdahl, and A. R. Akhmerov, *Qsymm: algorithmic symmetry finding and symmetric hamiltonian generation,* New Journal of Physics **20**, 093026 (2018).

[46] B. Béri, *Topologically stable gapless phases of time-reversal-invariant superconductors,* Phys. Rev. B **81**, 134515 (2010).

[47] G.-B. Liu, W.-Y. Shan, Y. Yao, W. Yao, and D. Xiao, *Three-band tight-binding model for monolayers of group-vib transition metal dichalcogenides,* Phys. Rev. B **88**, 085433 (2013).

[48] K. Kosmider, J. W. González, and J. Fernández-Rossier, *Large spin splitting in the conduction band of transition metal dichalcogenide monolayers,* Phys. Rev. B **88**, 245436 (2013).

[49] A. Kormányos, G. Burkard, M. Gmitra, J. Fabian, V. Zólyomi, N. D. Drummond, and V. Fal'ko, $k \cdot p$ *theory for two-dimensional transition metal dichalcogenide semiconductors,* 2D Mater. **2**, 022001 (2015).

[50] S. Datta, *Electronic Transport in Mesoscopic Systems*, Cambridge Studies in Semiconductor Physics and Microelectronic Engineering (Cambridge University Press, 1995).

[51] C. W. Groth, M. Wimmer, A. R. Akhmerov, and X. Waintal, *Kwant: a software package for quantum transport,* New Journal of Physics **16**, 063065 (2014).

[52] P. Delplace, D. Ullmo, and G. Montambaux, *Zak phase and the existence of edge states in graphene,* Phys. Rev. B **84**, 195452 (2011).

[53] J. N. Coleman, M. Lotya, A. O'Neill, S. D. Bergin, P. J. King, U. Khan, K. Young, A. Gaucher, S. De, R. J. Smith, I. V. Shvets, S. K. Arora, G. Stanton, H.-Y. Kim, K. Lee, G. T. Kim, G. S. Duesberg, T. Hallam, J. J. Boland, J. J. Wang, J. F. Donegan, J. C. Grunlan, G. Moriarty, A. Shmeliov, R. J. Nicholls, J. M. Perkins, E. M. Grieveson, K. Theuwissen, D. W. McComb, P. D. Nellist, and V. Nicolosi, *Two-dimensional nanosheets produced by liquid exfoliation of layered materials,* Science **331**, 568 (2011).

[54] M. Chhowalla, H. S. Shin, G. Eda, L.-J. Li, K. P. Loh, and H. Zhang, *The chemistry of two-dimensional layered transition metal dichalcogenide nanosheets,* Nat. Chem. **5**, 263 EP (2013).

[55] X. Wang, Y. Gong, G. Shi, W. L. Chow, K. Keyshar, G. Ye, R. Vajtai, J. Lou, Z. Liu, E. Ringe, B. K. Tay, and P. M. Ajayan, *Chemical vapor deposition growth of crystalline monolayer mose2,* ACS Nano **8**, 5125 (2014).

[56] J. Chen, X. Zhao, S. J. R. Tan, H. Xu, B. Wu, B. Liu, D. Fu, W. Fu, D. Geng, Y. Liu, W. Liu, W. Tang, L. Li, W. Zhou, T. C. Sum, and K. P. Loh, *Chemical vapor deposition of large-size monolayer mose2 crystals on molten glass,* J. Am. Chem. Soc. **139**, 1073 (2017).

[57] D. Costanzo, H. Zhang, B. A. Reddy, H. Berger, and A. F. Morpurgo, *Tunnelling spectroscopy of gate-induced superconductivity in mos2,* Nat. Nanotechnol. **13**, 483 (2018).

[58] T. Hanaguri, Y. Kohsaka, J. C. Davis, C. Lupien, I. Yamada, M. Azuma, M. Takano, K. Ohishi, M. Ono, and H. Takagi, *Quasiparticle interference and superconducting gap in ca2-xnaxcuo2cl2,* Nat. Phys. **3**, 865 EP (2007).

[59] H. Rostami, R. Asgari, and F. Guinea, *Edge modes in zigzag and armchair ribbons of monolayer mos_2,* Journal of Physics: Condensed Matter **28**, 495001 (2016).

[60] R. Roldán, M. P. López-Sancho, F. Guinea, E. Cappelluti, J. A. Silva-Guillén, and P. Ordejón, *Momentum dependence of spin–orbit interaction effects in single-layer and multi-layer transition metal dichalcogenides,* 2D Mater. **1**, 034003 (2014).

[61] C. L. Kane and E. J. Mele, *Quantum spin hall effect in graphene,* Phys. Rev. Lett. **95**, 226801 (2005).

[62] J. C. Slater and G. F. Koster, *Simplified lcao method for the periodic potential problem,* Phys. Rev. **94**, 1498 (1954).

[63] R. Peierls, *Zur theorie des diamagnetismus von leitungselektronen,* Z. Physik **80**, 763 (1933).

[64] D. R. Hofstadter, *Energy levels and wave functions of bloch electrons in rational and irrational magnetic fields,* Phys. Rev. B **14**, 2239 (1976).

[65] T. B. Boykin, R. C. Bowen, and G. Klimeck, *Electromagnetic coupling and gauge invariance in the empirical tight-binding method,* Phys. Rev. B **63**, 245314 (2001).

6

Breakdown of the Law of Reflection at a Disordered Graphene Edge

This chapter has been previously published as E. Walter, T. Ö. Rosdahl, A. R. Akhmerov, and F. Hassler, *Breakdown of the Law of Reflection at a Disordered Graphene Edge*, Phys. Rev. Lett. **121**, 136803 (2018).

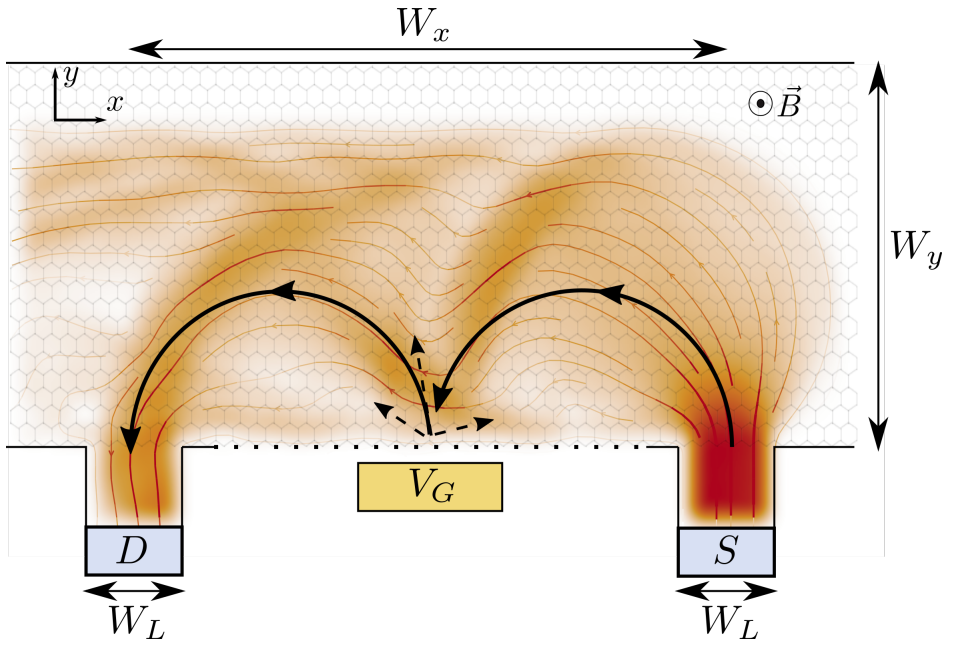

Figure 6.1: Sketch of the setup. Electrons injected at the source (S) follow cyclotron trajectories due to the perpendicular magnetic field $\boldsymbol{B} = B\hat{z}$, forming a hot spot at the boundary where most trajectories scatter. If the trajectories specularly reflect at the boundary and the separation W_x between the midpoints of the source and the drain (D) matches two cyclotron diameters, most trajectories enter the drain, and a focusing peak manifests in the nonlocal conductance. The focusing is evident in the classical cyclotron trajectory of an electron normally incident from S at the Fermi level (solid curves), and in the computed current distribution that is superimposed on the device (flow lines, colored background). A side gate V_G controls the average potential at the disordered boundary (dotted line), and allows to tune between regimes of specular and diffusive reflection (see main text). In the diffusive regime, electrons scatter into random angles as shown schematically with the dashed lines, resulting in a drop in the focusing peak conductance compared to the regime of specular reflection. The graphene sheet is grounded, such that current due to off-resonance trajectories may drain away to the sides (open boundaries).

6.1. INTRODUCTION

The law of reflection is a basic physical phenomenon in geometric optics. As long as the surface of a mirror is flat on the scale of the wavelength, a mirror reflects incoming waves specularly. In the opposite limit when the surface is rough, reflection is diffusive and an incident wave scatters into a combination of many reflected waves with different angles. This picture applies to all kinds of wave reflection, including sound waves and particle waves in quantum systems. The phenomenon has been extensively investigated both theoretically and experimentally in the past, *e.g.*, in order to understand sea-clutter in radar [1] as well as a method to measure surface roughness [2].

Graphene [3, 4] is a gapless semiconductor with a linear dispersion relation near the charge neutrality point, and therefore a diverging Fermi wavelength. Modern techniques allow for the creation of graphene monolayers of high mobility, with mean free paths of tens of microns [5–8]. This makes it possible to realize devices in which carriers

propagate ballistically over mesoscopic distances, facilitating the design of electron optics experiments [9–11]. For example, recent experiments employ perpendicular magnetic fields to demonstrate snaking trajectories in graphene *p*-*n* junctions [12, 13], or the magnetic focusing of carriers through cyclotron motion [14]. The latter tests the classical skipping orbit picture of carrier propagation along a boundary [15], and using a collimator to focus a narrow beam of electrons with a small angular spread enhances the focusing resolution [16]. The high mobility in the bulk together with a large Fermi wavelength suggest that graphene is a promising medium for the design of advanced electron optics and testing the law of reflection, cf. Fig. 6.1.

Graphene edges are rough due to imperfect lattice termination or hydrogen passivation of dangling bonds [17, 18]. Boundary roughness may adversely affect device performance [19–22]. On the other hand close to the charge neutrality point the Fermi wavelength in graphene diverges, and by analogy with optics, one may expect that the law of reflection holds and suppresses the diffusive boundary scattering.

In this chapter, we study how the microscopic boundary properties influence electron reflection off a graphene boundary. Most boundaries result in the self-averaging of the boundary disorder, and therefore obey the law of reflection. However, we find that, due to resonant scattering, electrons are reflected diffusively regardless of the Fermi wavelength when the disorder-broadened edge states overlap with $E = 0$. As a result, in this situation, the boundary of graphene never acts as a mirror and thus breaks the law of reflection. We demonstrate that this phenomenon can be observed as a dip in the nonlocal conductance in a magnetic focusing setup (see Fig. 6.1). We confirm our predictions by numerical simulations.

6.2. REFLECTION AT A DISORDERED BOUNDARY

To demonstrate the breakdown of the law of reflection, we first analyze scattering at the edge of a semi-infinite graphene sheet. We consider a zigzag edge, since the zigzag boundary condition applies to generic lattice terminations [23]. To begin with, we neglect intervalley scattering to simplify the analytical derivation, and focus on the single valley Dirac Hamiltonian

$$H = v_F \boldsymbol{\sigma} \cdot \mathbf{p}, \tag{6.1}$$

with v_F the Fermi velocity, $\boldsymbol{\sigma} = (\sigma_x, \sigma_y)^T$ the vector of Pauli matrices in the (sublattice) pseudospin space, and $\mathbf{p}$ the momentum. We later verify the validity of our conclusions with tight-binding calculations that include intervalley scattering. We introduce edge disorder by randomly sampling the most general single-valley boundary condition [23–25] over the edge, such that the boundary condition for the wave function reads

$$\psi(x, y = 0) = [\cos\theta(x)\sigma_z + \sin\theta(x)\sigma_x]\,\psi(x, y = 0), \tag{6.2}$$

where disorder enters through the position-dependent parameter θ, and $\theta = 0$ gives a zigzag segment. We take $\theta(x)$ to follow a Gaussian distribution with mean value $\mathrm{E}[\theta(x)] = \theta_0$ and covariance $\mathrm{Cov}[\theta(x), \theta(x')] = s_\theta^2 e^{-\pi(x-x')^2/d^2}$, with d the correlation length. In this work, $\mathrm{E}[A]$ is the statistical average of A over the disordered boundary, and the corresponding variance $\mathrm{Var}(A)$. The boundary condition (6.2) applies to different

microscopic origins of disorder, such as hydrogen passivation of dangling bonds [23] or edge reconstruction [26].

To solve the scattering problem, we introduce periodic boundary conditions parallel to the boundary with period L, such that the momentum $k_\parallel \in \{2\pi n/L \mid n \in \mathbb{Z}\}$ is conserved. At the Fermi energy E_F, the disordered boundary scatters an incident mode $\psi^{\text{in}}_{k_\parallel}$ into the outgoing modes $\psi^{\text{out}}_{k'_\parallel}$. The scattering state is

$$\psi_{k_\parallel} = \psi^{\text{in}}_{k_\parallel} + \sum_{k'_\parallel} \psi^{\text{out}}_{k'_\parallel} S_{k'_\parallel k_\parallel}, \tag{6.3}$$

where modes with $k_\parallel > k_F$ are evanescent but others propagating, with k_F the Fermi momentum, and $S_{k'_\parallel k_\parallel}$ the reflection amplitudes. An outgoing propagating mode moves away from the edge at the angle $\varphi_{k_\parallel} = \arctan(v_\parallel / v_\perp)$ relative to the boundary normal, with $v_\parallel$ and $v_\perp$ the velocities along and perpendicular to the boundary. For the incident propagating mode at $k_\parallel$, the quantum mechanical average reflection angle is therefore

$$\langle \varphi_{k_\parallel} \rangle = \sum_{k'_\parallel} \varphi_{k'_\parallel} |S_{k'_\parallel k_\parallel}|^2, \tag{6.4}$$

where the sum is limited to propagating modes, and $|S_{k'_\parallel k_\parallel}|^2$ is the reflection probability into the outgoing mode at $k'_\parallel$. An incident mode reflects specularly if $S_{k'_\parallel k_\parallel} = \delta_{k'_\parallel k_\parallel}$, but diffusively if it scatters into multiple angles, and the variance $\sigma^2(\varphi_{k_\parallel})$ is therefore finite for the latter. If N modes are incident, diffusiveness manifests in a finite mode-averaged variance $\sigma^2(\varphi) = \sum_{k_\parallel} \sigma^2(\varphi_{k_\parallel})/N$, or its statistical average $\mathrm{E}[\sigma^2(\varphi)]$ over the disordered boundary. If $\lambda_F \ll L$, then $\sigma^2(\varphi)$ automatically includes the statistical average $\mathrm{E}[\sigma^2(\varphi)]$, because the incident waves sample multiple different segments of the boundary within each period.

The scattering problem simplifies at the charge neutrality point $E_F = 0$, where only two propagating modes are active, one incident and one outgoing, both with $k_\parallel = 0$. The scattering matrix relating the propagating modes is therefore a phase factor $e^{i\phi}$, with ϕ the scattering phase, and the quantum mechanical averages of the preceding paragraph are not necessary. We expect diffusiveness to manifest as a finite variance $\mathrm{Var}(\phi)$, and have verified this numerically. To compute ϕ, we impose the boundary condition (6.2) on the scattering state (6.3).

If θ_0 is nonzero and $s_\theta \ll \theta_0$, ϕ follows a Gaussian distribution (see Supplementary Material 6.5.1) with the mean

$$\mathrm{E}[\phi] \overset{L \gg d}{=} -\theta_0 + \frac{s_\theta^2}{2\sin(\theta_0)} + \mathcal{O}\left(\frac{s_\theta^3}{\theta_0^3}\right) \tag{6.5}$$

and variance

$$\mathrm{Var}(\phi) = \frac{d}{L} s_\theta^2 + \mathcal{O}\left(\frac{s_\theta^3}{\theta_0^3}\right). \tag{6.6}$$

Thus $\mathrm{E}[\phi]$ is given by θ_0, with the addition of a random walk-like drift term proportional to s_θ^2. In addition, $\mathrm{Var}(\phi)$ increases with s_θ^2, but increasing the boundary length suppresses

it as $1/L$. In the limit $L \to \infty$ reflection is thus completely specular, with a fixed scattering phase ϕ. This algebraic decay of diffusive scattering resembles a classical optical mirror [2].

If $\theta_0 = 0$, surprisingly there is no suppression of $\mathrm{Var}(\phi)$ with L. Rather, we find (see Supplementary Material 6.5.1) that $\tan\phi$ follows a Cauchy distribution $f(\tan\phi) = \gamma/\pi(\tan^2\phi + \gamma^2)$ with $\mathrm{E}[\phi] = 0$, $\mathrm{Var}(\phi) \approx 2.2\, s_\theta$ linear in s_θ instead of quadratic, and $\gamma \approx 0.8\, s_\theta$ obtained numerically. In this case, the law of reflection therefore breaks down and scattering is always diffusive. The distribution of the scattering phase follows the Cauchy distribution also when the disorder is non-Gaussian and even asymmetric, as long as θ_0 is sufficiently small. For an asymmetric distribution, the value of γ/s_θ weakly depends on higher cumulants of the distribution of $\theta(x)$.

Generic graphene boundaries support bands of edge states with a linear dispersion [23, 26]. Because the matrix element between the edge state and the edge disorder is inversely proportional to the spatial extent of the edge state, the disorder broadening of these edge states is proportional to the momentum along the boundary [see Fig. 6.2(c,d)]. In other words linearly dispersing edge states turn into disorder-broadened bands with both the average velocity and the bandwidth proportional to $k_\parallel$. When these bands overlap with $E = 0$ they serve as a source of resonant scattering responsible for the breakdown of the law of reflection. Indeed, we find that the condition for diffusive scattering occurs for any $\theta_0 \lesssim s_\theta$.

To include intervalley scattering, we compute the scattering phase at the charge neutrality point using the nearest neighbour tight-binding model of graphene, with random on-site disorder in the outermost row of atoms taken from a Gaussian distribution with mean V_d and variance s_d^2. The results, shown in Fig. 6.2(b), agree with the single valley prediction of the Dirac equation up to numerical prefactors [27].

To extend our analysis to nonzero E_F, we employ the tight-binding model with on-site disorder to study the reflection angle φ at the disordered boundary numerically using Kwant [28]. The disordered edge band now resides at the energy V_d, as Figs. 6.2(c) and (d) show. Fig. 6.2(a,b) confirm that $\sigma^2(\varphi) \approx \mathrm{Var}(\phi)$ at $E = 0$. The law of reflection is broken for all s_d at $V_d = E_F$ and $\mathrm{Var}(\phi)$ increases linearly with s_d, independent of λ_F. Further, the reflection becomes specular for $s_d \lesssim |V_d - E_F|$. As Fig. 6.2(b) shows, $\mathrm{Var}(\phi)$ [$\sigma^2(\varphi)$] increases quadratically with the disorder strength s_d, but decays as $1/L$ [$1/\lambda_F$] (Fig. 6.2(a)) when the Fermi wavelength becomes large compared to the lattice constant a, such that scattering is predominantly specular. However, for $s_d \gtrsim |V_d - E_F|$ reflection becomes diffusive, and moving V_d closer to E_F [Fig. 6.2(b)] shifts the transition from specular to diffusive reflection to smaller s_d.

6.3. EXPERIMENTAL DETECTION

Any experiment that is sensitive to the microscopic properties of a disordered boundary will detect the breakdown of the law of reflection if the disordered edge band overlaps with the Fermi level. We propose to search for a transport signature of the breakdown of the law of reflection in the magnetic focusing experiment sketched in Fig. 6.1. The idea is to study the reflection of ballistic cyclotron trajectories in a magnetic field B off a graphene edge [9, 14, 15]. The use of a collimator could improve such an experiment [16].

Magnetic focusing refers to the appearance of peaks in the nonlocal conductance

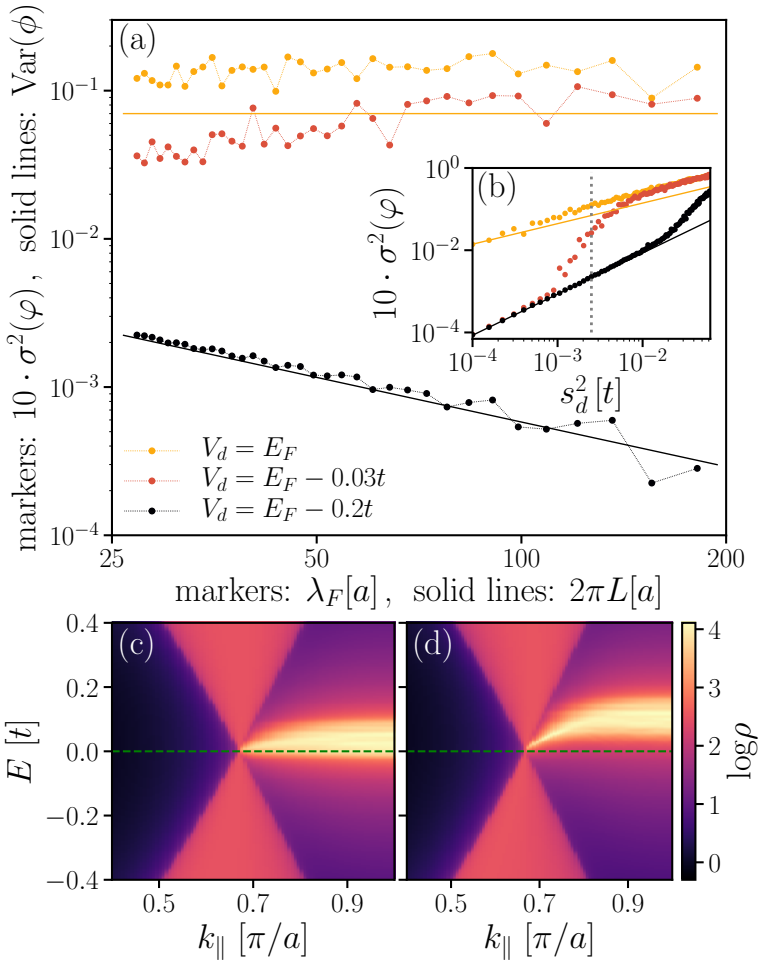

Figure 6.2: (a) Solid lines: Var(ϕ) at the Dirac points ($E_F = 0$) as a function of the boundary length L, for a disorder strength $s_d = 0.05t$ obtained from the tight-binding model. Markers: $\sigma^2(\varphi)$ at finite E_F, averaged over all incoming modes and 10^2 disorder configurations, as a function of the Fermi wavelength λ_F for the same disorder strength, obtained numerically for a semi-infinite graphene sheet with a boundary of length $L = 300a$. The values chosen for $\lambda_F = \sqrt{3}\pi ta/E_F$ correspond to E_F ranging from $0.2t$ to $0.03t$. (b) Same as (a), as a function of the disorder strength s_d^2, for a value of $2\pi L \approx 27a$ [$\lambda_F \approx 27a$, $E_F = 0.2t$]. The dotted line indicates the value of s_d used in (a). For $V_d = E_F$ the variances of both the scattering phase at $E_F = 0$ and the reflection angle at $E_F > 0$ increase linearly with s_d, independent of the Fermi wavelength, exhibiting the breakdown of the law of reflection. For $|V_d - E_F| \gtrsim s_d$, Var(ϕ) [$\sigma^2(\varphi)$] decays with increasing L [λ_F] as $1/L$ [$1/\lambda_F$] and increases quadratically with the disorder strength [as given by Eq. (6.6)]. Reflection is thus specular, but becomes diffusive for $|V_d - E_F| \lesssim s_d$. Setting V_d closer to E_F moves transition between the regimes of specular and diffusive reflection to smaller s_d. This is because of the overlap of E_F with the disorder-broadened edge band. (c, d) Momentum-resolved density of states at the disordered zigzag edge of a semi-infinite graphene sheet with a boundary of length $L = 300a$. A band of edge states with bandwidth $\propto s_d = 0.05t$ extends between the Dirac cones, residing mostly at energy V_d, with $V_d = 0.03t$ in (c) and $V_d = 0.2t$ in (d) [dashed lines].

between the source and the drain when a voltage is applied between the source and the grounded ribbon, cf. Fig. 6.1. There is an increased probability for electrons to end up in the drain whenever the separation W_x between source and drain matches an integer multiple of the cyclotron diameter $2r_c$, where $r_c = \hbar k_F / eB$ is the cyclotron radius with k_F the Fermi momentum, $\hbar$ the reduced Planck constant, and e the elementary charge. Due to the linear dispersion near the charge neutrality point in graphene, $k_F = E_F / \hbar v_F$ is linear in E_F, such that focusing peaks appear at the magnetic fields $B_n^f = 2nE_F / ev_F W_x$, $n \in \mathbb{N}$. For the setup in Fig. 6.1 but with a clean, specularly reflecting system edge, Fig. 6.3(a) shows a map of the first few focusing conductance peaks with their predicted locations marked. At resonance p, the electron beam reflects specularly $p-1$ times at the system edge before exiting into the drain, as Fig. 6.1 demonstrates for $p = 2$. On the other hand, if reflection from the boundary is diffusive, the electrons scatter into random angles off the boundary, which in general no longer result in cyclotron trajectories that are commensurate with the distance from the focus point at the boundary to the drain. In comparison with the case of specular reflection, the focusing beam at the drain is therefore diminished for diffusive edge scattering, resulting in a drop in the $p > 1$ conductance resonances. Because the reflection is diffusive when the disordered edge band overlaps with the Fermi level, by using a side gate (see Fig. 6.1) to tune the average potential at the disordered boundary, it is therefore possible to observe signatures of the breakdown of the law of reflection in the form of a conductance drop at a focusing peak.

To verify our prediction, we perform numerical simulations of the graphene focusing device with a side gate sketched in Fig. 6.1. We implement the tight-binding model for graphene in Kwant [28] and include the magnetic field via a Peierls substitution. We apply a random uniformly distributed onsite potential with mean V_d and variance s_d^2 to the first several rows of atoms adjacent to the system edge. We simulate the effect of a side gate by applying an extra potential with amplitude V_G exponentially decaying away from the sample edge on a length scale comparable to the size of the disordered region. Away from the charge neutrality point, we expect peak diffusive edge scattering to occur when the average potential by the boundary matches the Fermi energy. The relevant scales for our simulations are the hopping t, the graphene lattice constant $a = 2.46\,\text{Å}$, and the magnetic flux $\Phi \propto Ba^2$ per unit cell. Scaling the tight-binding Hamiltonian with a scaling factor s [29] by reinterpreting $t/s \equiv t$, $sa \equiv a$ and $B/s^2 \equiv B$ such that Φ is unchanged by the scaling, our simulations apply to graphene devices of realistic and experimentally realizable dimensions [14, 15]. Note that the onsite disorder correlation length is not scale invariant, and the disorder thus correlates s lattice sites in the original model.

Tuning the average potential at the disordered system edge by varying the side gate V_G reveals a clear dip in the conductance Fig. 6.3(b) around the second focusing resonance $p = 2$, which is absent when no edge disorder is included (see Supplementary Material 6.5.2). Outside the dip the conductance only changes weakly with V_G, which is the expected behavior for a clean specularly reflecting boundary. Here, the first $N = 6$ rows of sites adjacent to the edge are disordered, and the extent of the disordered region into the graphene sheet thus approximately $2.1a \ll \lambda_F \approx 18a$, such that the length scales are consistent with specular reflection. The conductance fluctuates erratically within the dip, as the line cut Fig. 6.3(c) taken from Fig. 6.3(b) at $B = 0.256\,\text{T}$ shows. These are universal conductance oscillations particular to an individual disorder configuration.

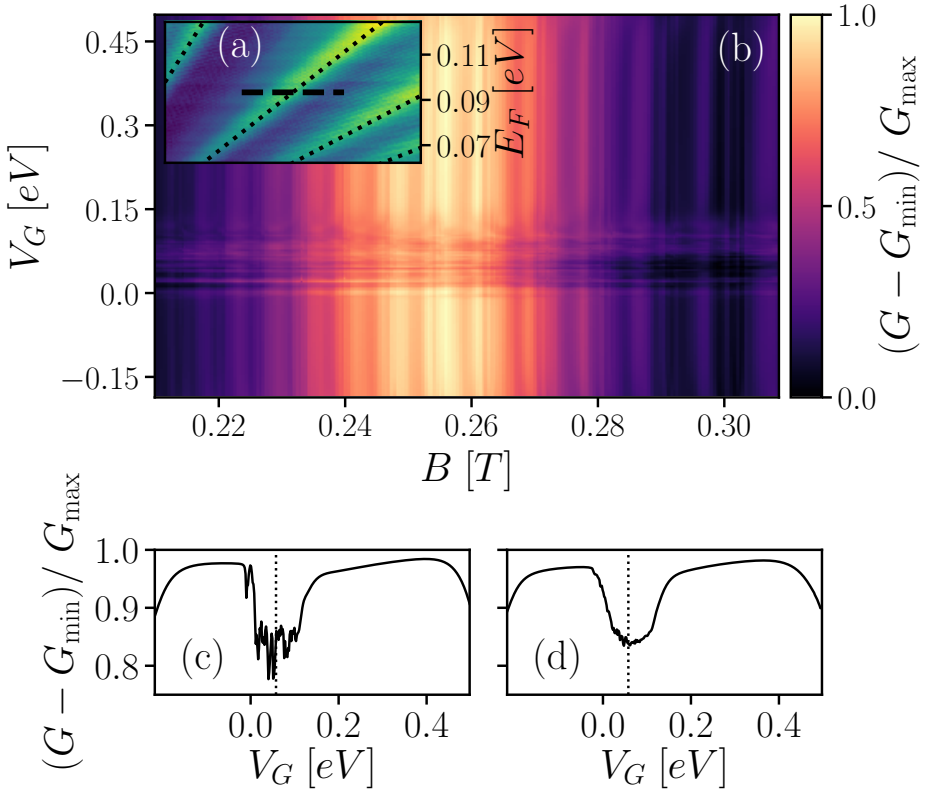

Figure 6.3: (a) Conductance as a function of Fermi energy and magnetic field showing the first 4 magnetic focusing peaks for the device sketched in Fig. 6.1 in the absence of edge disorder and with $V_G = 0$. Superimposed are the predicted locations of the focusing peaks (dotted lines), $1 \le p \le 4$ from left to right across the diagonal. The color scale is linear and ranges from about $4e^2/h$ (dark) to $28e^2/h$ (bright). (b) Conductance around the $p = 2$ focusing peak at $E_F = 0.093$ eV [dashed line in (a)] versus gate voltage. We include disorder with $V_d = 0.062$ eV and $s_d = 0.047$ eV in the first $N = 6$ rows next to the boundary. Reflection at the boundary is specular and the conductance smooth in V_G, except for a dip when the disordered edge band overlaps with the Fermi level, and reflection becomes diffusive. (c) Line cut from (b) at $B = 0.256$ T with the predicted voltage value for the dip marked. Within the dip, the conductance exhibits fluctuations dependent on the particular disorder configuration, that are washed out by disorder averaging in (d). We assume the scaling factor $s = 9$ in the tight-binding model, such that $W_x = 1.6$ μm, $W_y = 1$ μm and $W_L = 0.2$ μm.

They are washed out by disorder averaging as Fig. 6.3(d) shows, revealing an omnipresent conductance dip. Furthermore, the conductance dip appears when the disordered edge band overlaps with E_F, which is the condition for the breakdown of the law of reflection, with the V_G that aligns the band with E_F marked in Figs. 6.3(c) and (d).

6.4. CONCLUSION AND DISCUSSION

Our analysis of scattering at a disordered graphene boundary reveals a regime where specular reflection is suppressed in favor of diffusive scattering. This counterintuitive

conclusion holds even when conventional wisdom dictates that specular reflection should dominate and the boundary should act as a mirror, namely when a boundary is rough on a length scale smaller than the Fermi wavelength. The origin of this breakdown of the law of reflection is resonant scattering of the electron waves from a linear superposition of localized boundary states. Our calculations show that this phenomenon is detectable in transverse magnetic focusing experiments, by employing a side gate to tune the average potential at the boundary. In these experiments the breakdown of specular reflection manifests as a dip in the nonlocal conductance at the second focusing resonance. Because the zigzag boundary condition is generic in graphene, we expect our results to apply to an arbitrary termination direction, and to be insensitive to microscopic details. We are thus confident that this effect is experimentally observable in present day devices.

6.5. SUPPLEMENTARY INFORMATION

6.5.1. COMPUTATION OF THE SCATTERING PHASE IN THE CONTINUUM DESCRIPTION

In the following, we present the derivation of the scattering phase at $E_F = 0$ from the continuum description governed by the Dirac equation, which is valid within the linear regime of the graphene dispersion.

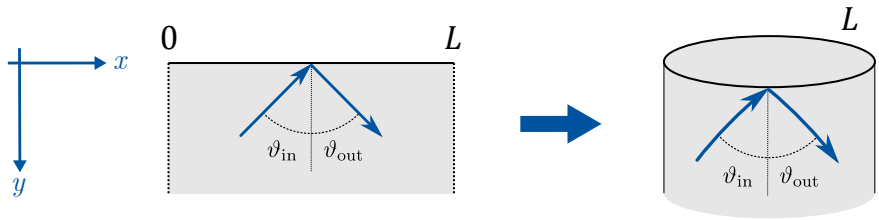

Figure 6.4: Scheme of the system geometry: A graphene sheet (gray) with translational invariance in y-direction is terminated by a single boundary at $y = 0$. Applying periodic boundary conditions (left, dotted lines) in x-direction on the semi-infinite plane is equivalent to rolling it up to a cylinder (right). L is the boundary length after applying periodic boundary conditions. Blue arrows indicate schematically the paths of an incoming and an outgoing mode, with angles relative to the surface normal of ϑ_{in} and ϑ_{out}, respectively.

We consider a cylindrical geometry as sketched in Fig. 6.4 with a boundary of length L, which in the limit $L \to \infty$ resembles a semi-infinite sheet with a single boundary at $y = 0$. We describe electronic properties in terms of the Dirac Hamiltonian of a single valley,

$$H = v_F \boldsymbol{\sigma} \cdot \mathbf{p} = -i\hbar v_F \begin{pmatrix} 0 & \partial_x - i\partial_y \\ \partial_x + i\partial_y & 0 \end{pmatrix}, \tag{6.7}$$

as defined in the main text. With the ansatz $\psi(\mathbf{r}) = e^{i\mathbf{q}\cdot\mathbf{r}} \left(\psi_A, \psi_B\right)^T$ we obtain from the Dirac equation at zero energy $H\psi = 0$

$$\begin{cases} (q_x - i q_y)\psi_B = 0, \\ (q_x + i q_y)\psi_A = 0. \end{cases} \tag{6.8}$$

Periodic boundary conditions in x-direction $\psi(x, y) = \psi(x + L, y)$ restrict the momentum $q_x = 2\pi n/L$, with $n \in \mathbb{Z}$. With the boundary at $y = 0$ and the graphene sheet extending to

positive y as shown in Fig. 6.4, we can write down all non-trivial solutions of Eq. (6.8) for given n. We can distinguish two cases, depending on the behavior for $y \to \infty$:

For $n = 0$ we have $\mathbf{q} = 0$ and therefore all states $\psi = (\psi_A, \psi_B)^T$ are solutions to the Dirac equation (6.8). We can choose an orthonormal basis $\{\psi_+, \psi_-\}$ of that two-dimensional subspace that diagonalizes the y-component of the current operator $\mathbf{J} = v_F \boldsymbol{\sigma}$, such that $\psi_\pm$ have well-defined current $\pm v_F$ perpendicular to the boundary,

$$\psi_\eta^\dagger J_y \psi_\nu = \eta v \delta_{\eta\nu}, \quad \eta, \nu = \pm, \tag{6.9}$$

$$\psi_\eta^\dagger \psi_\nu = \delta_{\eta\nu}. \tag{6.10}$$

The propagating modes are therefore the eigenstates of σ_y that can be written as $\psi_\pm = \frac{1}{\sqrt{2}}(1, \pm i)^T$. As ψ_- has a velocity $-v_F$ and is thus moving in negative y-direction, we consider it to be incoming and ψ_+ to be outgoing, respectively.

For $n \neq 0$ the Dirac equation (6.8) becomes

$$\begin{cases} (2\pi n/L - i q_y)\psi_B = 0, \\ (2\pi n/L + i q_y)\psi_A = 0. \end{cases} \tag{6.11}$$

such that we get two non-trivial solutions for each n: For $q_y = -2\pi i n/L$ and $\psi_A = 0$ we have $\psi_{n,-} = e^{2\pi i n x/L} e^{2\pi n y/L}(0,1)^T$. This mode decays exponentially into the bulk for $y \to \infty$ if $n < 0$, but is not normalizable for positive y if $n > 0$. For $q_y = 2\pi i n/L$ and $\psi_B = 0$ we have $\psi_{n,+} = e^{2\pi i n x/L} e^{-2\pi n y/L}(1,0)^T$. This mode is evanescent if $n > 0$, but not normalizable if $n < 0$. In total we thus remain with one evanescent mode for each $n \in \mathbb{Z} \setminus \{0\}$.

We can now construct a scattering state ψ from the incoming mode ψ_-, outgoing mode ψ_+ and evanescent modes $\psi_{n,\pm}$ as

$$\psi = \psi_- + S\psi_+ + \sum_{n=1}^{\infty} (\alpha_n \psi_{n,+} + \alpha_{-n} \psi_{-n,-}), \tag{6.12}$$

where $S = e^{i\phi}$ is the scattering phase that the incoming mode acquires when scattered into the outgoing one, and α_n is the amplitude to scatter into the n-th evanescent mode. A boundary is introduced by requiring this scattering state to fulfill the boundary condition

$$M\psi(x, y = 0) = \psi(x, y = 0). \tag{6.13}$$

A disordered boundary interpolating between a clean zigzag boundary and an infinite-mass (Berry-Mondragon [24]) boundary condition constitutes the most general single-valley boundary condition. This boundary condition applies to different microscopic origins of disorder, such as the staggered potential on a zigzag boundary which is produced by a passivation of the dangling bonds [23], or effects of edge reconstruction [26]. The zigzag boundary is given by the matrix $M_{zz} = \sigma_z$, whereas the Berry-Mondragon boundary is specified by $M_{\mathrm{BM}} = \boldsymbol{\sigma} \cdot (\hat{\mathbf{z}} \times \mathbf{n}_B) = \sigma_x$ for the boundary normal $\mathbf{n}_B = -\hat{\mathbf{y}}$. We therefore consider the boundary condition matrix

$$M = \cos\theta(x) M_{zz} + \sin\theta(x) M_{\mathrm{BM}} = \begin{pmatrix} \cos\theta(x) & \sin\theta(x) \\ \sin\theta(x) & -\cos\theta(x) \end{pmatrix}, \tag{6.14}$$

with a random function $\theta(x)$ to introduce disorder by a spatially fluctuating staggered potential, such that we obtain a zigzag boundary for $\theta = 0$ and an infinite-mass boundary for $\theta = \pi/2$. The value of $\theta(x)$ at the position x on the boundary is randomly taken from a Gaussian distribution with mean value θ_0 and variance s_θ^2. Furthermore, we assume a Gaussian correlation in space,

$$\mathrm{Cov}[\theta(x),\theta(x')] = s_\theta^2 e^{-\pi(x-x')^2/d^2}\,, \tag{6.15}$$

with a correlation length d that corresponds to a lattice constant, since the real problem lives on a lattice. In the limit $d \to 0$ the correlations become $\mathrm{Cov}[\theta(x),\theta(x')] \to s_\theta^2 d\delta(x-x')$.

With $\psi(x, y=0) = (\psi_A(x), \psi_B(x))^T$ we obtain from the boundary condition Eq. (6.13)

$$\mu(x)\sum_{n=0}^{\infty}\alpha_n e^{2\pi i n x/L} - \sum_{n=-1}^{-\infty}\alpha_n e^{2\pi i n x/L} - i\alpha_0 = -i\sqrt{2}\,, \tag{6.16}$$

with $\mu(x) = \tan(\theta(x)/2)$ (being 0 for a clean zigzag and 1 for the infinite-mass type boundary) and $\alpha_0 = (1+S)/\sqrt{2}$. We Fourier-transform Eq. (6.16) by applying to both sides $\frac{1}{L}\int_0^L \mathrm{d}x\, e^{-2\pi i m x/L}$, with $m \in \mathbb{Z}$, to obtain

$$\sum_{n=1}^{\infty}\tilde{\mu}_{n-m}\alpha_n + (\tilde{\mu}_{-m} - i\delta_{m,0})\alpha_0 - \sum_{n=-1}^{-\infty}\delta_{m,n}\alpha_n = -i\sqrt{2}\delta_{m,0}\,, \tag{6.17}$$

with the Fourier components of the disorder function μ,

$$\tilde{\mu}_m = \frac{1}{L}\int_0^L \mathrm{d}x\, e^{2\pi i m x/L}\mu(x)\,, \quad m \in \mathbb{Z}\,. \tag{6.18}$$

We can rephrase Eq. (6.17) in matrix form as

$$\underbrace{\begin{pmatrix} \tilde{\boldsymbol{\mu}} & \tilde{\mu}_\uparrow & 0 \\ \tilde{\mu}_\uparrow^\dagger & \tilde{\mu}_0 - i & 0 \\ \tilde{\boldsymbol{\mu}}' & \tilde{\mu}_\downarrow & -\mathbb{1} \end{pmatrix}}_{\tilde{\boldsymbol{A}}} \cdot \begin{pmatrix} \alpha_+ \\ \alpha_0 \\ \alpha_- \end{pmatrix} = \begin{pmatrix} 0 \\ -i\sqrt{2} \\ 0 \end{pmatrix}, \tag{6.19}$$

with

$$\alpha_+ = \begin{pmatrix} \vdots \\ \alpha_3 \\ \alpha_2 \\ \alpha_1 \end{pmatrix}, \quad \alpha_- = \begin{pmatrix} \alpha_{-1} \\ \alpha_{-2} \\ \alpha_{-3} \\ \vdots \end{pmatrix}, \quad \text{and}$$

$$\tilde{\boldsymbol{\mu}} = \begin{pmatrix} \ddots & \ddots & \ddots & \vdots \\ \ddots & \tilde{\mu}_0 & \tilde{\mu}_1^* & \tilde{\mu}_2^* \\ \ddots & \tilde{\mu}_1 & \tilde{\mu}_0 & \tilde{\mu}_1^* \\ \cdots & \tilde{\mu}_2 & \tilde{\mu}_1 & \tilde{\mu}_0 \end{pmatrix}, \quad \tilde{\boldsymbol{\mu}}' = \begin{pmatrix} \cdots & \tilde{\mu}_4 & \tilde{\mu}_3 & \tilde{\mu}_2 \\ \iddots & \tilde{\mu}_5 & \tilde{\mu}_4 & \tilde{\mu}_3 \\ \iddots & \tilde{\mu}_6 & \tilde{\mu}_5 & \tilde{\mu}_4 \\ \iddots & \iddots & \iddots & \vdots \end{pmatrix}, \tilde{\mu}_\uparrow = \begin{pmatrix} \vdots \\ \tilde{\mu}_3^* \\ \tilde{\mu}_2^* \\ \tilde{\mu}_1^* \end{pmatrix}, \quad \tilde{\mu}_\downarrow = \begin{pmatrix} \tilde{\mu}_1 \\ \tilde{\mu}_2 \\ \tilde{\mu}_3 \\ \vdots \end{pmatrix}. \tag{6.20}$$

Hence, we have transformed the general boundary condition Eq. (6.13) into a system of equations for the scattering phase (expressed through α_0). This system is specified by the Fourier coefficients of the disorder function μ. To solve Eq. (6.19) for S, we have to invert $\tilde{\boldsymbol{A}}$ to obtain $S = \sqrt{2}\alpha_0 - 1 = -1 - 2i\,(\tilde{\boldsymbol{A}}^{-1})_{0,0}$, where $(\tilde{\boldsymbol{A}}^{-1})_{0,0}$ is the component in the center of $\tilde{\boldsymbol{A}}^{-1}$, referring to the $n = m = 0$ Fourier components.

Due to the Gaussian correlation of $\theta(x)$ in space (Eq. (6.15)), the Fourier components $\tilde{\theta}_n = \frac{1}{L}\int_0^L \mathrm{d}x\, e^{2\pi i n x/L}\theta(x)$ decay for large n,

$$\mathrm{E}[\tilde{\theta}_n] = \theta_0\delta_{n,0}\,, \quad \mathrm{Cov}[\tilde{\theta}_n^*, \tilde{\theta}_m] \overset{d\ll L}{\approx} \delta_{n,m}\frac{s_\theta^2}{\sqrt{2\pi n_0^2}}\, e^{-n^2/2n_0^2}\,, \tag{6.21}$$

on a length scale $n_0 = L/\sqrt{2\pi}d$. The same holds for $\tilde{\mu}_n$, hence we can imagine to cut off at some $N \gg n_0$, such that the matrices in Eq. (6.20) are finite-dimensional and we can safely use standard formulae for block-wise matrix inversion to formally obtain

$$S = \frac{i - \tilde{m}}{i + \tilde{m}}\,, \tag{6.22}$$

with $\tilde{m} = \tilde{\mu}_\uparrow^\dagger \tilde{\boldsymbol{\mu}}^{-1}\tilde{\mu}_\uparrow - \tilde{\mu}_0$, and therefore

$$\phi = \arg(S) = \mathrm{atan2}\,(\mathfrak{Re}(S), \mathfrak{Im}(S)) = \mathrm{atan2}\left(1 - \tilde{m}^2, 2\tilde{m}\right), \tag{6.23}$$

where the atan2-function is closely related to the arctangent but adjusted such that it properly gives the angle between its arguments.

The inversion of $\tilde{\boldsymbol{\mu}}$ is not generically possible. However, an approximate solution can be found when $\tilde{\boldsymbol{\mu}}$ is dominated by its diagonal. We split up $\theta(x)$ into its mean value and fluctuations, $\theta(x) = \theta_0 + \delta\theta(x)$, with

$$\mathrm{E}[\delta\theta(x)] = 0\,, \tag{6.24}$$

$$\mathrm{Cov}[\delta\theta(x), \delta\theta(x')] = s_\theta^2 e^{-\pi(x-x')^2/d^2}\,, \tag{6.25}$$

according to Eq. (6.15). Assuming the disorder to be weak, $s_\theta \ll 1$, we can similarly expand $\mu(x) = \tan(\theta(x)/2)$ to get

$$\begin{aligned}\mu(x) &= \tan\left(\frac{\theta_0}{2}\right) + \frac{1 + \tan^2\left(\frac{\theta_0}{2}\right)}{2}\,\delta\theta(x) + \mathcal{O}\left(\delta\theta(x)^2\right) \\ &= \mu_0 + \delta\mu(x) + \mathcal{O}\left(\delta\mu(x)^2\right).\end{aligned} \tag{6.26}$$

The Fourier coefficients read

$$\tilde{\mu}_n = \mu_0\,\delta_{n,0} + s_\mu \tilde{x}_n\,, \tag{6.27}$$

where

$$s_\mu = \frac{1 + \tan^2\left(\frac{\theta_0}{2}\right)}{2}\, s_\theta \tag{6.28}$$

is the standard deviation of μ and

$$\tilde{x}_n = \frac{1}{L}\int_0^L \mathrm{d}x\, e^{2\pi i n x/L}\,\frac{\delta\mu(x)}{s_\mu} \tag{6.29}$$

is normalized to have variance 1 and by definition a mean value of 0. Furthermore, from Eq. (6.21) we see that

$$\mathrm{Cov}(\tilde{x}_n^*, \tilde{x}_m) \overset{d\ll L}{\approx} \delta_{n,m}\frac{1}{\sqrt{2\pi n_0^2}}\, e^{-n^2/2n_0^2}. \tag{6.30}$$

With Eq. (6.27) we get

$$\tilde{\boldsymbol{\mu}} = \mu_0\,\mathbb{1}_N + s_\mu\tilde{\boldsymbol{x}}, \tag{6.31}$$

thereby splitting it up into a diagonal part which is trivial to invert and a random Toeplitz matrix

$$\tilde{\boldsymbol{x}} = \begin{pmatrix} \ddots & \ddots & \vdots \\ \ddots & \tilde{x}_0 & \tilde{x}_1^* \\ \cdots & \tilde{x}_1 & \tilde{x}_0 \end{pmatrix}, \tag{6.32}$$

that cannot be inverted explicitly analytically.

For $\theta_0 = 0 = \mu_0$, the disorder potential $\theta(x)$ is zero on average such that the disorder-broadened edge states overlap with $E = 0$, whereas a finite $\theta_0 > s_\theta$ (or $\mu_0 > s_\mu$) shifts them away from $E = 0$. We can directly translate these two cases to the structure of $\tilde{\boldsymbol{\mu}}$:

- For finite μ_0 with small fluctuations s_μ on top, $\tilde{\boldsymbol{\mu}}$ is dominated by its diagonal. Hence, we can expand its inverse in powers of s_μ. In this case, where the law of reflection is expected to hold, we can therefore give an explicit expression for ϕ for sufficiently weak disorder.
- For a boundary with $\mu_0 = 0$ that fulfills the condition for diffusive scattering, this consideration does not work as then $\tilde{\boldsymbol{\mu}} = s_\mu\tilde{\boldsymbol{x}}$. In this case we have to rely on a numerical analysis.

SCATTERING PHASE IF LAW OF REFLECTION HOLDS

In the limit where $s_\mu \ll \mu_0$, we can expand

$$\tilde{\boldsymbol{\mu}}^{-1} = \frac{1}{\mu_0}\,\mathbb{1} - \frac{s_\mu}{\mu_0^2}\,\tilde{\boldsymbol{x}} + \mathcal{O}\left(\frac{s_\mu^2}{\mu_0^2}\right) \tag{6.33}$$

to obtain

$$\tilde{m} = -\mu_0 - s_\mu\tilde{x}_0 + \frac{s_\mu^2}{\mu_0}\sum_{n=1}^{\infty}|\tilde{x}_n|^2 + \mathcal{O}\left(\frac{s_\mu^3}{\mu_0^3}\right). \tag{6.34}$$

Expanding ϕ in powers of s_μ/μ_0, we get with Eqs. (6.26) and (6.28)

$$\phi = -\theta_0 - s_\theta \tilde{x}_0 + \frac{1}{2}\left(\tilde{x}_0^2 + \frac{1}{\sin^2\left(\frac{\theta_0}{2}\right)} \sum_{n=1}^{\infty} |\tilde{x}_n|^2\right) \tan\left(\frac{\theta_0}{2}\right) s_\theta^2 + \mathcal{O}\left(\frac{s_\theta^3}{\theta_0^3}\right). \tag{6.35}$$

Knowing the distribution of $\tilde{x}_n$ (Eq. (6.30)), we can average over all $\tilde{x}_n$ to compute mean value and variance of ϕ. We obtain

$$\mathrm{E}[\phi] = -\theta_0 + \frac{s_\theta^2}{2\sin(\theta_0)} - \frac{d}{L}\frac{s_\theta^2}{2\tan(\theta_0/2)} + \mathcal{O}\left(\frac{s_\theta^3}{\theta_0^3}\right), \tag{6.36}$$

$$\mathrm{Var}(\phi) = \frac{d s_\theta^2}{L} + \mathcal{O}\left(\frac{s_\theta^3}{\theta_0^3}\right). \tag{6.37}$$

SCATTERING PHASE FOR BROKEN LAW OF REFLECTION

For $\mu_0 = 0$, where the disorder-broadened edge states overlap with the Fermi energy $E = 0$, we have $\tilde{\boldsymbol{\mu}} = s_\mu \tilde{\boldsymbol{x}}$, and hence with Eqs. (6.27), (6.28)

$$\tilde{m} = \frac{s_\theta}{2}\chi, \quad \text{with} \quad \chi = \tilde{x}_\uparrow^\dagger \tilde{\boldsymbol{x}}^{-1} \tilde{x}_\uparrow - \tilde{x}_0. \tag{6.38}$$

6

We obtain

$$\phi = \mathrm{atan2}\left(1 - s_\theta^2 \chi^2/4, s_\theta \chi\right). \tag{6.39}$$

For small s_θ we have $\phi = s_\theta \chi + \mathcal{O}(s_\theta^3)$, hence the distribution of ϕ is directly linked to the distribution of χ, which we will now further explore.

Due to Eq. (6.30), the elements of $\tilde{\boldsymbol{x}}$ decay away from the diagonal, $\mathrm{E}[|\tilde{x}_n|^2] \sim \exp(-n^2/2n_0^2)$. In the limit $n_0 \to 0$, which corresponds to the limit $d/L \to \infty$, *i.e.*, completely correlated (constant) disorder, the matrix $\tilde{\boldsymbol{x}}$ will therefore be essentially diagonal. In 0th order we have $\tilde{\boldsymbol{x}} = \tilde{x}_0 \mathbb{1}$, and therefore

$$\chi = \frac{\sum_{n=1}^{\infty} |\tilde{x}_n|^2}{\tilde{x}_0} - \tilde{x}_0. \tag{6.40}$$

Assuming the $\tilde{x}_n$ to still be approximately independent (although the approximation made in Eq. (6.30) does not hold in the limit $d/L \to \infty$), due to the central limit theorem the numerator and denominator are independent Gaussian distributed variables, with zero (or approximately zero) mean. As a result, the first term χ_1 of Eq. (6.40) follows a Cauchy distribution

$$f_{\chi_1}(x) = \frac{1}{\pi}\frac{\gamma}{x^2 + \gamma^2}. \tag{6.41}$$

However, its scale parameter scales as $\gamma \sim \exp(-1/n_0^2)$, therefore in the limit $n_0 \to 0$ we remain with the second term χ_0 of Eq. (6.40), $\chi = \chi_0 = -\tilde{x}_0$. In the limit $d/L \to \infty$ the approximation of Eq. (6.30) does not hold for $\tilde{x}_0$; instead we find $\mathrm{Var}(\tilde{x}_0) = 1$, such that ϕ is normally distributed with mean 0 and variance s_θ^2.

In fact, we are however interested in the distribution of ϕ in the opposite limit, $L/d \to \infty$. In this limit $\chi_0 = -\tilde{x}_0$ becomes small, $\mathrm{Var}(\tilde{x}_0) = 1/\sqrt{2\pi n_0^2} = d/L$, whereas we find numerically that χ_1 still follows a Cauchy distribution, with a scale parameter γ that becomes independent of L/d and can be evaluated numerically as $\gamma \approx 0.8\, s_\theta$. Remarkably, the value of γ/s_θ we obtain numerically is not universal, but depends weakly on the original distribution of the disorder $\theta(x)$. If we choose these parameters to be not normally distributed but to follow any other distribution, χ is still Cauchy distributed, but the scale parameter γ will also depend on the higher cumulants of the chosen disorder distribution.

Based on this distribution, we can evaluate mean value and variance of the scattering phase ϕ. Since f_{χ_1} is even and ϕ is an odd function of χ, we directly see that $\mathrm{E}[\phi] = 0$. Furthermore, we can numerically evaluate the integral in $\mathrm{E}[\phi^2]$ to obtain

$$\mathrm{Var}(\phi) \approx 2.2\, s_\theta\,. \tag{6.42}$$

6.5.2. MAGNETIC FOCUSING CONDUCTANCE IN THE ABSENCE OF EDGE DISORDER

In order to verify that the conductance dip at the second focusing resonance is a consequence of edge disorder, we compare the focusing conductance with edge disorder to the focusing conductance of a device with a clean boundary. The setup is otherwise the same as the one we present in the main text, with the parameters identical to those used to obtain Figs. 3 (b)-(d) of the main text.

The results are shown in Fig. 6.5, where Fig. 6.5 (a) shows the focusing conductance versus gate voltage and magnetic field strength without disorder, *i.e.*, with $V_d = s_d = 0$. The average potential at the boundary aligns with the Fermi level at a gate voltage $V_G \approx 0.2$ eV, which is larger than in the case with disorder included (see also Fig. 3 (b) of the main text). This distinction arises due to the difference in the average edge disorder potential V_d, which is nonzero when disorder is included. At large negative gate potentials $V_G \lesssim -0.15$ eV, resonant conductance oscillations also appear because the gate forms a quantum well by the boundary. A similar phenomenon occurs in the case with edge disorder, but outside the energy window we consider, and is unrelated to the mechanism we are investigating. In Fig. 6.5 (a), some conductance oscillations appear in the conductance around the charge neutrality point $V_G \approx 0.2$ eV, but no clear dip is visible. Furthermore, Fig. 6.5 (b) gives a comparison of conductance line cuts at $B = 0.255$ T for a clean boundary with the case including edge disorder from Fig. 3 (b) of the main text. We see that the oscillations when the edge potential aligns with the Fermi level in the clean case are much smaller in scale than the conductance dip that appears with the inclusion of edge disorder. The same trends are visible in Fig. 6.5 (c), which compares the focusing conductance averaged over magnetic field values at the second focusing peak, with and without edge disorder. Therefore, we conclude that the dip in the focusing conductance at the second focusing peak arises due to edge disorder, namely when the average potential at the boundary aligns the disordered band of edge states with the Fermi level.

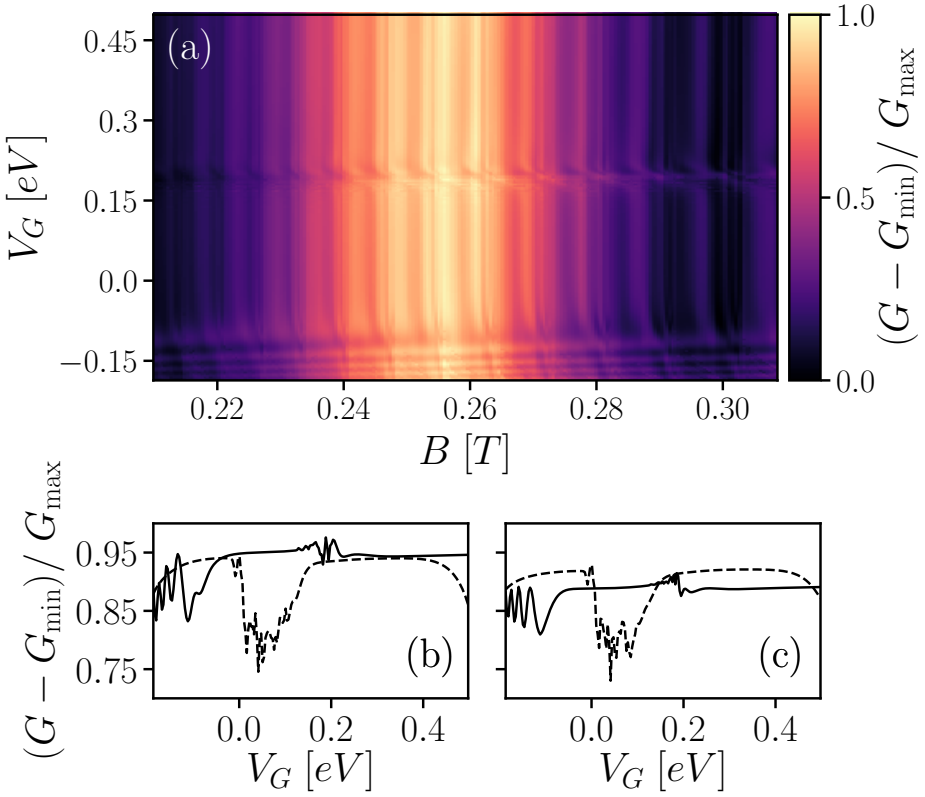

Figure 6.5: (a) Conductance around the second focusing peak at $E_F = 0.093$ eV versus gate voltage without edge disorder, *i.e.*, $V_d = s_d = 0$. (b) Line cuts of the focusing conductance at $B = 0.255$ T versus gate voltage, without edge disorder (solid line) from (a), and with edge disorder from Fig. 3 (b) of the main text (dashed line). (c) Line cuts of the focusing conductance versus gate voltage averaged over the magnetic field values $0.247 \leq B \leq 0.259$ T at the second focusing resonance, without (solid line) and with (dashed line) edge disorder. The data with disorder is taken from Fig. 3 (b) of the main text. In the absence of edge disorder, a small region of resonant conductance peaks appears around $V_G = 0.2$ eV, as the average potential in the boundary aligns with the Fermi level, but unlike the case with disorder, no clear dip is present. When the boundary is clean, the gate forms a quantum well by the boundary at large negative gate potentials $V_G \lesssim -0.15$ eV, resulting in resonant oscillations in the conductance. Similar oscillations also appear in the case with edge disorder, but at even larger negative gate potentials because of an overall average potential shift by the boundary due to onsite disorder, $V_d = 0.062$ eV.

REFERENCES

[1] H. Davies, *The reflection of electromagnetic waves from a rough surface,* Proc. Inst. Elec. Eng. IV **101**, 209 (1954).

[2] H. E. Bennett and J. O. Porteus, *Relation between surface roughness and specular reflectance at normal incidence,* J. Opt. Soc. Am. **51**, 123 (1961).

[3] A. K. Geim and K. S. Novoselov, *The rise of graphene,* Nature Materials **6**, 183 (2007).

[4] A. H. Castro Neto, F. Guinea, N. M. R. Peres, K. S. Novoselov, and A. K. Geim, *The electronic properties of graphene,* Rev. Mod. Phys. **81**, 109 (2009).

[5] C. H. Lui, L. Liu, K. F. Mak, G. W. Flynn, and T. F. Heinz, *Ultraflat graphene,* Nature **462**, 339 (2009).

[6] C. R. Dean, A. F. Young, I. Meric, C. Lee, L. Wang, S. Sorgenfrei, K. Watanabe, T. Taniguchi, P. Kim, K. L. Shepard, and J. Hone, *Boron nitride substrates for high-quality graphene electronics,* Nature Nanotech. **5**, 722 (2010).

[7] A. S. Mayorov, R. V. Gorbachev, S. V. Morozov, L. Britnell, R. Jalil, L. A. Ponomarenko, P. Blake, K. S. Novoselov, K. Watanabe, T. Taniguchi, and A. K. Geim, *Micrometer-scale ballistic transport in encapsulated graphene at room temperature,* Nano Lett. **11**, 2396 (2011).

[8] L. Banszerus, M. Schmitz, S. Engels, M. Goldsche, K. Watanabe, T. Taniguchi, B. Beschoten, and C. Stampfer, *Ballistic transport exceeding 28 μm in cvd grown graphene,* Nano Lett. **16**, 1387 (2016).

[9] H. van Houten and C. Beenakker, *Analogies in optics and micro electronics,* (Kluwer, Dordrecht, 1990) Chap. Quantum Point Contacts and Coherent Electron Focusing.

[10] V. V. Cheianov, V. Fal'ko, and B. L. Altshuler, *The focusing of electron flow and a veselago lens in graphene p-n junctions,* Science **315**, 1252 (2007).

[11] S. Chen, Z. Han, M. M. Elahi, K. M. M. Habib, L. Wang, B. Wen, Y. Gao, T. Taniguchi, K. Watanabe, J. Hone, A. W. Ghosh, and C. R. Dean, *Electron optics with p-n junctions in ballistic graphene,* Science **353**, 1522 (2016).

[12] P. Rickhaus, P. Makk, M.-H. Liu, E. Tóvári, M. Weiss, R. Maurand, K. Richter, and C. Schönenberger, *Snake trajectories in ultraclean graphene p–n junctions,* Nature Commun. **6**, 6470 (2015).

[13] T. Taychatanapat, J. Y. Tan, Y. Yeo, K. Watanabe, T. Taniguchi, and B. Özyilmaz, *Conductance oscillations induced by ballistic snake states in a graphene heterojunction,* Nature Commun. **6**, 6093 (2015).

[14] T. Taychatanapat, K. Watanabe, T. Taniguchi, and P. Jarillo-Herrero, *Electrically tunable transverse magnetic focusing in graphene,* Nature Phys. **9**, 225 (2013).

[15] S. Bhandari, G.-H. Lee, A. Klales, K. Watanabe, T. Taniguchi, E. Heller, P. Kim, and R. M. Westervelt, *Imaging cyclotron orbits of electrons in graphene,* Nano Lett. **16**, 1690 (2016).

[16] A. W. Barnard, A. Hughes, A. L. Sharpe, K. Watanabe, T. Taniguchi, and D. Goldhaber-Gordon, *Absorptive pinhole collimators for ballistic dirac fermions in graphene,* Nature Communications **8**, 15418 EP (2017).

[17] Y.-W. Son, M. L. Cohen, and S. G. Louie, *Energy gaps in graphene nanoribbons,* Phys. Rev. Lett. **97**, 216803 (2006).

[18] D. Halbertal, M. Ben Shalom, A. Uri, K. Bagani, A. Y. Meltzer, I. Marcus, Y. Myasoedov, J. Birkbeck, L. S. Levitov, A. K. Geim, and E. Zeldov, *Imaging resonant dissipation from individual atomic defects in graphene,* Science **358**, 1303 (2017).

[19] D. A. Areshkin, D. Gunlycke, and C. T. White, *Ballistic transport in graphene nanostrips in the presence of disorder: Importance of edge effects,* Nano Lett. **7**, 204 (2007).

[20] M. Evaldsson, I. V. Zozoulenko, H. Xu, and T. Heinzel, *Edge-disorder-induced anderson localization and conduction gap in graphene nanoribbons,* Phys. Rev. B **78**, 161407 (2008).

[21] S. Masubuchi, K. Iguchi, T. Yamaguchi, M. Onuki, M. Arai, K. Watanabe, T. Taniguchi, and T. Machida, *Boundary scattering in ballistic graphene,* Phys. Rev. Lett. **109**, 036601 (2012).

[22] V. K. Dugaev and M. I. Katsnelson, *Edge scattering of electrons in graphene: Boltzmann equation approach to the transport in graphene nanoribbons and nanodisks,* Phys. Rev. B **88**, 235432 (2013).

[23] A. R. Akhmerov and C. W. J. Beenakker, *Boundary conditions for Dirac fermions on a terminated honeycomb lattice,* Phys. Rev. B **77**, 085423 (2008).

[24] M. V. Berry and R. J. Mondragon, *Neutrino billiards: time-reversal symmetry-breaking without magnetic fields,* Proc. R. Soc. Lond. A **412**, 53 (1987).

[25] E. McCann and V. I. Fal'ko, *Symmetry of boundary conditions of the Dirac equation for electrons in carbon nanotubes,* J. Phys. Condens. Matter **16**, 2371 (2004).

[26] J. A. M. van Ostaay, A. R. Akhmerov, C. W. J. Beenakker, and M. Wimmer, *Dirac boundary condition at the reconstructed zigzag edge of graphene,* Phys. Rev. B **84**, 195434 (2011).

[27] E. Walter, T. O. Rosdahl, A. R. Akhmerov, and F. Hassler, *Breakdown of the law of reflection at a disordered graphene edge,* Phys. Rev. Lett. **121**, 136803 (2018).

[28] C. W. Groth, M. Wimmer, A. R. Akhmerov, and X. Waintal, *Kwant: a software package for quantum transport,* New Journal of Physics **16**, 063065 (2014).

[29] M.-H. Liu, P. Rickhaus, P. Makk, E. Tóvári, R. Maurand, F. Tkatschenko, M. Weiss, C. Schönenberger, and K. Richter, *Scalable tight-binding model for graphene,* Phys. Rev. Lett. **114**, 036601 (2015).

CURRICULUM VITÆ

Tómas Örn ROSDAHL

27-08-1989 Born in Reykjavík, Iceland.

EDUCATION

1995–2005 Elementary and middle school (*grunnskólapróf*)
Grunnskóli Seltjarnarness, Seltjarnarnes, Iceland

2005–2009 Junior college (*stúdentspróf*)
Menntaskólinn í Reykjavík, Reykjavík, Iceland

2009–2012 B.Sc. in Physics, *summa cum laude*
University of Iceland, Reykjavík, Iceland

2012–2014 M.Sc. in Physics
University of Iceland, Reykjavík, Iceland (2012-2014)
Lund University, Lund, Sweden (2012-2013)

M.Sc. Thesis: Snaking states and flux-periodic oscillations in cylindrical core-shell nanowires
Promotor: Prof. dr. V. Guðmundsson
Copromotor: Prof. dr. A. Manolescu

2014 Research assistant
Reykjavík University, Reykjavík, Iceland
Supervisor: Prof. dr. A. Manolescu

2015–2019 PhD. in Physics
Delft University of Technology, Delft, Netherlands

Thesis: Symmetries and Boundary Conditions of Topological Materials: General Theory and Applications
Promotor: Dr. A. R. Akhmerov
Copromotor: Dr. M. T. Wimmer

LIST OF PUBLICATIONS

1. **Tómas Örn Rosdahl**, Dániel Varjas, and Anton Roustiamovich Akhmerov, *General approach to boundary conditions and spectra of continuum Hamiltonians: matching to tight binding edges*, manuscript in preparation.

2. Lin Wang, **Tomas Orn Rosdahl**, and Doru Sticlet, *Platform for nodal topological superconductors in monolayer molybdenum dichalcogenides*, Phys. Rev. B **98**, 205411 (2018).

3. E. Walter, **T. Ö. Rosdahl**, A. R. Akhmerov, and F. Hassler, *Breakdown of the Law of Reflection at a Disordered Graphene Edge*, Phys. Rev. Lett. **121**, 136803 (2018).

4. Dániel Varjas, **Tómas Ö. Rosdahl**, and Anton R. Akhmerov, *Qsymm: Algorithmic symmetry finding and symmetric Hamiltonian generation*, New J. Phys. **20**, 093026 (2018).

5. **T. Ö. Rosdahl**, A. Vuik, M. Kjaergaard, and A. R. Akhmerov, *Andreev rectifier: A nonlocal conductance signature of topological phase transitions*, Phys. Rev. B **97**, 045421 (2018).

6. Andrei Manolescu, George Alexandru Nemnes, Anna Sitek, **Tomas Orn Rosdahl**, Sigurdur Ingi Erlingsson, and Vidar Gudmundsson, *Conductance oscillations of core-shell nanowires in transversal magnetic fields*, Phys. Rev. B **93**, 205445 (2016).

7. **Tomas Orn Rosdahl**, Andrei Manolescu, and Vidar Gudmundsson *Signature of Snaking States in the Conductance of Core–Shell Nanowires*, Nano Lett., **15**, 254 (2015).

8. **Tomas Orn Rosdahl**, Andrei Manolescu, and Vidar Gudmundsson *Spin and impurity effects on flux-periodic oscillations in core-shell nanowires*, Phys. Rev. B **90**, 035421 (2014).

9. Andrei Manolescu, **Tomas Orn Rosdahl**, Sigurdur I. Erlingsson, Llorens Serra, and Vidar Gudmundsson, *Snaking states on a cylindrical surface in a perpendicular magnetic field*, Eur. Phys. J. B **86**, 445, (2013).